DETERMINATION OF CRYSTALLIZATION KINETICS USING *IN-SITU* MEASUREMENT TECHNIQUES AND MODEL-BASED EXPERIMENTAL DESIGN & ANALYSIS

Dissertation

Zur Erlangung des akademischen Grades
Doktoringenieur (Dr.-Ing.)

genehmigt durch das
Zentrum für Ingenieurwissenschaften
der Martin-Luther-Universität Halle-Wittenberg
als organisatorische Grundeinheit für Forschung und Lehre im Range einer Fakultät
(§75 Abs. 1 HSG LSA, §19 Abs. 1 Grundordnung)

von
Dipl.-Ing. Jörg Heinrich
geboren am 11. Mai 1978 in Wolfen, Deutschland

Geschäftsführender Direktor (Dekan) und Vorsitzender der Promotionskommission:
Prof. Dr.-Ing. habil. Dr. h. c. H. Altenbach (Martin-Luther-Universität Halle-Wittenberg)

Gutachter:
1. Prof. Dr.-Ing. habil. J. Ulrich (Martin-Luther-Universität Halle-Wittenberg)
2. Prof. Dr. M. Mazzotti (ETH Zürich)

Tag der Verteidigung: 15. Dezember 2008

Acknowledgments

Erklärung an Eides statt

Hiermit erkläre ich, Jörg Heinrich, dass ich die vorliegende Dissertation selbständig und ohne fremde Hilfe verfasst, andere als die von mir angegebenen Quellen und Hilfsmittel nicht benutzt und die den benutzten Werken wörtlich oder inhaltlich entnommenen Stellen als solche kenntlich gemacht habe.

Halle (Saale), 19.09.2008   Jörg Heinrich

Table of Contents

1 Crystallization as a Separation and Particle Generation Process

Crystallization is a common process in nature and every day's life. Since millions of years it has played a vital role in the formation of stalactites within caves and precious stones such as diamonds and sapphires. The knowledge of crystallization of salt from seawater can be dated back as far as 2700 BC found on a Chinese print and on an Egyptian "Papyrus Ebers" at around 1500 BC. In 800-700 BC Homer described frozen water by using the Greek term "crymos/crymyos" [Hur93]. Besides the wonderful different snowflakes, nature controls the formation of ice in a very efficient manner using additives. Fish that inhabit the polar seas are using anti-freeze proteins [Kni91], whereas other proteins can induce the formation of ice already at 5 °C [Pat97].

Performance criteria of consumer products are strongly dependent on the understanding of crystallization phenomena. The mouth feel of chocolate is mainly determined by the crystal form of the cocoa butter [Cos06]. In the making of ice cream, crystals should have a size smaller than 100 μm to control the texture [Cos06]. Furthermore, crystallization can determine the free flowing and non-caking behaviour of table salt and the brightness of colours (pigments) [Aue05].

Crystallization, however, is not always desired. It can become a sincere problem such as in the occurrence of kidney and ureteric stones [Gro06]. Lime depositing inside kettles or sediments forming in wine are further examples. Polymorphism can cause problems in intellectual property rights as the cases Ritonavir and Zantac^{TM} showed [Sed99, Dat04]. The law case of the latter had an estimated value of US$ 1,500,000,000 [Sed99]. This situation is further complicated by the report of "disappearing" polymorphs leading to an apparent loss of control [Dun95]. The manufacturing of crystals and layers can be characterised as a "multi-billion-dollar industry" [Sch00]. Charpentier [Cha07] noted that crystalline, amorphous or polymeric substances represent 60% of all products sold by the chemical industry.

However, in comparison with fluid phase processes, particulate processes are still not as developed as documented by the "Rand and Merrow Reports" [Mer00a], summarising significant differences in scale-up and start-up performances. Possible reasons might be the complex physics of particulate processes that are much harder to model and/or the non-availability of appropriate measuring instruments. This is mirrored by the "use maturity versus technological maturity" diagram shown in figure 1-1 that was proposed by Keller [Kel87] and still declared valid in 2005 [Gór05]. It compares the crystallization process to other separation methods.
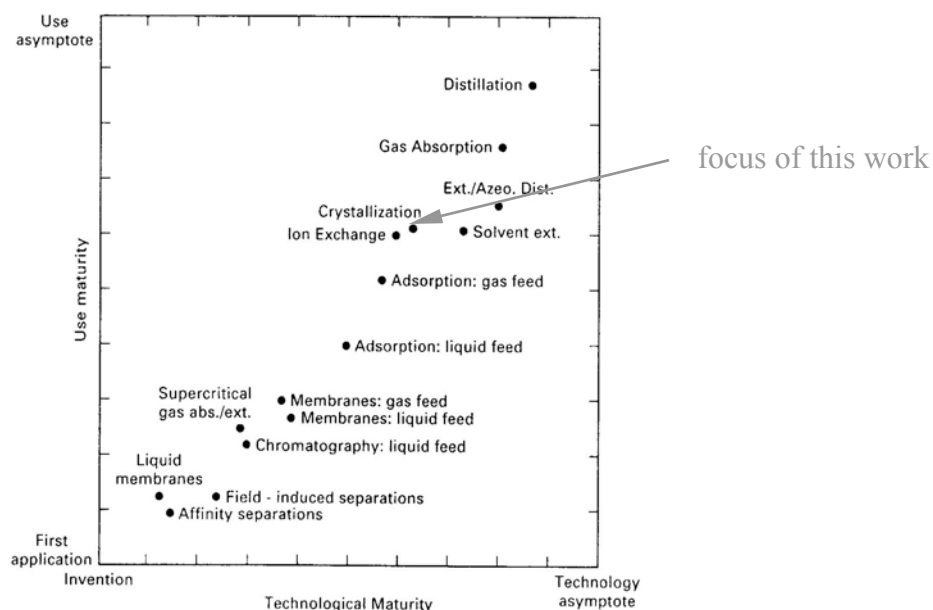
Figure 1-1: Position of crystallization within the "use maturity versus technological maturity" diagram [Kel87] (taken from Seader et al. [Sea06])

From a historical point of view, the process of crystallization was in 1984 still described as an "art" [Gar84]. Concerted effort has since been made to represent crystallization within the general framework of chemical (reaction) engineering [Gar84, Kle91, Lor04, Sch05]. Although crystallization has gained increasing importance during the last decades, surprisingly little has changed in the actual design of crystallizers [Hof05, Hei06]. According to Hofmann [Hof05], 92% of the current build crystallizers are of "Forced-Circulation" type. It seems to be that industry does not ask for a more well defined larger particle size distribution that can be produced by a "Draft-Tube-Baffle" (7%) or "Oslo" (1%) crystallizer. For the production of particles in the sub-micron range, the use of micro-reactors, T- or Y-Mixers, Impinging Jet, Taylor-Couette or Oscillatory Flow Reactor as well as working with supercritical solutions might be appropriate [Hei06]. However, the developments of most of these reactors are still only at the research or pilot-plant level and do not always offer an improvement over conventional techniques. Therefore, industry is still mainly using the "old" equipment, often just simple stirred tank reactors [Hei06]. Downstream processes such as filtration and drying, size enlargement (tableting), size reduction (grinding) up to packaging of the product can significantly alter the carefully controlled product properties produced in the crystallizer [Jon02].

During the last years a refocusing of the industry, from "commodities" to fine, specialty, pharmaceutical, food and biotechnology industries took place. Crystallization is thereby often the key step in the production of high-value added products with specific properties and functionalities. Févotte [Fév07] and Nagy [Nag07] estimated that crystallization is involved in 80 to 90% of the production processes of high-performance chemicals. All of these products must meet defined physical (size, morphology, surface properties, polymorph) and chemical (purity, composition) properties. From a conceptual point of view, independent of the

respective industry, the desired product quality of the final crystals is influenced by the technical equipment, the kinetics and the underlying thermodynamics (chemistry). Figure 1-2 illustrates the product design that can be seen as a forward and an inverse problem (see also Wibowo et al. [Wib05]).
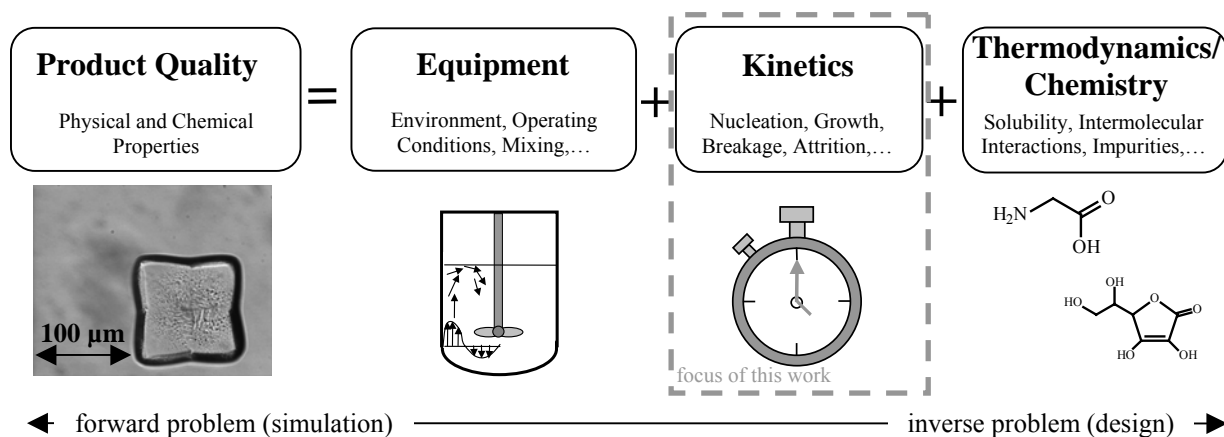
Figure 1-2: Product design as a forward and inverse problem

The work will restrict itself to the kinetics. Kinetics are describing the time behaviour of a particle generation process. The rate constants are the key to answer the following questions:

- How long must the residence time be to get 10 nm or 1000 µm crystals?
- How must the process be operated to get a narrow or broad size distribution of a median size of 200 µm?
- Is the desired size distribution feasible at all (reverse engineering)?

Without the knowledge of the kinetics designing any crystallizer becomes speculative and difficulties arise when estimating capital and operating costs. In other word, although the process might, in principle, be possible from a thermodynamic point of view (solid-liquid equilibrium phase diagram) the kinetics can still make the process infeasible. Because of the competitive market situation, a faster development and implementation of new and more reliable crystallization processes becomes increasingly critical. The kinetic rate constants must often be determined under minimising time and resource expenditure, reducing the amount of starting material by simultaneously increasing the statistical confidence of the derived constants.

Within this work, special emphasis is placed on crystallization from solution. Important trends in this field have been reviewed on a regular basis [Gar85, Ulr94, Ulr03a, Kra03a, Ulr04]. The main points can be summarised as:

- Still, although much progress has been made, the development of sensors that measure supersaturation and particle size distributions (in-line or in-situ, fast)
- Working on and combining of all length and time scales
- Finding and predicting polymorphs
- Crystallization of substances originating from bioprocesses, for example proteins
- Modelling of multiphase flow, particle-particle interactions

The work will focus on the first bullet point and its application towards the determination of crystallization kinetics although the second bullet point will be partly touched on. Many advances have been made in the field of in-situ measurement techniques that allow the actual recording of product properties in "real time". In particular, the pharmaceutical industry is forced by the Food and Drug Administration to implement "Process Analytical Technologies (PAT)", whereas other "commodity" industries are already advanced in applying it [Dün07]. This strategy has led to a shift from quality-by-testing towards quality-by-design. However, the use of these in-situ measurement techniques often pose new challenges in evaluating the large amount of recorded data, especially if quantitative information must be obtained.

2 Crystallization from a Multiscale Point of View

2.1 Length Scale

Macroscopic properties are the consequences of nano- and microscopic properties [Kna86, Peu05]. From a crystal-engineering point of view the control at the molecular level allows, in principle, the tuning of macroscopic properties [Des03]. However, there is still a long way to go, to finally use information from the molecular scale for process modelling [Hor06].

The length scale might span from 10^{-17} metres for a quark or lepton up to 1000 metres for a chemical site. Within crystallization, the focus is "only" on 1,000,000 orders of magnitude in size ranging from nanometer to millimetre that are the size of an ion or molecule and the size of a crystal, respectively. Figure 2-1 illustrates important length scales within crystallization for the precipitation of calcium carbonate [Sch06a]. Additional information have been added by considering data from various references [Gar85, Kin02, Gar02, Jud04, Koc06, Sch06]. The arrows only indicate the range and not an exact value.
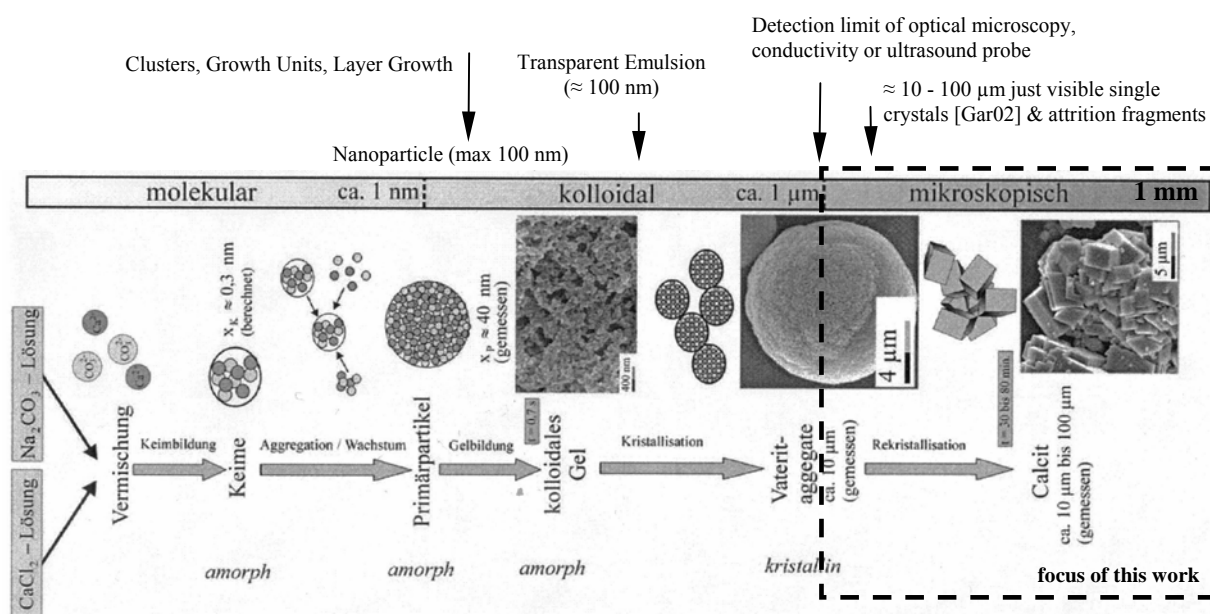
Figure 2-1: Length scales within crystallization according to Schlombach [Sch06a]

According to Larson et al. [Lar86] and Ginde et al. [Gin92] the cluster size in supersaturated solutions of citric acid, urea, sodium nitrate and potassium sulphate ranges between 1 and 10 nm ($L_{critical} \sim 1/S$). In the nanoparticle size range surface rather than volume forces control the process. Consequently, interfacial and surface properties (surface chemistry and physics) are coming into focus [Peu05]. Current research ranges from tailoring particle morphology by additives using molecular modelling [Fie07], via the precipitation of nanoparticles [Sch06b], up to hollow needles [Det07]. The entire crystal becomes visible to the "naked eye" when it reaches the microscopic range. The error associated with considering particles only from a size of about 1 μm, being the detection limit of many measuring probes, was studied by Farell et al. [Far94]. It was concluded that for a system with a low nucleation and fast growth rate

the percentage of uncounted particles (< 4 μm) is at around 6%. For systems with a high nucleation and low growth rate the percentage of uncounted particles (< 4 μm) increases up to 35%.

2.2   Time Scale

The time scale of each mechanism is ultimately related to the kinetic. The characteristic times can vary from femto (10^{-15}) seconds on an atomic level up to days (> 10^{+5} seconds) for the production of a consumer product. Table 2-1 summarises characteristic times relevant for crystallization processes, taken from various references [Dir91, Ath99, Bal99, Mer01, Mul01, Hof04, Mar06]. Beside the approximate values given in table 2-1, the following average values might be assumed: $\rho_{Crystal,mol}$ = 30,000 mol/m³, d_m = 1·10^{-9} m, D_{AB} = 1·10^{-9} m²/s, K = 0.414 [-], R_{uni} = 8.314 J/(mol·K), k_{Boltz} = 1.38·10^{-23} J/K, ν = 1, $c_{eq,mol}$ and c_{mol} ≈ 0.01 - 5000 mol/m³.

Table 2-1: Characteristic times of kinetic mechanisms observed within crystallization processes

Mechanism	Characteristic Equation		Approximate Values
Kinetics			
Primary Nucleation (Induction Time) [Dir91, Bal99]	$\tau_{Induction} = \dfrac{6 \cdot (d_m)^2 \cdot n^*}{D_{AB} \cdot \ln S} \sim \dfrac{1}{B}$	(2.1)	B ≈ 10^{10} - 10^{17} #/(m³·s) n* ≈ 5 - 1000, here 50 S ≈ 1.001 – 1000 L < 10 nm
Growth [Bal99]	$\tau_{Growth} = \dfrac{c_{mol}}{\rho_{Crystal,mol} \cdot G \cdot a_{Surf}}$	(2.2)	G ≈ 1·10^{-9} - 1·10^{-7} m/s a_{Surf} ≈ 10^2 - 10^6 m²$_{Crystal}$/m³ a_{Surf} = 6·φ_V/L L = 0.005 – 1000 μm
Dissolution [Mul01]	$\tau_{Diss} = \dfrac{L^2 \cdot \rho_{Crystal,mol}}{8 \cdot D_{AB} \cdot c_{eq,mol}}$	(2.3)	L = 0.005 – 1000 μm
Agglomeration (half-life) [Hof04, Mar06]	$\tau_{Agg} = \dfrac{1}{\beta_0 \cdot \underbrace{\dfrac{6 \cdot \varphi_V}{\pi \cdot L^3}}_{Number\ per\ m^3}}$	(2.4)	φ_V ≈ 0.01 - 0.2 m³$_{Crystal}$/(m³$_{Susp}$) β_0 ≈ 10^{-17} - 10^{-15} m³$_{Susp}$/(#·s) L < 50 μm
Ripening [Mul01, Mer01]	$\tau_{Rip} \approx \dfrac{\nu \cdot R_{uni} \cdot L^3 \cdot (\rho_{Crystal,mol} \cdot d_m)^2}{8 \cdot k_{Boltz} \cdot K \cdot \ln\left(\dfrac{\rho_{Crystal,mol}}{c_{eq,mol}}\right) \cdot D_{AB} \cdot c_{eq,mol}}$	(2.5)	L = 0.01 - 1 μm
Mixing (Stirred Tank Reactor [Ath99, Mer01])			
Macro [Mer01]	$\tau_{macro} \approx 5 \cdot \left(\dfrac{(T_{Vessel})^2}{\varepsilon_{mean}}\right)^{\frac{1}{3}}$	(2.6)	ε_{mean} ≈ 0.01 - 5 W/kg* τ_{macro} ≈ 1 - 40 s up to minutes
Micro [Mer01]	$\tau_{micro} \approx 5 \cdot \ln(Sc) \cdot \left(\dfrac{\upsilon_F}{\varepsilon_{local}}\right)^{\frac{1}{2}}$	(2.7)	ε_{local} ≈ 0.001 - 50 W/kg* υ_F ≈ 1.0 10^{-6} m²/s (water) Sc = (υ_F/D_{AB}) τ_{micro} ≈ 2 - 4 ms (max. ε_{local})

*In a T-Mixer the specific power input ε is in the order of 10^5 W/kg [Sch06b]

The characteristic time for ripening can be calculated by combining equation 2.8 [Mer88, Mul01, Jud04]

$$\tau_{Rip} \approx \frac{v \cdot R_{uni} \cdot T \cdot L^3}{8 \cdot \gamma_{CL} \cdot (V_{molar})^2 \cdot D_{AB} \cdot c_{eq,mol}} \qquad (\textbf{2.8})$$

with equation 2.9 for calculating the interfacial tension [Mer90, Mer01]

$$\frac{\gamma_{CL} \cdot (d_m)^2}{k_{Boltz} \cdot T} = K \cdot \ln\left(\frac{\rho_{Crystal,mol}}{c_{eq,mol}}\right) \qquad (\textbf{2.9})$$

A similar relation as equation 2.9 was derived by Nielsen et al. [Nie71]. Although equation 2.9 and the equation by Nielsen et al. [Nie71] were derived by only considering aqueous electrolyte solutions, it was shown that these relations are likewise applicable for aqueous organic or even protein solutions [Dav82, Bla88, Ber04].

The calculation and ranking of characteristic times allows identifying scale-up problems where the characteristic time of mixing overlaps with the characteristic time of a kinetic mechanism. A detailed treatment of characteristic times for reactions and mixing can be found by Baldyga et al. [Bal99] and Bourne [Bou03].

2.3   Organising Length and Time Scales

The understanding and organising of complex multiscale processes is becoming increasingly important to successfully convert ions and molecules into high performance products at the process scale [Cha04, Win99, Gro00, Cha02]. However, physical theories are often only valid for a certain size and time level and have been derived independently from each other [Kna86]. Figure 2-2 summarises length and time scales from a chemical engineering point of view forming a so called "multiscale map" [Gro00, Cha02].
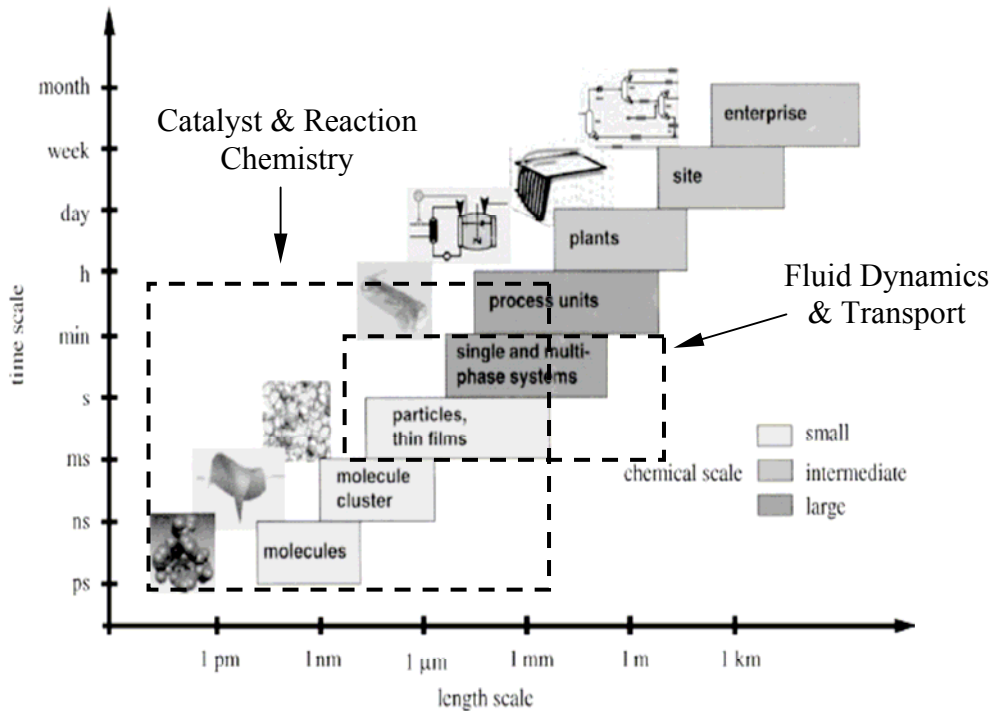
Figure 2-2: Length and time scales in chemical engineering (multiscale map) according to Grossmann et al. [Gro00] and Charpentier [Cha02]

Other "multiscale maps" can be found for example for granulation [Cam05b] or paint spray processes [Li07b]. An attempt was made to construct such a multiscale map also for crystallization (see figure 2-3) with a clear focus on a length scale between 1 nm and 1 mm and a time scale between 1 ms and 1 h. On a larger scale, crystallization processes show no differences to figure 2-2.

Figure 2-3 was derived in two steps. Apart from solution-mediated phase transformation, the equations and parameter ranges that are outlined in table 2-1 were used to calculate the respective characteristic times as a function of the particle size L. In a second step, the calculated predominated areas were compared to experimental data from the literature. Most of the experimental work that can be found refer to the quarter described by "larger 1 s and larger 1 µm". It is only recently that due to the technical advances the focus is shifting towards the quarter "smaller 1 s and 1 µm". The effort that is necessary to study processes at such a scale is described in detail by Judat et al. [Jud04] for barium sulphate and by Schlombach [Sch06a] for calcium carbonate and silica oxide. The calculated predominant areas in this range are consequently difficult to verify from an experimental point of view. A similar figure was developed by Jansens taking the supersaturation as the abscissa [Jan06].
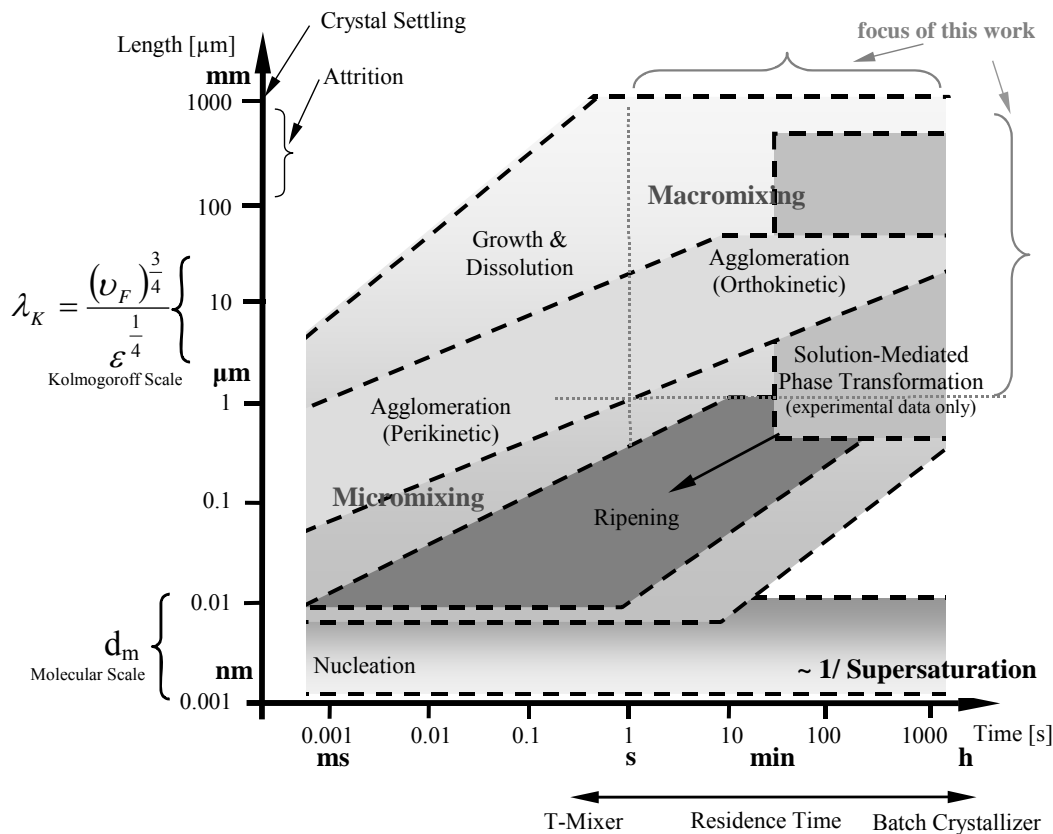
Figure 2-3: Time and length scales in crystallization from solution (dL/dt ~ G, see also Jansens [Jan06])

Nucleation is often characterised by the induction time [Bal99] being inversely proportional to the supersaturation. The induction time can range from "ms to s" for many soluble inorganic substances having a small metastable zone width [Mul01, Jud04] to 1600-6000 s in the case of lysozyme [Ber04] and up to days in the case of sugar [Hof04]. Induction times in the range of "min to h" could not be predicted by equation 2.1.

The attachment of ions or molecules to the crystal surface (growth) or the reverse process (dissolution) can span all length and time scales. For barium sulphate, having a low solubility, a characteristic time of larger 1000 s (particles < 6 µm) was calculated by Vicum et al. [Vic07]. For L-glutamic acid a time of 120 s (particles < 400 µm, $a_{surf} = 350$ m²/m³) was determined by Lindenberg et al. [Lin08]. The characteristic time for crystal growth significantly reduces for larger suspension density and hence surface areas.

Agglomeration is mainly observed for particles smaller 10 - 50 µm [Mer00b, Mer01, Bec04]. Depending on particle size, agglomeration can be induced due to fluid velocity gradients (orthokinetic, particles > 1 µm [Jon02, Bal05]) or because of Brownian motion (perikinetic, particles < 1 µm [Mer00b]). The agglomeration is strongly dependent on the number of particles in solution and therefore on the suspension density. Lindenberg et al. [Lin08] determined the characteristic time for agglomeration to be 13 s for the precipitation of L-glutamic acid. Sessiecq et al. [Ses00] derived a characteristic time of 2.3 s for the agglomeration of 5 µm primary ammonium chloride particles. A time scale much smaller 1 s can be expected for nuclei that aggregate to primary particles [Sch06a, Jan06] (see figure 2-1).

The next two mechanisms, Ostwald ripening and solution-mediated phase transformation are each the sum of several individual processes that take place at a rather low supersaturation and therefore often at a longer time scale in the range of up to hours [Jan06]. Ostwald ripening becomes relevant for particles smaller 1 μm [Mul01]. According to the Gibbs-Thomson equation barium sulphate crystals with a size of 0.1 μm have a 6% and with 0.01 μm a 72% higher solubility than 1 μm crystals, respectively [Mul01]. Therefore, larger crystals grow on the expense of smaller ones that dissolve. The driving force is consequently the difference in solubility values between the respective particle sizes. Experimental data are only available for substances that have a low solubility. For a review of the respective literature it is referred to Myerson [Mye02]. From equations 2.3 and 2.5 it can be seen the higher the solubility the faster the dissolution and subsequently ripening process [Mul01]. Additionally, a higher solubility is often related to a faster growth rate (see also figures 2-4 and 2-5).

For the solution-mediated phase transformations it is assumed that the metastable form is already crystallized and in equilibrium with the saturated solution. The supersaturation lies therefore between the solubility difference of the metastable (that is dissolving) and stable polymorph (that is nucleating and growing). The experimental observed transformation times are ranging from 200 s for sodium carbonate (anhydrate to monohydrate) [Sha05] to 4 - 10 h for the transforming α to β glutamic acid ($c_{eq}(\alpha)$-$c_{eq}(\beta) \approx$ 3 g/kg) [Ono04, Sch06c] or up to 8 - 33 h for copper phthalocyanine (α to β) [Car85]). Also within this work, α-glycine will be crystallized being the metastable form, however, stable during the course of the experiment. This timescale is especially important to isolate the right polymorph. The indicated area in figure 2-3 shows the predominant range where experimental data were found. However, the transformation is not only limited to this area, indicated by the arrow.

For all kinetic processes the characteristic time is inversely proportional to the driving force, being the supersaturation. Only agglomeration can also take place without supersaturation. However, the higher the supersaturation the higher the nucleation rate leading to smaller overall particles sizes that are more prone to agglomeration; additionally, the higher the supersaturation the higher the "sticking probability" (formation of solid bridges) [Dav95, Mar02, Mer02]. Further important phenomena are attrition that must be considered when particle sizes exceed 100 μm [Gah99a,b] and crystal settling that is often only relevant for particles in the range of mm.

To complement figure 2-3 mixing characteristics are indicated that influence the respective kinetic mechanisms. The mixing quality depends ultimately on the equipment that is used (T-mixer versus stirred tank). For a stirred tank containing an aqueous solution the Kolmogoroff length microscale λ_K is approximately 20 - 40 μm [Ath99]. Micromixing (by molecular diffusion or engulfment) refers mainly to the quarter "smaller 1 s and 1 μm" [Mer01, Bou03] whereas macromixing (bulk blending) to the quarter "larger 1 s and 1 μm" [Ath99, Bou03]

Figures 2-1 and 2-3 have to be interpreted carefully. These figures are an illustration, in other words a simplification of a complex multiphase process. The borders of a predominate area of a specific mechanism are not the result of fundamental science and not clearly defined, however, compromising experimental findings and common experiences within industrial mass crystallization. Exceptions and many definitions of the respective

characteristic times exist in literature. The multiscale map is therefore more a "mental roadmap" illustrating the relation of different individual mechanisms. It allows selecting the right measurement instrument in view of resolution and particle size, helps to find appropriate experimental conditions as well as to choose the right modelling strategy.

2.4   Experimental Findings

Within this work, the focus is on nucleation and growth kinetics, although agglomeration and solution-mediated phase transformation will be partly touched on. The growth rate spans the entire multiscale map whereas the induction time ranges from microseconds up to hours. It would be desirable to have at least a guide if a substance can be classified a-priori as a "fast or slow grower" [Hou06]. Does a certain group of substances have different rate coefficients than another group? Can a plausible range of the kinetic constants be derived a-priori to any experiment?

It is generally believed that all substances no matter if inorganic, organic (petrochemical or biochemical) grow and nucleate under common physical laws [Mah93, Mah94, Che97, McP99]. To compare individual case studies the MSMPR crystallizer can be chosen as a reference process. Equation 2.10 allows the calculation of the median particle size dependent on the kinetic parameters [Bau84]:

$$L_{50,3} = 3.67 \cdot \left(6 \cdot k_V \cdot \rho_{Crystal} \cdot k_{bSusp}\right)^{-\frac{g}{3 \cdot g + b}} \cdot \left(k_g\right)^{\frac{b}{3 \cdot g + b}} \cdot \left(m_T\right)^{\frac{(1-j) g}{3 \cdot g + b}} \cdot \left(\tau_{Res}\right)^{\frac{b-g}{3 \cdot g + b}} \approx 3.67 \cdot \underbrace{\sqrt[4]{\frac{G \cdot m_T}{6 \cdot k_V \cdot \rho_{Crystal} \cdot B}}}_{g=b, j=1} \quad (\ 2.10\ )$$

Typical values of the kinetic orders b, g and j were collected from various references [Gar80, Mer88, Kin89, Mer01, Hei94, Tav95, Ulr05, Kel99, Ulr05]. They are indicated in equations 2.11 and 2.12 (j = 1 crystal-impeller collision, j = 2 crystal-crystal collision).

$$G = k_g \cdot \left(S - 1\right)^{g=1-3} \qquad\qquad\qquad\qquad\qquad\qquad\qquad\qquad\qquad\quad (\ 2.11\ )$$

$$B = k_{bSusp} \cdot \left(S - 1\right)^{b=1-5} \cdot \left(m_T\right)^{j=0.5-2} \qquad\qquad\qquad\qquad\qquad\qquad\quad (\ 2.12\ )$$

Nielsen [Nie84a] concluded from experimental studies that a linear rate law is often found for soluble electrolytes. In comparison, electrolytes with a low solubility often showed an exponential rate law. Approximate values for the nucleation rate B and growth rate G can be infer from figure 2-4. Values of the suspension density m_T lie in the range of 10 - 200 kg/m³$_{Susp}$ for laboratory studies [Gar80] and in the range of 200 - 600 kg/m³$_{Susp}$ [Mer01] for industrial crystallizers. Figure 2-4 was developed by Mersmann and Kind [Mer88, Mer89, Kin94].
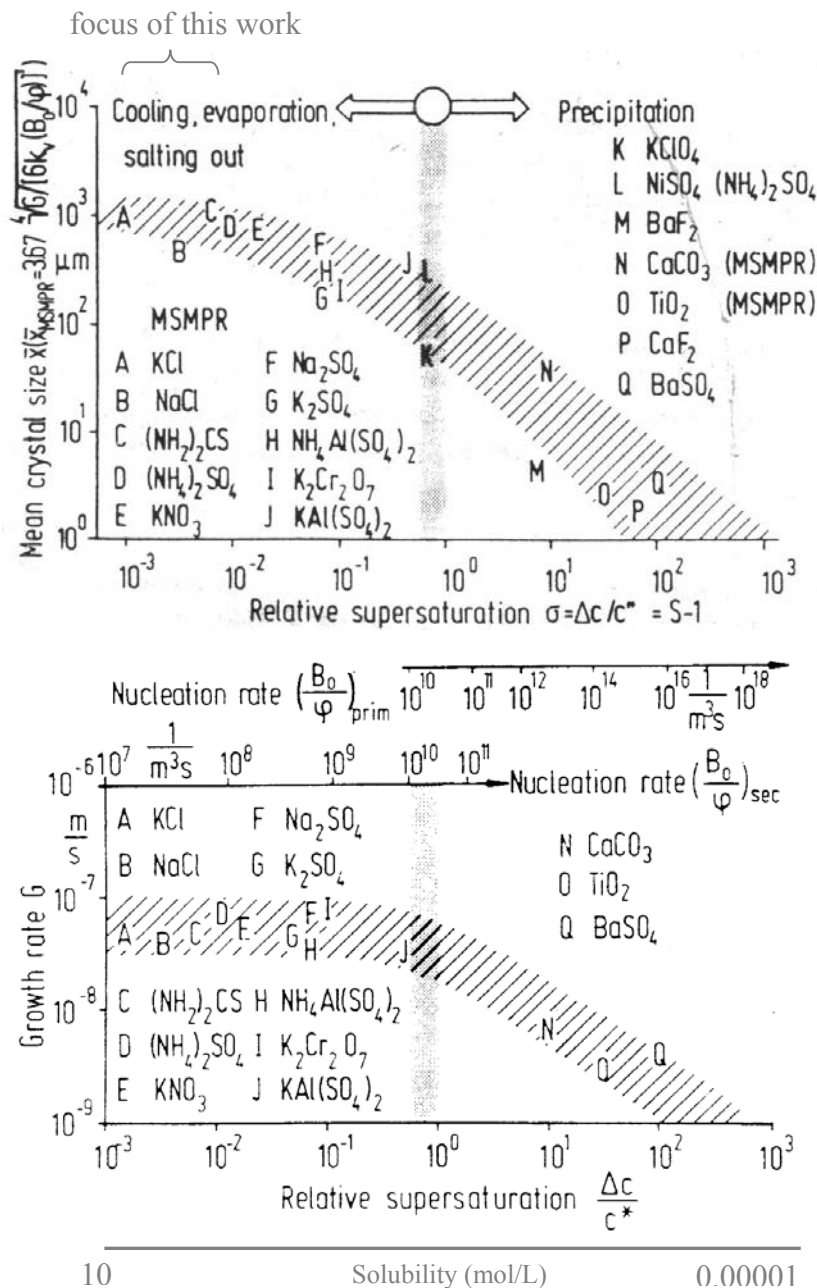
Figure 2-4: Experimental observed median particle sizes, nucleation and growth rates as a function of supersaturation and solubility (MSMPR crystallizer) [Mer88]

From figure 2-4 it can be seen that the solubility, being a sum of all kind of equilibria, has a strong influence on nucleation and growth rates. However, differences can only be observed by comparing extreme cases, for example freely soluble (> 1 mol/L) versus very slightly soluble (0.01-0.001 mol/L) substances. A similar diagram to figure 2-4 (lower diagram) was derived from experimental data by Schreiner et al. [Sch02] for binary systems within melt crystallization. For a thorough discussion it is referred to Mersmann [Mer01].

Exceptions to figure 2-4 are for example ammonium chloride and ammonium bromide that are freely soluble (> 1 mol/L) but form dendrites prone to breakage [Oht98] as well substances that are freely soluble but have an inverse solubility line (negative slope, endothermic crystallization) [Hei05]. The situation gets challenging for organic substance that can be crystallized from various solvents. Each solvent can interact differently with the

specific crystal faces leading to changes in the growth rate and hence morphology. It is referred to a review by Davey [Dav82] as well as to case studies on the crystallization of hexamethylenetetramine [Bou76b, Bou76c, Bou78, Mye86, Roh90, Ala04], paracetamol [Gra01, Gra05 and references therein] and others [Lie99].

Whereas in figure 2-4 only inorganic substances are considered, numerous authors discuss the differences in crystallization between inorganic and small organic on the one and proteins on the other hand [Ros86, Che97, Gar04, Nan07]. Mersmann et al. [Mer88] concluded that the rate coefficient for crystal growth is smaller for molecules with complex shape, functional groups (dipole moment) and a larger molecular weight. Similar conclusions are derived by Rittner et al. [Rit85], Dennehy [Den03] and Beckmann [Bec04]. Whereas it is straightforward for an ion to enter the lattice, a large macromolecule might has to re-orientate numerous times. Reviakine et al. [Rev03] and other authors [Boi91, Che97, McP99, Nan07] summarised various research results and concluded that proteins have often a diffusion coefficient by a factor of 100 and a kinetic coefficient roughly by a factor 100 - 1000 smaller than various inorganic systems.

Proteins that are made out of amino acids have a molecular weight that ranges from 10,000 to 1,000,000 g/mol (for example lysozyme: 14,100 g/mol), have often a very low solubility ($\approx$ 0.01 - 0.1 kg/L) and an open structure (uncoordinated water molecules) [Boi91, McP99, Sch05, Li07a]. Protein crystals are soft and crush easily compared to most inorganic ones [Kin94, Tai07]. The density is often close to water (for example lysozyme: 1350 kg/m³ [Whi07]). Figure 2-5 compares the experimental measured growth rate of lysozyme [Shi05, Sai98] to various other inorganic and organic substances (potassium chloride, saccharose, L-glutamic acid, calcium oxalate [Moh02], ascorbic acid [Oma06b]). The solvent is in all cases water.

In agreement with figure 2-4 substances that have a high solubility have a faster growth rate than those that have a lower solubility. However, by comparing calcium oxalate, barium sulphate (see figure 4-4 (chapter 4)), gibbsite [Joh99] (not shown) and aluminium fluoride trihydrate [Nie84b] (not shown) with proteins such as lysozyme, canavalin, insulin or ovalbumin [Jud95, Oht98, Sai98, Joh99, McP99, Shi05, Lu06], it can be concluded that the size of the respective ion or molecule has no significant influence on the growth rate. All of these substance have a similar low solubility but also a similar low growth rate. Consequently, the general conclusion that proteins grow by the factor 100 to 1000 slower than "conventional" crystals depends on the base that is used for comparison. It might be better to say that proteins grow slowly according to their solubility just as other inorganic substances do.
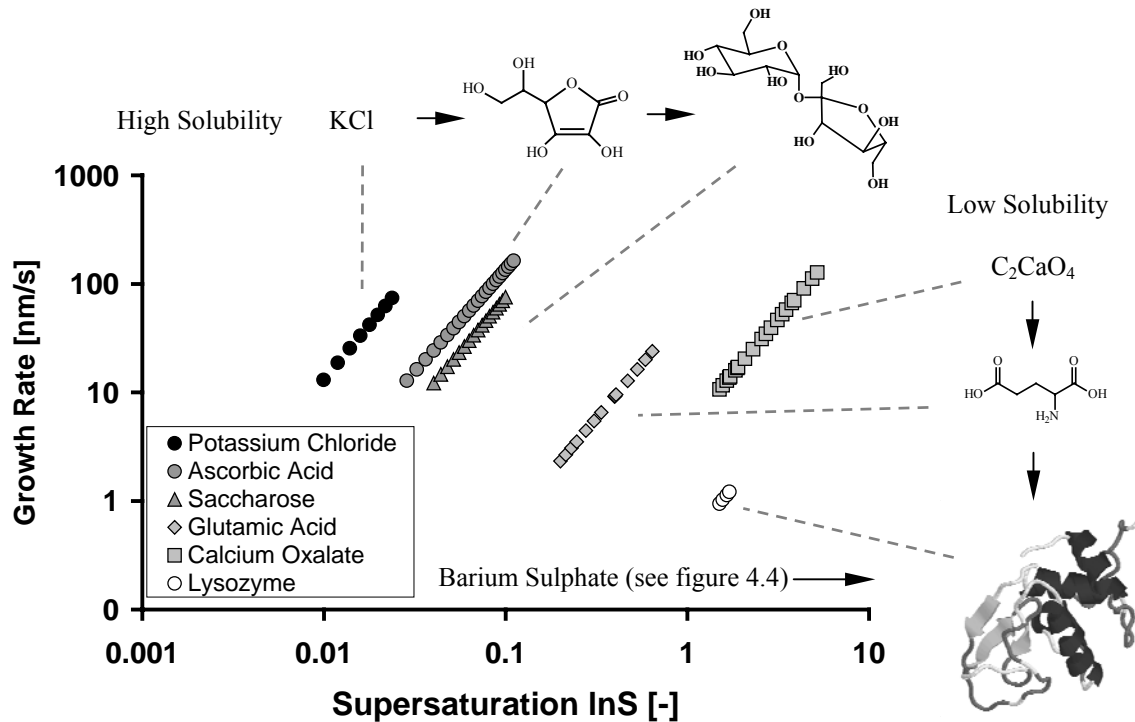
Figure 2-5: Experimental observed crystal growth rates for various substances, high solubility: $c_{eq,mol} > 1.4$ mol/L, 20 °C, low solubility: $c_{eq,mol} < 0.06$ mol/L, 20 °C (structure of lysozyme by Georgia State University [Geo07])

Chew et al. [Che07b] started a larger research effort into the hypothesis that larger molecules grow slower than smaller ones. It was concluded that the growth rate is a function of the intermolecular interactions and crystal structure but is not simply related to the size of the molecule [Che07b]. An illustrative example is α- and γ-glycine where the growth rate differs by a factor of 500 (see also chapter 10.3). Because of the individual structural properties of each substance and the high "variance" in kinetic measurements (see chapter 4.3) a general comparison between individual case studies remains difficult, so does the prediction of the behaviour of an unknown substance. The challenges of comparing kinetics obtained within this work to literature data is described in chapters 10.1, 10.2 and 10.3.

But still, using the data provided in figure 2-4 an overall range of nucleation and growth rates can be clearly defined, where also yet not investigated substances will very likely lie in. The solubility might be used as a first indicator to decide how fast or slow a substance grows under a given supersaturation. This is confirmed by the growth rate equations derived by Nielsen [Nie84a], Mersmann [Mer95a] and Treivus [Tre96] that are direct proportional to the solubility. In future, first estimates of nucleation and growth parameters might also be derived from "Molecular Simulations" [Hor06].

3 Crystallization from Solution

3.1 Solubility and Supersaturation

For a comprehensive treatment of crystallization from different perspectives, it is referred to several textbooks [Mer01, Mul01, Mye02, Jon02, Hof04]. Textbooks with more in depth coverage on specific subject areas can be found for crystallization from melt [Ulr03b], crystallization of foods [Har01], crystallization of proteins [McP99], precipitations [Söh92], on the effect of additives [San07], polymorphism [Hil06], on the application of molecular modelling [Mye99] or on the determination of kinetics [Gar02]. Introductions to crystallization processes can also be found in many general chemical engineering textbooks [Per97, Mer05, Ulr07] and encyclopaedias [Ulr02b, Mul05].

For the design of crystallization processes the solid-liquid phase diagram is a prerequisite. In general, only temperature and composition swings are considered, since the pressure has often only a minor influence on the solid-liquid equilibrium. For rigorous process design the phase diagram must be available in numerical form that is challenging for multicomponent systems especially for electrolytes. Models are ranging from electrolyte NRTL activity coefficient model, extended UNIQUAC to Equations of State models (for example: extended PC-SAFT model) [Cam05a, Tho05, Lin07, Ola07]. For an introduction to "Heterogeneous Systems", with special emphasis on solid-liquid phase behaviour, it is referred to the book by Vogel [Vog59] that compromises the pioneer works from van't Hoff, Schreinemakers, Tammann, Jänecke or to Hofmann [Hof04]. The graphical representation of the phase behaviour becomes important for multicomponent systems. For methods of visualisation and representation it is referred to papers from Ng et al. [Sam00, Sam01, Wib02a, Wib02b] that form the base of the commercial software called SLEEK^{TM} (Solid-Liquid Equilibrium Engineering Kit).

Figure 3-1 shows an eutectic phase behaviour for water (A) and an arbitrary substance (B).

$$x_{eq} = \frac{1}{\gamma_{eq}} \cdot \exp\left(\frac{\Delta H_m}{R_{uni}} \cdot \left(\frac{1}{T_m} - \frac{1}{T} \right) \right)$$
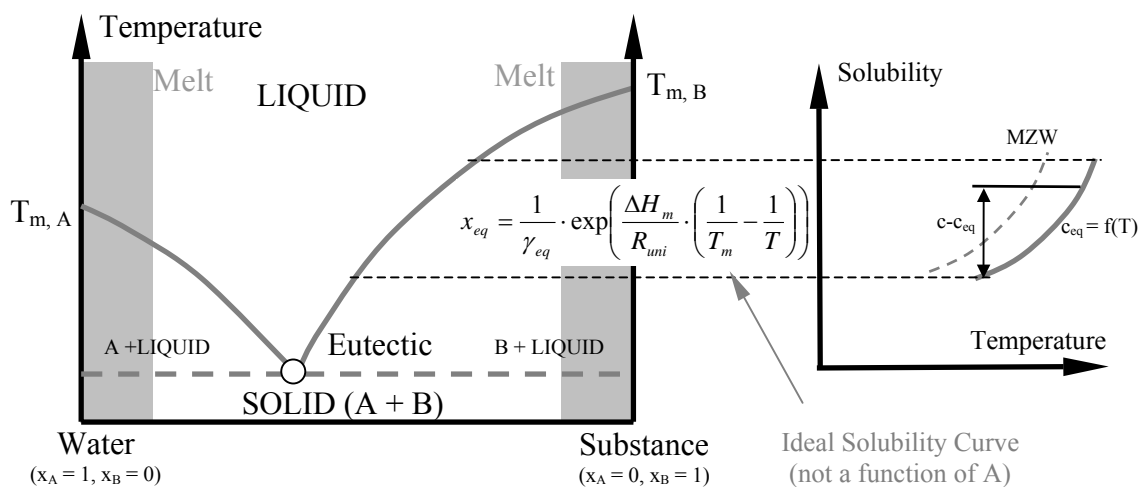
Figure 3-1: Eutectic solid-liquid phase diagram (ideal solubility curve: equation (3.1))

Eutectic systems can be compared to an azeotropic behaviour in vapour-liquid systems, characterising boundaries limiting the degree of separation [Sla95]. Thereby interesting combinations of crystallization – distillation hybrid processes arise, allowing to bypass azeotropes or eutectics [Ber97, Hei06]. It becomes evident that there is no clear borderline between crystallizing from melt and from solution. Ulrich et al. [Ulr88] suggested that whenever heat-transfer limits the process, the word "melt-crystallization" should be used. Does mass transfer dominates the process "crystallization from solution" might be appropriate. Often not the entire phase diagram must be known for process design. In case of crystallization from solution only a small part of the phase behaviour, the solubility curve in a certain temperature range, must be identified.

Solubility values for crystallization, precipitation processes cover up to 7 orders of magnitude and can be grouped into different categories [Eur07]. From the amount that is soluble and from the slope of the solubility line the method of crystallization can be determined [Mer01]. Figure 3-2 shows some examples of substances that crystallize or precipitate from solution. For experimental methods to determine the solubility it is referred to Hefter et al. [Hef03] or Kwok et al. [Kwo06].
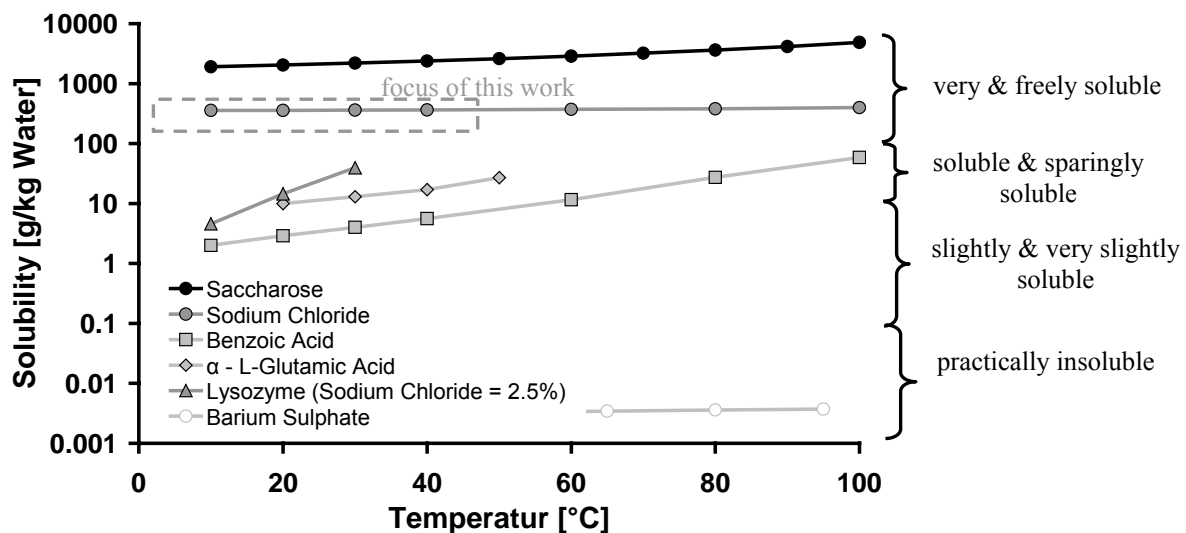
Figure 3-2: Solubility of various substances as a function of temperature [Mul01, Jud03, Shi05, Sch06c]

Closely connected to the solubility is the supersaturation. The driving force for crystallization can be defined by equation 3.2:

$$\frac{\Delta\mu}{R_{uni} \cdot T} = \nu \cdot \ln\left(\frac{a}{a_{eq}}\right) = \nu \cdot \ln\left(\frac{\gamma \cdot c}{\gamma_{eq} \cdot c_{eq}}\right) \approx \nu \cdot \ln S \approx \nu \cdot (S - 1) \sim c - c_{eq} \sim \Delta T \qquad (3.2)$$

Two major simplifications are often made being in general only valid for soluble systems. The activity coefficients are set to unity that is reasonable for small concentration differences. A second approximation is the transformation of the logarithmic driving force $\ln S = \ln(c/c_{eq})$ to a relative concentration difference $S - 1 = (c - c_{eq})/c_{eq}$. The use of $\ln S$ instead of $(S-1)$ or $c - c_{eq}$

becomes important for values larger 1 [Kim96, Moh02]. According to various authors [Mer01, Mul01, Gar02, Jon02, Ulr02b], the most widely used expression for the supersaturation is (S-1) or simply c-c$_{eq}$, the former will be used within this work.

The ν is the number of ions or molecules formed by dissociation, being in general 1 for molecules and for example 2 for electrolytes such as sodium chloride. The value is generally "fused" with the rate coefficient. Finally, when hydrates are crystallized, the supersaturation must be calculated with the concentration of the hydrate and not with the anhydrate [Söh78].

Besides the various ways of characterising the supersaturation, numerous concentration units can be used to calculate the actual driving force [Mul01]. Although mol/L might be appropriate from a theoretical point of view [Gar02], kg solute/kg solvent seems to be more practical. It avoids the need for knowing the density of the saturated solution as a function of temperature and concentration.

3.2   Nucleation

Before a crystal can grow, a nuclei or an attrition fragment must be formed. Nucleation can occur by different mechanisms. The total nucleation rate is the sum of all individual contributions (equation 3.3) [Mer01] that is often approximated by a simple power law:

$$\frac{dN}{dt \cdot V_{Suspension}} = B_0 = \underbrace{B_{\text{hom}} + B_{het}}_{Primary} + \underbrace{B_{surf} + B_{att}}_{Secondary} \approx \underbrace{k_{bm} \cdot (S-1)^b \cdot m_{PSD,3}}_{within\ this\ work} \qquad (3.3)$$

measured signal (pointing to $(S-1)^b$)

measured signal (pointing to $\frac{dN}{dt \cdot V_{Suspension}}$)

Primary nucleation occurs in the absence of solution own crystals (hom: no particles, het: foreign particles). According to Mersmann [Mer01], even in bi-distilled water there is a foreign particle surface of up to 2500 m²/m³, making homogeneous nucleation rarely happen in conventional crystallization processes. If nuclei form in the presence of solution-own crystals, it is called secondary nucleation. It occurs at a lower driving force than primary nucleation. Nuclei formed by surface nucleation (B$_{surf}$) might form as pre-ordered species or clusters close to the crystals surface or are the result of dendrite detachment [Mer01]. The first three nucleation mechanisms (B$_{hom}$, B$_{het}$, B$_{surf}$) are activated processes [Mer01]. Finally, secondary nuclei can form due to fracture, particle disruption or attrition even at zero supersaturation. The efficiency of crystal-stirrer, crystal-wall and crystal-crystal collision is roughly 1000 : 10 : 1 [Hof04]. Attention must be paid that via attrition the number of small crystals increases (B$_{att}$), however, not all attrition fragments are active and contribute to the consumption of the supersaturation [Ulr85, Mer01]. Finally, also fluid shear might induce nucleation [Tav95, Jon02].

Table 3.1 summarises some common equations for the individual nucleation rates. For a detailed review on nucleation mechanisms it is referred Kashchiev [Kas00].

Table 3-1: Nucleation mechanisms

Equation		Reference
Homogeneous Nucleation		
$B_{\text{hom}} = A_{\text{hom}} \cdot e^{\left(\frac{-16 \cdot \pi \cdot (\gamma_{CL})^3 \cdot (V_m)^2}{3 \cdot (k_{Boltz} \cdot T)^3 \cdot (\ln S)^2} \right)}$	(3.4)	[Mul01]
$B_{\text{hom}} = 1.5 \cdot \sqrt{K} \cdot \frac{D_{AB}}{(d_m)^5} \cdot \left(\frac{c_{mol}}{\rho_{Crystal,mol}} \right)^{\frac{7}{3}} \cdot \sqrt{\ln\left(\frac{\rho_{Crystal,mol}}{c_{eq,mol}} \right)} \cdot e^{\left(\frac{-16 \cdot \pi}{3} \cdot \frac{\left(K \cdot \ln\left(\frac{\rho_{Crystal,mol}}{c_{eq,mol}} \right) \right)^3}{(\nu \cdot \ln S)^2} \right)}$	(3.5)	[Mer01]
Heterogeneous Nucleation (0 < f < 1)		
$B_{het} = A_{het} \cdot e^{\left(-f \cdot \frac{16 \cdot \pi \cdot (\gamma_{CL})^3 \cdot (V_m)^2}{3 \cdot (k_{Boltz} \cdot T)^3 \cdot (\ln S)^2} \right)}$	(3.6)	[Mul01]
$B_{het} = 1.5 \cdot \sqrt{K} \cdot \sqrt{f} \cdot \frac{D_{AB}}{(d_m)^5} \cdot \left(\frac{c_{mol}}{\rho_{Crystal,mol}} \right)^{\frac{7}{3}} \cdot \sqrt{\ln\left(\frac{\rho_{Crystal,mol}}{c_{eq,mol}} \right)} \cdot e^{\left(-f \cdot \frac{16 \cdot \pi}{3} \cdot \frac{\left(K \cdot \ln\left(\frac{\rho_{Crystal,mol}}{c_{eq,mol}} \right) \right)^3}{(\nu \cdot \ln S)^2} \right)}$	(3.7)	[Löf02]
Surface Nucleation ($a_{surf} = 6 \cdot \varphi_V / L_{[3,2]} \approx 100 - 100{,}000 \ \text{m}^2/\text{m}^3_{Susp}$ [Mer01])		
$B_{surf} = E \cdot \frac{6 \cdot \varphi_V}{L_{[3,2]}} \cdot \frac{D_{AB}}{(d_m)^4} \cdot e^{\left(-\pi \cdot \frac{\left(K \cdot \ln\left(\frac{\rho_{Crystal,mol}}{c_{eq,mol}} \right) \right)^2}{\nu \cdot \ln S} \right)}$	(3.8)	[Mer01]
Attrition		
$B_{att} \approx k_{att} \cdot \left[\frac{(H_V)^5}{\mu^3} \cdot \left(\frac{K_{eff}}{\Gamma} \right)^3 \right] \cdot m_T \cdot \varepsilon_{mean}$	(3.9)	[Mer01]

Homogeneous and heterogeneous nucleation can experimentally be distinguished by plotting B versus $1/(\ln S)^2$ for a wide range of supersaturations. At the point where the slope changes, the predominant mechanism changes too. The extent to which a substance is prone to attrition can easily be evaluated by keeping a saturated solution with relatively speaking large crystals stirred by simultaneously monitoring the change in particle number and/or size.

By plotting equations derived by Mersmann [Mer01] (see table 3-1) using typical values of the physical properties and simplifying it, figure 3-3 can be obtained, being a "road map" [Kin02]. For the model systems used within this work, the expected range of nucleation rates are indicated. It can be seen that depending on the solubility and supersaturation not all nucleation mechanisms are always predominant. A similar figure, as figure 3-3, is described by Mersmann [Mer01], however, normalising the solubility and supersaturation by the crystal density that has become under sincere criticism.
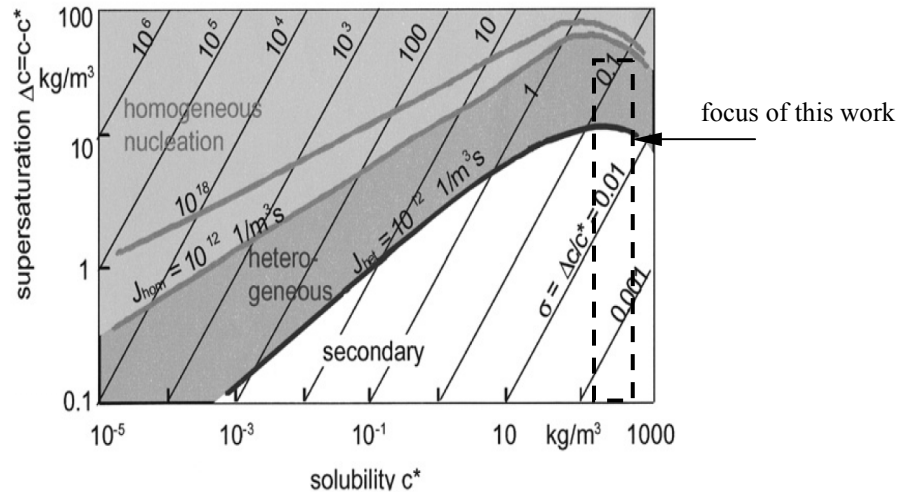
Figure 3-3: A-priori prediction of nucleation mechanisms and rates as a function of solubility and supersaturation [Kin02]

An important parameter that is closely connected to nucleation is the *m*etastable *z*one *w*idth (abbreviation **MZW**). It is also called "Ostwald-Miers" range or supersolubility line. The metastable zone width is the range where rarely any nuclei are formed. Although it is not a fundamental quantity, the metastable zone width is a useful measure for the operation of a crystallizer and provides valuable insight into nucleation kinetics [Jon02]. In 1970, Nývlt et al. [Nýv70] compared experimental determined metastable zone widths of 25 aqueous inorganic systems. It was concluded that the zone width expressed in temperature difference is often larger for substances having a low solubility.

Mersmann et al. [Mer98] derived equation 3.10 to estimate the metastable zone width when secondary nucleation prevails. For other nucleation mechanisms it is referred to Kim et al. [Kim01].

$$(S-1)_{MZW,Secondary} = 12 \cdot \left[\frac{d(\ln c_{eq,mol})}{d(\ln T)} \cdot \left(\frac{\rho_{Crystal,mol}}{c_{eq,mol}} \right)^{\frac{4}{3}} \cdot \ln\left(\frac{\rho_{Crystal,mol}}{c_{eq,mol}} \right) \cdot \frac{\dot{T}}{T} \cdot \frac{d_m \cdot L_{Det}}{D_{AB}} \right]^{\frac{1}{3}} \qquad (\textbf{3.10})$$

Equation 3.10 summarises important factors that influence the absolute value of the metastable zone width being the cooling rate, the slope of the solubility line and the solubility itself, the kind of substance and the measurement principle employed (L_{Det}). The optimal supersaturation is approximately half of the maximum of the metastable zone width, in order to maximise the growth rate by simultaneously minimising the nucleation rate [Hof04]. From an industrial point of view, the "secondary nucleation limit" is of primary interest, since batch processes are often seeded and continuous processes always have seeds present. An illustrative example for the different nucleation mechanisms is water. Whereas tap water crystallizes at around -2 to -3 °C, can purified water be cooled down to -30 °C without any nucleation taking place [Dav00, Jon02].

Although nucleation seems to be theoretically rather well understood, it remains difficult to measure directly [Oht98]. In recent years, it proved to be successful to combine solution and solid-state chemistry to gain a deeper understanding of the underlying mechanisms [Gav97, Dav01, Dav02, Wei03, Bur08]. Nucleation is a very fast process that refers to the creation of small nuclei with an approximate size of 1 nm influenced by traces of impurities (see chapter 2). However, many instruments (optical microscopy, turbidity, conductivity and ultrasound probe) recognise particles only when they reach a size range of approximately 1 μm. Additionally, measurement probes have in general a time resolution of not faster than 1 second. The time up to the detection of nuclei is consequently influenced by the actual growth rate and agglomeration phenomena leading sometimes to contradictory results [Oht98, Mul01, Gar02].

Within the course of this work, the nucleation is detected by recording the change in number of particles that have at least a size of 1 μm. The overall nucleation mechanism within this work will be described by a simple power law.

3.3   Crystal Growth

The growth of a crystal is a complex process and many mechanisms contribute to it. The growth unit can be an ion, a molecule, a hydrated ion, dimers, trimers or clusters. Apart from crystals having a polar morphology it is assumed that symmetry related faces have the same growth rate [Dav00, Ma08, Hei08a]. Different crystal face pairs can grow with a different mechanism. A change to supersaturation therefore induces often a change in morphology [Fin99, San07].

According to Dirksen et al. [Dir91], the growth of a specific face of an ionic crystal can proceed via 8 steps, illustrated in figure 3-4 (compare also Mullin [Mul01] and Nielsen [Nie87]). Having an electrolyte, in principle, the cation and anion have their own diffusion, adsorption, integration and dehydration kinetics. Although the overall process can be monitored easily, hardly any experimental information is available for the individual steps.

1. Transport of solute from the bulk solution to the crystal surface
2. Adsorption on the crystal surface
3. Diffusion over the surface
4. Attachment to a step
5. Diffusion along a step
6. Integration into the crystal at a kink site
7. Diffusion of coordination shell of solvent molecules away from crystal surface
8. Liberation of heat of crystallization and its transport away from the crystal

Figure 3-4: Individual steps that take place during growth of an ionic crystal (steps are cited from Dirksen et al. [Dir91], illustration of crystal growth by Elwell et al. [Elw75] taken from Dirksen et al. [Dir91])

For each step a rate law can be defined and each step (or several) can determine the overall rate. From an engineering point of view step 1 is modelled using mass transfer equations whereas step 2 to 8 are summarised to an "incorporation" step [Jon02]. For growth of electrolytes, the dehydration of the cation often plays a limiting role [Nie84a, Oht98, San07]. The steps illustrated in figure 3-4 are likewise valid for molecules.

The face specific growth rate can be formulated by equation 3.11 ($dL/dt = G = 2 \cdot v$, $v =$ face growth rate perpendicular to the face) [Mer05]:

$$\frac{dL}{dt} \sim v_0 = \frac{1}{\dfrac{1}{v_{Heat}} + \underbrace{\dfrac{1}{v_{BCF} + v_{B+S} + v_{PN}}}_{Integration} + \dfrac{1}{v_{Diffusion}}} \sim k_\infty \cdot e^{\left(-\frac{E_G}{R_{uni} \cdot T}\right)} \cdot (S-1)^g \approx \underbrace{k_g \cdot (S-1)^g}_{within\ this\ work} \qquad (\ 3.11\ )$$

(measured signal — v_0) (measured signal — $k_g \cdot (S-1)^g$)

The activation energy is typically between $E_G \approx$ 8 – 20 kJ/mol for diffusion and $E_G \approx$ 40 – 100 kJ/mol for an integration process [Dav00, Hof04]. Consequently, with higher temperature diffusion will determine the overall rate, whereas at a low temperature the integration plays the dominant role. By assuming an activation energy of 50 kJ/mol, the growth rate doubles every 10 K. The influence of mass transfer can be modelled using an effectiveness factor [Gar84, Mar88, Dav00].

Table 3-2 summarises common equations for each mechanism. The most important parameters that influence the growth rate are supersaturation, temperature and fluid dynamics [Oha73]. The concept of using a dimensionless growth rate was pursued by different authors [Lee79, Hou81, Kin89, Kin90]. In principle, since most growth laws scale different with the supersaturation, the rate law of one specific face can be determined by single crystal face growth measurements complement with various microscopic techniques (for example atomic force microscopy) [Dav00]. Solution chemistry is generally not considered within the growth rate equations [Rod89, Wil99].

Table 3-2: Growth mechanisms

Equation		Reference
Screw Dislocation Mechanism (**B**urton-**C**abrera-**F**rank)		
$v_{BCF} = k_{BCF1} \cdot (S-1) \cdot \ln S \cdot \tanh\left(\dfrac{k_{BCF2}}{\ln S}\right)$ Low Supersaturation $v_{BCF} \sim (S-1)^2$ High Supersaturation $v_{BCF} \sim (S-1)$	(3.12)	[Mer01]
Surface Nucleation Mechanism (**B**irth and **S**pread)		
$v_{B+S} = k_{B+S1} \cdot (S-1)^{\frac{2}{3}} \cdot (\ln S)^{\frac{1}{6}} \cdot e^{\left(-\frac{k_{B+S2}}{\ln S}\right)}$	(3.13)	[Mer01]
$v_{B+S} = \left(\dfrac{2}{\pi}\right)^{\frac{1}{3}} \cdot \dfrac{D_{Surface}}{d_m} \cdot \left(\dfrac{c_{eq,mol}}{\rho_{Crystal,mol}}\right)^{\frac{2}{3}} \cdot (S-1)^{\frac{2}{3}} \cdot (\ln(S))^{\frac{1}{6}} \cdot e^{\left(\frac{-\frac{\pi}{3}\left(K \cdot \ln\left(\frac{\rho_{Crystal,mol}}{c_{eq,mol}}\right)\right)^2}{v \cdot \ln S}\right)}$	(3.14)	[Mer02]

Equation		Reference
Poly-Nuclear Mechanism		
$$v_{PN} = \frac{D_{AB}}{3 \cdot d_m} \cdot \left(\frac{c_{eq,mol}}{\rho_{Crystal,mol}}\right)^{\frac{2}{3}} \cdot (S-1)^{\frac{2}{3}} \cdot e^{\left(\frac{-\pi \cdot \left(K \cdot \ln\left(\frac{\rho_{Crystal,mol}}{c_{eq,mol}}\right)\right)^2}{v \cdot \ln S}\right)}$$	(**3.15**)	[Mer02]
Diffusion		
$$v_{Diffusion} = \frac{k_A}{k_V} \cdot k_D \cdot \frac{c_{eq,mol}}{\rho_{Crystal,mol}} \cdot (S-1)$$	(**3.16**)	[Mer02]
A-priori Prediction (Semi Empirical, based on the BCF Law)		
$$v_{BCF} = 2.25 \cdot 10^{-3} \cdot \frac{D_{AB}}{d_m} \cdot \frac{\left(\frac{c_{eq,mol}}{\rho_{Crystal,mol}}\right)^{\frac{4}{3}}}{\ln\left(\frac{\rho_{Crystal,mol}}{c_{eq,mol}}\right)} v^2 \cdot (S-1)^2$$	(**3.17**)	[Mer02]
A-priori Prediction (Valid for Electrolytes ($c_{eq,mol}$ [mol/m³], v_{dh} [1/s]))		
$$v_0 = 5 \cdot 10^{-19} \cdot (v_{dh}) \cdot (c_{eq,mol})^{1.36} \cdot (S-1)^2$$	(**3.18**)	[Nie84a]

The "Birth and Spread" and "Poly Nuclear" rate laws fail to describe the crystal growth at a low supersaturation range. They are activated processes, having a weak increase in growth rate at low supersaturation values and a fast increase at higher values. The influence of heat transfer limitations that is observed within melt crystallization can generally be neglected for solution crystallization processes [Mer01]. Matsuoka et al. [Mat91, Mat93], however, showed that the onset of heat transfer limitations is "observable" for freely soluble substances (> 1 mol/L).

As shown by number of authors [Gar75, Bou76a, Dav86, Gra05] different growth laws can be fitted to the same experimental data (see figure 3-5 (b)). Often significant measurement errors especially in the small supersaturation range and scattering of growth rate for the same supersaturation are observed [Dav86]. By calculating the Jackson factor a likely growth mechanism can be identified, based on solute and solution properties. The Jackson factor is related to the surface roughness of a crystal face [Dir91, Dav00, Mer01]. The method was applied successfully to a limited number of systems [Bou76a, Bou78, Bou80, Zip92]. Others authors [Li92, Lec95, Dav00] reporting only mixed results by applying the Jackson factor.

Figure 3-5 (a) was derived by Mersmann [Mer01] using physical-based kinetic equations (see table 3-2) in combination with typical values for the respective physical properties. For the model systems used within this work, the expected range of growth rates are indicated.
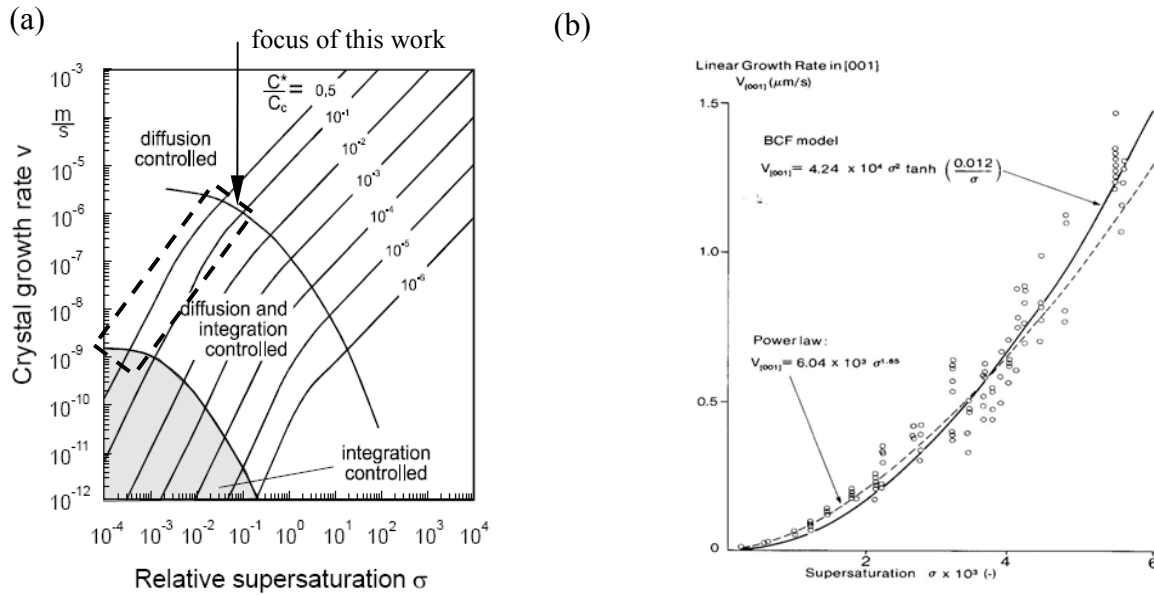
Figure 3-5: (a) A-priori prediction of growth mechanisms and rates as a function of solubility, crystal density and supersaturation (valid for $D_{AB}/d_m \approx 2$ m/s [Mer02]), (b) Modelling of experimental growth rate data using different growth mechanisms [Dav86]

A widespread phenomenon that appears in both organic and inorganic aqueous systems, independent if the substance has a small or large metastable zone width is growth rate dispersion [Ber86]. In other words, crystals of the same size, exposed to the same environment grow with a different speed, leading to a growth rate distribution. Already in 1949, Bunn [Bun49] observed that the two half of a broken crystal grew with different speeds. Ulrich [Ulr89] made a comprehensive review summarising and systemising the results on growth rate dispersion in 1989. Later reviews are given by Tanneberger et al. [Tan96], Lacmann et al. [Lac99] and Sherwood et al. [She01].

The actual verification which specific rate law is active needs extensive studies on single crystals. Additionally, all described rate laws above refer to a single crystal face. However, particle size analysers generally measure one characteristic size that is not equal to the distance of two opposite faces. The overall growth rate mechanism within this work will be approximated by a simple power law.

3.4   Population Balance Concept

3.4.1   Population Balance

The population balance allows to model the change in number and size of particles, dependent on various kinetic mechanisms and therefore to design a crystallizer. The introduction of the populcation balance is closely related to the paper by Hulbert and Katz [Hul64] about "Some Problems in Particle Technology" and the book by Randolph and Larson about the "Theory of Particulate Processes" [Ran88]. Population balances are popular in various fields such as

polymerisation, bubble columns, biological processes (fermentation or cell culture), granulation, grinding up to aerosol reactors. A general review of population balances can be found by Ramkrishna et al. [Ram85, Ram00, Ram02]. In view of crystallization, Tavare reviewed in 1987 the modelling and analysis of batch crystallizers [Tav87]. This was followed by Rawlings et al. in 1993, who reviewed the application and use of the population balance in crystallization from a model identification and control perspective [Raw93]. A more recent review was made by Braatz et al. [Bra02] in 2002. The modelling of crystallization might be graphically illustrated by figure 3-6 demonstrating the complex interrelations.
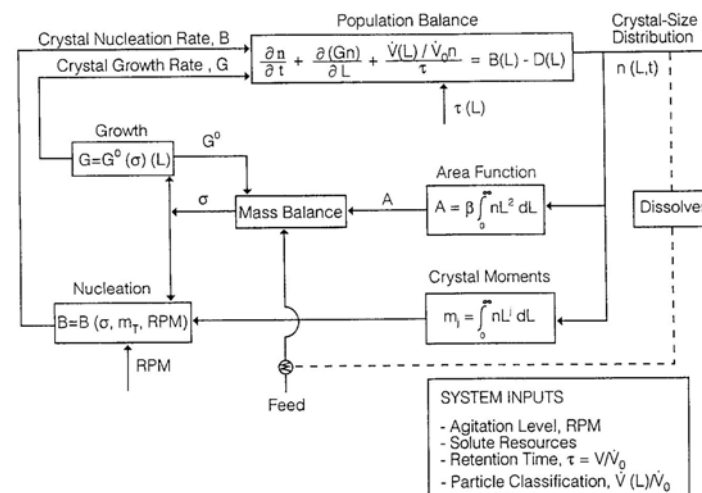
Figure 3-6: Relationship among population- and mass balance as well as nucleation and crystal growth rates [Mer01]

The population balance can be modelled in a multi-dimensional space as well as formulated with number coordinates but also in volume or mass coordinates. The latter two are of advantage when describing agglomeration and breakage processes. When two particles agglomerate, the total volume is the sum of each individual volume. This does not apply for the length. Therefore, if the population balance is conserved so is automatically the mass balance [Ver02, Sca02]. Furthermore, the volume of a particle is the only size parameter that is independent of the particle shape. Especially when using a Coulter Counter particle analyser the formulation in volume coordinates is of an advantage [Nai98, Xu03]. The choice for number or volume coordinates therefore depends on what kind of experimental distribution is available. By converting a number to a volume distribution and vice versa, the error scales to the power of three (L^3).

Nowadays two-dimensional population balances are becoming increasingly popular and state of the art (n = f(length, second property, time)). A particle is thereby characterised by its length and a second particle property. For example, by introducing a second length, morphological changes of crystals can be modelled. This is of special interest for crystallization processes where particles generally deviate from simple shapes such as sphere or cubes [Pue03, Bri06, Oul07, Ma08, Kem08]. Two-dimensional population balances are also common to model growth rate dispersion. Examples are described by Baumann [Bau93, Bau99], Gerstlauer et al. [Ger01] and Westhoff et al. [Wes03]. A detailed modelling can

therefore become complex. Besides the actual particle size distribution also the nuclei that form, the growth rate, the attrition fragments, the breakage fragments (daughter crystals), agglomerates and the shape of crystals can have a specific distribution. For certain crystallization processes where polymorphs or attrition fragments are present, a population balance for each individual substance or class of crystals (for example: polymorph 1 and 2, crystals and attrition fragments) can be used to model the behaviour [Mit02, Ono04].

The population balance is in its general form a nonlinear partial (integro)-differential equation that must be solved numerically. The "integro" results from the fact that agglomeration and breakage terms are expressed as integrals [Cos07]. The method for solving the respective equation is often depending on the actual kinetic mechanisms that are active. Since the methods for solving the population balance are not standardised, as for example for solving ordinary differential equations, it is common that different authors have their own method to solve the equations. Problems often arise because the number distribution can be sharp and cover a wide range of size and time classes (1 nm to 1000 μm, 1 ms to 1000 min). According to Ramkrishna et al. [Ram00, Ram02] individual methods to solve the population balance equations can be grouped into four main categories:

- Method of Moments (deterministic)
- Weighted residuals/orthogonal collocation methods (deterministic)
- Finite difference methods/discretised population balances (deterministic)
- Monte-Carlo Simulations (stochastic)

A detailed recent review can be found by Costa et al. [Cos07]. For special cases, an alternative numerical method called "Method of Characteristics" can be applied [Ran88, Boh92, Bau99]. It is a computationally efficient method and ideally in conjunction with model-based control strategies and reverse engineering [Cha82, Sot00, Lee02, Vol03, Vol06, Hou06, Bri06, Kem08, Qam08a].

3.4.2   Moment Model

Within the scope of this work, the following assumptions are made: temperature, fluid velocity, liquid and particle concentration are not depending on space (ideal mixed conditions). Furthermore, it is assumed that only nucleation and growth are taking place and that all crystals having the same morphology. Assuming furthermore a batch process with a constant volume the population balance can be formulated by equation 3.19.

$$\frac{\partial n_{PSD}}{\partial t} + \frac{\partial (G \cdot n_{PSD})}{\partial L} = 0 \qquad\qquad (\text{ 3.19 })$$

The nucleation rate is introduced via the boundary condition (nuclei of zero size ($L_N = 0$)) given by equation 3.20.

$$n(L = 0, t) = \frac{B}{G\big|_{L=0}}$$

(3.20)

Equation 3.19 can be further simplified by approximating the particle size distribution by its moments defined by equation 3.21.

$$m_{PSD,j} = \int_0^\infty n_{PSD} \cdot L^j \cdot dL$$

(3.21)

The time-dependence of the first five moments of the respective seed crystals as well as the entire crystal population ($m_{PSD,0}$…$m_{PSD,4}$) is modelled by equations 3.22 to 3.25.

$$\frac{dm_{PSD,0}}{dt} = B$$

(3.22)

$$\frac{dm_{PSD,Seed,0}}{dt} = 0$$

(3.23)

$$\frac{dm_{PSD,j}}{dt} = j \cdot G \cdot m_{PSD,j-1} + B \cdot (L_N)^j \quad j = 1, 2, 3, 4$$

(3.24)

$$\frac{dm_{PSD,Seed,j}}{dt} = j \cdot G \cdot m_{PSD,Seed,j-1} \quad j = 1, 2, 3, 4$$

(3.25)

This set of equations can easily be solved in conjunction with the mass balance (equation 3.26) and kinetic equations using a standard ordinary differential equation solver.

$$-\rho_{Crystal} \cdot k_V \cdot \frac{dm_{PSD,3}}{dt} = \frac{dc_{mass}}{dt} = -\rho_{Crystal} \cdot k_V \cdot \left(3 \cdot G \cdot m_{PSD,2} + B \cdot (L_N)^3\right)$$

(3.26)

As described in chapter 3.3, the energy balance can be neglected for most solution crystallization processes. Important integral values such as the total number of crystals, specific surface area and suspension density can be calculated via the respective moments. Various mean particle sizes can be determined via equation 3.27 (i > j, i = 1 − 4, j = 0 - 3) [Les84, Mer01]

$$L_{PSD,[i,j]} = \left(\frac{m_{PSD,i}}{m_{PSD,j}}\right)^{\frac{1}{(i-j)}}$$

(3.27)

and the *c*oefficient of *v*ariation (abbreviation ***CV-value***) via equation 3.28 (i = 0 - 3).

$$CV\left(Q_{PSD,i}\right) = \sqrt{\frac{m_{PSD,i} \cdot m_{PSD,i+2}}{\left(m_{PSD,i+1}\right)^2} - 1}$$

(3.28)

By incorporating additional kinetic mechanisms apart from nucleation and growth into the moment model, a so called "closure problem" occurs. In other words, the number of unknowns and number of equations is not balanced anymore [Hul64]. The use of the "Quadrature Method of Moments" or related methods becomes necessary [Dor06, Gro07]. The reconstruction of the full distribution out of a finite number of moments is for example discussed by John et al. [Joh07] and Qamar et al. [Qam08b].

By incorporating agglomeration into the moment model and converting the derivatives of the model to differentials (linearisation), following equations can be obtained (table 3-3) [Ran88, Tav95, Bra96].

Table 3-3: Calculation of nucleation and growth rates as well as the agglomeration kernel using a "differential approach" (j = 1, 2, 3, 4) [Ran88, Tav95, Bra96]

Mechanism	Number Distribution		Volume Distribution	
Moment	$m_{PSD,j} = \int n_{PSD}(L) \cdot L^j \cdot dL$	(3.29)	$m_{v,PSD,j} = \int n_{v,PSD}(V) \cdot V^j \cdot dV$	(3.33)
B (Nucleation)	with $\beta_0 = 0$ $$B = \frac{\Delta m_{PSD,0}}{\Delta t}$$	(3.30)	$B = \frac{\Delta m_{v,PSD,0}}{\Delta t} + \frac{1}{2} \cdot \beta_0 \cdot \left(\overline{m}_{v,PSD,0}\right)^2$	(3.34)
G, G_v (Growth)	with $\beta_0 = 0$ (except for j = 3) $$\frac{dL}{dt} = G_j = \frac{\Delta m_{PSD,j}}{j \cdot \overline{m}_{PSD,j-1} \cdot \Delta t}$$	(3.31)	$\frac{dV}{dt} = G_v = \frac{\Delta m_{v,PSD,1}}{\overline{m}_{v,PSD,0} \cdot \Delta t}$	(3.35)
β_0 (Agglomeration)	with B = 0 $$\beta_0 = -2 \cdot \frac{\Delta m_{PSD,0}}{\left(\overline{m}_{PSD,0}\right)^2 \cdot \Delta t}$$	(3.32)	$\beta_0 = \frac{\Delta m_{v,PSD,2}}{\left(\overline{m}_{v,PSD,1}\right)^2 \cdot \Delta t} - 2 \cdot \frac{G_v}{\overline{m}_{v,PSD,1}}$	(3.36)

The Δ (delta) refers to a difference between two successive time points, whereas the bar represents the arithmetic average between these two successive time points $((m_{0,t1}+m_{0,t2})/2)$. Using the number distribution either the growth and nucleation rate (zero agglomeration) or the growth rate and the agglomeration kernel (zero nucleation) can be extracted. If the moment equations are transformed into volume coordinates the nucleation, growth and agglomeration kernel can be determined [Tav95, Mou96, Che03, Ntu07]. Generally, the following empirical equation 3.37 is formulated for the size-independent kernel [Mer00b].

$$\beta_0 \approx k_1 \cdot G^{k_2} \cdot B^{k_3} \cdot \left(m_T\right)^{k_4} \cdot \left(N_{Stirrer}\right)^{k_5}$$

(3.37)

According to Mersmann [Mer02], more than 50 different agglomeration kernels are available in the literature, all being independent of supersaturation. However, for crystallization processes, crystal growth causes often a cementing of particles that must be accounted for [Dav95, Mat02, Mer02].

Within this work, two ways of determining the kinetics will be applied. The "integral approach" allows determining the kinetic rate constants by fitting the population balance approximated by moments (equations 3.22 to 3.25), the respective mass balance (equations 3.26) and kinetic equations (equation 3.3 and 3.11) against the experimental data. It allows the simultaneous determination of all rate constants, however, the kinetic model must be provided a-priori (see chapter 9.2.1). The so called "differential approach" uses the equations given in table 3-3 that permit the determination of the kinetic behaviour without any a-priori assumption about the kinetic rate law. Individual rates or constants are determined separately (see chapter 9.2.2).

4 Determination of Crystallization Kinetics

4.1 Simultaneous Determination of Nucleation and Growth Rates

At the "heart" of the population balance are the kinetic equations. The right use and the right parameters determine the performance and predictability of the model. The book: Measurement of Crystal Growth and Nucleation Rates (2nd edition) that was released by the Working Party on Crystallization [Gar02] describes common methods that are categorised in figure 4-1.
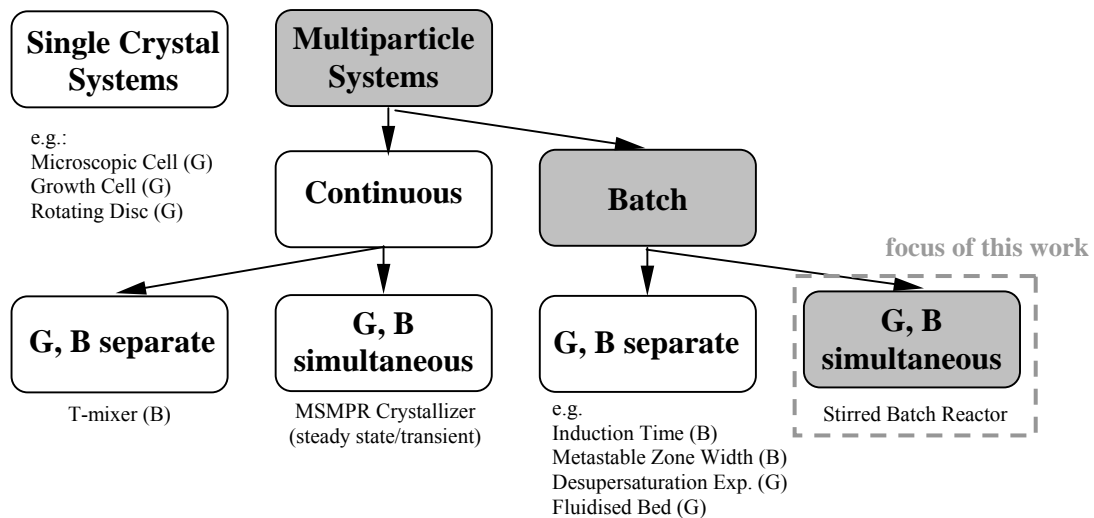
Figure 4-1: Classification of common methods to determine crystallization kinetics

Single crystal measurements are important to gain an insight into growth mechanisms of a specific crystal face and to validate growth theories. From a crystallizer design point of view as well as having growth rate dispersion in mind, multiparticle systems are more appropriate. The methods differ mainly within the equipment, the amount of material and mathematical treatment necessary as well as the information content that can be obtained. These are all factors related to time and resource expenditure. For example the fluidised bed is easy to operated, to evaluate and does not need a calibration of instruments. However, a relatively large amount of material and time is necessary to extract the growth rate as a function of supersaturation. The choice of the method ultimately depends on the objective and resource constraints of the project.

The work restricts itself to the simultaneous determination of nucleation and growth kinetics within a stirred reactor, although agglomeration will be partly touched. A stirred solution has the advantage that crystal-impeller collisions are present that will likely also be the case in large-scale production. Additionally, nucleation and growth rates are referring to the same supersaturation that is one of the critical parameter to measure. One of the oldest methods is the MSMPR crystallizer operating in steady state. Although the evaluation of experimental data is simple, the disadvantages are [Gar02]:

- Time consuming (one point per steady state)
- Laborious (large amount of material, steady state often after 8 – 15 residence times)
- Complex experimental set-up of a continuous process

Contrary, time-dependent batch processes are easy to operate, need much less material and many parameters can be studied simultaneously. These advantages are offset by the complexity of the analysis.

Methodologies and case studies for the simultaneous estimation of nucleation and growth kinetics from batch experiments were reviewed in 1987 by Tavare [Tav87]. Generally, at this time only off-line measurement techniques were applied. Two years later, in 1989 the group of Rawlings demonstrated that the continuous on-line measurement of supersaturation (on-line densitometer) and the second moment of the particle size distribution (on-line turbidity) throughout the experiment are possible and that kinetic parameter can be estimated accurately if the solute concentration and particle size distribution are recorded. Although the entire particle size distribution was measured with a Malvern Particle Sizer 3600Ec, it was decided to make use only of the obscuration. At this time it was believed that the deconvolution of the laser diffraction signal does not lead to accurate results [Wit90, Raw93, Mil94, Mat98]. By assuming Fraunhofer diffraction ($Q(L) = 2$, $L \approx\ > 2\text{-}5\ \mu m$ [Raw93, Sev97]) equation 4.1 relates the transmittance (obscuration = 1 - transmittance) to the turbidity [Box92, Mil94, Mat98]:

$$Transmittance = \exp\left(-\underbrace{\int n_{PSD}(L)\cdot A_{Projected}(L)\cdot Q(L)\cdot dL}_{Slurry\ Turbidity\ (\tau)}\cdot l_{Cell} \right) \tag{4.1}$$

Assuming convex particles, the theorem of Cauchy can be applied. In other words, the total surface of a particle is 4 times the projected area ($4\cdot A_{Projected} = A_{Surface} = k_A\cdot L^2$) [Sti95]. Consequently, equation 4.2 relates the second moment of the particle size distribution to the transmittance.

$$Transmittance = \exp\left(-\frac{l_{Cell}\cdot k_A}{2}\cdot \int n_{PSD}(L)\cdot L^2\cdot dL \right) \tag{4.2}$$

For the determination of mean particle sizes from turbidity data see Raphael et al. [Rap96] and Tadayyon et al. [Tad97]. It must be noticed that transmittance measurement is only applicable to low solid concentrations (transmittance > 0.7 [Mil94, Tad97]).

Within the last decade, there has been a tremendous development in high-resolution in-situ measurement techniques, commercial software packages for solving population balances and an increase in computational capabilities. Since around the year 2000, numerous articles have been published, using the moment model or the full population balance, in-situ, on-line or off-line concentration measurement and in-situ, on-line or off-line particle size measurements and various combinations thereof to determine the kinetics [Aou99, Sta01,

Bla01, Bra04, Hu04, Pue03, Qui04, Ono04, Oul07]. The various combinations of equipment and "position" results from the fact that not all possible measurement techniques are available at one particular place and that certain measurement techniques are only applicable to certain classes of substances or certain experimental conditions.

Up to now, the simultaneous use of in-situ measurement techniques for the supersaturation and particle size distribution with the objective to extract kinetic data (quantitative analysis) is, due to the often complex mathematics involved, seldom applied [Tog04, Tri08]. It is clearly the next major step after 1989. It avoids any errors associated with taking a sample that is critical for measuring supersaturation and particle size distributions. The current challenges are clearly associated with the in-situ measurement of particle size distribution at various suspension densities. Only laser scanners seem to be applicable at the moment. For a detailed discussion see chapter 5.3.2. The instrument is popular and widely used for qualitative monitoring the onset of nucleation or following changes in the size distribution. Due to the complex mathematics that is necessary to deconvolute the recorded information often only the raw measured data, a chord length distribution, without any pre-treatment is used [Euh03, Tog04, Sha05, Mén06, Sch06c, Dan07, Al08, Tri08]. Table 4-1 summarises a survey forming the baseline of this work.

Table 4-1: Survey of substances and suspension density ranges that have been used in combination with the "Focused Beam Reflectance Measurement" instrument (laser scanner) to determine crystallization kinetics

Substance	Suspension Density [g/kg Solvent]	Determined Parameters	Reference
Simultaneous Determination of Nucleation and Growth Kinetics			
Paracetamol/Isopropanol/ Water	< 90	k_b, b, k_g, g (raw measured data)	[She08, Tri08]
L-Glutamic Acid/Water	< 30	k_b, b, k_g, g (raw measured data)	[Sch06c]
Paracetamol/Ethanol	< 70	k_b, b, k_g, g, E_G (deconvolution of chord length distribution)	[Wor04]
Cox-2-Specific Inhibitor/Toluene	< 130	k_b, b, k_g, g (raw measured data)	[Tog04]
Determination of Nucleation and/or Growth Rates (no rate constants given)			
Phosphoric Acid Hemihydrate	melt	G_{CLD} (raw measured data)	[Dan07]
Paracetamol/Ethanol/ Methanol	< 320	B_{CLD} (raw measured data)	[Mén06]
Sodium- and Calcium Carbonate/Water	< 680	G_{CLD} (raw measured data)	[Sha05, Al08]
Sodium Carbonate and Sulphate/Water	-	B_{CLD}, G_{CLD} (raw measured data)	[Euh03]

For the course of this work it is assumed that the measurements contain too less information to be capable of discriminating between different nucleation and/or growth mechanisms. In other words, even by using the latest in-situ technologies, an imbalance between the actual theoretical knowledge and the measured information content often remains (compare chapter 3 to chapters 5 and 8) [Mar05]. The more mechanisms are simultaneously active the more

information (in other words: the more measurement instruments) are necessary in order to be still capable of uniquely extracting all kinetic information.

The use of laser scanner for the determination of agglomeration and breakage kinetics is discussed by Williams et al. [Wil92], Kougoulos et al. [Kou05] and Heath et al. [Hea06].

4.2   Model-based Experimental Design and Analysis

Experiments can be designed in different ways often by intuition, trial-and-error or by applying the one-factor-at-a-time approach. The first two can work well. However, even if a satisfactory result is obtained, there is no guarantee that the "best solution" has been found. The one-factor-at-a-time approach is simple and effective, however, fails if parameters are interacting or many parameters need to be studied [Ull07]. Within batch crystallization for example: seed mass, seed size, seed distribution, temperature level, temperature profile and batch time can be used as a parameter.

One possible way to avoid "random walks" and to provide structure to experiments and the subsequent analysis is using a model-based approach that is illustrated in figure 4-2.
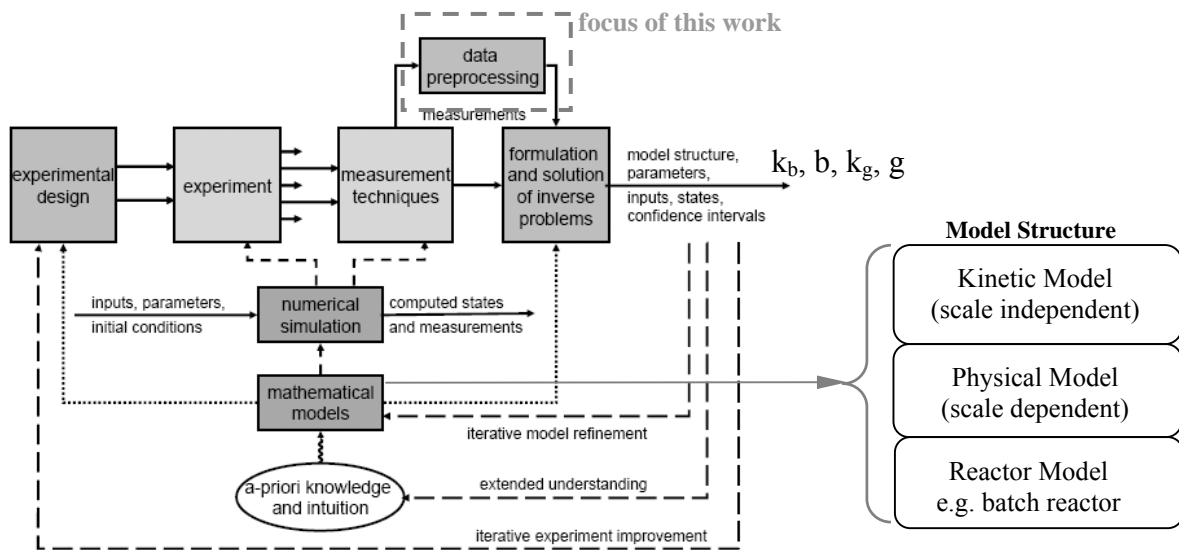
Figure 4-2: Illustration of the model-based approach ("MEXA work process") based on Marquardt [Mar04, Mar05] as well as the corresponding model structure

The described method is only partly touched by the book: Measurement of Crystal Growth and Nucleation Rates [Gar02]. It uses all a-priori knowledge that is available in form of balance equations, kinetics and boundary conditions. The same model can thereby be used for different objectives: to simulate a process, to estimate parameters by fitting a model against experimental data (solution of the inverse problem) or for "*M*odel-*b*ased *E*xperimental *D*esign" (abbreviation **MBED**), sometimes also called "Optimal Experimental Design". The described framework assumes time-dependent experiments, utilization of high-resolution measurement techniques and the use of mathematical models. The sensors should be applied

in-situ and if any possible non-invasive. So far, this systematic work process has only been applied in minor cases. Individual parts are still under active research [Bar04]. Examples are the investigation of kinetics in heterogeneous reactive systems or enzymatic reactions, multicomponent diffusion in liquids or transport in a falling liquid film [Kör02, Bar04, Mar05, Iss05, Fra08]. Applications to crystallization are reported by Matthews et al. [Mat98], Chung et al. [Chu00], Togkalidou et al. [Tog04] and Chen et al. [Che04]. It should be noted, although MBED and analysis is a data driven tool it cannot be a substitute for creative thinking and scientific intuition.

Figure 4-2 can be reorganised to figure 4-3 with special emphasis on MBED. It assumes that the right model (kinetic equations) has been selected and therefore no model discrimination between different rate laws is necessary. A wrong model selection can be recognised by large deviations between experimental results and model predictions.
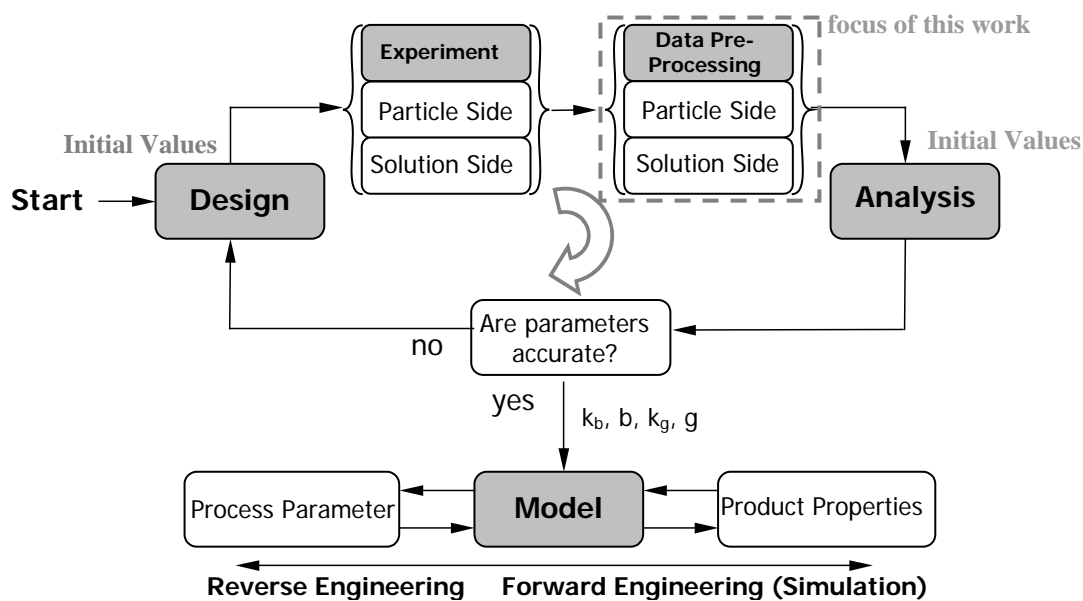
Figure 4-3: Illustration of the sequential experimental design strategy using model-based experimental design and analysis (estimation of kinetic parameters); based on Marquardt [Mar04] and Fujiwara et al. [Fuj05] (see also figure 9-2 (chapter 9))

The experimental procedure follows a sequential experimental design strategy (design – execution – analysis – design…) leading to a progressive reduction of parameter uncertainties [Are07, Bar08]. Within this work, the analysis refers to the estimation of kinetic parameters. A parallel approach, where no iteration is necessary (parallel experimentation) was proposed by Galvanin et al. [Gal07].

The aim of the design is to reduce the confidence intervals and any correlation between the kinetic parameters. In other words, to make the elements of the parameter variance-covariance small until a user defined limit is reached and/or the parameters and confidence intervals do not change significantly between successive experiments [Chu00, Asp02]. In general, it can be distinguished between A, E and D-optimality [Asp02, Kör02, Ber03, Are07]. In other words, MBED allows designing experiments that maximise the information content. It systematically explores the whole design region by varying all parameters in a balanced fashion. All kinetic constants for a crystallization process dominated by nucleation and

growth can typically be obtained in as few as 2-4 batch experiments [Chu00, Fuj05]. The method offers therefore a way to reduce the amount of starting material as well as time and resource expenditure. It is a promising method especially for expensive substances such as certain intermediates or proteins. The decision at which point the parameters are accurate depends on the objective of the work as well as the resource and time constraints. It is closely related to the number of population balance models available and the quality of the experimental data.

Besides the general strategy figure 4-3 also indicates another peculiar but important aspect. Although the aim is to determine kinetic constants that are not known, it is necessary to have already some pre-knowledge of the kinetic constants, as close as possible to the "true" value being a standard dilemma in MBED and parameter estimation [Are07, Bar08]. In other words, the results of MBED and the subsequent estimation of the parameters are strongly dependent on the actual pre-knowledge of the parameters [Hei07]. A good initial guess or knowledge can significantly reduce the experimental effort. If only minor a-priori knowledge (for example: maximum-minimum values of the parameters) is available a robust design formulations [Asp02, Bar08] and global optimisation methods can be used [Ban02, Eft02, Bar08].

Model-based experimental design in its simplest form is known under the word "Design of Experiments (abbreviation DOE)". The model that is used is just a simple polynomial with interaction terms. It can only construct empirical relations between process conditions and the product properties of interest. It is a convenient tool to screen different parameters in a systematic manner. Examples are given by Charmolue et al. [Cha91] and Burke et al. [Bur01] who used a 2^3 (2 level, 3 factors) factorial design to investigate the crystallization of an amino acid and proteins, respectively. Ukrainczyk et al. [Ukr07] applied a D-optimal design for studying the precipitation of calcium carbonate whereas Liu et al. [Liu07] used virtual experiments in conjunction with a factorial design and Box-Behnken optimization in order to find optimal conditions for an anti-solvent crystallization.

Once the kinetic parameters are obtained, the model can be used for simulating all desired process conditions and for optimising specific properties of interest. In general, for a simulation very advanced models compromising all applicable physical and chemical effects of interest can be used. Multi-dimensional population balances with nucleation, growth, agglomeration, breakage and combinations with "Computational Fluid Dynamics" are state of the art. The limits are mainly set by the solvability of the corresponding equations. For a recent review see for example Ulrich et al. [Ulr05]. The kinetics and the model can also be used to calculate reverse. In other words, to obtain the temperature profile and seed characteristics that optimise one or a number of product characteristics [Chu99, Cho04, Wor04, War06, Sar07]. This is closely connected to model-based control [Chr02, Vol03, Zha04, Vol06]. Models developed at an early state of research, used for MBED, can later be applied for optimising the product quality and process conditions and finally in manufacturing plants for model-based control ("product life cycle" modelling).

For individual steps of the described methodology commercial software like gProms (Process Systems Enterprise) or Parsival (Dr. M. Wulkow, Computing in Technology GmbH) is available. For each individual step many specialised software from academia exist. The

choice of the complexity of the model must be balanced with the objective of the work, quality of the experimental data and resources available. The focus of this work lies on the data pre-processing of measurement data that plays a central and important role.

4.3   Comparison between Kinetic Measurements

Many different methods can be used for the determination of kinetics. A comparison between individual methods and authors, however, remains challenging. This is attributed to different experimental ranges in view of supersaturation and temperature, various experimental equipments (mixing behaviour), different measurement instruments (see chapter 5), unnoticed impurities and various ways of evaluating the same data (see chapter 9). Additionally, different characteristic sizes of the same crystal might be defined. The growth rate can thereby refer to a crystal face, to a single crystal or a crystal collective.

Barium sulphate has been subjected to numerous investigations since the very early years. It will serve as an extreme example to illustrate the variance between individual case studies. Aoun et al. [Aou99] listed in 1999 nine quotes that studied nucleation rates and twelve who studied growth rates of barium sulphate, mentioning difficulties in comparing these data. Figure 4-4 that is adopted from Judat [Jud03] shows experimentally determined growth rates from different researchers.
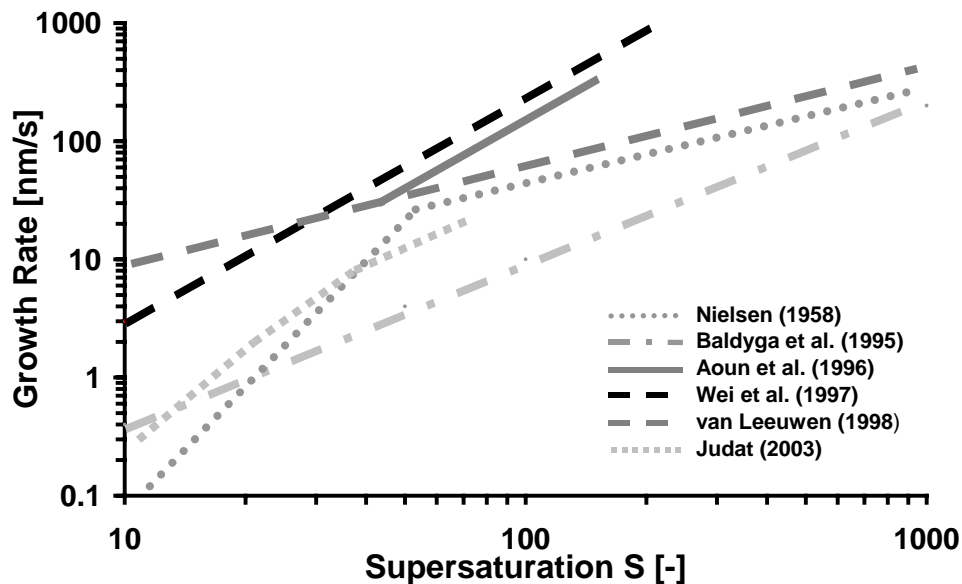
Figure 4-4: Comparison between different experimental determined growth rates of barium sulphate as a function of supersaturation (adopted from Judat [Jud03])

Söhnel et al. [Söh92] found out that the growth rate mechanism was determined to be "diffusion-controlled", of screw dislocation or surface nucleation type depending on the reference. The growth rate order was determined between 1 and 4. In other words, even for widely studied substances such as barium sulphate contradictory results are reported [Söh92]. This is typical because even today with advanced instrument techniques it is still time

consuming to verify exactly which mechanism takes place and to measure supersaturation and particle sizes accurately. The determined kinetic parameters can also compromise to a certain extent mechanisms that have been overlooked. For a comparison between experimental determined nucleation rates for barium sulphate it is referred to Aoun et al. [Aou99], Judat [Jud03] and Roelands et al. [Roe06].

Similar results as for barium sulphate are reported for potassium sulphate [Tav79, Jon86, Bud87, Tav95, Sha96, Peb96a, Sch99] and ammonium sulphate [Tad02]. Mohan et al. [Moh02] compared the growth rate coefficient k_g for potash alum from 4 references. It ranged between $1.87 \cdot 10^{-6}$ and $5.65 \cdot 10^{-5}$ m/s at 25 °C. Söhnel et al. [Söh92] concluded that rate constants have at least an error of ±30%.

To judge model predictions confidence intervals should be calculated. Without theses information it remains difficult to actually judge the determined kinetics [Che00, Bla01, Abb07, Ono04, Oul07]. Confidence intervals can be rather large. For example Togkalidou et al. determined a nucleation order of b = 1.05±0.48 and a growth order of g = 1.09±0.43 [Tog04] for an organic substance (see also Miller et al. [Mil94] and Tavare et al. [Tav86]). High values often indicating that a kinetic mechanism is not modelled or the experimental data contains larger errors.

5 Measurement Techniques

5.1 Introduction

A central part of the determination of kinetics forms the actual recording of experimental data. Measuring instruments can thereby be classified as off-, on-, at(ex-line), in-line or in-situ. For a detailed differentiation and definition of each term it is referred to Kessler [Kes06], Bohnet [Boh07] or Bröckel et al. [Brö07]. Throughout this work, the word in-situ will be used, since the employed measurement probes record a local change of a characteristic property at a specific place in the crystallizer [Boh07, Brö07].

The advantage of an in-situ measurement is that no errors are introduced via sampling, sample transport and sample preparation. The feedback time is often instantaneous (minutes or seconds) and not hours as in case of off-line sampling. This "real-time measurement" allows immediately reacting to faults that occur. Disadvantages being clearly that occasionally operational difficulties arise caused by encrustation on the probe [Lew01, Sch06c, Al08]. Contrary to off-line (and often on-line) instruments that operate at constant operating conditions the calibration for in-situ probes must account for changing process conditions (temperature, solid content, solution composition). Spectroscopic methods might encounter peak shifts [Tog01a, Lew01], similar to the particle size instrument used within this work (see chapter 8).

In general it can be said, the more advanced a measurement method is the more information can be obtained, however, the more mathematics to extract a specific information must be applied. The question, which location in the reactor is representative for the measurement (or to take a sample for off-line analysis), remains. Reviews on measuring methods in the field of crystallization can be found by Braatz et al. [Bra02] and Lawrence et al. [Law04].

5.2 Solution Side (Supersaturation)

For the determination of the supersaturation, in principle, all methods that are capable of measuring a concentration can be used. Apart from "special devices" [Kue97, Loe02, Pos05], the exact knowledge of the solubility as a function of dissolved impurities must be known in advance. This makes the determination of supersaturation often challenging in rough industrial crystallization processes. The measurement of the supersaturation is eased at higher concentration differences because the error of the measurement does not coincide with the error of the solubility curve (problem of subtracting two large values from each other). In contrast to particle size instruments, a thorough comparison between different supersaturation measurement techniques, applied to the same system, has only been made in minor studies [Per05a]. Table 5-1 summarises experimental methods for the determination of supersaturation.

Table 5-1: Experimental methods for the determination of supersaturation

Type of Instrument	f(T)	f(solid)	Calibration	Position	Reference	Notes
Spectroscopic Methods						
ATR-FTIR Spectroscopy (more common)	yes	no	chemometric	in-situ	[Dun97, Tog01a]	
Near Infrared Spectroscopy (less common)	yes	yes	chemometric	in-situ	[Vac03]	-mainly used for solid state analysis -limit to systems with minor amount of water
Raman Spectroscopy (less common)	yes	yes	chemometric	in-situ	[Hu05, Cai06]	-strength in detecting different polymorphs
Physical Methods						
Refractive Index (K-Patents)	yes	no	simple	in-situ	[Gen05, Roz06]	-older instruments work on-line and are affected by solids
Density	yes	yes	simple	on-line	[Mil94, Sch99]	
Conductivity	yes	yes	simple	in-situ	[Nýv94, Jag96]	-suited for electrolytes
Ultrasound	yes	yes	simple	in-situ	[Oma99, Per05a]	
Calorimetry (less common)	-	-	complex	non-invasive	[Fév96, Mon97]	-suited for systems with a high heat of crystallization
Special Devices (not common)						
Encrustation on a Peltier Element	-	-	-	in-situ	[Kue97, Löf02]	-still at research
Total Reflection Polarimeter with a Reference Cell	-	no	simple	in-situ	[Pos05]	-still at research

Whereas near infrared spectras contain information about the liquid phase properties, mean particle sizes, solid concentration and polymorphs [Vac03, Aal03, Fév04, Abe08], does Raman spectroscopy has its clear strength in tracking different polymorphs. For a detailed recent review it is referred to Févotte [Fév07]. However, for the determination of the supersaturation the most common method is "*A*ttenuated *T*otal *R*eflection *F*ourier *T*ransform *I*nfra *R*ed Spectroscopy" (abbreviation **ATR-FTIR**) [Dun97, Tog01a, Fév02, Grö03, Sch06c]. Even though simple calibration routines using one wavelength [Lew01, Sch06c] to a certain number of wavelengths [Grö03] have been reported, advanced chemometric methods using the entire spectra are recommended [Tog01a, Pöl05]. This often implies the use of principle component regression, partial least squares and spectra pre-processing tools such as multiplicative signal correction, Savitzky-Golay smoothing or orthogonal signal correction to name just a few. Although the concentration of more than one substance can be followed using the spectra, the supersaturation can only be calculated if the solubility behaviour of all respective substances is exactly known. The time interval between two consecutive measurements mainly depends on the spectral resolution that is chosen.

Physical methods are easy to calibrate and allow the concentration measurement of one substance within time intervals of seconds. The refractometer PR-03-P of K-Patents Process Instruments seem to be a promising instrument, since the readings are not influenced by solids. However, so far it has only been applied to the crystallization of sugar [Roz06] and magnesium sulphate [Gen05]. Within this work, an ultrasound probe will be used to determine the concentration, as described by Omar et al. [Oma99]. According to Machefer et al. [Mac07] the advantage of the probe can be summarised as follows: measurement

independent of the optical properties of the system, stainless steel one piece construction, resistant to pressure, temperature and fouling. The ultrasound velocity has a clear strength in detecting molecular differences. Positional isomers can be clearly identified in their melt (o-xylene (1349 m/s), m-xylene (1321 m/s), p-xylene (1310 m/s) at 25 °C) [Al06] and sucrose (1690 m/s) can be distinguished from reducing sugar (50/50 glucose and fructose, 1735 m/s) [Hei08c].

The probe has been used for detecting nucleation events in pure solution (metastable zone width measurement), to study the influence of additives [Tit02, Ulr02a, Kal05], to measure the initial supersaturation before seeding [Kal07], to determine growth kinetics (desupersaturation experiments) [Gla04, Per05b, Oma06b] and to monitor phase transformations [Str04]. If only the solute concentration is of interest, the signal must be protected from the influence of solids (see Machefer et al. [Mac07] for gas-liquid systems) [Tit03, Per05]. High power ultrasound devices are used for enhancing nucleation [Den03, Lou06], however, the specific energy input are up to orders of magnitude higher than the energy input by the probe used within the work. The use of the ultrasound probe for the simultaneous determination of nucleation and growth rate has, to the authors knowledge, not been made before.

5.3   Solid Side (Particle Size Distribution)

5.3.1   Comparison between Instruments

A detailed review on particle sizing techniques can be found by Allen [All03]. Within crystallization processes, only a minor number of instruments are often used being summarised in table 5-2. The data has been taken from vendors brochures and respective homepages.

Table 5-2: Experimental methods for measuring particle size distributions within crystallization processes

Type of Instrument	Distribution	Size Range [μm]*	Position	Notes
Sieve (wet/dry)	mass	20 - 1000	off-line	- dry: 63 – 1000 μm
Electrical Sensing Zone Method	number & volume	0.4 - 1000	off-line	- occasionally in-situ use [Ulr85, Ran88]
Laser Diffraction & Scattering	volume	0.02 - 1000	on-line	- deconvolution of signal
Laser Scanner	"number"	0.5 - 1000	in-situ	- deconvolution of signal
Optical Microscopy	number	1 - 1000	in-situ	- image analysis

*Although some instruments are also capable of measuring particles larger 1000 μm, it is generally of no importance for crystallization processes.

The instruments mainly differ in the covered size range, resolution (number of channels), distribution type, characteristic size that is measured and the capability to measure in-situ or on/at/off-line. The information included in table 5-2 is a current snapshot due to the ongoing

instrument developments. The indicated size range might differ between different vendors and instrument versions. By comparing different instruments, it is important to agree on a common standard in representing *p*article *s*ize *d*istribution data (abbreviation **PSD**) [Les84, Som01] as illustrated by the article "40 Years of Presentation Particle Size Distributions – Yet Still Incorrect?" [Som01].

The choice of an in-situ particle size analyser is limited. The current advantages and disadvantages of optical microscopy are described by various authors [Cal05, Lar07, Kem07, Wan08]. The current bottleneck is the evaluation of low quality images that is strongly dependent on the suspension density and type of crystal (transparent versus opaque). Commercial image analysis software generally fails [Wan08]. Larson et al. [Lar07] applied model-based object recognition and Calderon de Anda et al. [Cal05] and Kempkes et al. [Kem08] multi-scale segmentation. The latter includes edge detection, morphology closing, region filling and object measurement. The current instruments can capture in the range of 10-30 images per second [Lar07, Kem07] with an image analysis time in the order of 6-10 images per minute [Lar07, Kem07]. For a number distribution several thousand particles need to be clearly identified to ensure an appropriate statistic [Dav06]. Since not every image is a successful image, the measurement time between two successive distributions can become long. An automated image analysis is compulsory. Therefore, image analysis is currently mainly used to detect changes in morphologies. However, a first proof of concept in the determination of growth rates was described by Wang et al. [Wan07], whereas strategies are given by Kempkes et al. [Kem08]. According to Davies [Dav06] crystal shape as a property has been "under-rated, under-studied and under-utilised".

Whereas for the measurement of the supersaturation different instruments could have been used, laser scanners seem to be the only particle size analyser suitable for the objective of this work. These instruments are capable of covering a wide size range with a high resolution with respect to size and time. Since the measurement is based on backscattering, the laser must not pass through a layer of particles (multiple scatter) making it more capable of handling higher suspension densities. However, as with image analysis, the current challenge is associated with transforming the raw measured data. In other words, the *c*hord *l*ength *d*istribution (abbreviation **CLD**) must be deconvoluted into a PSD. Depending on the substance and suspension density, a reliable distribution of approximately 5000 particles can be obtained in the order of 30 to 60 seconds [MTS07]. The time for deconvoluting one CLD is in the range of several seconds up to a minute. For a comparison between laser scanner and other sizing techniques, it is referred to the appendix (chapter A.2).

In future, besides optical microscopy, ultrasonic spectroscopy might become applicable that shows increasing applications within crystallization processes and research. It is capable of measuring particles up to 50 vol% and particle sizes from 0.01 µm to 1000 µm [Cao99, Hip00, Mye02, Neu02, Kes06]. Current instruments can only be used on an on-line basis. As for other sizing instruments, a deconvolution of the raw signal is necessary. For doing so, physical parameters (ultrasound, density, viscosity, heat capacity, thermal conductivity) for both the liquid and solid phase must be known in advance in order to reconstruct the PSD from the raw measured signal.

5.3.2   Laser Scanning Technique

5.3.2.1   Measuring Principle

Laser scanners (or laser backscattering instruments) produced and sold by Messtechnik Schwartz GmbH ("*3* Fold *D*ynamical *O*ptical *R*eflectance *M*easurement" (abbreviation *3D-ORM*)) and Mettler-Toledo GmbH ("*F*ocused *B*eam *R*eflectance *M*easurement" (abbreviation *FBRM*)) are often used [Kes06]. Besides crystallization, other areas of applications are liquid-liquid systems [Spa93, Dow01, Alo02, Dan04, Rou05, Hu06], bioprocesses [McD01, Jef03, Pea03, Pea04, Mat07] and polymerisations [Vac06b]. Due to the intrinsic measuring principle the instruments are more suitable for crystals that "keep" their morphology over the process time and less suitable for needle like particles that mainly grow along a single spatial direction [Hof04, Vac06a]. Figure 5-1 shows the principles of both instruments.
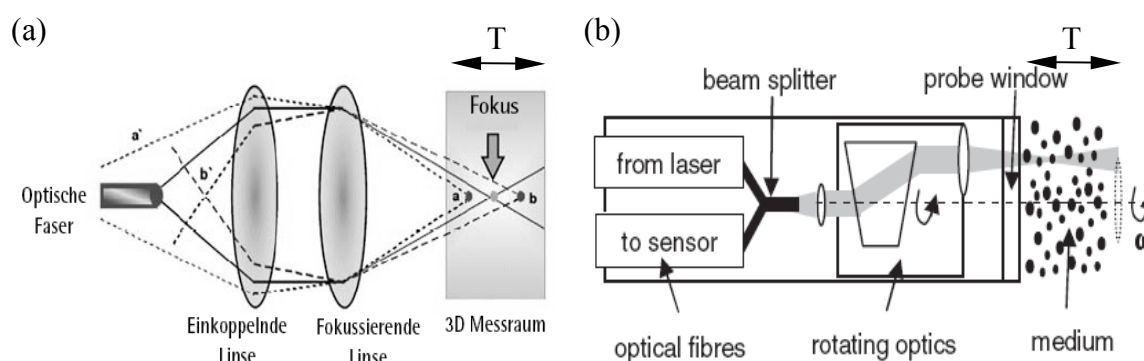
Figure 5-1: Measuring principle of laser scanners: (a) 3D-ORM instrument [MTS06], (b) FBRM instrument [Kai07] (T = travelling distance or scanning depth of the laser, Optische Faser: optical fibre, Einkoppelnde Linse: coupling lens, Fokussierende Linse: focusing lens, 3D Messraum: 3D measuring area)

Using the FBRM a focal point position of the laser as well as fine or coarse electronics must be specified by the user [Met06]. Both settings influence the measured CLD [Hea02, Wor03b, Ehr06, Pon06, Yu08b]. Often a focal point position inside the instrument (for example: -20 μm) is chosen [Wor04, Ehr06, Yu08a]. In comparison, the 3D-ORM technique uses a dynamical focal point, in other words, besides the circular motion, the laser moves in a normal direction to the probe window, describing an elliptical orbit (spiral) [Dan04, MTS06, Mat07]. According to the vendor, the focal point is always set in front of the probe window [MTS06]. It is claimed that only particles in the respective focal point are measured. The signal filter and "measuring area" of the 3D-ORM are pre-set by the vendor. Compared to the FBRM, the 3D-ORM has only been reported on a smaller number of publications [Mah00, Cul02, Dan04, Lov05, Qu05, Mat07, Hei08b].

Wynn [Wyn03] and Kail et al. [Kai07] discussing several assumptions and problems related to laser scanners that have to be kept in mind throughout this work. In batch reactors the flow near the probe window can be considered chaotic, with particles having a random orientation towards the laser. Any violation of the following assumptions leads to a shift of the distribution towards smaller chords:

- It is assumed that the laser speed is much faster than the velocity of the crystal. According to Wynn [Wyn03] and Kail et al. [Kai07], this assumption might be partially violated within standard laboratory equipment using older laser scanners with a laser speed of 2 m/s (newer equipment: 6 m/s).
- It is assumed that the measured chord represents the entire chord length of the particle silhouette (2 dimensional projection). According to Euhus [Euh03], the assumption is violated for particles that have a high curvature.
- It is assumed that the particle backscatters uniform over the entire "surface". According to Kail et al. [Kai07], the assumption is violated for transparent crystals that only backscatter at the edges. A so called chord splitting has been observed for quartz, pentaerythritol and glass [Ruf00, Kai07], resulting in an increased number of counts compared to "reality".

It is further assumed that the extension of the laser beam is much smaller than the particle size. For instruments with a detection size limit of 1 μm it can be concluded that the laser beam spot has an approximate diameter of 0.6 to 2 μm [Spa94, Lov05, MTS07]. However, as the laser propagates into the liquid, the laser broadens (signal gets weaker, decrease in laser intensity) up to one order of magnitude within the measurement zone [Ruf00, Pon06, Kai07, Kai08]. The resolution of the instrument towards particles less or equal to the laser diameter remains unclear [Spa94, Pon06]. The propagating of the laser into the liquid is illustrated in figure 5-2 (FBRM instrument). Similar considerations can be made for the 3D-ORM probe.
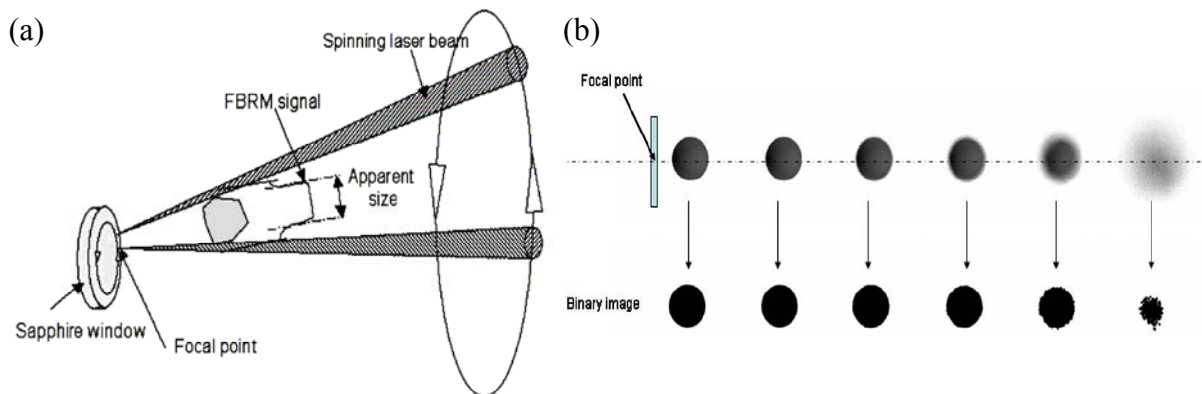
Figure 5-2: Rotating laser beam of the FBRM instrument (a) broadening of the laser beam with increasing distance from the focal point (b) blurring of the particle contour with increasing distance from the probe tip (focal point close to the sapphire window) [Pon06]

Figure 5-2 illustrates two competing effects. The further the particle is from the focal point the larger it looks, however, it gets more difficult to detect [Ruf00, Pon06] ("blurring" of the particle contour). The further the crystal is from the focal point the noisier will be the measured CLD. Ruf et al. [Ruf00] could experimentally demonstrate for single crystals that a measurement up to the actual size of the particle occurs only in a very narrow zone close to the probe window. Measurements outside this zone are noisier, introducing additional chord measurements at lower channel sizes, leading again to a shift of the distribution towards smaller sizes [Ruf00, Pon06]. For a detailed discussion on single crystal behaviour from an experimental and modelling perspective it is referred to Worlitschek [Wor03a,b] and Pons et al. [Pon06]. The assumption that the scanning depth T is size-independent [Wyn03, Kai07]

might not always be fulfilled, as experimental results confirm [Ruf00]. Finally, since the laser describes a circular motion it does not pass the particle in a straight line introducing an increasing systematic error with increasing particle size (important for particles > 500 μm) [Wyn03, Dan04, Kai08].

Within reality, many particles are present in solution close to each other. Figure 5-3 shows possible situations that might occur at the probe tip of a laser scanner. For the 3D-ORM instrument it is assumed that the movement of the laser in the normal direction is much slower than its radial movement.

Lateral View

(a)

Probe

Rotating Laser Beam

Particles

Chord Length = $v_{Laser} \cdot \Delta t$

Signal (Ideal)

Black: raw signal
Grey: filtered signal (rectangular shape)

Threshold Value

t_0 t_1 t_2 t_3 t_4 t_5 time

(b)   (c)   (d)

Probe   Probe   Probe

Signal   Signal   Signal

time   time   time

Rejection of measurement due to   **Particles are counted and sized**   **"Screening Effect", smaller**
non-ideal signal shape   **as one ("Chord Concatenation")**   **particles crowding in front of the**
                                                                                              measurement window

Figure 5-3: The effect of different positions of multiple particles in front of the probe tip on the raw and filtered signal measured by a laser scanner (lateral view), (a) ideal conditions, (b) non-ideal signal shape, (c) "Chord Concatenation", (d) "Screening Effect" (for the 3D-ORM it is assumed that the movement of the laser in the normal direction is much slower than its radial movement)

For the FBRM and 3D-ORM the filtering algorithm is proprietary. It is therefore not known how the instrument differentiates between good and misshapen pulses or how it handles the scenarios illustrated in figure 5-3. Within this work, it is assumed that the filter consists of several of the following criteria [Spa93, Dan04]:

- the scattering intensity must be above a certain threshold
- the signal must return to zero for a certain time interval between two consecutive measurements
- the signal must pose a certain symmetry and the slopes must exceed a certain value

Hence, the first scenario (figure 5-3 (b)) leads to a rejection of the measurement since the shape of the pulse is not "ideal". Larger particles and fewer counts than "in reality" are observed within the second scenario (figure 5-3 (c)). The second scenario is sometimes called chord concatenation [Kai08]. It is similar to primary coincidence observed by Coulter Counter instruments [Wyn97]. The third scenario (figure 5-3 (d)) leads to a shift of the distribution towards smaller particle sizes since smaller particles are counted more often (not representative sample). This scenario is also called "Masking or Particle Screening Effect" [Ruf00, Huk03]. Further geometrical scenarios can be constructed, for example, two particles that are each smaller than the lower detection limit of the instrument are sized as one that is larger than the given detection limit (secondary coincidence – Coulter Counter [Wyn97]). According to the vendor's user manual of the 3D-ORM the following general sentence, without quantifying the extent, is given: "when the optical density of the dispersed phase increases, the resolution of the total measuring range could reduce" [MTS04, cited]. A general increased influence of the suspension density on the measured size distribution with increasing suspension density is also reported by Kessler [Kes06]. According to Wynn [Wyn03], the more particles are in the solution the lower the penetration depth of the laser. Since the laser does not widen and weaken, the problem of "blurring" reduces, leading to an improved measurement.

In summary, both the FBRM and 3D-ORM probes are scanning a specific volume with a depth T in front of the instrument window recording a CLD. Because of the different instrument characteristics, especially with regard to the focal point (static and dynamic) and filter algorithm, the recorded CLD of both instruments, for the same sample might not necessarily be the same. To the author's knowledge, a comparative study has not been made, yet. However, current methods to deconvolute the measured CLD rest on geometrical effects, only. The same applies to the deconvolution of the respective moments that was derived for ideal measuring conditions of the FBRM instrument (see equation 5.3 [Wyn03, Vac06a]). Therefore, the methods and models used throughout this work are applicable to all laser scanners.

In future, however, as recently shown by Kail et al. [Kai07, Kai08], also specific instrument settings, characteristics and optical properties can be taken into account during the deconvolution of the CLD. A tailoring of the respective model towards each vendor might become necessary.

5.3.2.2   Deconvolution Techniques

Often particle size instruments do not measure directly a PSD, instead, some related properties are recorded. Laser scanners are measuring a CLD that must be deconvoluted (transformed) into the corresponding PSD.

An example of a measured square weighted CLD over time is given in figure 5-4. It was obtained during a linear cooling experiment of ammonium chloride. The plot is based on 5824 data points (64 channels, 91 time points). In an ideal case, the largest chord length is equal the largest particle length that is present.
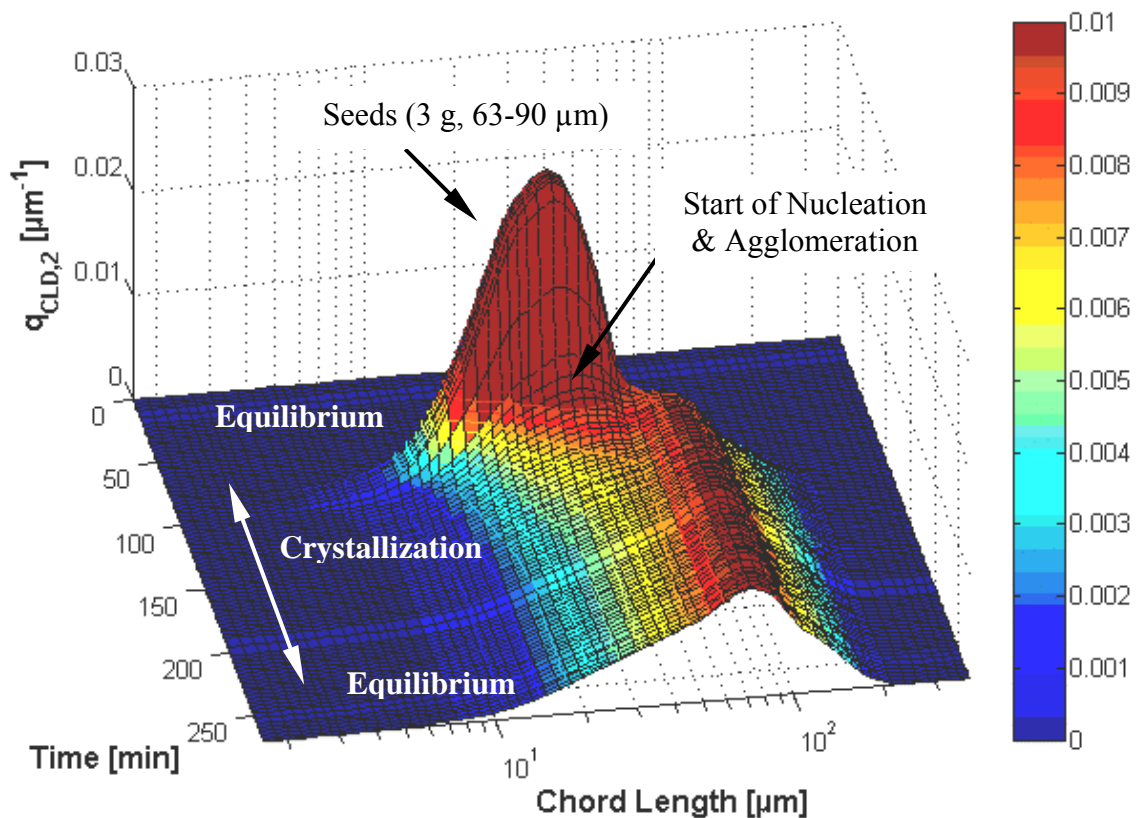
Figure 5-4: Development of the square weighted chord length distribution during the crystallization of ammonium chloride using 250 ppm $MnCl_2$ (sat. S.) as an additive

For a detail discussion on the kinetic behaviour illustrated in figure 5-4 it is referred to chapter 10.1. Table 5-3 summarises empirical and theoretical methods that relate or convert a CLD into its corresponding PSD. Within this work, the focus is on Roman numerals II, IV and V.

Table 5-3: Common methods that relate and convert a chord length distribution to a particle size distribution (or its respective moments or mean sizes)

Equation	Reference
I. Relating Mean Particle Sizes	
• Laser Diffraction = (FBRM-10.09)/0.586 • Coulter Counter = 19.24+1.064·FBRM • Sieve = $2.04 \cdot 10^{-3} \cdot$ (FBRM)$^{2.28}$ • Chemometrics (mean sizes)	[Tog01b, Hea03 and references therein]
II. Weighting of Chord Length Distribution (Square or Cubic Weightings)	
$q_{CLD,j}(L) = \dfrac{n(L)_{CLD} \cdot L^j}{\int\limits_0^\infty n(L)_{CLD} \cdot L^j \cdot dL}$ (5.1)	j = 2: [Hea03, Che07a] j = 3: [Per05a, McD01]
III. Converting the Chord Length Distribution (Empirical Kernel)	
$q_{PSD} = k \cdot q_{CLD}$ (calibration against a known standard) (5.2)	Neural Network [Giu03] Least Square [Mah02]
IV. Relating Moments (First Principle)	
$m_{CLD,j} = v_{Laser} \cdot T \cdot S_j \cdot m_{PSD,j+1}$ (5.3)	[Wyn03,Vac06a]

V. Converting the Chord Length Distribution (First Principle Kernel)			
		Method	Reference
$\underbrace{q_{CLD,0}}_{\text{measured}} = \int k \cdot \underbrace{q_{PSD,1}}_{\text{unknown}} \cdot dL$ (5.4)	•	Chahine Method	[Dan04]
	•	Peeling Method	[Hob91, Wyn03]
	•	Least Squares	[Tad98]
	•	Constrained Least Squares	[Wor03a, Huk03, Blo05, Bar06, Hu06]
	•	Non Negative Least Square	[Li05b]
	•	Probability Apportion Method (Bayes' Theorem)	[Lan01, Lan02]
	•	Projection onto Convex Sets	[Wor05]

Equation 5.4 relates the CLD to the PSD by "first principles". It can be regarded as a "Fredholm Integral Equation (first kind)" that can be found within various engineering problems. One example closely related to this work is the deconvolution of the laser diffraction signal [Box92, Mah02, Dan04, Bar08]. Although the calculation of $q_{CLD,0}$ from the corresponding PSD and kernel "k" is straight forward, the inverse problem is often ill-conditioned. In other words, small perturbations in the measurement can result in a considerable changes within the reconstructed particle size distribution.

For solving equation 5.4 with regard to an unknown PSD, various methods have been proposed that are summarised in table 5-3. Using a least square method can lead to negative values (oscillating) within the PSD. Therefore, additional constraints must be applied to stabilise the inversion leading to a physically meaningful solution. One way is to use Miller-Tikhonov or Phillips-Twomey regularization [Wor03a, Huk03, Blo05, Bar05]. It results in a "smooth" PSD. However, it does not guarantee to give no negative values [Wor03a, Li05b]. Additionally, the method might eliminate useful information. Another way is to explicitly

define that the solution should have only positive values using for example the method of "Non Negative Least Square" [Li05b] or "Projection onto Convex Sets" [Wor03a, Wor05]. The latter method allows imposing several constraints to narrow down the solution space of the ill-posed problem [Wor05]. The constraints are subdivided in:

a-priori constraints
- Non-negativity
- Constant area (normalised distribution, problem with defining L_{min}, L_{max})

a-posteriori constraints (bound on residuals)
- Bounded residual norm
- Bounded residual elements

The application of bounds on the residuals is a balance between robustness against outliers and the sensitivity to changes within the CLD in a small number of channels [Wor05]. Although the inversion is mathematical complex, it is generally desired since a PSD is easier to interpret and to compare to other sizing techniques.

An important assumption of equation 5.4 is that the probability of measuring a chord is dependent on the actual particle size [Hob91, Ruf00, Lan02, Wyn03, Hu06, Vac06a, Ehr06] that is experimentally demonstrated by Ruf et al. [Ruf00]. In other words, the measured chord length distribution is proportional to the length weighted particle size distribution ($q_{CLD,0} \sim q_{PSD,1}$). This is also indicated by equation 5.3 relating the moments of the CLD to the moments of the corresponding PSD, being valid for any convex shape [Wyn03, Vac06a]. The weighting, however, can also be incorporated into the "kernel". Contrary, Shaikh et al. [Sha05] concluded that the jth - moment of the CLD is directly proportional to the jth - moment of the corresponding PSD. Other literature references are not indicating clearly, what kind of PSD (number or length weighted) is obtained after the deconvolution [Tad98, Huk03, Li06], leaving the results difficult to interpret.

Using equation 5.3 in combination with equations 3.27 and 3.28 average particle sizes and the coefficient of variation of the respective PSD can easily be extracted from the CLD (see chapter 5.3.2.3 for the respective S_j - values). Equation 5.5 relates the mean size of the CLD to the mean size of the PSD.

$$L_{CLD,[3,2]} = \frac{m_{CLD,3}}{m_{CLD,2}} = \frac{v_{Laser} \cdot T \cdot S_3 \cdot m_{PSD,4}}{v_{Laser} \cdot T \cdot S_2 \cdot m_{PSD,3}} = \frac{9 \cdot \pi}{\underbrace{32}_{Sphere}} \cdot L_{PSD,[4,3]} \qquad (5.5)$$

From equation 5.5 it can be seen that for spheres the mean chord length $L_{CLD,[3,2]}$ is 0.88 times smaller than the mean particle size $L_{PSD[4,3]}$. Comparing $L_{CLD,[1,0]}$ with $L_{PSD[2,1]}$ the factor equals $\pi/4 = 0.785$. In other words, the higher the weight the smaller the difference between these mean sizes that is in accordance with empirical findings that simple square or cube weighted CLDs compare well with a volume based PSD [McD01, Hea02, Per05a, Che07a, Yu08a].

Ehrl et al. [Ehr06] compared equation 5.5 and related ones to experimental results [Ehr06]. A laser scattering instrument was used to measure the PSD and the FBRM to measure the respective CLD. The theoretical relation between the lower order moments ($L_{CLD,[0,-1]} \sim L_{PSD,[1,0]}$) was found to be in good agreement with experimental data whereas the relation between higher order moments ($L_{CLD,[3,2]} \sim L_{PSD,[4,3]}$) was not.

5.3.2.3   Single Particle Chord Length Distribution

Whereas the previous chapter has focused on the mathematical routines to convert the CLD into a PSD or its corresponding moments, does the following chapter concentrates on how the actual kernel or the shape factor S_j is derived that are at the centre of the transformation process. In general, only geometrical factors are considered. Additionally, it is assumed that all crystals have the same shape and no overlapping particles occur.

In a first step a single particle CLD must be calculated. For sphere-like and ellipsoidal particles analytical solutions can be derived that are used by most authors [Hob91, Tad98, Lan02, Wyn03, Huk03, Li05b, Blo05, Hu06]. For other shapes a virtual simulation of one rotating particle in front of the sensor tip is necessary [Ruf00, Dan04, Pon06, Bar06]. If the flow towards the probe is not chaotic, because of particles position themselves towards the flow, like in a pipe, this has to be considered as well [Ner07]. The final single particle CLD therefore, depends on the individual method of each author(s):

- Type of equation to approximate the particle
- Choice of the characteristic size describing the particle
- Assumption about the distribution of particles within a each bin (midpoint, uniform or linear) [Huk03]
- Consideration of instrument settings and optical properties [Pon06, Kai07, Kai08]

Figure 5-5 shows the single particle CLDs for a sphere and a plate. Each CLD of a specific projection of the single particle is weighted by the height of that projection ($h_{Projection}$). This is a logical conclusion from the previous chapter that larger particles are more likely to be scanned than smaller ones; applying also to the individual projections of the single particle [Ruf00, Vac06a, Kem07].
Scaling the single particle CLDs by its characteristic length L_{char} leads to a CLD that is a function of the particle shape, only [Wyn03, Sha05, Vac06a].
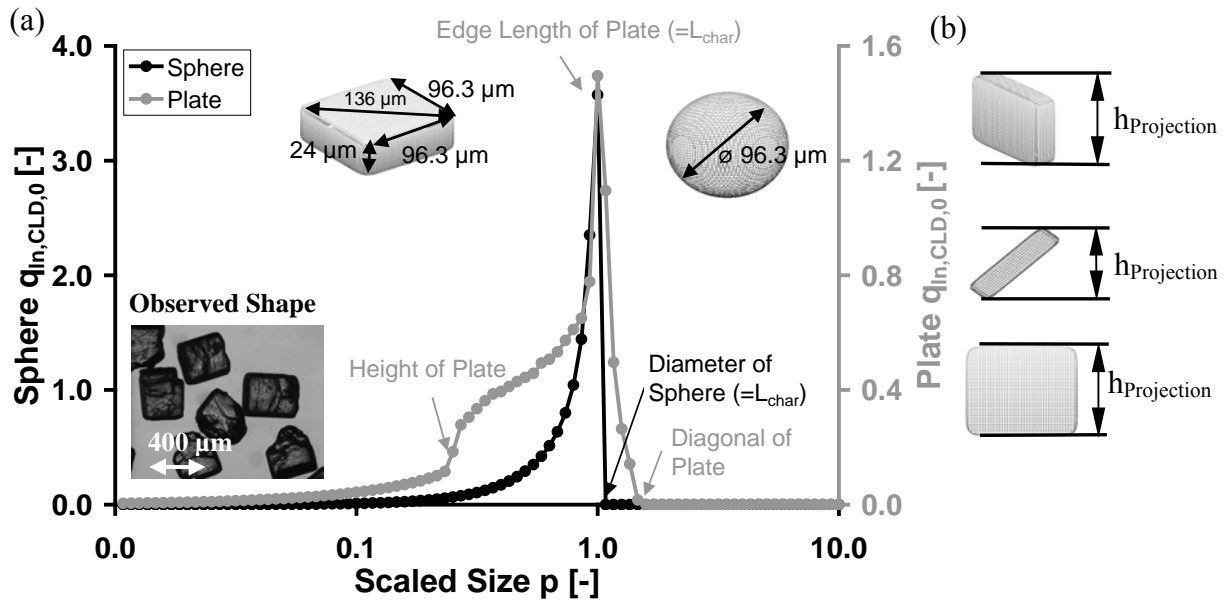
Figure 5-5: (a) Chord length distribution of a spherical and plate like single particle; the characteristic length (L_{char}) is 96.3 µm, corresponding to the midpoint of the channel boundaries 92.6 to 100 µm, (b) illustration of the height of projection ($h_{Projection}$) that is used as a weighting factor (see chapter 9.2.1)

The jth moment of the scaled single particle CLD can be used to calculate the S_j − values using equation 5.6 [Wyn03, Sha05, Vac06a]. The values are tabulated in table 5-4.

$$S_j = \int_0^\infty (p)^j \cdot q_{CLD,Single\,Particle}(p) \cdot dp = \underbrace{\frac{\sqrt{\pi} \cdot \Gamma\left(\frac{2+j}{2}\right)}{2 \cdot \Gamma\left(\frac{3+j}{2}\right)}}_{analytical\;solution\;for\;spheres} \qquad (\,5.6\,)$$

Table 5-4: S_j - value for sphere and plate like particles (see also Kempkes et al. [Kem08])

Shape	Characteristic Length	S_{-1}	S_0	S_1	S_2	S_3
Sphere	Diameter	$\pi/2$	1	$k_A/4 = \pi/4$	2/3	$3\cdot\pi/16$
Plate	Edge Length (longest)	2.84	1	0.67	0.56	0.52

By definition, S_0 equals 1. Because of the weighting by the height of the projection, the theorem of Cauchy is only applicable for spheres, leading to $S_1 = k_A/4$ [Wyn03].

By assuming that all crystals have the same shape, the kernel, valid for a crystal collective, can easily be derived from the single chord length distribution [Wor03a]. Thereby it is advantageous if the CLD and PSD are logarithmic spaced (geometric progression). The transformation becomes homologous, resulting in a simple banded matrix [Hob91, Wyn03, Wor05]. For spheres, the kernel is a simple upper-triangular diagonal matrix [Tad98, Wyn03]. Due to the various methods to construct a single particle CLD, the various characteristic sizes that can be defined as well as the different mathematical methods, objective functions and

constraints that can be applied to deconvolute the CLD, methods derived from different authors can lead to different PSDs for the same experimental CLD.

5.3.2.4   Empirical Data

Laser scanners are described as a promising tool to aid crystallization process development. Numerous papers are published using the probe in detecting nucleation, to follow changes within the size distribution and to detect phase transformation [Bar05]. The literature about laser scanners can be largely grouped into 4 categories:

1. Qualitative monitoring [e.g. Fuj02, Lio04, Yu05, Vac06b, Wan06, Sch06c, Che07a]
2. Testing/comparing the instrument performance to other sizing techniques (chapter 8)
3. Development of CLD deconvolution techniques (chapter 5.3.2)
4. Using the experimental CLD or reconstructed PSD for modelling (chapter 4.1)

Table 5-5 summarises a survey of category 2 and 3 (for category 4 see chapter 4.1). It is by no means complete, however, it provides a first overview about common characteristics. All references used a stirred beaker or reactor where the probe was immersed.

Table 5-5: Survey of substances, sieve cut and suspension density ranges that have been used to test and compare the "Focused Beam Reflectance Measurement" instrument (laser scanner) and to validate deconvolution techniques

Substance (Solvent: Water)	Sieve Cut Range [μm]	Suspension Density [g/kg Solvent]	Reference
Category 2: Testing/Comparing (see Heath, A. R. et al.[Hea02] for 11 references before 2000)			
PVC*	90 – 300	170	[Yu08a]
Glass Beads, Silica	20 – 90	< 40 (< 1 vol%)	[Li05a]
Calcium Carbonate, Aluminium	0 – 400	< 200	[Hea02]
Alkaline Frit (Calcinated Silicate)	< 100	< 40	[Bar99]
Category 3: Validating Models for Deconvoluting of the Chord Length Distribution			
Lewatit MP500	630	< 30 (< 2 vol%)	[Kai07]
Gibbsite	< 200	-	[Pon06]
Ceramic Beads	0 – 425	< 80 (< 2 vol%)	[Ehr06]
Zinc Dust/Ceramic Beads/ Plasma Aluminium	60 – 120	< 450 (< 10 vol%)	[Li05c, Li06]
Ceramic Beads	50 – 800	< 1600 (< 30 vol%)	[Wor05]
Paracetamol/Toluene (c_{eq} = 0.37 g/kg solvent)	50 – 560	15 (1 vol%)	[Wor05]
PVC* and FCC Catalyst	< 250	< 330	[Giu03]
PVC*	< 200	90	[Huk03]
Amberlite (R) IRA-904	212 – 850	10	[Tad98]

*density of PVC can range between 1190 – 1680 kg/m³ [Ull07]

Several conclusions can be drawn from the data in table 5-5. Although the instrument is capable of measuring up to 1000 μm, in the majority of the cases sieve cuts smaller than 500 – 600 μm are used. The same conclusion can be made from the review by Heath et al. [Hea02] who summarised 11 research papers up to the year 2000. However, this might also be simply due to the fact that many chemicals that can be purchased from various vendors often have a particle size smaller 500 – 600 μm. Where larger sieve cuts were used an undersizing of larger crystals was reported [Law97, Tad98, Mah02].

The majority of the investigations are often made in rather diluted solutions (< 200 – 400 g/kg solvent (< 5-10 vol%)), typical for laboratory investigations [Gar80]. It is not taking advantage that the instrument is supposed to be suited for "higher suspension densities" [Kes06]. The vendor of the 3D-ORM claims a measuring range up to 40 vol% [MTS06]. For the FBRM a working range of up to 30 vol% is reported [Mer01, page 485].

For testing the instrument performance and validating the CLD to PSD transformation, generally, only substances that are insoluble, often spherical to compact with a narrow sieve cut are used [Hea02, Wor05, Li05c, Li06]. However, these conditions are rather non-typical for crystallization systems.

Laser scanners are not general-purpose instruments. The applicability must be proven on a case specific basis. The instrument is based and deemed on the fact that light is reflected. The amount that is reflected depends, besides the property of the laser and the solvent on the refractive index, colour and surface properties of the corresponding crystal [Spa93, Mon96, Ruf00]. The refractive index is thereby the only easy accessible parameter that is tabulated for various substances. It is often assumed: the larger the difference in refractive index between the fluid and dispersed phase, the better the instrument performance, as shown by Monnier et al. [Mon96] and Yu et al. [Yu08a]. Monnier et al. [Mon96] and Yu et al. [Yu08a] placed the same inert particles in different solvents. It was found: the smaller the difference in refractive index, the lower the total measured counts.

Figure 5-6 shows the distribution of refractive indices from solvents and organic and inorganic substances taken from several databanks [Per97, Wyp00, Yaw03]. Because of the compilation from various sources, the values refer to different frequencies of light and temperatures. In figure 5-6, also substances from table 4-1 (chapter 4.1), table 5-5 are indicated. For substances that are highlighted in "bold grey", a poor performance of the instrument was reported [Lüh96, Ruf00] or noticed within this work.
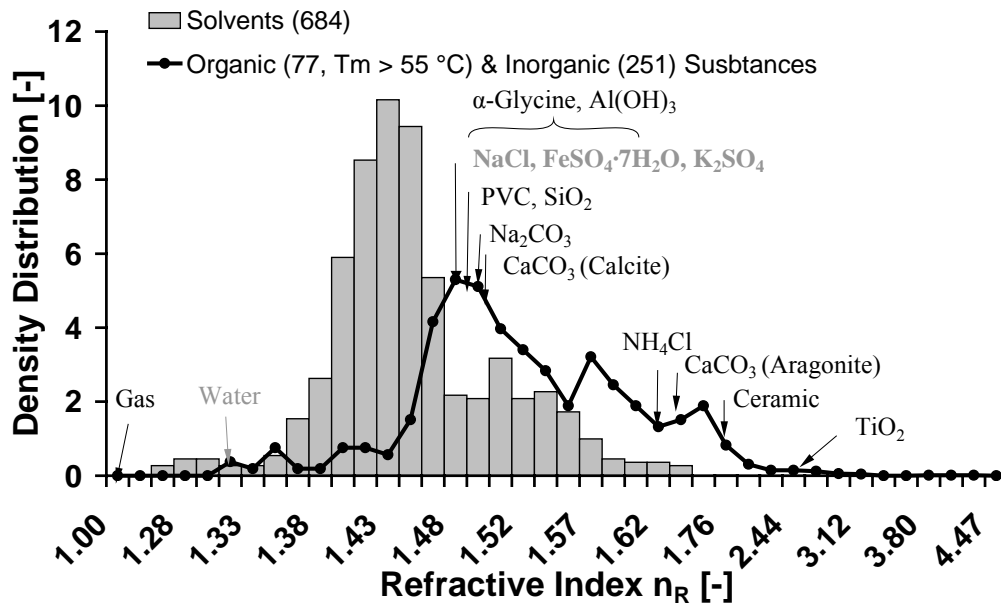
Figure 5-6: Density distribution of the refractive index among different organic and inorganic substances and solvents [Per97, Mal97, Nic98, Wyp00, Yaw03, Ehr06], for substances in "bold grey" a poor performance of the instrument was reported or noticed within this work

Other substances that have been reported as not suitable are: potassium alum [Lüh96], optically clear polystyrene or pure oils in water [Met06]. For glass spheres, results are ranging from works [Mon96, Li05a] to not applicable [Lüh96, Ruf00, Met06]. This might be explained by the various types of glass that are available (n_R = 1.48 to 1.96 [Mal97]). Within this work, a poor performance of the 3D-ORM was noticed by a low value of the "backscattering signal", by a high fluctuation of the measurement (for example: iron sulphate heptahydrate, n_R = 1.47-1.48 [Mal97]) or a constant CLD no matter what sieve cut was used (potassium chloride, n_R = 1.5 [Per97]). Often studied model substances are glycine [Dok04b, Yi06, Che07a, c] and paracetamol [Fuj02, Wor03a, Yu05, Hoj07] (form I: n_R = 1.58-1.7, form II: n_R = 1.49-1.84 [Nic98]).

The value of the refractive index is only an indicator, if a particular material is suitable for the laser scanner instrument. This is illustrated by PVC that is provided as a reference material by both instrument vendors, however, has a relatively low refractive index of n_R = 1.55 [Yu08a].

6   Aim of the Work

In 2002, the European Federation of Chemical Engineering (Working Party on Crystallization) summarised and standardised proven methods, equipment and procedures for measuring nucleation and crystal growth rates within the 2nd edition of the book "Measurement of Crystal Growth and Nucleation Rates" [Gar02]. It is partly based on the German engineers association brochure: "Messanordnungen zur Bestimmung von Kristallwachstumsgeschwindigkeiten" dated back to 1982.

These methods, although proven and applied today, have come under increasing pressure. Although only a couple of years have gone by there has been a tremendous development in high-resolution in-situ measurement techniques, commercial software packages for solving population balances (for example: gProms and Parsival) and an increase in computational capabilities. This allows solving the full time-dependent population balance on a standard personal computer that was in 2002 still believed to be of limited practical value due to difficulties in solving the corresponding equations and accurate specification of realistic boundary and initial conditions [Dav00]. Especially, the measurement of the supersaturation and the whole particle size distribution throughout the experiment at small time intervals is now possible leading to new and fast insights into crystallization phenomena. On the methodology side, the so called systematic work process: model-based experimental design and analysis is gaining more and more importance [Mar05]. A model-based approach reduces any "random walks" by providing structure to the experimentation and the subsequent evaluation. It answers the question: How to choose the many parameters that can be adjusted during a batch experiment in such a way that the information content of the experiment is maximised. This all led to new ways of measuring kinetics that have hardly been covered by the aforementioned book. A review of nucleation and growth mechanisms, methods to determine crystallization kinetics and measurement techniques was made within chapter 3, 4 and 5, respectively.

First studies showed that by combining a model-based approach with in-situ measurement techniques kinetic constants for a crystallization process dominated by nucleation and growth can typically be obtained in as few as 2-4 batch experiments [Chu00, Tog04, Che04]. On the backside, the more mathematics are applied, the more following "dilemma" comes into focus: Although the aim is to determine kinetic constants that are not known, it is necessary to have already some pre-knowledge of the kinetic constants, as close as possible to the "true" value. In other words, the performance of model-based experimental design and the subsequent estimation of parameters are dependent on the actual a-priori knowledge of the parameters that are supposed to be not known [Bar08]. The "dilemma" has been approached from different perspectives within the previous chapters by looking at the govern length and time scales (chapters 2.1 to 2.3), on experimental data (chapters 2.4 and 4.3) and on a-priori predictions (chapters 3.2 and 3.3, see also chapters 9.1 and 9.2.2).

By taking advantage of the above described recent developments the current wider application is mainly limited by the in-situ measurement of particle size distributions. The following three sequential tasks arise:

I.   Pre-Processing of Laser Scanner Instrument Data (see chapters 5 (theory) and 8)

The model-based framework is asking for time dependent crystallization experiments, utilisation of high-resolution measurement techniques and the use of population balance models. The sensors should be applied in-situ and if any possible non-invasive. Laser scanners such as the "Focused Beam Reflectance Measurement" probe or the "3 Fold Dynamical Optical Reflectance Measurement" probe are one of the very few in-situ probes that can actually handle all conditions the framework is asking for (fast measurement, in-situ, at various suspension densities). Based on a detailed literature review, it was found out that, although the instrument is very popular within crystallization research or industrial applications it is generally only used for qualitative analysis, whereas the framework requires quantitative data.

The performance testing of the instrument (comparison to other sizing techniques) and the validating of the mathematical methods to extract the particle size distribution from the raw measured data is generally tested only on ideal particle systems (insoluble, spherical to compact particles, narrow sieve cut), non-typical for crystallization processes. Additionally, the instrument is used often within rather diluted systems, although the instrument is supposed to be suited for higher suspension densities (see Kessler [Kes06]). The following sequential questions arise:

- Can typical crystallization substances be identified that fulfil the following criteria?
    - Suitable for laser scanning instruments
    - Availability of coarse non-spherical particles to obtain several sieve fractions of various sizes
    - Availability of basic thermodynamic data

- How does the instrument perform under different suspension densities, typical for in-situ monitoring, using "typical" crystallization substances? What is the maximum suspension density the instrument can operate?

- Is it possible to use the laser scanner data for quantitative purposes? Can a procedure be developed that transforms the raw measured data to a particle size distribution that fulfils the mass balance?

II.   Overall Work Process and Software Implementation (see chapters 4 (theory) and 9)

Up to now, only a few applications of model-based experimental design and analysis to crystallization processes have been reported [Chu00, Tog04, Che04]. Since it is a relatively new approach, all individual steps of the framework are still under active research and therefore not common applied [Bar04]. For each individual task, being the deconvolution of the chord length distribution as well as model-based experimental design and analysis various software programs have been developed, independently, throughout the literature or an a commercial basis. Because of the enormous amount of data that is recorded by in-situ measurement probes and the type and number of calculation steps that must be performed, the

automation of data handling and evaluation is critical and compulsory. The following tasks need to be resolved:

- Selection of individual software programs that allow to deconvolute the chord length distribution as well as to perform model-based experimental design and analysis

- Programming of interfaces between the data files that are exported by the software that accompanies the measuring instruments, the software developed for data pre-processing within Roman numeral I and the individual software programs selected within the previous bullet point

III.   Determination of Crystallization Kinetics (see chapters 3 (theory) and 10)

The final part focuses on the actual application of in-situ measuring instruments and the procedure (work process) and software developed within this work, to determine the kinetics for the identified model systems. The scope of this work is clearly on "first pass kinetics" for nucleation and growth described by power law kinetics, valid for a crystal collective. They can form the base for a more elaborative and fundamental kinetic mechanistic investigation. The supersaturation will be measured using an in-situ ultrasound technique, whereas the particle size distribution will be recorded using a laser scanner. The simultaneous use of in-situ measurement techniques for the supersaturation and particle size distribution with the objective to extract kinetic data (quantitative analysis) is, due to the complex mathematics involved, seldom applied within the literature. Instead, often only the raw measured data in form of a chord length distribution is used for evaluation (short-cut method). The following questions arise:

- Does the overall work process used within this work lead to kinetic constants comparable to literature data?

- Within literature a short-cut method has become popular. It allows a fast way of evaluating any recorded data by circumventing the complex mathematics to reconstruct the particle size distribution. How does the short-cut method compare to the procedure development within this work?

7   Experimental Equipment and Procedures

7.1   Laboratory Batch Reactor

A batch reactor can be equipped with various in-situ probes for the measurement of concentration, particle size distribution or to track different polymorphs. Additionally, non-invasive techniques such as calorimetry [Fév96, Mon97] and electrical resistance tomography [Kag05, Ric05] can be implemented to complement the measurement. By finally combining the stirrer with a torque measurement, changes in viscosity can be traced.

Within this work a 600 mL temperature controlled, double-jacketed laboratory batch reactor (Gebr. Rettberg GmbH) designed according to DIN 28131 ("Rühren und Stromstörer für Rührbehälter", excluding baffles) with a 3-blade propeller (stainless steel, diameter: 5 cm) was used. The 3-blade propeller is an axial pumping impeller typically used for suspending particles [Sti95, Kra03b]. The reactor was equipped with a MTS 523 PsyA CSD Particle Analyzer (3D-ORM, Messtechnik Schwartz GmbH, Software: WinORM V 4.56, scanner speed: 2 m/s) and LiquiSonic 30 probe (Ultrasound Probe, 1.2 cm gap, SensoTech GmbH, Software: SonicWork® 4.1.17) covered by a 200 µm mesh (Paul GmbH & Co, Metallgewebe- und Filterfabriken, material: stainless steal 1.4301, wire thickness: 50 µm) as also described by Perlberg et al. [Per05a]. A lower mesh size (63 µm) as used by Titiz-Sargut et al. [Tit03] led to a too high pressure drop, decreasing the exchange of liquid. A higher mesh size increased the probability that crystals enter the probe fork. The reactor was temperature controlled by a thermostat (Julabo HL FP50). All instruments were connected to a standard Windows operating computer. Figure 7-1 shows the experimental set-up and respective probe locations.
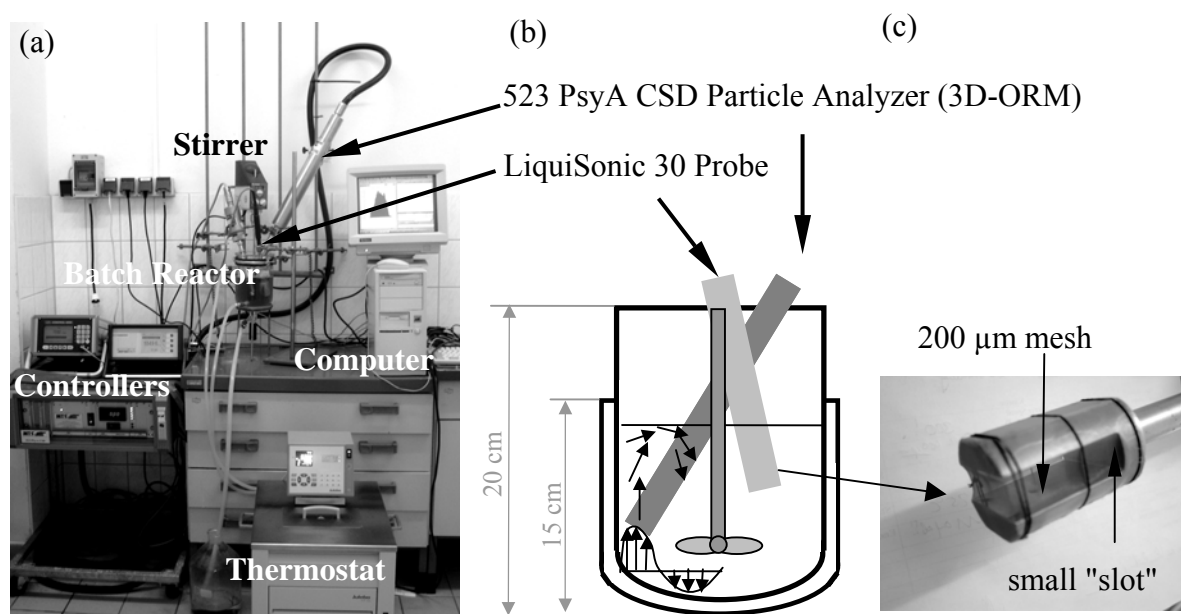

Figure 7-1: (a) Experimental set-up, (b) probe locations within the batch reactor, (c) ultrasound probe

A measurement time of 2 seconds was set for the ultrasound probe. For the 3D-ORM probe a measurement time of 20.8 s for ammonium chloride and 40 s for ascorbic acid and α-glycine, respectively, was chosen. The time is a balance between measuring a sufficient number of particles and being capable of capturing all events immediately. The higher the number of particles the better the "statistics" and therefore the deconvolution of the chord length distribution using the method of "Projection onto Convex Sets" (see chapter 9). The measurement range of the 3D-ORM was set to 1.56 – 400 µm within the vendor's software.

The angle of the 3D-ORM had a range of 45 to 60 ° [Met06, MTS06]. The tip of the 3D-ORM was located near the reactor wall where an upflow regime can be assumed. The ultrasound probe was placed in the upper half of the liquid volume. The stainless steal mesh that covered the instrument had a small slot allowing bubbles to leave the "fork" when placed into the liquid. During the measurement, the slot remained always above the liquid level to avoid the entering of particles. All probes served as "baffles".

A detailed discussion and review on the mixing behaviour within batch reactors can be found by Kraume et al. [Kra03b, Kra88]. The higher the stirrer speed the better the mass-transfer coefficient (see figure 7-2 (a)), however, often on the expense of a higher rate of breakage. The impeller speed was set to 300 rpm for ammonium chloride and 400 rpm for ascorbic acid and α-glycine, respectively (agitator: Heidolph RZR 2021). It ensured an appropriate mixing having all solids suspended within the entire reactor ("Complete Suspension Criteria"). A further increase in stirrer speed was limited due to the formation of a vortex and air entrainment resulting in bubbles sticking to the 3D-ORM probe. Although the particles were optically homogenous suspended, a homogeneous suspension is hardly achievable within a stirred tank reactor [Kra03b, Mer01]. This is illustrated in figure 7-2 (b) showing the volume fraction of solids as a function of the reactor height.

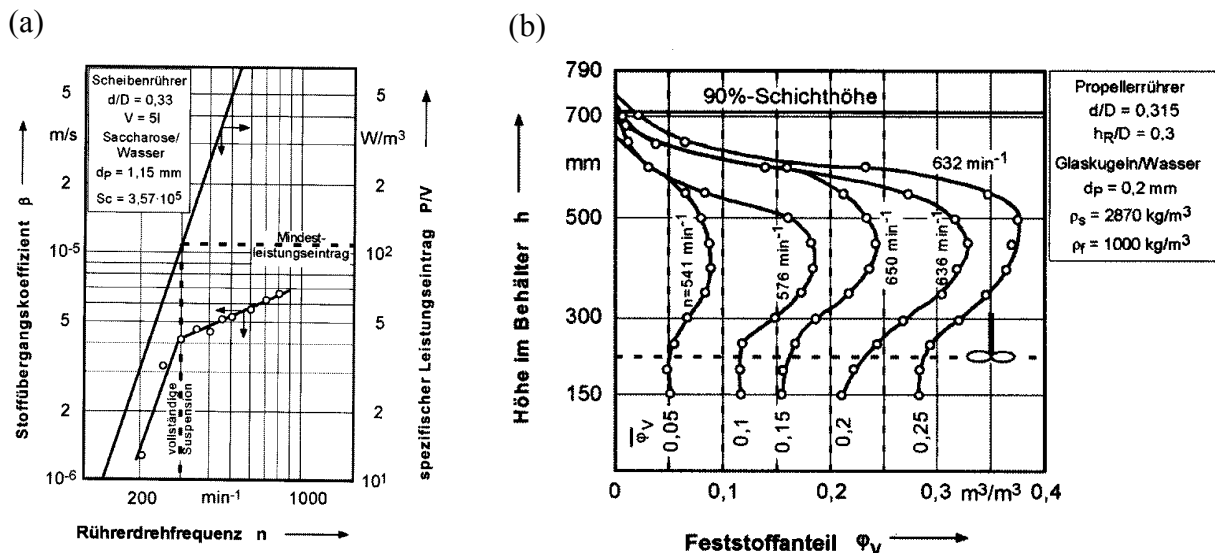(a)   (b)

Figure 7-2: (a) Mass transfer coefficient ("Stoffüberganskoeffizient") and specific power input ("spezifischer Leistungseintrag") as a function of stirrer speed ("Rührerdrehfrequenz"), (b) volume fraction of solids ("Feststoffanteil") over the reactor height ("Höhe im Behälter") for different suspension densities and stirrer speeds [Kra03b]

All measuring instruments provide therefore only local information. The derived calibration constants in chapter 8 and the experimental results in chapter 10 are consequently only valid for the specific fluid dynamics of the investigated reactor, the process conditions and the corresponding probe position [Bar99]. In order to achieve the same mixing quality ("90% Schichthöhe") throughout the batch time, the stirrer speed must ideally be varied as the suspension density changes. However, within this work the actual suspension density varied only within a small range being $0 < \varphi_V < 0.08$.

According to Kraume [Kra03b] the mixing time for a suspension can be approximated by the mixing time for a single phase fluid as long as the volumetric hold-up is approximately less than $\varphi_V = 0.05$ that can be assumed throughout this work. Using equations 2.6 and 2.7 the macro- and micromixing time for the described batch reactor can be calculated to 2.5 s and 100 ms, respectively. The energy dissipation rate ε_{mean} and ε_{local} were taken to be 0.12 W/kg [Lin08, Aki05]. An overall heat transfer coefficient of 140 W/(K·m²) between the suspension and the coolant was determined from heating and cooling profiles [Elt07].

7.2   Secondary Equipment

The following additional equipments were used to support the experiments: For weighing a Sartorius LA42000S and/or Mettler Toledo AX 205 Delta Range analytical balance were used, dependent on the amount to be weighed. All substances were sieved using a Retsch AS200 sieving machine with the corresponding standard sieves sizes (63 μm, 90 μm, 160 μm 250 μm, 315 μm, 400 μm, 450 μm). Microscopic pictures were made using an Olympus BH2 (MTV-3) microscope connected to a PixeLINK FireWire Camera (PL-A662) and a standard Windows operating computer running the Digital Image Processing System (DIPS) software 2.6.11.6 (e-point electronic GmbH). The microscope was equipped with an objective lens of S&H10 and an ocular lens Olympus NFK 2.5. To complement the 3D-ORM recordings laser diffraction measurements were made using the Mastersizer 2000 with the Scirocco 2000 unit (2 bar, sample tray: small volume 10-200 g, Fraunhofer - general purpose model, measurement time 15 s, measurement snaps 15,000, Malvern Instruments Ltd., Software Version 5.1). The experimental data were exported and converted to a standard logarithmic distribution (see Sommer [Som01]).

7.3   Experimental Procedure

Experiments for the Determination of Kinetics:
The batch reactor was filled with 600 g water as well as the appropriate amount of solute to obtain a saturated solution at 20 °C for ammonium chloride and α-glycine. A saturated solution at 40 °C or 50 °C was prepared for ascorbic acid. To ensure that all crystals were dissolved, the solution was stirred for at least 30 minutes 5 K above the respective saturation

temperature. For starting the experiment, the solution was cooled down to the saturation temperature. The corresponding concentration was confirmed by the ultrasound signal.

The temperature profile, seed size and seed mass for the individual experiment were calculated using model-based experimental design (see chapter 9) or were defined by engineering judgement. The seeds were weighed using the balance and the temperature profile was set using the programmable thermostat. In parallel with starting the program of the thermostat also the recording of the ultrasound probe and 3D-ORM was initiated via the individual software. The seeding point of ammonium chloride was chosen to be T_{start} - 0.5 to 1 K. For α-glycine and ascorbic acid seeds were either introduced at a temperature of $T_{start} - 1$ to 3 K or after the final temperature was reached ("desupersaturation experiments"). The final temperature was generally 15 K lower than the respective starting temperature. At the end of the experiment, the recorded data were subsequently saved and exported into individual files (.csv format) using the software provided by the instrument vendors. Screening experiments and individual experiments to determine the kinetics can deviate from the general described procedure with regard to the temperature level and seeding point (see chapter 10).

Unfortunately, during the initial experiments it was noticed that on the ultrasound probe encrustation formed leading to unreliable measurements. The extent being dependent on the substance investigated. Therefore, it was decided to measure the ultrasound velocity continuously up to first nucleation burst and afterwards only at specific time points. Between the intervals the ultrasound probe was taken out off the reactor and was placed into a 400 mL double-jacketed beaker connected to the same thermostat, having the same temperature as the reactor, containing pure water. The clear change in ultrasound signal from concentrated solution to water and vice versa allowed a filtering of the signal using the software described in chapter 9. The time between two measurement points was dependent on the dynamic of the experiment. Whereas within the early phase of the experiment the ultrasound velocity was measured every 5th minute, the probe was inserted only every 15th minute at the end of an experiment. When the system approached equilibrium, the crystals where allowed to settle and a final ultrasound reading was taken from the clear saturated solution.

Calibration of Ultrasound Probe and 3D-ORM Probe:
The ultrasound probe was calibrated in a 400 mL double-jacketed beaker placed on a magnetic bar stirrer, connected to the thermostat, 200 g of water was added. The solution was heated up to 50 °C and a known amount of material, equivalent to the amount that is soluble at 5 °C, was added and dissolved (undersaturated). The solution was subsequently slowly cooled down to 5 °C with a rate of 5 K/h by simultaneously recording the ultrasound velocity and temperature using the LiquiSonic Probe 30 without any net. These steps were repeated several times by subsequently adding more material to cover the entire concentration range of interest.
In order to test the performance of the 3D-ORM with respect to different suspension densities, known amounts of a sieve cut or non-sieved material were added subsequently to a stirred saturated solution at 10 °C using the batch reactor described above. The measurement at each suspension density was averaged over 7 consecutive measurements. The variations between the individual measurements were small.

8 Calibration, Evaluation and Data Pre-Processing

8.1 Calibration of the Ultrasound Probe

For the calibration of the ultrasound probe the experimental protocol described in chapter 7.3 was used that is illustrated in figure 8-1, along with a standard procedure for calibrating ATR-FTIR spectroscopy instruments [Pöl05, Lew01]. The latter uses only calibration points in the undersaturated regime at different temperatures and concentrations.
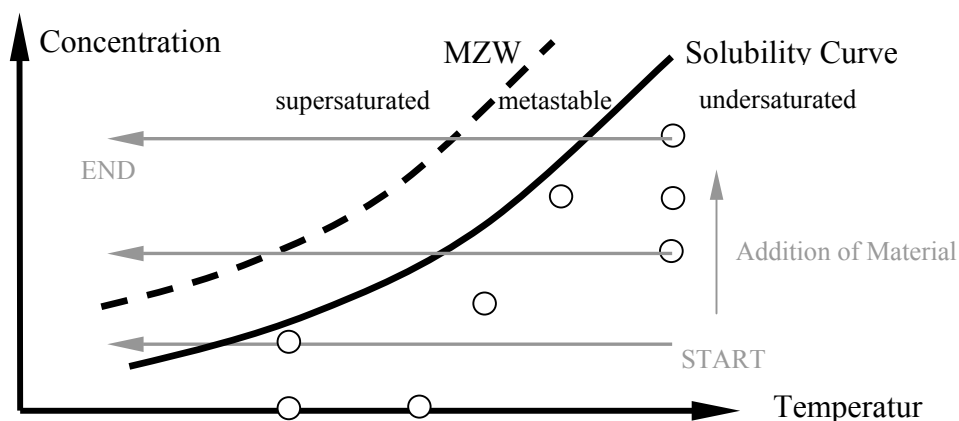

Figure 8-1: Illustration of the experimental protocol for calibrating the ultrasound probe (this work: grey lines, procedure for ATR-FTIR instrument: black circles)

The experimental procedure applied within this work also considers measurement points within the metastable zone width, reducing the extent of extrapolation. As a byproduct of the calibration protocol, information on the metastable zone width prior to any kinetic experiments can be obtained. An example of the ultrasound velocity for a constant solute concentration, within a temperautre interval of 12.5 to 30 °C is given in figure 8-2.
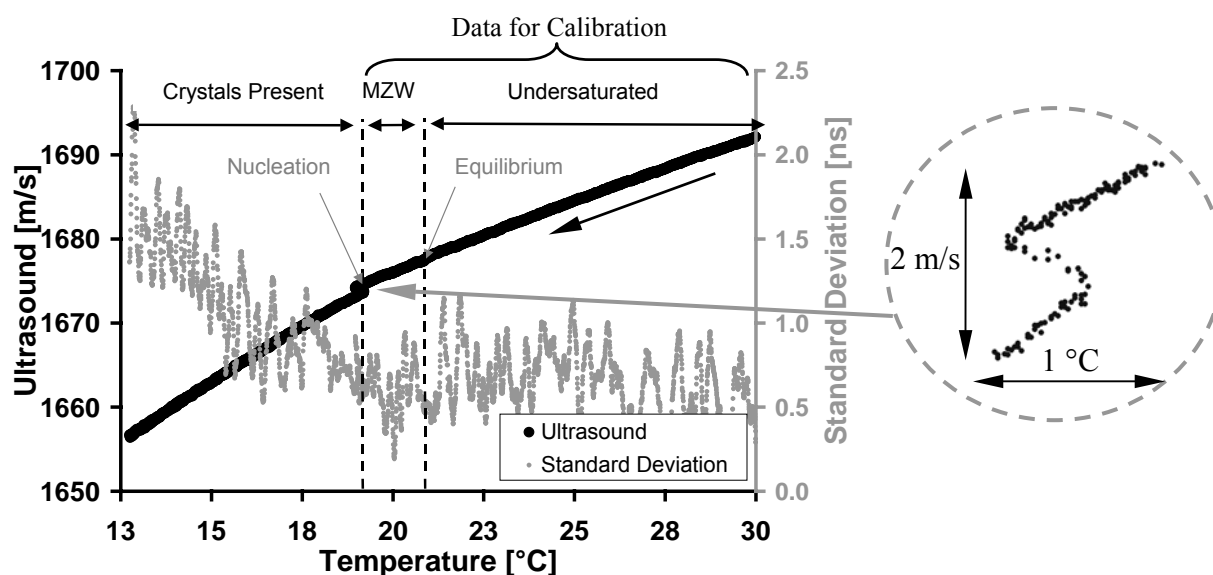

Figure 8-2: Ultrasound velocity and standard deviation of the sound wave's runtime by cooling an aqueous solution of ammonium chloride (37 g ammonium chloride/100 g water, probe without a net)

For a particular concentration, the ultrasound velocity decreases with decreasing temperature. The nucleation of crystals is detected by a sudden change in ultrasound velocity or a continous increase within the standard deviation of the sound wave's runtime. The change of signal due to nucleation is according to the literature in the range of $2 - 20$ m/s [Ulr02a, Tit02, Tit03, Str04], within this work it was always less than 5 m/s.

The influence of crystals on the instrument signal was studied by intentionally adding 40 g of ammonium chloride crystals (sieve cut: $0 - 250$ μm) to a saturated solution. By doing so, the ultrasound velocity increased by 21 m/s (saturated at 25 °C: 1688 m/s, no net). Similar results were obtained for ascorbic acid and glycine, as also described by Sayan et al. [Say02]. In other words, if unwanted crystals are present within the fork of the instrument, the ultrasound value increases leading to a higher concentration, and hence supersaturation value compared to reality. As a result, the fork of the instrument was covered with a net, described in detail in chapter 7, to avoid having crystals present during the measurement. One may wonder why the ultrasound velocity in figure 8-2 still decreases after the nucleation burst. This can be explained by the fact that the decrease in solution concentration is causing a higher reduction in ultrasound velocity than the increase caused by crystals.

For deriving the calibration constants only data points referring to a clear solution were used (standard deviation of the sound wave's runtime less than 1 ns, see figure 8-2). The ultrasound velocity and concentration are related to each other by equation 8.1.

$$U = \frac{1}{\sqrt{\rho_{Solution}(c,T) \cdot \beta_{ad}(c,T)}} \quad\quad\quad (\text{ 8.1 })$$

Solving equation 8.1 for the concentration remains difficult. Machefer et al. [Mac07] suggested equation 8.2 as a calibration function.

$$U = w_1 \cdot U_1 + w_2 \cdot U_2 + w_2 \cdot (1 - w_2) \cdot \left(k_1 + (2 \cdot w_2 - 1) \cdot k_2 + (2 \cdot w_2 - 1)^2 \cdot k_3 \right) \quad (\text{ 8.2 })$$

It is based on a simple mixing rule and a Redlich-Kister polynomial. The constants k_1, k_2 and k_3 are dependent on temperature. For applying equation 8.2 the ultrasound velocities of the pure melted substances (U_1 and U_2) must be known. Within this work a simple polynomial with interaction terms was used (equation 8.3 with c [kg solute/kg solvent], T [°C] and U [m/s]).

$$c = a_0 + a_1 \cdot T + a_2 \cdot U + a_3 \cdot T \cdot U + a_4 \cdot T^2 + a_5 \cdot U^2 \quad\quad\quad (\text{ 8.3 })$$

The coefficients a_0 to a_5 for the individual model systems are summarised in table 8-1, whereas figure 8-3 shows a graphical representation for ammonium chloride (for additional data see appendix, chapter A.3). The experimental data were evaluated using the Matlab routine "rstool". The determined empirical constants for all substances are valid for a temperature range of 5 to 50 °C.

Table 8-1: Empirical constants for equation 8.3 (calibration of the ultrasound probe)

Substance	a_0	a_1	a_2	a_3	a_4	a_5	Data Points
Ammonium Chloride	6.92217	5.59281E-03	-1.05518E-02	-7.48244E-06	4.14880E-05	4.00744E-06	61510
Ascorbic Acid	3.28057	-1.01533E-01	-6.98955E-03	5.85926E-05	4.58635E-05	3.34067E-06	292*
Glycine	2.72991	-9.71100E-03	-4.78779E-03	2.56904E-06	3.92699E-05	2.03608E-06	250*

*for ascorbic acid and glycine a data reduction prior to the determination of the empircal constants was made (1 data point per °C)
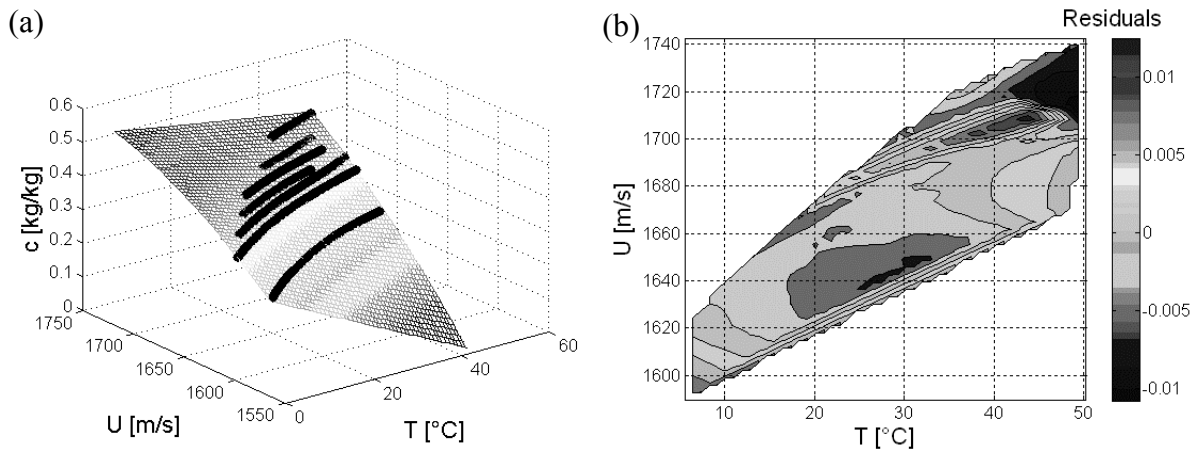

Figure 8-3: Calibration of ultrasound probe: (a) Comparision between experimental data for ammonium chloride (black dots) and model prediction using equation 8.3 (shaded surface), (b) residuals between experimental data and prediction

Table 8-2 summarises statistical data regarding the respective regressions, sensitivities as well as determined metastable zone widths.

Table 8-2: Root mean square error (RMSE) of the calibration function, concentration sensitivity of the ultrasound probe and measured metastable zone widths (referring to a cooling rate of 5 K/h)

Substance	RMSE	Saturated Solution		Δc and ΔU (for 15 K)	$\Delta U/\sigma_{Ultra}$ [-] (for 15 K)	MZW
		initial T/U	final T/U			
Ammonium Chloride	0.006 m/s	T = 20 °C U_{eq} = 1676.2 m/s	T = 5 °C U_{eq} = 1620.7 m/s	Δc=57 g/kg H_2O ΔU=55.5 m/s	1110	1-3 K
Ascorbic Acid	0.0031 m/s	T = 40 °C U_{eq} = 1617.2 m/s	T = 25 °C U_{eq} = 1571.3 m/s	Δc=178 g/kg H_2O ΔU=45.9 m/s	918	> 20 K
Glycine	0.0012 m/s	T = 20 °C U_{eq} = 1623.3 m/s	T = 5 °C U_{eq} = 1547.6 m/s	Δc=58 g/kg H_2O ΔU=75.5 m/s	1510	10 K

ultrasound velocity of water: U = 1482.6 m/s (20 °C)

According to the manufacture's manual, the instrument has an accuracy of σ_{Ultra} = 0.05 m/s and 0.1 °C for the ultrasound and temperature, respectively [Sen06]. The error introduced by the empirical calibration function is always less than the accuracy of the ultrasound probe (RMSE < σ_{Ultra}). A concentration sensitivity value can be calculated by deviding the change of ultrasound signal by the accuracy of the instrument. Although ascorbic acid shows the highest change in concentration, it has the lowest sensitivity, with glycine having the highest.

8.2   Evaluation of the Laser Scanning Technique

8.2.1   Influence of the Suspension Density on the Counts

In an ideal case, by adding continuously a constant sieve fraction to a saturated solution the measured "counts" should increase in a linear fashion. However, for various insoluble substances a "tapering off" of the measured "counts" is observed. Examples along with the respective investigated suspension density range are:

- calcinated silica (0 - 40 g/kg solvent) [Bar99]
- kaolin and silica (5 - 110 g/kg solvent) [Day99]
- calcite and aluminium particles (0 - 200 g/kg solvent) [Hea02]
- PVC (0 - 170 g/kg solvent) [Giu03, Yu08a]
- fluidised catalytic cracking catalyst (0 - 330 g/kg solvent) [Giu03]

Yu et al. [Yu08a] explained the "tapering off" at higher suspension densities with an increasing probability of measuring overlapping particles. Incrementally less total "counts" are therefore recorded per time. Additionally, at higher suspension densities the laser becomes "saturated" and can no longer detect all new particles passing the probe window [Yu08a]. Similar conclusions are made by Heath et al. [Hea02] who discussed the observed behaviour from the background of an increase in the instrument dead time. A linear dependence of the "counts" versus suspension density was observed for glass beads (0 - 450 g/kg solvent) [Mon96] and for suspension cultures [McD01, Jef03, Pea04].

Figure 8-4 illustrates the influence of the suspension density on the "counts" observed within this work. A sieve cut of 90 – 160 μm was used for ammonium chloride, ascorbic acid and α-glycine. Three zones can be differentiated.

I.   A linear zone with an ideal behaviour
II.   A non-linear zone where corrections (a calibration) can be made
III.   A "saturated" zone where adding new material results in no significant change of the corresponding signal (low resolution, sensitivity)

The borders of each zone are dependent on the respective substance. Larger sieve cuts tend to behave linear over a wider range of suspension densities (for additional data see appendix, chapter A.4). The dynamical measurement zone, that is important for the determination of kinetics, is therefore only characterised by zone one and two. Comparing figure 8-4 with the above discussed literature, that all used the FBRM, it can be concluded that the "tapering off" at higher suspension densities can be observed no matter if the 3D-ORM, FBRM, soluble or insoluble substances are used.
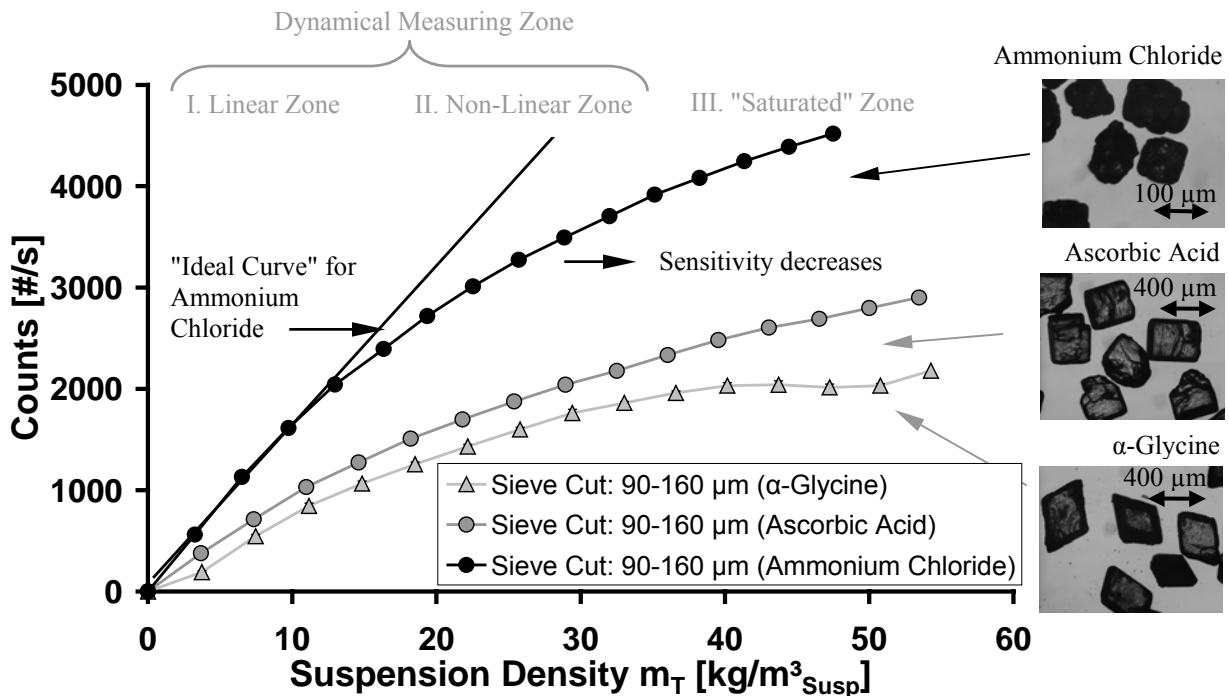
Figure 8-4: The effect of the suspension density on the recorded "counts" for ammonium chloride, ascorbic acid and α-glycine

Ammonium chloride leads roughly to twice as much "counts" for the same sieve cut and mass compared to α-glycine and ascorbic acid. Since all substances have a similar morphology, the difference can only be attributed to the optical properties of the respective particle-solvent system. It can be assumed that more "misshapen signals" are rejected for α-glycine and ascorbic acid compared to ammonium chloride, leading to a lower overall count rate.

To study the influence of optical properties on the measurement, Monnier et al. [Mon96] and Yu et al. [Yu08a] placed the same inert particles within different solvents. It was found that the smaller the difference in refractive index between particle and solvent, the lower the absolute value of the measured "counts". The refractive indices for the model substances used within this work are summarised in table 8-3.

Table 8-3: Refractive indices for ammonium chloride, ascorbic acid and glycine crystals and solutions

Substance	Refractive Index (Solid) [-]		Refractive Index (Solution) [-]	
Ammonium Chloride	1.64	[Mal97]	1.38 (15 °C, sat. S.)	[Tak90]
Ascorbic Acid	-		1.36 (25 °C, 1 mol/L)	[Sha79]
α-Glycine*	1.50-1.66	[Ort67]	1.36 (20 °C, sat. S.)	own measurement

*β-glycine: n_R = 1.49-1.66, γ-glycine: n_R = 1.58-1.61 [Ort67]

From table 8-3, it must be concluded that the refractive index alone, cannot explain the behaviour shown in figure 8-4. It should be mentioned that for the case of α-glycine the 3D-ORM recognises smaller particles over-proportional better, that might be explained by

different surface properties (see appendix, chapter A.4). Duplicates of the respective measurements confirmed the behaviour of α-glycine.

The so-called "tapering off" of the instrument response, is typical for various measurement probes (concentration measurements, Coulter Counter [Wyn97]). It is also predicted by an optical model that simulates the FBRM described in detail by Kail et al. [Kai08]. It has been demonstrated by Heath et al. [Hea02] that this non-ideal "behaviour" can be corrected by applying equation 8.4. The equation introduces a dead length "k" before and after each particle. The aim is to determine a "k" value that produces a linear relationship between the "counts" and the suspension density [Hea02].

$$N_{LS,corr} = \underbrace{N_{LS,meas}}_{\sum_{i=1}^{M} N_{LS,meas,i}} \cdot \frac{v_{Laser}}{v_{Laser} - \left(\sum_{i=1}^{M} N_{LS,meas,i} \cdot \left(L_{Channel,i} + 2 \cdot k \right) \right)} \qquad (8.4)$$

The effect of equation 8.4 on the "counts" is demonstrated in figure 8-5 for k = 96.3 μm.

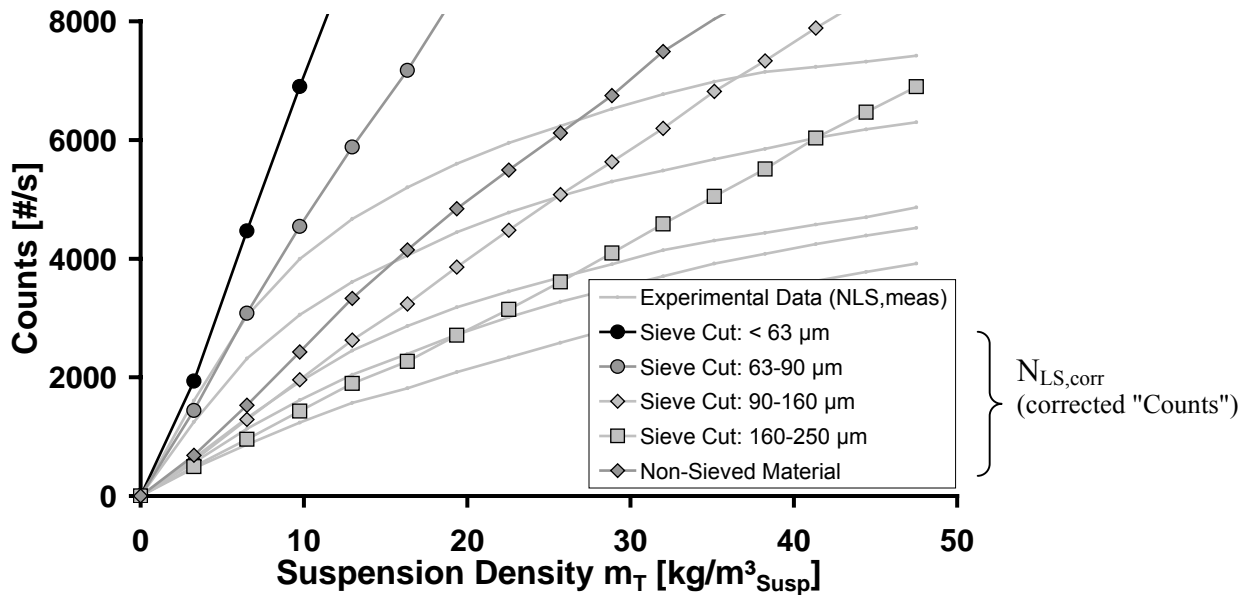**Figure 8-5: Influence of the dead length k = 96.3 μm on the recorded "counts" versus the suspension density (ammonium chloride)**

The "k" value is estimated over all sieve cuts (i = 1…P) and suspension densities (j = 1…O) for each substance individually. The objective function is formulated by equation 8.5 [Elt07].

$$F = \sum_{i=1}^{P} \sum_{j=1}^{O} \left(\left(N_{LS,corr}(k) \right)_{i,j} - \underbrace{a_i(k) \cdot m_{T,i,j}}_{linear\ equation\ (intercept=0)} \right)^2 \rightarrow min \qquad (8.5)$$

The slope "a" can be calculated via a = $\Delta N_{LS,corr} / \Delta m_T$ or via the first derivative of the objective function (dF/da = 0) given by equation 8.6. The latter is used within this work.

$$a_i = \frac{\sum\limits_{j=1}^{o}\left((N_{LS,corr})_{i,j} \cdot m_{T,i,j}\right)}{\sum\limits_{j=1}^{o}\left(m_{T,i,j} \cdot m_{T,i,j}\right)}$$

(8.6)

A Matlab program was written that performs the determination of the "k" value [Elt07]. Table 8-4 contains the estimated dead lengths and times for all model systems studied within this work (see also appendix, chapter A.4). Heath et al. [Hea02] derived a dead length of k = 26 μm for calcite and k = 11 μm for aluminium particles from FBRM measurement data.

Table 8-4: Determined dead lengths, dead times and correlation coefficients (R)

Substance	Dead Length k [μm]	Dead Time* [μs]	R
Ammonium Chloride	96.30	48.38	0.99
Ascorbic Acid	125.19	62.59	0.96
α-Glycine	138.49	69.24	0.95

*dead time = dead length/laser speed (2 m/s)

The dead time can be interpreted as the minimal average time that elapse during two successful measurements, when the "detector is saturated". The larger the dead length or time the less particles can be measured. This mirrors the behaviour shown in figure 8-4.

Assuming mono-dispersed sphere like particles with a diameter of 200 μm and assuming for the sake of simplicity that the laser only crosses the diameter, the instrument is, in principle, capable of measuring 10,000 particles per second (laser speed of 2 m/s ($2 \cdot 10^{+6}$ [μm/s] / 200 [μm]). However, because rejection of misshapen pulses, a specific time the laser must return to zero and a certain time the laser must travel trough the liquid from one particle to the other, the instrument is only capable of measuring considerable less particles. Using the "k" value determined for ammonium chloride of 96.3 μm, the instrument can "ideally" measure a maximum of 5090 particles per second ($2 \cdot 10^{+6}$ [μm/s] / (200 + 2·96.3) [μm]). At a lower particle number the length between two successful measurements becomes larger than the dead length and is not limiting the measurement.

It is important to stress that although equation 8.4 is capable of "correcting" the measured "counts" to a linear form (see figure 8-5), the measurement range can only be improved up to the end of zone two. Beyond this, the sensitivity of the measured "counts" becomes too low, even though the instrument will be still capable of measuring a distribution even at much higher suspension densities. If no mass balance is of interest, the non-linear increase in "counts" can be cancelled by normalising the distribution.

The operating windows for all substances used within this work are rather small. The sensitivity of the instrument recordings, essential for monitoring, is only given for suspension densities smaller than 50 kg/m³$_{Susp}$ ($\approx$ 3 vol%) for ammonium chloride and α-glycine. For ascorbic acid, a slightly higher value was obtained. These are typical suspension density ranges for laboratory investigations but far from industrial ones (see chapter 2.4). The simple experiment discussed within this chapter allows "simulating" an artificial nucleation.

8.2.2   Influence of the Suspension Density on the Distribution

In an ideal case, by adding continuously a constant sieve fraction to a saturated solution the same normalised distribution should be obtained. However, for various insoluble substances a shift of the chord length distribution towards smaller sizes is observed [All88, Hea02, Giu03, Yu08a, Kai08]. Heath et al. [Hea02] and Yu et al. [Yu08a] are making this shift responsible to smaller particles "crowding" close to the probe tip. Similar conclusions are made by Hukkanen et al. [Huk03] proposing that particles crowding in front of the probe occur when a broad particle size distribution with a high part of fines is subjected to a measurement ("Particle Screening"). In comparison, Kail et al. [Kai08] concluded for mono-dispersed particles, based on an optical model that the shift is caused by the broadening of the laser beam and the filter algorithm. Giulietti et al. [Giu03] are calling this effect "dispersion". In other words, besides the shift to smaller sizes also a broadening of the distribution takes place, as was also observed by Heath et al. [Hea02]. Contrary, Dowding et al. [Dow01] and Law et al. [Law97] reported a slight increase in mean size versus suspension density, whereas, a constant mean size versus suspension density was observed by Monnier et al. [Mon96].

Figure 8-6 illustrates the effect of suspension density on the chord length distribution for ascorbic acid using non-sieved material. For additional data see appendix (chapter A.5).
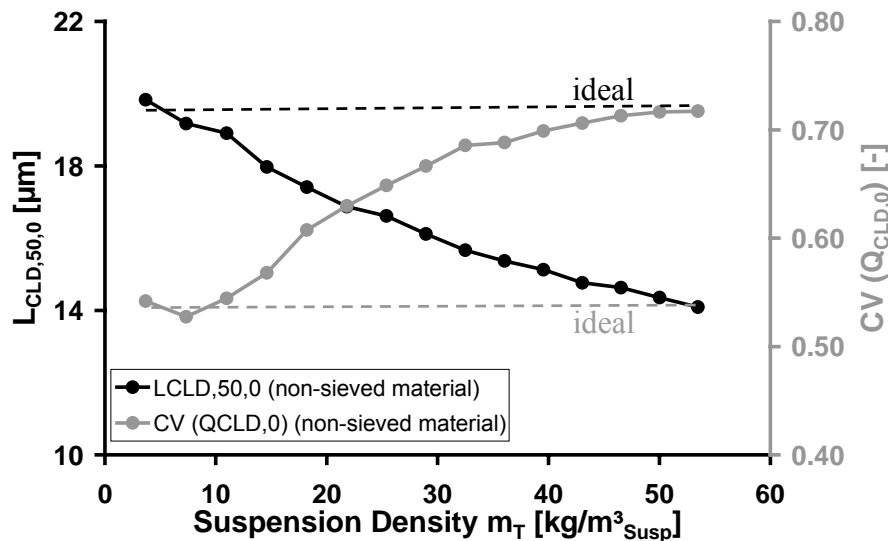

Figure 8-6: The effect of the suspension density on the recorded median chord length and CV-value of the $Q_{CLD,0}$ distribution (non-sieved ascorbic acid crystals)

A pronounced decrease in $L_{CLD,50,0}$ and increase in the CV-value takes place. In comparison to chapter 3.4.2, the CV-value is characterised as CV $(Q_{CLD,0}) = (L_{CLD,75,0}-L_{CLD,25,0})/(2 \cdot L_{CLD,50,0})$. Comparing figure 8-6 with the above given literature data it can be concluded that these "shifts" occur no matter if the 3D-ORM, FBRM, soluble or insoluble substances are used. The hypothesis of fines crowding near the probe window [Hea02, Huk03, Yu08a] is supported by ascorbic acid, where non-sieved material showed a systematic shift of the distribution towards smaller sizes and sieved material only a minor dependence (see appendix, chapter A.5). The second hypothesis making the broadening of the laser beam and the filter algorithm

responsible [Kai08] is supported by ammonium chloride that showed a systematic shift no matter if sieved or non-sieved material was used. For additional data it is referred to the appendix (chapter A.5). It is interesting to note that the described shift is also reported for emulsions by increasing the oil phase content from 20 to 60 vol% [Dan04] as likewise for the response of laser diffraction devices [Ulr90].

To further study the influence of the suspension density, the data from figure 8-6 is plotted as a cumulative distribution (see figure 8-7). In a first step, a reference cumulative distribution is defined that is equal to the distribution measured at a suspension density of $m_T = 11$ kg/m³$_{Susp}$.
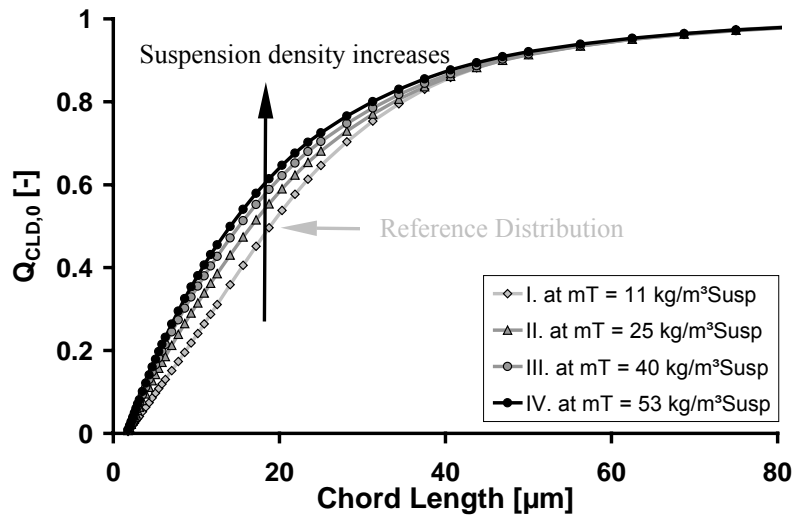

Figure 8-7: The effect of the suspension density on the recorded cumulative chord length distribution ($Q_{CLD,0}$) (non-sieved ascorbic acid crystals)

In a second step, this reference cumulative distribution is subtracted from the remaining cumulative distributions that refer to a suspension density of $m_T = 25$, 40 and 53 kg/m³$_{Susp}$, respectively. The obtained "differences" are plotted in figure 8-8.

$$y = k \cdot \frac{1}{b^a \cdot \Gamma(a)} \cdot L^{a-1} \cdot e^{-\frac{L}{b}} \quad with \quad a = 3.5$$
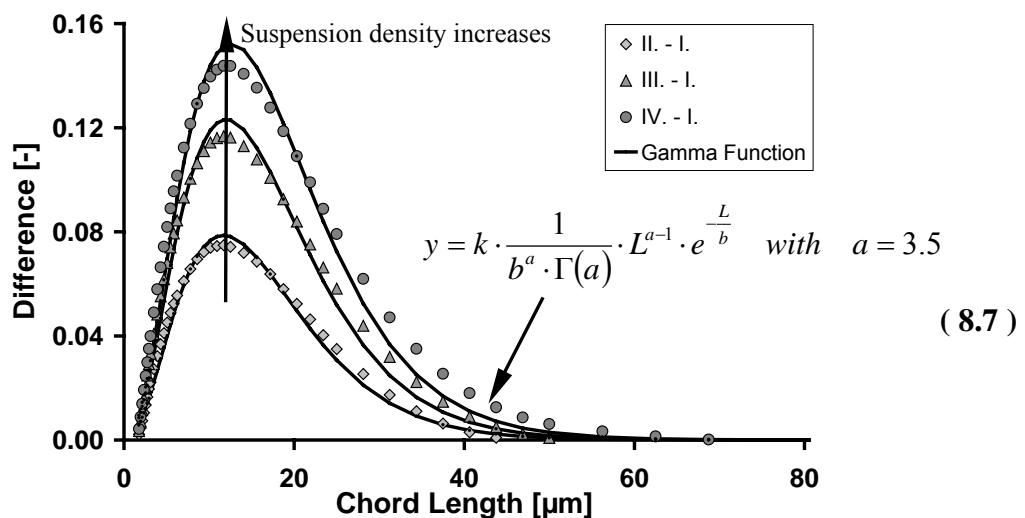
(8.7)

Figure 8-8: Differences between the cumulative chord length distributions shown in figure 8-7 (grey data points); Approximation of the observed "differences" by a gamma distribution (equation (8.7) with a shape factor of a = 3.5 (black line)

For non-sieved and sieved ammonium chloride as well as for non-sieved ascorbic acid these "differences" could all be modelled by a Γ-distribution (equation 8.7) with a constant shape factor of a= 3.5 (see also appendix, chapter A.5).

For ammonium chloride, only, an attempt was made to develop a calibration based on the Γ-distribution (see Elter [Elt07]). However, a subsequent cross-validation led only to mixed results. Heath et al. [Hea02] proposed to use only square or cube weighted distribution, to compensate for any shift. The recent described optical model by Kail et al. [Kai08] allows simulating the influence of suspension density on the chord length distribution for ideal particle systems and hence also its correction. In future work, it might also be worthwhile to look at the mathematics that has been put forward to correct peak shifts and broadening of spectras [Wes99, Wit00]. The consequence of not correcting the shift towards smaller sizes is a lower growth rate during the model-based analysis than actually present. Further detailed investigations are necessary.

The investigation of different sieve cuts allows studying the capability of the instrument in differentiating particle sizes (resolution capability) that is dependent on the substance and size range studied. In other words, the experiment "simulates" the capability of the instrument to detect crystal growth. Figure 8-9 illustrates the results for ascorbic acid.
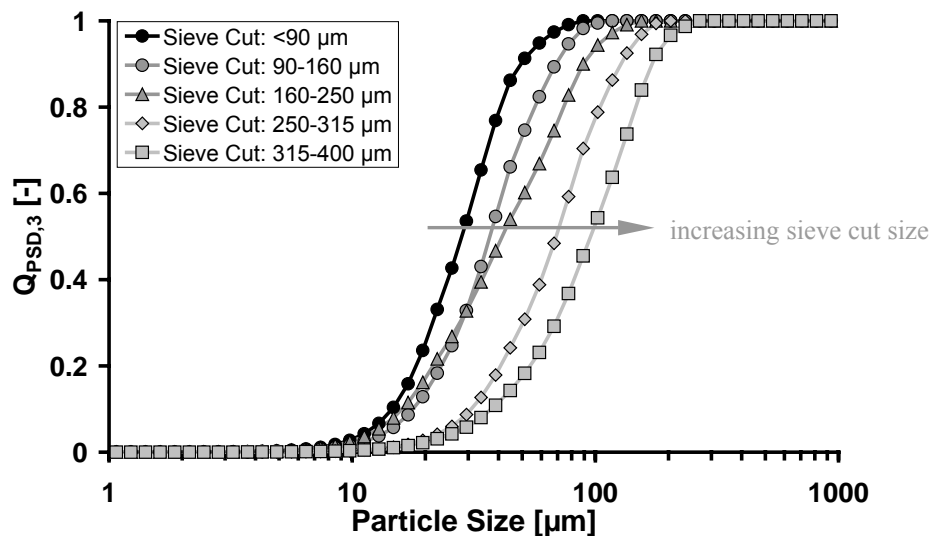

Figure 8-9: Cumulative particle size distributions ($Q_{PSD,3}$) for different sieve cuts of ascorbic acid; the chord length distribution was deconvoluted using the method described in chapter 9 and subsequently weighted to a $Q_{PSD,3}$ distribution

It can be seen that the sensitivity of the instrument in detecting different particle sizes of ascorbic acid is good. Only the sieve cut of $160 - 250$ μm is slightly deviating. For additional data it is referred to the appendix (chapter A.2). Whereas the sensitivity to differentiate between individual sieve cuts is small for ammonium chloride compared to ascorbic acid, it decreases with larger particles for α-glycine. A reduced sensitivity of the FBRM instrument in detecting changes of larger glycine crystals (sieve cut > 250 μm) is also reported by Yu et al. [Yu08b].

During the calibration it was noticed that the instrument starts working well above a suspension density of roughly $m_T = 10$ kg/m³$_{Susp}$. This value is only valid for the respective

chosen measurement times (see chapter 7). As discussed in chapter 5.3.2, the more particles are in the solution the lower the penetration depth of the laser. Consequently, the laser does not widen and weaken as much leading to an improved measurement.

8.3   Closure of Mass Balance (Consistency Check)

8.3.1   Step 1: Introduction of an Optical Factor

This chapter assumes that the measured CLD is corrected using equation 8.4 (chapter 8.2.1) and converted to a PSD using a method described in chapter 5.3.2. The objective is now to ensure that the normalized PSDs are in line with the corresponding mass balance. For doing so, in general, the total number of crystals (N_{Total}) is calculated by dividing the suspension density by the shape factor, the crystal density and the third moment of the normalised PSD (equation 8.11, left part) [Sch99, Gar02]. In this way, however, any errors within the PSD are disguised. On the other hand, it is often the only way since particle size instruments provide frequently just a normalised distribution.

Within this work, an alternative two-step approach is developed for laser scanners. The first step is based on the work by Wynn [Wyn03] and Vaccaro et al. [Vac06a] who derived an explicit theoretical relationship between the CLD and PSD for perfectly backscattering particles (see chapter 5.3.2). The sample volume the laser scans during the measurement is given by equation 8.8 (v_{Laser} = scanning speed, t_m = measurement time),

$$V_{Sample} = v_{Laser} \cdot T \cdot C \cdot t_m \qquad\qquad\qquad (8.8)$$

where T is the scanning or penetration depth [Wyn03, Mén06], extinction length [Vac06a] or travelling distance [Dan04] of the laser into the liquid. It is the maximum depth where particles are detected by the laser (not necessarily equal to the focal point position). The C is the corridor width [Wyn03] or distance from the laser axis [Vac06a]. Approximate values for T and C differ widely in the literature. Values for the scanning depth are ranging from 250 μm [Dan04] to 1.5 mm [Mén06], being mainly dependent on the instrument settings and experimental conditions. The corridor width C the laser scans is related to the particle size. The larger the particle the higher the probability the laser will scan a part of it [Wyn03, Vac06a]. In comparison, Méndez del Rio et al. [Mén06] are taking the width of the laser as C (C = 5.8 μm). Assuming a measuring time of 60 s, a laser speed of 2 m/s, a T-value of 500 μm and a C value ranging from 5 μm to 500 μm a sample volume of 0.3 to 30 mL, respectively, is scanned per minute. The effective sample volume will be smaller, when "misshapen pulses" are rejected by the filtering algorithm.

Equation 8.8 is "incorporated" within equation 5.3 (chapter 5) during its derivation [Wyn03, Vac06a], allowing theoretically calculating the number of particles per volume. According to equation 5.3 (chapter 5) the jth moment of the PSD scales with the (j-1)th moment of the CLD. Hence, the total number of particles that is given by the zero moment of

the PSD is related to the minus first moment of the CLD and is not the "counts" given by the instrument. Additionally, as shown in chapter 8.2.1, the number of counts strongly depends on the optical properties of the substance that is investigated. To compensate for the all uncertainties, especially for the optical properties of the individual substance, an optical factor ($k_{optical}$ [-]) is introduced into equation 5.3 (chapter 5). To finally calculate the total number of particles equations 8.9 to 8.11 are used (N_{Total} [#/m³], $n_{CLD,meas}$ [#/(s·m)], n_{PSD} [#/(m·m³)], $m_{CLD,j}$ [#·m^j/s], $m_{PSD,j}$ [#·m^j/m³]):

$$m_{CLD,j} = \int_0^\infty n_{CLD,meas}(L) \cdot L^j \cdot dL \qquad\qquad (\,8.9\,)$$

$$k_{optical} \cdot m_{CLD,j} = v_{Laser} \cdot T \cdot S_j \cdot m_{PSD,j+1} = v_{Laser} \cdot T \cdot S_j \cdot \int_0^\infty n_{PSD}(L) \cdot L^{j+1} \cdot dL \qquad (\,8.10\,)$$

$$N_{Total} = \underbrace{\frac{m_{T(Solubility)}}{k_V \cdot \rho_{Crystal} \cdot \int_0^\infty q_{PSD,0} \cdot L^3 \cdot dL}}_{\text{conventional}} = \underbrace{\frac{k_{optical} \cdot m_{CLD,-1}}{v_{Laser} \cdot T \cdot S_{-1}} = \frac{\int_0^\infty k_{optical} \cdot n_{CLD,meas}(L) \cdot L^{-1} \cdot dL}{v_{Laser} \cdot T \cdot S_{-1}}}_{\text{this work}} \qquad (\,8.11\,)$$

Using the "conventional method", reconciliation is made for each distribution separately. In comparison, within this work, the factor $k_{optical}$ increases all "counts" of the raw measured data of all individual channels and all measured distributions throughout the experiment by the same factor and is "theoretically" constant for a substance (see discussion in chapter 10.2). It ensures that the distribution and therefore the growth kinetics are not affected. Only the particle number in the system is increased up to the point where the mass balance is closed (see also next chapter). The optical factor is simply estimated by minimising the difference between the predicted suspension density using the PSD and the suspension density calculated via the solubility and concentration measurement. For doing so, equation 8.11 (right part) is coupled with equation 8.12. Throughout this work following values are used: T =1 mm, $S_{-1} = \pi/2$.

If only the moments of the PSD are of interest, the mass balance can be closed by relating the second moment of the CLD ($m_{CLD,2}$) to the suspension density ($\sim k_V \cdot \rho_{Crystal} \cdot m_{PSD,3}$) (see equation 8.10 with j = 2). The optical factor is again obtained by minimizing the differences in suspension densities as already discussed.

The effect of the optical factor ($k_{optical}$) on the overall "counts" and therefore on the suspension density is illustrated in figure 8-10. It shows the results of a batch cooling experiment of ascorbic acid (experiment 1 in chapter 10.2). Using an optical factor of 130 the suspension density of the measured PSD is equal to the suspension density calculated via the solubility and supersaturation ($m_{T(Solubility)}$) (for additional data see appendix, chapter A.6).
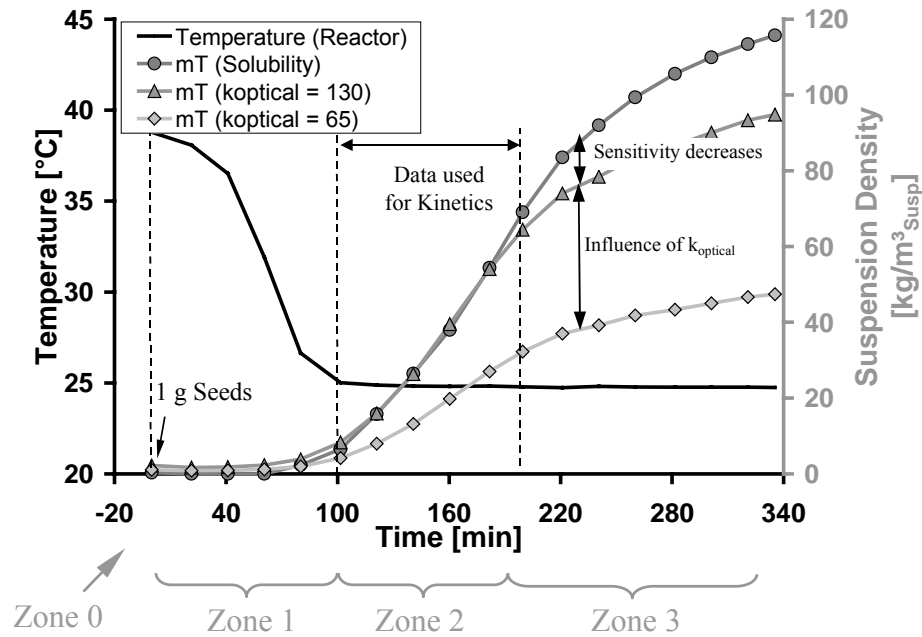
Figure 8-10: Influence of the optical factor on the calculated suspension density (m_T) in comparison with the suspension density calculated via the solubility and supersaturation measurement ($m_{T(Solubility)}$) (see equation 8.12, only every 10th measurement point is shown, data taken from experiment 1 in chapter 10.2)

The measurement can be split into four characteristic zones that were observed for all model systems. Zone zero is characterised by the time until seed crystals are added. In zone one, deviations from the mass balance occur, resulting mainly from the low particle concentration that affects the general statistic of the measured distribution as well as the subsequent deconvolution of the CLD (see Worlitschek et al [Wor05]). Roughly, for all substances and the measuring time employed the instrument starts to work reasonably well for a suspension density larger 10 kg/m³$_{Susp}$ (see also previous chapters). On the other hand, in the zone three the sensitivity of the instrument decreases due to higher suspension densities (for a detailed discussion see chapter 8.2). Therefore, for any determination of kinetics only the data points in zone two are used (see figure 8-10). This corresponds often to a suspension density range of (see also chapter 10):

- 10 kg/m³$_{Susp}$ < m_T < 30 kg/m³$_{Susp}$ for ammonium chloride (< 2 vol%)
- 10 kg/m³$_{Susp}$ < m_T < 100 kg/m³$_{Susp}$ for ascorbic acid (< 6 vol%)
- 10 kg/m³$_{Susp}$ < m_T < 40 kg/m³$_{Susp}$ for α-glycine (< 2.5 vol%)

The narrow operating window in view of the suspension density is closely linked to the time interval of zone two and the respective number of measurement points that can be made. Apart from ammonium chloride (see chapter 10.1), all experiments with a time interval of zone two of less than 20 minutes were disregarded.

8.3.2   Step 2: Data Reconciliation using Lagrange Multipliers

All steps applied so far: linearisation of the "counts" versus suspension density (chapter 8.2.1), converting the CLD into a normalized PSD (chapters 5.3.2 and 9.2.1), calculating the actual number of particles per sample volume (see previous chapter) are important to improve the measured data. However, there are still some typical differences of up to 5% between the measured and predicted suspension densities in zone two. This magnitude is also observed, comparing the theoretical crystal mass with the experimental one that is obtained by filtering and drying of the respective suspension [Sch99]. Also particle size analysers show a precision of a similar order of magnitude (see appendix, chapter A.2).

The second step of the procedure developed within this work (see previous chapter) is based on the subject of data reconciliation. The general idea is to improve experimental measurements by exploiting their statistical properties along with the corresponding balance equations [Rom00]. In other words, the aim of the reconciliation is to vary the PSD within its error range in such a way that the mass balance is closed. The method becomes feasible since, as shown in equation 8.12, the total mass of crystals per volume is measured via two independent methods ($m_T = m_{Crystal}/V_{Suspension}$). On the one hand, via the PSD (left part, plus equation 8.11 (right part)) and on the other hand via the temperature and concentration measurements. The latter is considered more accurate.

$$\underbrace{N_{Total} \cdot k_V \cdot \rho_{Crystal} \cdot \int_0^\infty q_{PSD,0} \cdot L^3 \cdot dL}_{m_T} = \underbrace{\frac{m_{Seed} + \left(c_{eq}\left(t_{start}, T_{start}\right) - c_{eq}\left(t, T\right) - \Delta c\right) \cdot m_{Solvent}}{V_{Suspension}}}_{m_{T(Solubility)}} \qquad (8.12)$$

Several mathematical techniques have been developed to deal with all sorts of data reconciliation problems including gross errors [Rag05]. It is referred to the book by Narasimhan et al. [Nar00] or Romagnoli et al. [Rom00]. Using the "Method of Lagrange Multipliers" [Gel69, Rom00, Nar00] the following minimization problem with one equality constraint can be formulated in matrix notation (equation 8.13 to 8.15, constrained weighted least-square problem) [Elt07].

$$F = \frac{1}{2} \cdot \sum_{i=1}^{M+1} \left(\frac{\left(x_{i,reconciled} - x_{i,meas}\right)^2}{f_i \cdot x_{i,meas}} \right) = \frac{1}{2} \cdot y^T \cdot P \cdot y \rightarrow min \qquad (8.13)$$

with

$$y = P^{-1} \cdot \left(x_{reconciled} - x_{meas}\right) \qquad (8.14)$$

$$P \equiv \left[diag\left(f \cdot x_{meas}\right)\right] \qquad (8.15)$$

The vector x consists of all individual channels of the number distribution of the PSD ($n_{PSD}(L)$) and the suspension density (M: entry streams (+), M+1: output stream (-)). P is a diagonal matrix that compromises the relative errors of each channel and the error of the suspension density that was set to zero. The solution is subjected to one equality constraint that is given by equation 8.16, whereas $Q \cdot x_{meas} = r$ contains the deviation from the mass balance, ε being the measurement error:

$$Q \cdot x_{reconciled} = Q \cdot (x_{meas} - \varepsilon) = \underbrace{\begin{pmatrix} \rho_{Crystal} \cdot k_V \cdot (L_1)^3 \cdot \Delta L_1 \\ ... \\ \rho_{Crystal} \cdot k_V \cdot (L_M)^3 \cdot \Delta L_M \\ -1 \end{pmatrix}^T}_{Q} \cdot \underbrace{\begin{pmatrix} N_{Total} \cdot q_{PSD,0,1} \\ ... \\ N_{Total} \cdot q_{PSD,0,M} \\ m_{T(Solubility)} \end{pmatrix}}_{x_{reconciled}} = 0 \qquad (8.16)$$

to be varied $n_{PSD}(L)$ $[\#/(m \cdot m^3_{Susp})]$

The method corrects therefore only channels where "counts" are recorded. It is not creating new entries in channels that have zero "counts". To solve the data reconciliation problem the Lagrangian L can be formulated by equation 8.17 [Nar00, Rom00].

$$L = \underbrace{\frac{1}{2} \cdot y^T \cdot P \cdot y}_{F} - \underbrace{\lambda^T \cdot (Q \cdot P \cdot y + r)}_{constraint} \qquad (8.17)$$

By setting the partial derivatives of the Lagrangian to zero (equations 8.18 and 19) [Rom00]

$$\frac{\partial L}{\partial y} = y^T \cdot P - \lambda^T \cdot Q \cdot P = 0 \qquad (8.18)$$

$$\frac{\partial L}{\partial \lambda} = Q \cdot x_{reconciled} = Q \cdot P \cdot y + r = 0 \qquad (8.19)$$

the following solution is obtained (equation 8.20).

$$x_{reconciled} = x_{meas} - P \cdot Q^T \cdot (Q \cdot P \cdot Q^T)^{-1} \cdot Q \cdot x_{meas} \qquad (8.20)$$

The solution is a simple algebraic equation that allows an efficient and stable way to reconcile the measured distribution. Having adjusted the "counts" of the raw measured data in step 1 (see previous chapter), in step 2 each bin of the number distribution $n_{PSD}(L)$ (q $[1/m] \cdot N_{Total}$ $[\#/m^3]$) is adjusted. Therefore, after applying equation 8.20 the total number of particles (N_{Total}) has to be re-calculated from the reconciled number distribution. If all channels are having the same error f, the result becomes independent of its absolute value.

The effect of data reconciliation on the PSD is illustrated in figure 8-11. It shows the Sauter diameter and the CV-value over time as well as two examples of a measured and reconciled distribution. The data were taken from experiment 1 in chapter 10.2.

It can be seen that during the time interval of 100 to 200 minutes (zone two) only minor variations of the PSD are necessary to finally close the mass balance that can hardly be seen by looking at the Sauter diameter, CV-value or the distribution itself (figure 8-11 (a, b)). Outside the given time interval (in zone one and three) the method is still capable of closing the mass balance, however, by varying the PSD to a large extent, rendering the results of no use (figure 8-11 (c)). This is characterised by a significant change in Sauter diameter and CV-value (for additional data see appendix, chapter A.7).

The method derived must be regarded as a first step. Using methodologies that are more advanced the procedure can be improved in such a way that only the normalised distribution is varied. Additionally, the error of each channel ($f \cdot x_{meas}$) might be calculated separately depending on the actual number of particles within the individual channel.

This chapter demonstrates the difficulties of using the PSD measurement as a soft sensor for supersaturation. In principle, with very accurate sizing techniques, the supersaturation could be calculated from a mass balance. However, the supersaturation is often small and the measurements of the PSD compromise large errors. By applying the developed consistency check it must be kept in mind that generally any conversion of a number to a mass distribution and hence suspension density should be avoided where possible (error scales to the power of 3 (L^3)). However, the suspension density is the only quantity that the PSD can easily be compared to. The use of a mass balance to improve the PSD is described by Wynn et al. [Wyn97] for Coulter Counter measurements. The application to laser scanners has to the author knowledge not been made before.
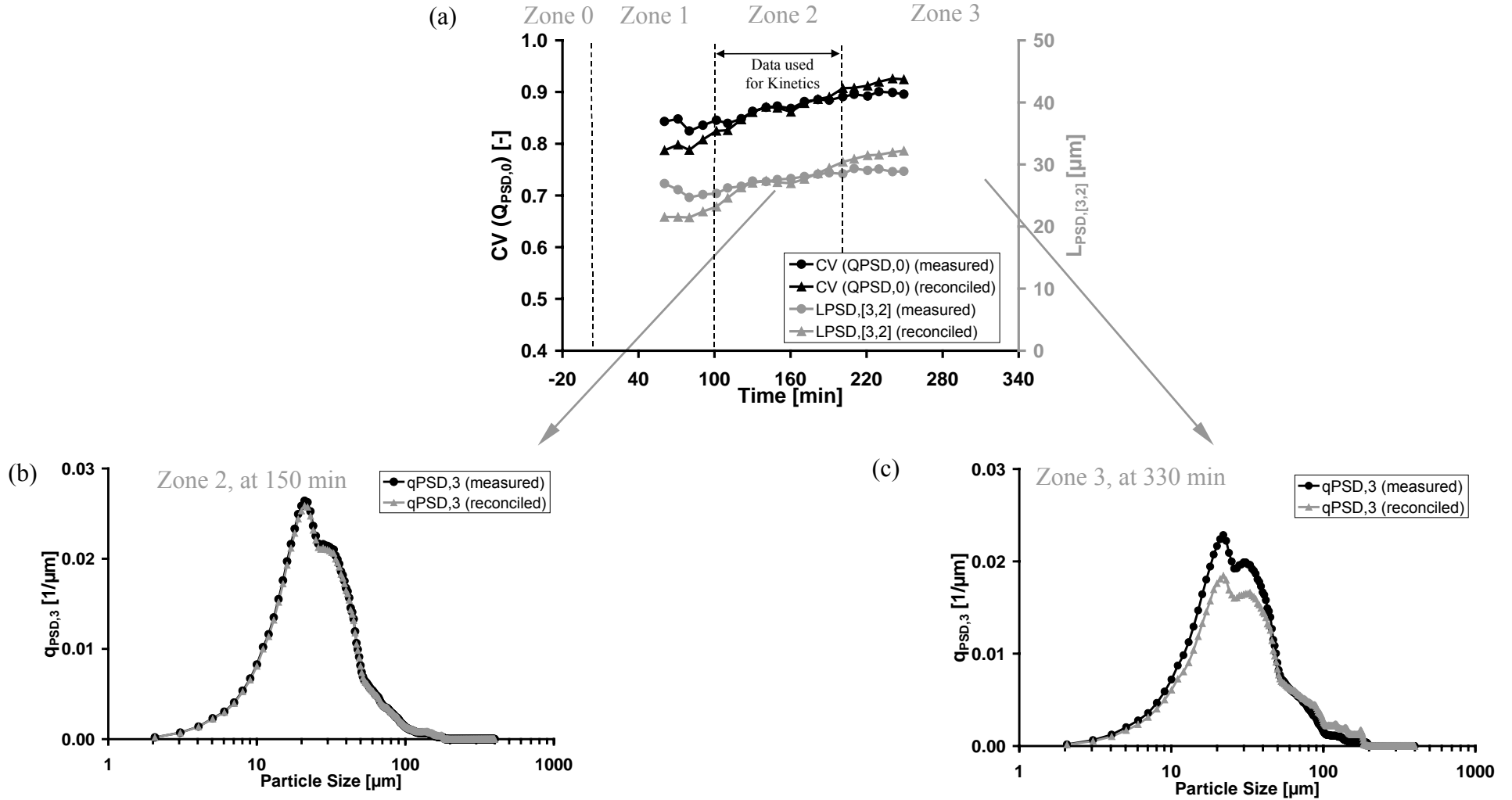
Figure 8-11: (a) Effect of data reconciliation on the Sauter diameter and CV-value using the same experimental data as shown in figure 8-10 (only every third measurement point is indicated), (b) example of a measured and reconciled distribution in zone 2, (c) example of a measured and reconciled distribution in zone 3

8.4   Conclusion

To study the performance of the in-situ "3 Fold Dynamical Optical Reflectance Measurement" three typical "crystallization" model systems were identified being: α-ammonium chloride (electrolyte), ascorbic acid (vitamin) and α-glycine (amino acid) that are used throughout this work. For all substances basic thermodynamic information as well as coarse particles to obtain several sieve fractions are easily available.

To test the capability of the instrument in handling different suspension densities known amounts of sieve cuts were added to a stirred saturated solution. It allowed simulating an "artificial" crystallization process. It was observed that with increasing concentration of a constant sieve cut or non-sieved material:

- a decrease in sensitivity of detecting changes in the number of particles occurred
- a systematic shift of the chord length distribution towards smaller mean sizes and larger CV-values occurred for sieved and non-sieved ammonium chloride and non-sieved ascorbic acid
- for sieved ascorbic acid and α-glycine a minor influence of the suspension density on the measured distribution was observed

From a detailed literature review it was found out that the described behaviour can be observed no matter if the "Focussed Beam Reflectance" or the "3 Fold Dynamical Optical Reflectance Measurement", insoluble or soluble substances are used. For the model systems studied, it was found out that the sensitivity of the instrument recordings is only given for suspension densities smaller than 50 kg/m³$_{Susp}$ ($\approx$ 3 vol%) for ammonium chloride and α-glycine. For ascorbic acid, a slightly higher value was obtained. The operating window for the actual experiment remains therefore rather small. A suitability of the instrument for "higher suspension densities" could not be verified for the model systems studied. It was found that the actual number of particles the instrument measures ("counts") is strongly dependent (up to a factor of 2) on the substance used. The capability of the instrument in differentiating between different sizes was dependent on the respective model system.

The results are particular important by the interpretation of raw measured data. A decrease in the mean chord length might not be necessarily due to breakage or nucleation, a constant reading might not be necessarily caused by a steady process or an increase in CV-value might not be necessarily because of growth rate dispersion. A compensation of the influence of the suspension density on the normalized chord length distribution itself remains challenging. This must be kept in mind during the subsequent evaluation and estimation of the respective rate constants.

In a second part, a new 4 step procedure for data pre-processing was developed that transforms the raw measured chord length distribution into a format suitable for population balance modelling. It combines various independently developed tools from literature with newly developed ones (see also figure 9-2 (chapter 9)) [Hei08b]:

I.   Extending the measurement range by introducing a "dead length", resulting in a linearisation of the measured "counts" versus suspension density (according to Heath et al. [Hea02])

II.   Converting the chord length to a normalized particle size distribution (see chapters 5.3.2 and 9.2)

III.   Calculating the total number of particles per volume by assuming that the zero moment of the particle size distribution relates to the minus first moment of the respective chord length distribution (according to Wynn [Wyn03] and Vaccaro et al. [Vac06a]). To compensate for model assumptions, an "optical factor" is introduced.

IV.   Improving the particle size distribution by exploiting their statistical properties along with the corresponding balance equations (data reconciliation using Lagrange Multipliers)

The procedure is associated with two constants. Whereas the "dead length" (step 1) is a constant for a given model system, the optical factor (step 3), as will be shown in chapter 10, does vary within a certain range between individual experiments. The latter increases all "counts" of the raw measured data of all individual channels and all measured distributions throughout the experiment by the same factor. Both constants affect the actual measured "counts" (~ nucleation rate) but do not influence the normalised distribution (~ growth rate).

By applying all four steps it was successfully shown that the particle size distributions satisfy the mass balance within a specific "time window" of the experiment. It corresponds to a maximum volume percentage of 2 to 2.5 vol% for ammonium chloride and α-glycine and to 6 vol% for ascorbic acid. If only the moments of the particle size distribution are of interest, step 2 and 3 can be combined and simplified along with step 4. The described procedure is a step forward to use the laser scanner data also on a quantitative basis.

Software was written that allows determining the calibration constants and the actual execution of steps 1 to 4 and therefore the automation of the data handling. Additionally, calibration constants were derived for measuring the concentration and hence supersaturation using an ultrasound velocity probe.

9 Overall Work Process and Software Implementation

9.1 Overall Work Process

This chapter forms the bridge between the theoretical part (chapters 2 to 5), the experiments (chapters 7 and 10), the developed procedure for pre-processing of the laser scanner data (chapter 8) and the actual objective of this work: the determination of kinetic rate constants. Figure 9-1 is an overall illustration of the underlying interactions:
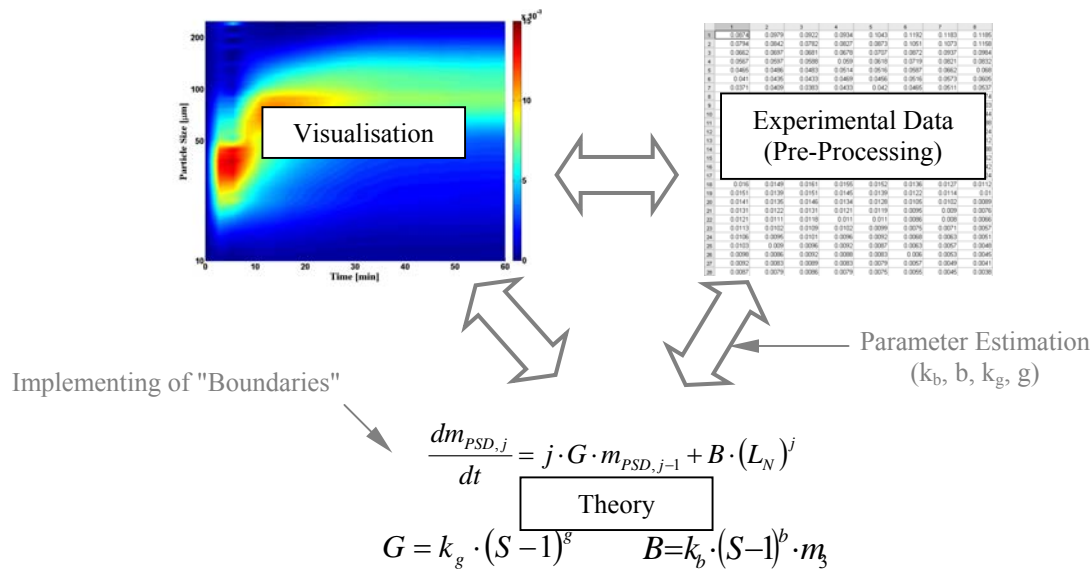

$$\frac{dm_{PSD,j}}{dt} = j \cdot G \cdot m_{PSD,j-1} + B \cdot (L_N)^j$$

Theory

$$G = k_g \cdot (S-1)^g \qquad B = k_b \cdot (S-1)^b \cdot m_3$$

Figure 9-1: "Relationship" between theory, experimental data and visualisation

During one experiment with a duration of 100 minutes, roughly 100 chord length distributions with a channel number of 64, 3000 ultrasound and 3000 temperature measurements are recorded, leading to a total number of approximately 12,400 data points per experiment. The data set is subsequently strongly compressed via:

- the use of moments
- the use of data within zone two, only (closure of mass balance)
- the use of ultrasound and temperature data, every minute, only

leaving approximately 175 measurement points. In a final step, these data points are further reduced to 4 constants being k_b, b, k_g and g. These rate constants are capable of describing the dynamic behaviour of the crystallization process. An automated data handling is compulsory. It allows an increased speed of the model-based analysis and avoids any errors that might occur during a manual data processing on a case-to-case basis. The visualisation of data is playing a critical role. Many different diagrams can be generated by plotting various measured and/or calculated parameters. Within this work, only a small representative selection can be presented.

Figure 9-2 shows a more detailed "overall work-process" that is related to the figures 4-2 and 4-3 (chapter 4).
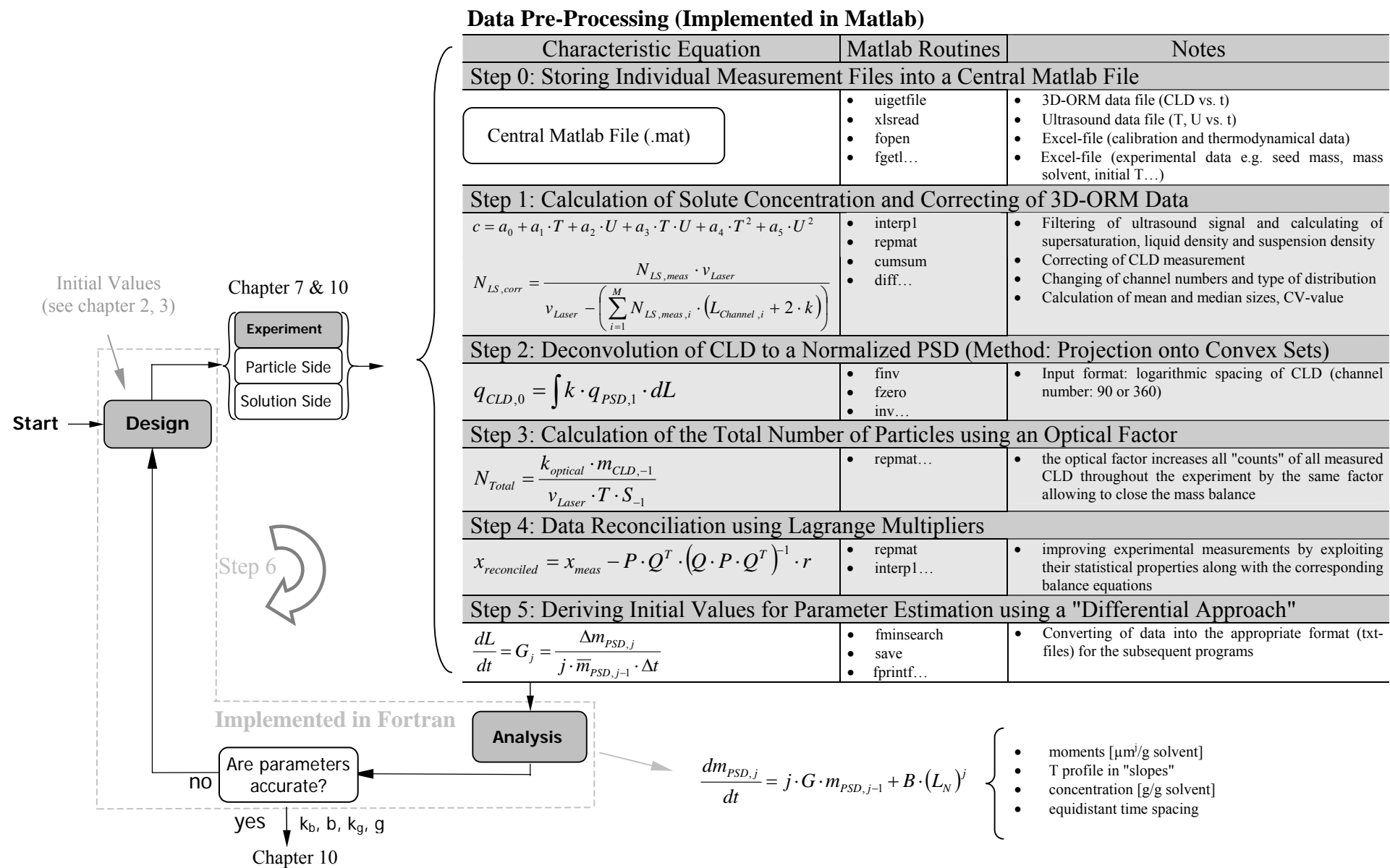
Figure 9-2: Overall work process to evaluate the experimental data (for steps 1 to 4 see chapter 4, see also figures 4-2 and 4-3)

An important step of the sequential experimental design strategy (design - execution - analysis - design…) forms the planning of the initial experiment. Although the aim is to determine kinetics that are supposed to be not known, it is necessary to have already some pre-knowledge of the kinetic constants. The farer the initial guess from the "true" value, the more time and resource consuming the method (more cycles) will be [Are07, Fra07, Hei07, Bar08]. If, for example, a too long batch time or too small supersaturation range is chosen, nucleation might hardly occur during the experiment, making it difficult to determine during the model-based analysis. Following approaches can be applied to determine the rate constants for the initial experiment.

By looking at the governed length and time scales and the empirical data given in chapter 2 the overall range of kinetic constants can be determined. In the absence of any information a nucleation rate range of $B = 10^{+6} - 10^{+17}$ #/(s·m³), a growth rate range of $G = 10^{-9} - 10^{-7}$ m/s and a supersaturation range of $S-1 = 0.01 - 100$ can be assumed. The nucleation and growth rate orders lies often between $b = 1 - 5$ and $g = 1 - 3$, respectively. By assuming a simple power law following range of rate coefficients can be calculated: $k_b = 10^{+8} - 10^{+16}$ #/(s·m³), $k_g = 10^{-1} - 10^{-15}$ m/s. The values are dependent on the definition of the supersaturation as well as if additional variables such as the suspension density or power input are considered within the nucleation rate equation. For the initial experiment the midpoints of these ranges can be applied [Chu00].

A more fundamental approach is to identify a likely nucleation or growth mechanism based on figures 3-3 and 3-5 (a). The respective physical based models for nucleation and/or growth derived by Mersmann [Mer01] can then be used to calculate a first guess of the rate coefficients (see chapters 3.2 and 3.3). For doing so, only the solubility, crystal density, molecular diameter and the volumetric diffusion coefficient are necessary. The latter can be estimated using the empirical relationship from Wilke and Chang [Wil55] or the Stokes-Einstein's relation. It might also be assumed that the growth rate is limited by bulk diffusion. The mass transfer coefficient can be calculated using various correlations; the associated error is likely to be in the range of ±50% [Mer01].

In particular for the growth rate, Mersmann et al. [Mer91, Mer95a] proposed a semi-empirical equation (equation 3.17 (chapter 3)) that was derived by fitting equation 3.17 against kinetic data from 41 organic and inorganic substances. The error associated with equation 3.17 lies between -66% to +270% [Mer95a]. The uncertainty of any a-prior prediction on the one hand must be compared to the several orders of magnitude the growth rate coefficient k_g can span on the other hand. Finally, also engineering judgment [Fuj05] or the "similar structure - similar property principle" [Gas03] can be applied, if applicable. The latter principle must be used with care as illustrated by α- and γ-glycine (see chapter 10.3.1).

Within this work, initial values for the kinetic constants were determined using a combined approach. It considered data from literature, equation 3.17 (chapter 3) and approximate values derived from experimental data prior to the actual kinetic experiments. It allows an estimate of the kinetics close to the "true" value within the first cycle (design - execution - analysis).

9.2   Software

9.2.1   Software from Third Parties

In order assist the implementation of the work process, it was necessary for step 2 and 6 to make use of software programs from third parties (see figure 9-2). For a detailed description of the respective programs and mathematics involved, it is referred to the original cited literature.

Step 2:
The chord length distribution was deconvoluted to its corresponding particle size distribution using the method of "Projection onto Convex Sets" that is described in detailed by Worlitschek et al. [Wor03a, Wor05]. For the reconstruction the a-priori constraint of non-negativity and the a-posteriori constraint of a bounded residual norm were applied. The derivation of the single particle chord length distributions and respective kernels is described in detail by Kempkes et al. [Kem08][1]. A wire frame model was used to model a plate and a cube, whereas the ellipsoid was modelled by a general 3-D ellipsoid equation. The single particle chord length distribution for the sphere was derived using an analytical solution. The software was modified to allow exporting of the particle size distribution with a linear spacing. An example of a deconvoluted chord length distribution assuming various shapes is illustrated in figure 9-3.
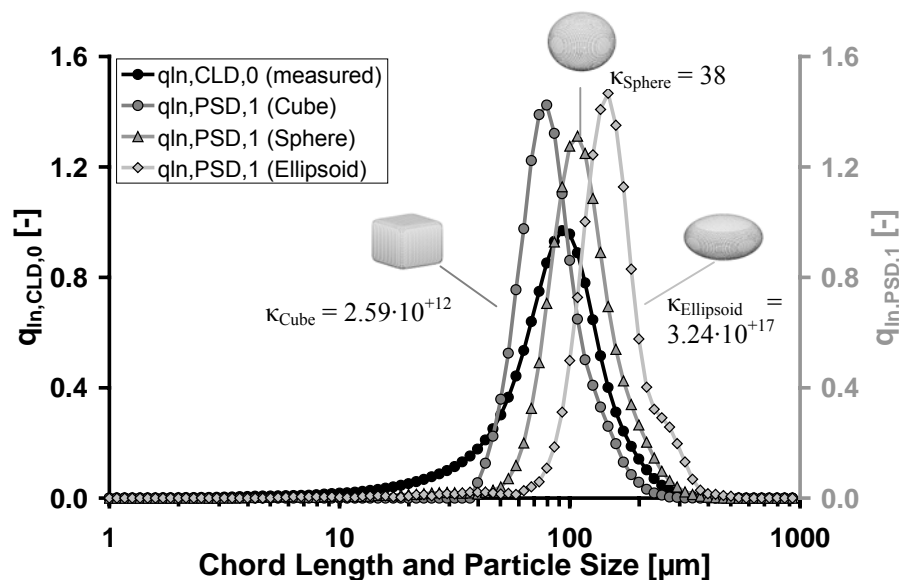

Figure 9-3: Deconvolution of an artificial chord length distribution into a particle size distribution using different kernels for cubic, spherical and ellipsoidal particles as well as the method of "Projection onto Convex Sets", conditions numbers (κ) of the respective kernel

The quality of the restoration of the particle size distribution depends on mathematical method, the kernel (particle shape) and the actual chord length distribution. The ill-posed character of an inverse problem can be determined using "Singular Value Decomposition" as described in detailed by Worlitschek et al. [Wor05]. For the matrices used within this work, a well-posed problem was only given for sphere like particles (condition number $\kappa < 1000$). However, as already demonstrated by Worlitschek et al. [Wor05], the deconvolution can still be made for regular chord length distributions (see figure 9-3).

The ill-posed character becomes apparent when a bimodal as well as broad chord length distribution, typical for crystallization processes, is deconvoluted. The chord length distribution given in figure 9-4 was selected from a crystallization experiment of ammonium chloride, described in chapter 10.1. For the specific case, spherical, elliptical and cube like shapes can be expected.
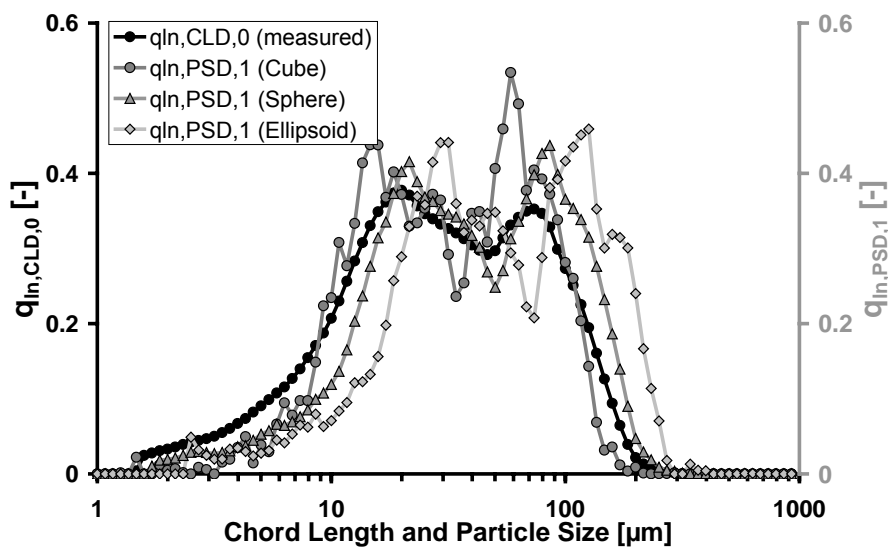

Figure 9-4: Deconvolution of an experimental chord length distribution (ammonium chloride) into a particle size distribution using different kernels for cubic, spherical and ellipsoidal particles as well as the method of "Projection onto Convex Sets"

By assuming an elliptical, cube or plate (not shown here) like morphology an oscillation of the solution for a certain number of experimental distributions, as shown in figure 9-4, was observed. For that reason, it was decided, to model all particles as spheres, as other sizing methods like laser diffraction do as well [Neu02]. By doing so, the problem becomes well posed allowing deconvoluting all experimental data for each substance consistently. The intention of approximating the observed crystal morphology as close as possible must be balanced with a stable solution for all measurements.

Much progress is to be expected within the next years. Algorithms will get more stable and will incorporate optical properties (see for example Kail et al. [Kai07, Kai08]). The actual mathematical methods for solving the ill-posed problem are basically the same as for laser scattering and diffraction devices [Box92]. It is therefore only a question of time until the deconvolution algorithms are implemented within the vendor's software. Unfortunately, the implementation within the 3D-ORM software led to non-physical results.

Step 6:

Within this work the software implementation of the moment model described in detail by Chung et al. [Chu99, Chu00] and Togkalidou et al. [Tog04] was used that can be downloaded from the internet [Chu04]. The programs are written in Fortran running under Digital Visual Fortran Professional Edition 6.0A (Windows operating computer). The following 4 programs were used:

- optexp.f for model-based experimental design
- param.f for kinetic parameter estimation
- dim1.f for simulation of the crystallization process
- conf.f for calculating confidence intervals

To solve the underlying equations the ODEPACK (*O*rdinary *D*ifferential *E*quation *Pack*age) [Hin83] and the FFSQP (*F*ortran *F*easible *S*equential *Q*uadratic *P*rogramming, Version 3.7b) routine[2] are necessary. The FFSQP routine solves constrained non-linear (minimax) optimisation problems. Modifications to the programs were made to ease the data transfer between specific programs used within the work process. The software was further modified to allow importing all initial values (temperature, noise estimates, batch time, best guesses) from a text file.

Model-based Experimental Design:

In principle, the model-based experimental design program calculates the temperature profile that should be applied to the reactor liquid. However, because of the relative good heat transfer conditions and the fact that the approach is aiming at providing approximate conditions for a good experiment, it was decided to set the calculated temperature profile equal to the temperature profile of the thermostat. An exception is described in chapter 10.1.

In chapter 8 it was shown that the limiting factor for the experimental investigation is the rather small operating window of the 3D-ORM instrument. The preferred suspension density is in the range of 10 - 50 kg/m³$_{Susp}$ (< 3 vol%) for ammonium chloride and α-glycine, whereas for ascorbic acid higher suspension densities can be applied. To be able to obtain as much as good data points, the mass of seed crystals should not exceed 10 kg/m³$_{Susp}$. These constraints set by the measurement probes were considered via the choice of the temperature range. For all case studies, a temperature difference of 15 K was therefore chosen (T_{start} − T_{final}). Table 9-1 summarises additional boundaries that were applied for experiments based on model-based experimental design. It ensured that the experiment run in well-defined "regions" where good measurements can be made.

The seed size was limited to the available crystal sizes within the material purchased by the supplier. The material was sieved, using standard sieves. The upper seed size was further restricted due to the difficulties of the 3D-ORM in measuring a small amount of large crystals with the set measuring time. The maximum sieve cut size was therefore taken to be

---

[2] The FFSQP routine was kindly provided by AEM Design, Inc. 3754 LaVista Rd., Suite 250, Tucker, GA 30084, USA

160-250 µm. The maximum cooling rate was restricted by the heat transfer coefficient and thermostat. The minimum cooling rate was set to zero.

Table 9-1: Applied boundaries for model-based experimental design**

Boundaries	Ammonium Chloride	Ascorbic Acid	α-Glycine
T_{min}/T_{max}	5/20 °C	25/40 °C	5/20 °C
$(dT/dt)_{min} < dT/dt < (dT/dt)_{max}$	0 - 0.33 °C/min	0 - 0.33 °C/min	0 - 0.33 °C/min
$m_{Seed,min} < m_{Seed} < m_{Seed,max}$	0.5 - 3 g	1 - 3 g	1 - 3 g
$(Sieve)_{min} < Sieve < (Sieve)_{max}$*	63-90 - 160-250 µm	< 90 - 160-250 µm	< 90 - 160-250 µm

*must be transformed to a number mean length
**experiments based on engineering judgment might apply parameters outside this range (see chapter 10)

Within these boundaries, the program calculated optimal experimental conditions using the criterion of D-optimality. According to Chung et al. [Chu00], the information content of the individual experiment increases with a decreasing crystal surface. In other words, a low seed mass and a high seed size are ideal. It ensures that the experiment has an adequate dynamic behaviour. Some authors are applying repeated ramps (heating and cooling sequences) with plateaus in between [Wor04]. Beside the model-based experimental design, a certain number of experiments were also made based on engineering judgment. The parameters can thereby slightly deviate from the boundaries given in table 9-1.

The only parameter that remains open within the program is the total batch time. Chung et al. [Chu00] and Togkalidou et al. [Tog04] provide no guideline on how to choose this value. The lower boundary of the batch time is characterised by the time the thermostat needs to cool down the solution to the desired temperature using the maximum cooling rate. The upper limit of the batch time can be defined as the time that ensures a low supersaturation throughout the experiment so that only crystal growth takes place. The batch time was chosen based on the derived initial values and engineering judgement.

Model-based Experimental Analysis (Estimation of Parameters):
To determine all kinetic rate constants simultaneously, the population balance approximated by moments, the respective mass balance (equations 3.22 to 3.26 (chapter 3)) and kinetic equations were fitted against the experimental data (so called "integral approach"). In contrast to the "differential approach", the kinetic model must be provided a-priori. Following objective function was used (equation 9.1),

$$F = \sum_{i=1}^{N_m} \sum_{j=1}^{N_d} w_{ij} \cdot \left(y_{i,j(meas)} - y_{i,j(model)}(\Theta) \right)^2 \rightarrow min \qquad (9.1)$$

with Θ representing the kinetic parameters (vector) that were estimated by minimising the difference between the model predictions ($y_{i,j(meas)}$) and experimental data ($y_{i,j(model)}$). N_d is the number of measurement points (j, sampling instances, every minute), whereas N_m is the number of measured variables (i, $m_{PSD,0}$ to $m_{PSD,4}$, concentration) and w_{ij} the inverse of the

measurement error variance (weighting factor). The software allows not to handle multiple experiments with different temperature profiles and, if applicable, different initial seed masses. Chung et al. [Chu00] and Togkalidou et al. [Tog04] used therefore the rate constants with the smallest confidence interval as a final set. However, also any appropriate form of average between different experiments can be made.

Although the "integral approach" is the method of choice, occasionally problems occurred in finding a unique solution (convergence). Qiu et al. [Qiu91] Granberg et al. [Gra05] and Forsberg et al. [For06] showed that the optimisation surface (value of the objective function versus k_b and b or versus k_g and g) has a ridge shaped character. In other words, different values of k_b and b or k_g and g can lead to similar values of the objective function (see also Oullion et al. [Oul07] and Schwaab et al. [Sch07]).

9.2.2   Development of Interface Software

To complement the "work process" interface software was written that builds the bridge between the raw measured data, the software developed within this work and the programs from third parties. These interfaces programs consist mainly out of matrix operations, algebra and least square estimation routines. They allow filtering, correcting, calibrating and transforming of experimental data. For example, each individual software program is asking for a different format of the size distribution with respect to number of channels, the type of spacing (logarithmic, linear) and applied weightings. Thereby, following situation occurred:

For all experiments, the laser scanner covered a size range of 1.56 to 400 μm. The vendor's software exports the data only with a default channel setting. It has 21 out of 64 channels within the size range of 1.56 to 10 μm. However, for the deconvolution of the chord length distribution (step 2), the distribution must have a resolution of at least 90 or 360 logarithmic spaced channels. In other words, by changing the channel number of the exported 3D-ORM data, a higher resolution was pretended than actual measured. Later onwards (> step 3), an equidistant linear spacing of the distribution with a channel width of 1 μm was required. The transformation of the channel number resulted in a partial loss of information at the lower end and a pretending of a higher resolution at the upper end of the respective size range. For changing the number and type of channels the Matlab function "interp1" was applied along with the cumulative distribution. For the respective equation it is referred to Allen [All03] or to any mechanical engineering book (for example Stieß [Sti95]).

Step 0:
The objective of the program is to import all recorded data from the 3D-ORM and ultrasound probe measurement files (.csv files) into a central Matlab document. Additionally, the program imports additional data such as solubility, calibration constants, seed mass, temperature profile and densities from individual Excel - files.

Step 1:

The objective of the program is to apply various transformation steps preparing the data for the calculations described in chapter 8.3.1. Following steps were implemented into the software code.

The 3D-ORM software (WinORM, Version 4.58) uses a non-typical format of presenting and exporting the chord length distribution data. The spacing of the channels is neither logarithmic nor linear. A screenshot of the software is given in figure 9-5.
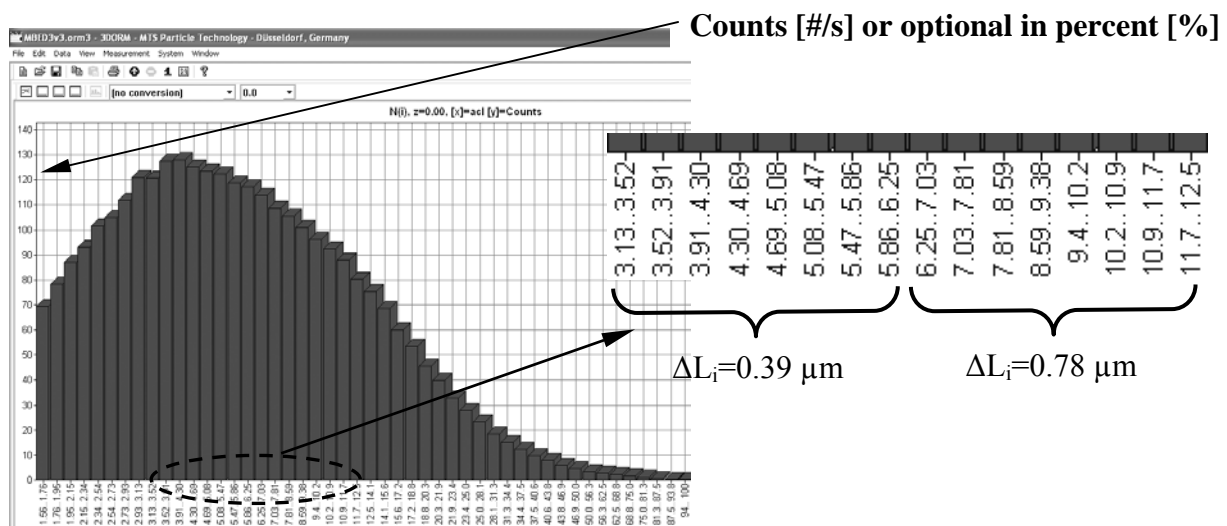

Figure 9-5: Screenshot of the 3D-ORM software showing a measured chord length distribution with "counts" on the ordinate

Figure 9-5 shows a measured chord length distribution with "counts" on the ordinate, optional percent can be chosen. The sum of the "counts" within each interval is equal to the total "counts", whereas the sum of the percentage values of each interval is equal to 100%. In other words, the unit of the ordinate is not normalized by the interval width. The default channel setting is characterised by a doubling of the channel width every 8th channel. However, if both description of the abscissa and ordinate are valid, a significant change in the number of counts (or percent) should be observed at the channel where the width is doubled. Because, the number of particles within each channel or the relative frequency $\Delta Q = Q(L_2) - Q(L_1)$ ultimately depends on the channel size (see also Sommer [Som01]). This is not mirrored by figure 9-5. Only if the "counts" or the relative frequencies ΔQ [%] are "normalized" by the interval width ΔL, the value on the ordinate becomes independent of the respective channel size (q [1/µm]). However, by definition the sum of each interval is then no longer equal to the total "counts" or to 100%. The influence of the interval width on an artificial distribution is illustrated within figure 9-6. It becomes evident that by having a doubling of interval width every 8th channel and "only" counts [#/s] or a relative frequency ΔQ [%] on the ordinate the distribution can not be as regular as shown in figure 9-5.
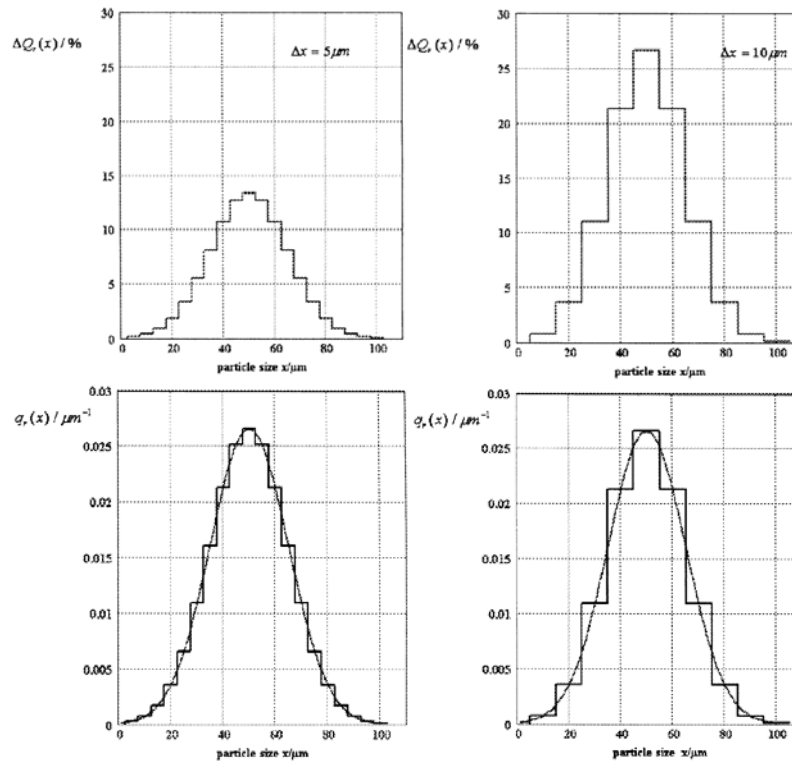
Figure 9-6: Influence of the interval width (5 or 10 µm) on the relative frequency ΔQ [%] and density distribution q [1/µm] [Som01]

It is therefore assumed that the underlying "true" unit of the ordinate used within the 3D-ORM software is percentage per interval width but normalised to 100% and if applicable, multiplied by the total number of counts.

To convert the exported distribution from the 3D-ORM software to a standard format (q [1/µm] or Q [-]), the data is multiplied by the respective channel width (ΔL_i (i = 1 to 64), equation 9.2)

$$\Delta Q^*_{CLD,0,i} = \Delta Q^{Export}_{CLD,0,i} \cdot \Delta L_i \qquad\qquad (\textbf{9.2})$$

and subsequently normalised to 1 (or 100%) according to equation 9.3.

$$\Delta Q_{CLD,0,i} = \frac{\Delta Q^*_{CLD,0,i}}{\displaystyle\sum_{i=1}^{M}\left(\Delta Q^*_{CLD,0,i}\right)} \qquad\qquad (\textbf{9.3})$$

Figure 9-7 shows an example of the exported distribution (grey triangles), the "intermediate" distribution after applying equation 9.3 (grey circles) and the final chord length distribution having a standard format calculated according to equation 9.4 (solid black line).
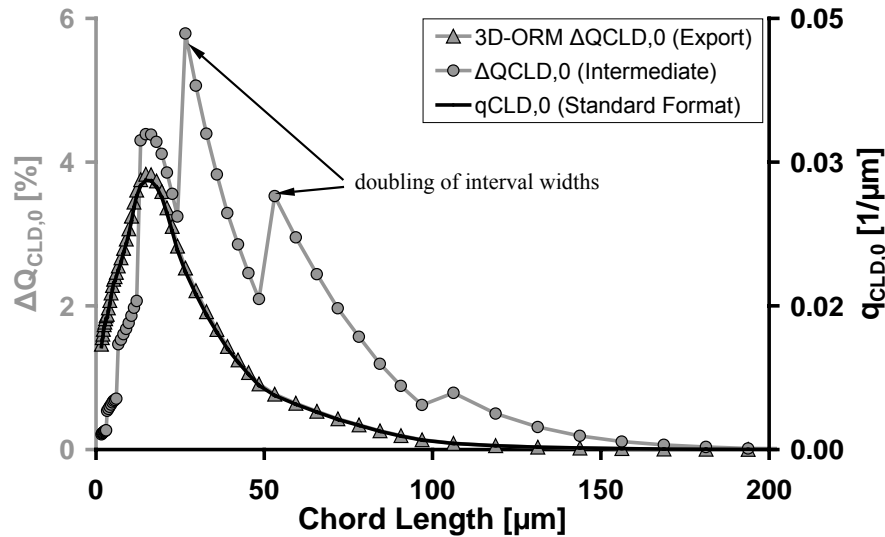
Figure 9-7: Conversion of the exported 3D-ORM measurement data to a standard format using equations 9.2 to 9.4

Although the distribution $\Delta Q_{CLD,0,i}$ (grey circles) looks unfamiliar it is in line with the described doubling in channel width. The cumulative distribution is obtained by summing up the individual contributions ($\Delta Q_{CLD,0,i}$) whereas the density distribution is obtained by applying equation 9.4.

$$q_{CLD,0,i} = \frac{\Delta Q_{CLD,0,i}}{\Delta L_i} \qquad\qquad\qquad (\textbf{ 9.4 })$$

From figure 9-7 it can be seen that the exported (ΔQ [%]) and final chord length distribution ($q_{CLD,0}$ [1/µm]) only differ in their unit and absolute value. In other words, if the final chord length distribution is normalized to 100%, the original exported distribution is obtained

In a second step the total "counts" detected within the measuring interval were normalised to "counts per second" using the measuring interval defined within the 3D-ORM software. Unfortunately, the measuring period set within the 3D-ORM software was not equal to the time between two successive recorded measurements. The latter was roughly 2.5 times larger and not constant. It remains unclear if this originates from a software error or caused by the time the instrument needs to process the raw measurement data. All distributions that correspond to a count rate smaller than 20 #/s were set to zero. In a subsequent step, the total number of particles for each distribution was corrected using the respective "dead length" derived in chapter 8 (equation 8.4). Additionally, all distributions are converted to a logarithmic distribution with optional 90 or 360 channels (see step 2).

For modelling purposes, especially for the mass balance closure, it is necessary to have the concentration measurement at the same instance of time as the particle size measurement. However, the ultrasound probe and the 3D-ORM were difficult to synchronize. Additionally, as described in chapter 7.3, the ultrasound probe had to be removed from the reactor at certain time intervals. Therefore, the ultrasound data was filtered for the respective times the probe was placed in a water bath (see chapter 7). The ultrasound values were

converted to concentration values applying equation 8.3 along with the respective empirical coefficients (see table 8-1 (chapter 8)). The supersaturation was easily obtained using the recorded temperature and solubility data (see appendix, chapter A.1). Finally, via the Matlab function "interp1", the supersaturation data was approximated by a spline. It allowed calculating the supersaturation for the discrete time points of the 3D-ORM measurements by interpolation. If necessary, a moving average filter was applied. For each discrete time point of the 3D-ORM measurement also the specific temperature, solubility and (theoretical) suspension densities were calculated and stored within the central Matlab file.

Step 3 and 4:

In step 3, the optical constant ($k_{optical}$) was estimated by minimising the difference between the "theoretical" suspension density and the suspension density calculated via the particle size distribution. Data outside zone two were now disregarded as described in chapter 8.3.1. For the remaining data, data reconciliation was made (step 4, see chapter 8.3.2).

Step 5:

Initial values of the rate constants were estimated using the so called "differential approach" opposed to the "integral approach" (see step 6). The growth rate was calculated by equations 3.31 or 3.35 (chapter 3) and plotted versus the supersaturation as illustrated in figure 9-8.
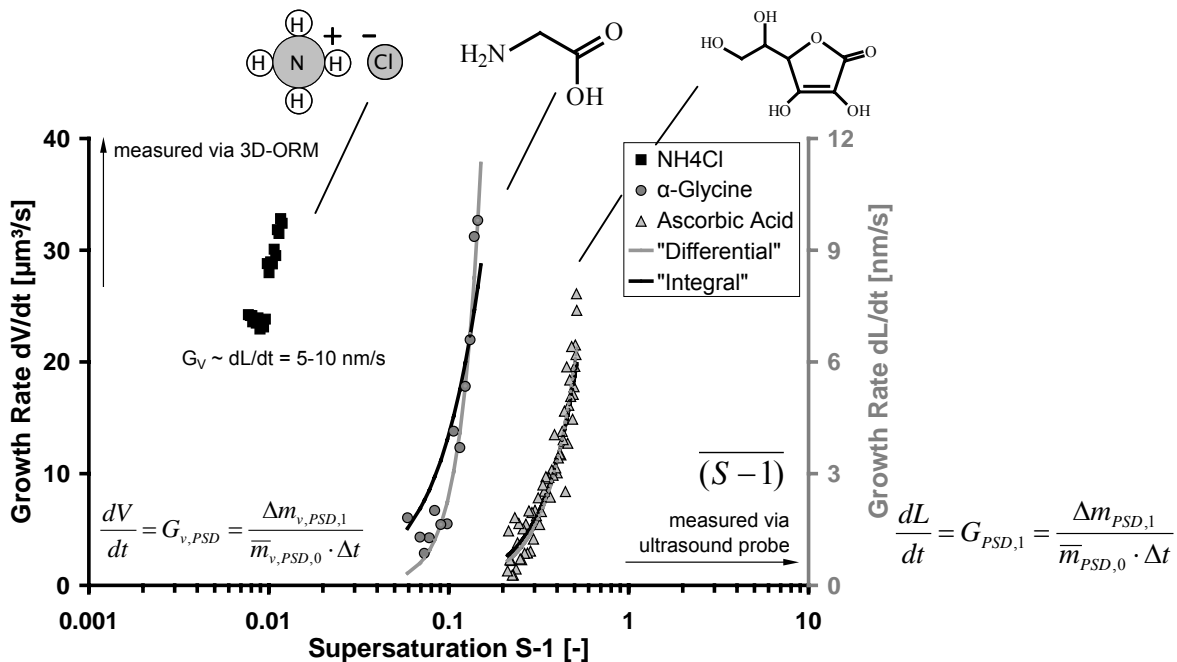

Figure 9-8: Determination of crystal growth rates using a "differential approach" (see chapter 3.4.2, experimental data was taken from chapter 10)

The "differential method" is a simple and fast method to look at the nucleation and growth rate, or if applicable, the agglomeration kernel independently. It has the advantage that no knowledge about the actual kinetic model is necessary. Additionally, since two independent measurements being the supersaturation (via the ultrasound probe) and the moments (via the 3D-ORM) are compared, the method allows a consistency check between the instruments.

The measurements were defined as consistent, if the data points fell on an approximate continuous line. A certain scattering of the data points is tolerated (see chapter 3.3, figure 3-5). Optional, a moving average filter was applied. Using a least square technique, the rate constant and rate order were estimated.

In table 9-2 the kinetic constants determined via the a-priori prediction (equation 3.17), the "differential" and "integral approach" are compared.

Table 9-2: Comparison between kinetic constants derived by using equation 3.17, a "differential" and an "integral approach"(experimental data taken from chapter 10)

Equation	Parameter	Equation 3.17 [Mer95a]	Differential Approach	Integral Approach
Ascorbic Acid (Experiment 1, see Chapter 10.2)				
$G = k_g \cdot (S-1)^g$	g [-]	2	2.26	2.55
	k_g [m/s]	$2.30 \cdot 10^{-4}$	$3.49 \cdot 10^{-8}$	$2.91 \cdot 10^{-8}$
α-Glycine (Experiment 1, see Chapter 10.3)				
$G = k_g \cdot (S-1)^g$	g [-]	2	3.78	1.84
	k_g [m/s]	$3.16 \cdot 10^{-4}$	$1.47 \cdot 10^{-5}$	$2.79 \cdot 10^{-7}$

Depending on the quality of the data points, the kinetic constants estimated using the "differential approach" can be close or far from the ones determined using the "integral approach". However, as described above, these differences must be discussed from the background of the overall range kinetic constants can span.

The same methodology was applied for the determination of the nucleation rate and agglomeration kernel (see chapters 3.4.2 and 10.1). The "differential approach" can also be used as a model discrimination tool [Peb96a, Peb96b, Bra96]. For example, van Peborgh Gooch et al. [Peb96a, Peb96b] derived tools that allow to distinguish between different size enlargement mechanisms such as growth rate dispersion and agglomeration using the growth rates $G_{PSD,1}$ and $G_{PSD,3}$ versus time as an indicator.

In a final step of the program, the supersaturation and particle size distribution (from zone two, only) was transformed to a format that suits the input format of the software program described in step 6. The moment model is thereby asking for an experimental data set with equidistant time intervals. Since the 3D-ORM records experimental data at non-constant time intervals an interpolation of the experimental data to a constant time interval of 1 minute was necessary (Matlab routine "interp1").

9.3   Conclusion

To determine the kinetics, an overall work process was defined (see figure 9-2) that is based on model-based experimental design and analysis (see chapter 4 (figures 4-2 and 4-3)) and the new 4 step procedure for data pre-processing developed in chapter 8.

To assist the implementation of the work process software programs from third parties were selected. For the deconvolution of the chord length distribution the method of "Projection onto Convex Sets" described in detail by Worlitschek et al. [Wor03a, Wor05], implemented in Matlab, was chosen. It assumes that the chord length distribution is proportional to the length weighted particle size distribution. The a-priori constraint of non-negativity and the a-posteriori constraint of a bounded residual norm were applied. A spherical crystal morphology was assumed throughout this work.

For the performing of model-based experimental design and analysis, the software package described in detail by Chung et al. [Chu00] and Togkalidou et al. [Tog04] was selected. It uses the "Ordinary Differential Equation Package" and a "Feasible Sequential Quadratic Programming" routine running under Fortran. The population balance is characterised by the moment model. For model-based experimental design the criterion of D-optimality in combination with a sequential experimental design strategy is used.

In a third step, interface software was written that allows exchanging of experimental data between the individual software programs (software that accompanies the instruments, software developed in chapter 8 and software described in chapter 9.2.1) that have developed independently from each other within different programming languages. These interfaces consist mainly out of simple matrix operations, algebra and least square estimation routines. They allow the filtering, correcting and transforming of the measured data to the appropriate input format of each software program. Initial parameters for the estimation of the kinetic constants are obtained using a "differential approach". It has the advantage that no a-priori knowledge about the actual kinetic model is necessary and a first discrimination between different kinetic mechanisms can be made.

The software implementation developed within this work allows executing all described steps in an automated way leading to an increased speed of the data evaluation. This is essential because of the enormous amount of data that is recorded by in-situ probes and the type and number of calculation steps that must be performed. It avoids any errors that might occur during a manual data processing on a case-to-case basis. The model-based approach incorporates all constraints set by the measurement probes (for example suspension density range smaller 3 or 6 vol%) via the choice of the temperature range and seed mass. It ensures that the "designed" experiment runs in a well-defined "region" and that for the evaluation the actual physical laws that describe the crystallization process are considered. The software implementation forms a central part of this work. It is the bridge between the theoretical and experimental part allowing determining the actual kinetic rate constants.

10 Case Studies

10.1 Ammonium Chloride

10.1.1 Tailoring Particle Morphology

Ammonium chloride (NH$_4$Cl) has two polymorphs. The α-form transforms (reversible) at a transition temperature of 184.4 °C to the β-form [Ull07]. Dendrites are forming when crystallized from water [Kah70, Han02, Dou07] (see figure 10-2, stagnant solution). From a process engineering point of view dendrites are fragile, leading to sincere breakage and problems within downstream processes. Figure 10-1 shows the result of a cooling experiment, without seeds, monitored by the 3D-ORM.
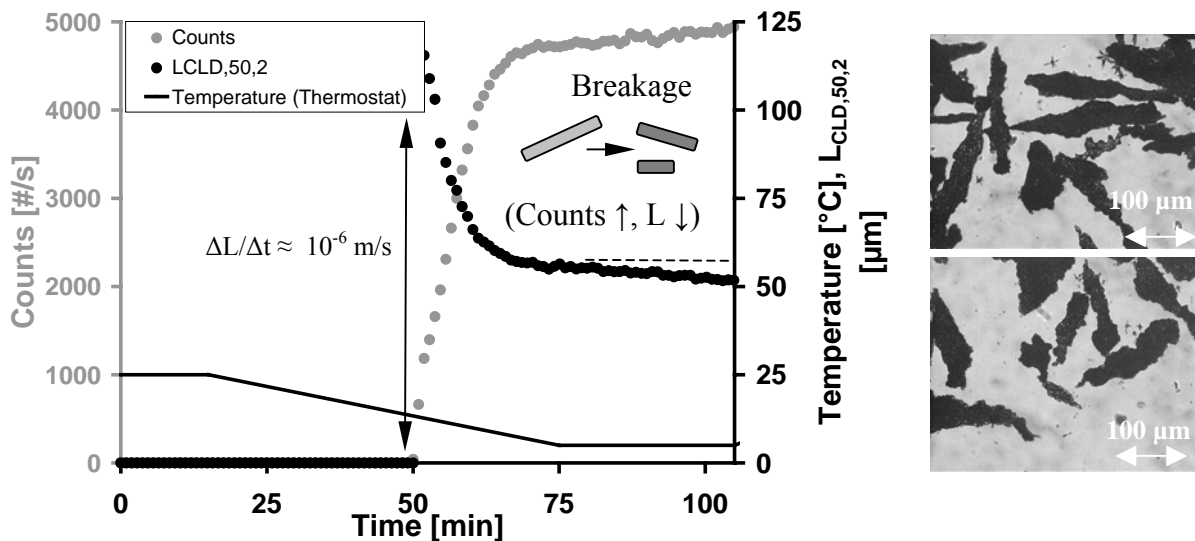
Figure 10-1: Development of the "counts" and median size (L$_{CLD,50,2}$) during the crystallization of ammonium chloride from an aqueous solution using a linear temperature profile (optical microscopy pictures were taken at the end of the experiment)

Crystals with a median size of L$_{CLD,50,2}$ = 125 μm occurred within an instant of a minute. The growth rate of dendrite branches was found to be in the order of 10^{-6} - 10^{-5} m/s [Kah70, Oht98]. Due to nucleation and breakage, a strong increase in counts by a simultaneous decrease in median size was observed.

Because of the measuring principle of laser scanner instruments, it remains difficult to monitor changes of needle like particles (see chapter 5.3.2). Therefore, it was decided to make use of an additive as a habit modifier to improve the measurement and to reduce any breakage. The effect of numerous inorganic and organic additives on the morphology of NH$_4$Cl was already summarised in 1892 by Retgers [Ret92]. Later works were compiled by Nývlt et al. [Nýv95]. From an initial screening study using different additives (CoCl$_2$, Cr$_2$Cl$_6$, MnCl$_2$, FeCl$_2$, Al$_2$Cl$_6$, urea, glycine), MnCl$_2$ was selected as an example. Manganese chloride is capable of changing the morphology to a cubic like form (see figure 10-2). It seems to be that also the seed crystals purchased from Carl Roth GmbH + Co. KG, were crystallized

under the influence of an additive. Additives allow thereby also the inverse, a change of a cubic like crystal to dendrites as described in detail by Jäger et al. [Jäg06] for the crystallization of sodium chloride with hexacyanoferrate as an additive.
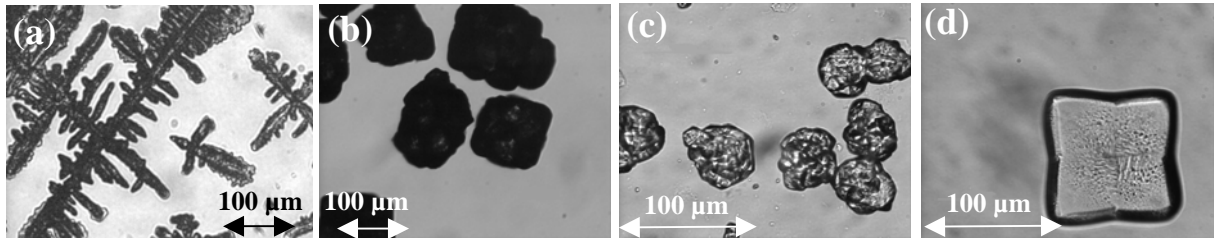

Figure 10-2: Experimental observed morphologies of ammonium chloride within a stagnant solution (a) from an aqueous solution, (b) seed crystals from Carl Roth GmbH, (c) from an aqueous solution with 3700 ppm $CoCl_2$ per saturated solution (d) from an aqueous solution with 3700 ppm $MnCl_2$ per saturated solution

Using a batch reactor the effect of the $MnCl_2$ concentration on the morphology was investigated. For the same additive concentration, the stirred solution led to slightly different morphologies as observed in a stagnant solution (figure 10-2). The results are summarised in figure 10-3.
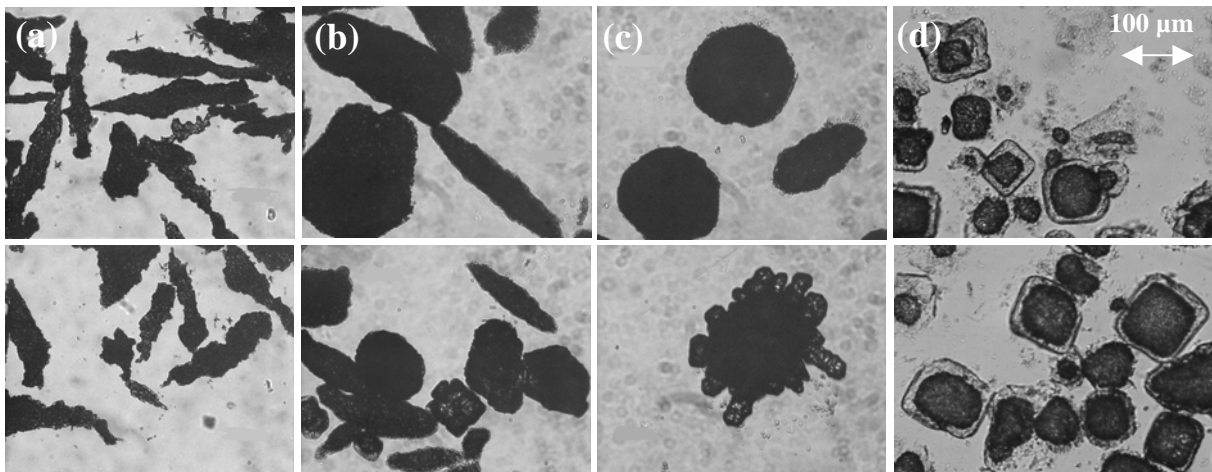

Figure 10-3: Experimental observed morphologies for different additive concentrations using a stirred batch reactor and a linear cooling profile, (a) 0 ppm $MnCl_2$, batch time: 1 h, (b) 125 ppm $MnCl_2$, batch time: 1 h, (c) 250 ppm $MnCl_2$, batch time: 1 h, (d) 3700 ppm $MnCl_2$, batch time: 8 h (concentration refers to ppm per saturated solution)

With increasing $MnCl_2$ concentration the morphology changes from a needle like to an elongated, elliptical up to a spherical shape. Sometimes an "outgrow" of dendrite branches was observed. At higher additive concentrations and batch times longer 8 hours a transparent layer formed around the seed crystals leading to cubic crystals as observed within stagnant solutions. In the presence of $MnCl_2$ also the optical property of the crystal changes (transparent to opaque).

10.1.2   Kinetic Mechanisms

To further study the crystallization of NH$_4$Cl various process conditions were investigated that are described in detail by Elter [Elt07]. Figure 10-4 shows experimental results for a constant additive concentration of 250 ppm MnCl$_2$ (sat. S.) and a constant seed size of 63-90 μm.
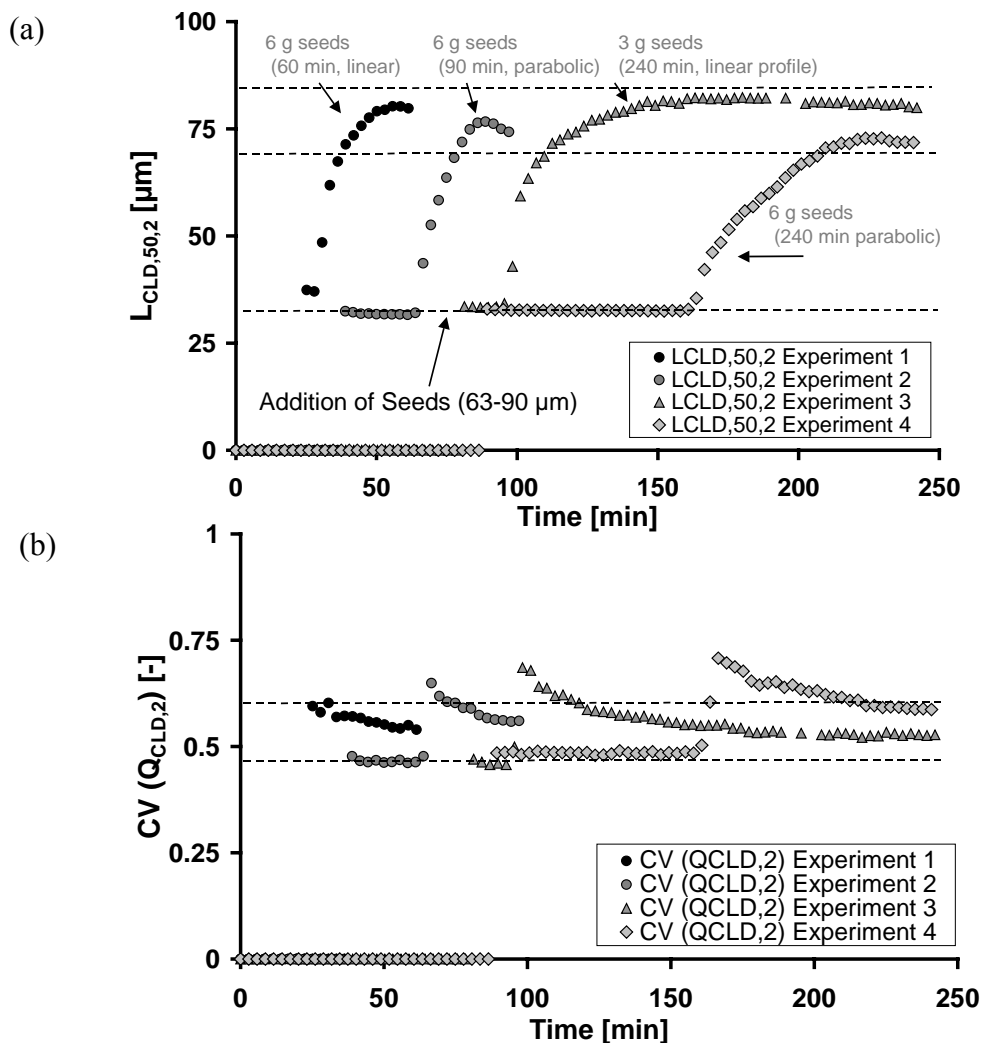

Figure 10-4: (a) Development of the median size L$_{CLD,50,2}$ (b) and the respective CV-value (Q$_{CLD,2}$) during the crystallization of ammonium chloride using seed crystals with a size of 63-90 μm and a additive concentration of 250 ppm MnCl$_2$ (sat. S.) (various process conditions)

Generally, the use of a parabolic temperature profile in combination with an extended batch time leads to a larger median size and a lower CV-value. However, figure 10-4 shows that the median size (L$_{CLD,50,2}$) and coefficient of variation (CV (Q$_{CLD,2}$)) are only slightly affected by the seed mass, temperature profile (linear, parabolic) and batch time. Additionally, all seeded experiments showed a so called dead supersaturation zone (threshold supersaturation for growth) that is discussed in detail for various substances by Sangwal [San02, San07]. In other

words, the seed crystals did not grow during a period of 5 to 50 minutes until a "threshold" supersaturation was reached.

As demonstrated in the previous chapter and reported by Chianese et al. [Chi96] a sphere like morphology of NH_4Cl was obtained by the addition of 250 ppm of $MnCl_2$ (sat. S.). Spherical morphologies are often the result of agglomeration, sincere attrition or spherulites that form at higher supersaturation values [San07]. Since spherical particles were observed at a relative low supersaturation from the very early moment on, agglomeration is the most likely mechanism. Figure 10-5 shows the recorded 3D-ORM measurement for an experiment without seed crystals. It is typical for all crystallization experiments with an additive concentration between 250 to 3700 ppm $MnCl_2$ (sat. S.).
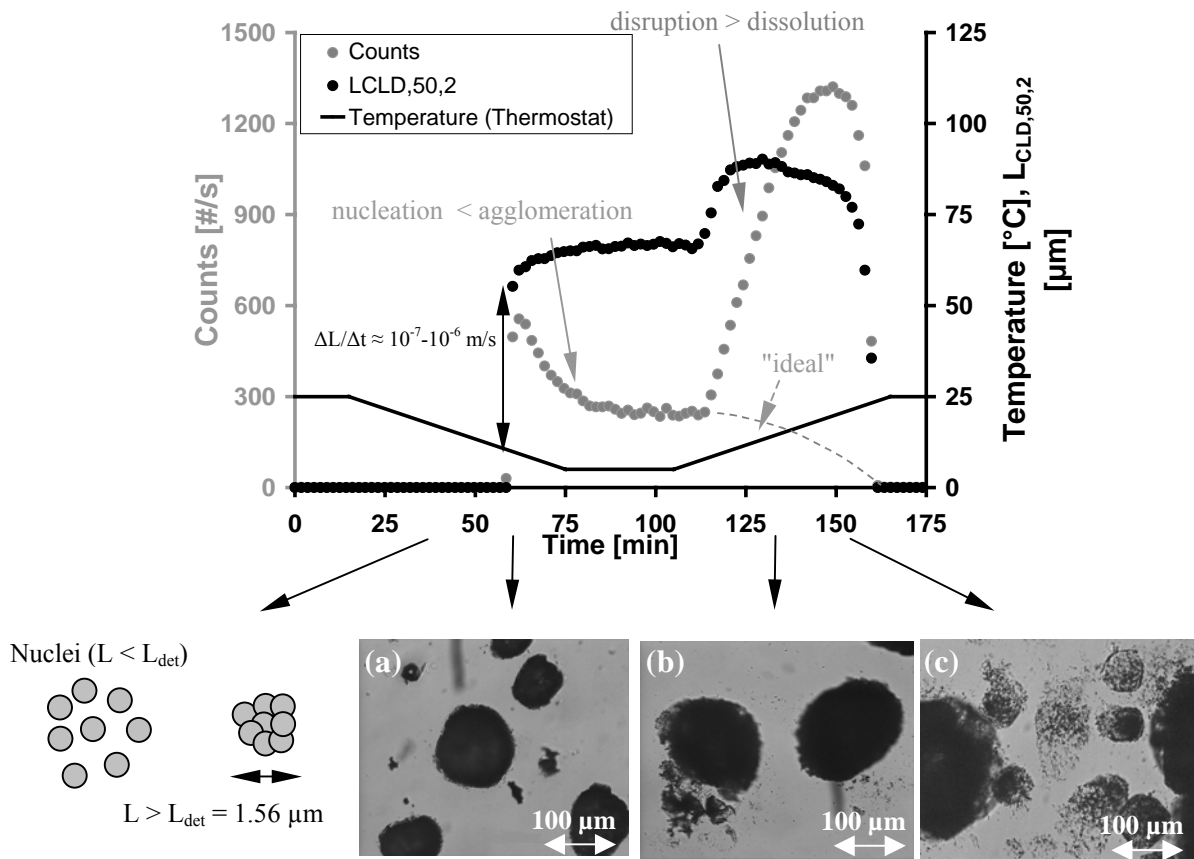

Figure 10-5: Development of the "counts" and median size ($L_{CLD,50,2}$) during the crystallization of ammonium chloride using a linear temperature profile and an additive concentration of 1975 ppm $MnCl_2$ (sat. S.) (optical microscopy pictures were taken at the indicated times)

After around 60 minutes nucleation starts, leading in an instant of time to particles with a median size of 60 μm, although the lower detection limit of the 3D-ORM is 1.56 μm (see left picture (a)). The "counts" are roughly only one third when compared to figure 10-1 and decrease as the crystallization proceeds. By dissolving the just crystallized NH_4Cl, an unexpected dissolution behaviour is observed. The "counts" are increasing as the dissolution proceeds. Microscopic images (see right pictures (b, c)) revealed that the particles "split up" into smaller particles of an approximate size of 1-5 μm (disruption). Therefore, it can be concluded that the particles are the result of an excessive agglomeration that must take place

prior to reaching the detection limit of the 3D-ORM (see also figure 2-1 (chapter 2)). A strong cementation of primary particles seems not taking place. It is known that agglomeration ceases when a critical size is reached [Mer00b, Mer01, Hof04], explaining besides the influence of the suspension density on the recorded chord length distribution (see chapter 8.2.2 and appendix, chapter A.5) the "non-sensitivity" of the final crystal size towards various process conditions (see figure 10-4). Agglomeration also helps in clarifying the observed changes in optical properties of NH_4Cl crystals (see figures 10-2 and 10-3).

The results reported closely coincidence with the work by Sessiecq et al. [Ses00] on the crystallization of NH_4Cl using potassium chloride as a precipitant (supersaturation range of (S-1) < 0.02). Sessiecq et al. [Ses00] also observed a sudden and steep increase in particle size at an early time point of the experiment leaving mainly large agglomerates consisting of 5 μm primary particles. The sizes of the individual primary particles and agglomerates remained thereby constant over the experimental time independent of the initial supersaturation. It is reported that individual particles smaller 5 μm could not be found [Ses00]. From their experimental results it was proposed that the crystallization is mainly determined by nucleation and agglomeration, whereas the crystal growth can be neglected [Ses00]. The characteristic time of agglomeration was calculated to be 2.3 seconds [Ses00].

Figure 10-6 shows the results obtained by Chianese et al. [Chi96]. NH_4Cl crystals crystallized from pure solution are characterised by a "cauliflower-like" structure, whereas crystals grown under the influence of Mn^{2+} are described as near-spherical with compact surfaces and porous structure [Chi96]. However, Chianese et al. [Chi96] assumed that no agglomeration took place.
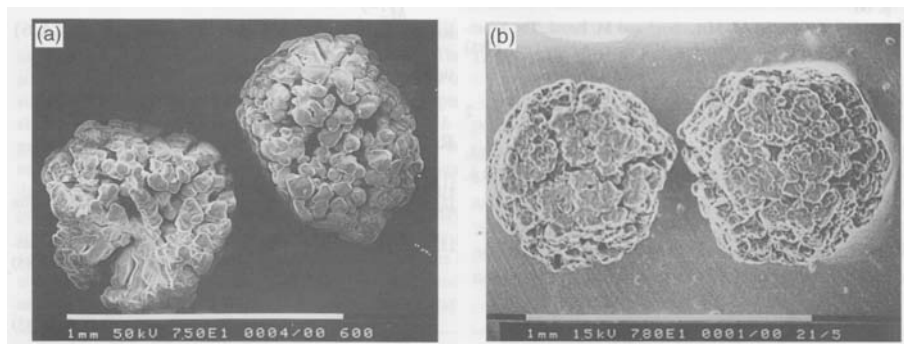

Figure 10-6: Ammonium chloride crystals: (a) pure solution, (b) with 150 ppm Mn^{2+} [Chi96]

10.1.3   Experimental Data

After the initial screening of the experimental conditions it was decided to use 250 ppm $MnCl_2$ (sat. S.) as an additive concentration. At a lower concentration, sincere breakage was induced due to needle like particles. At a higher concentration, the growth rate became too low and the transparent layer that formed around the seed crystals and/or agglomerates could only be detected by optical microscopy but not with the 3D-ORM. In comparison, the use of a concentration of 250 ppm $MnCl_2$ (sat. S.) resulted in ideal to measure near-spherical and opaque crystals. However, as evident from figure 10-3, partial breakage of dendrites growing out of the crystal might still occur. The $MnCl_2$ concentration did not affect the solubility.

Figure 10-7 shows 3 experimental temperature profiles as well as seed size and mass that were calculated using model-based experimental design.
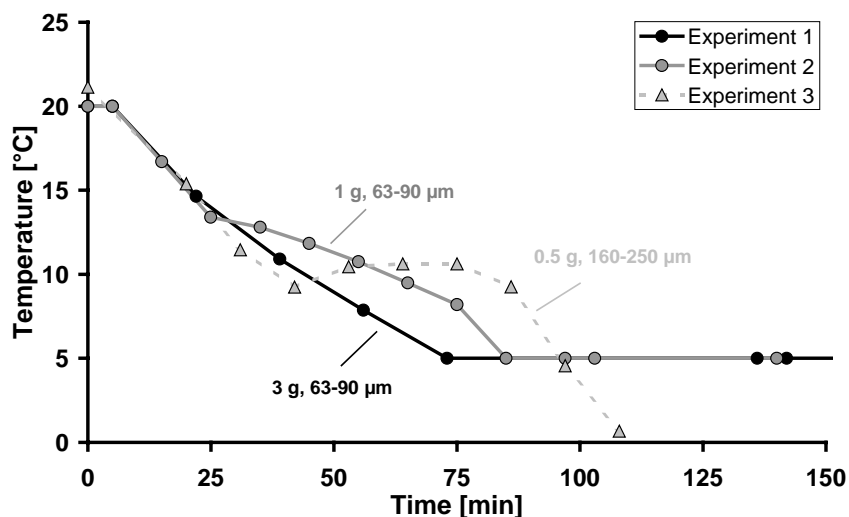

Figure 10-7: Temperature profiles of the thermostat as well as seed size and mass used for the kinetic experiments, all experiments were calculated using model-based experimental design (solid line: no heat transfer is considered, dashed line: heat transfer is considered)

As described in chapter 9, the calculated temperature profile was set to the profile of the thermostat. However, within experiment 3, the determined heat transfer coefficient was used to compensate for the temperature difference between the thermostat and the batch reactor. In other words, the temperature profile was chosen in such a way that the temperature in the reactor was equal to the calculated profile.

Figure 10-8 shows the square weighted chord length distribution versus time for experiment 2. A sudden increase in size is followed by a relatively low dynamic crystallization process as discussed within the previous chapter.
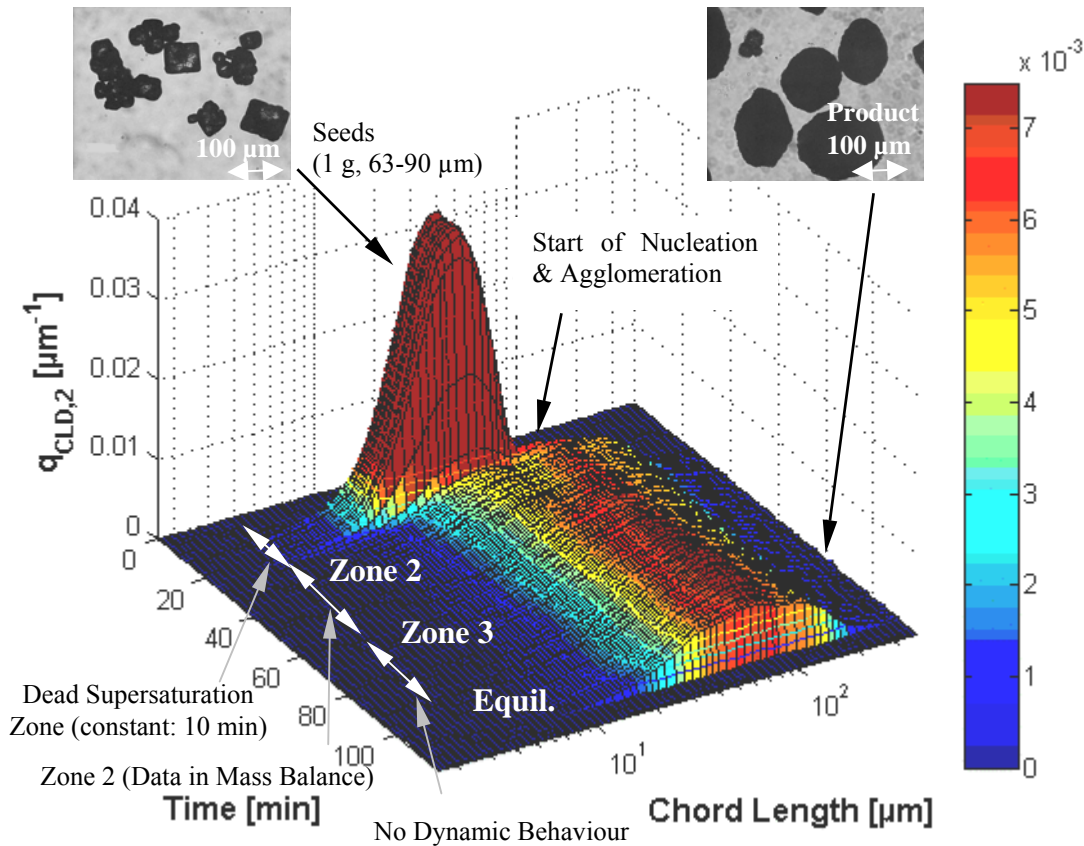
Figure 10-8: Development of the square weighted chord length distribution during the crystallization of ammonium chloride (experiment 2, see figure 10-7)

10.1.4 Results and Discussion

The effect of Mn^{2+} on the kinetics was studied by Chianese et al. [Chi96] and Wang et al. [Wan96] using a MSMPR crystallizer, however, neglecting any agglomeration. Chianese et al. [Chi96] used an additive concentration of 150 ppm Mn^{2+}, however, providing only information about the nucleation and growth rate, without any rate constants. Only the relation between the nucleation and growth order was determined to b/g = 10.9 [Chi96]. Wang et al. [Wan96] derived equations 10.1 and 10.2, valid for 7 °C (Δc [mol/L] = 0-0.5, m_T [kg/L], B [#/(s·L)], G [m/s]).

$$B = 1.32 \cdot 10^{11} \cdot G^{0.85} \cdot \left(m_T\right)^{0.04-0.2}$$

(**10.1**)

$$G = 8.72 \cdot 10^{-8} \cdot \Delta c$$

(**10.2**)

However, Wang et al. [Wan96] provided no information on the actual additive concentration of Mn^{2+}. In order to compare the results obtained within this work to the described literature data, all experiments were evaluated two times, using different assumptions. All grey data points within figures 10-9 and 10-10 were derived by neglecting any agglomeration, whereas

all black data points were derived by considering agglomeration. To extract kinetics from the experimental data the "differential approach" as described in detail in chapters 3 and 9 was used. All data were treated according to the procedure and work process discussed in detail in chapters 8 and 9. The few remaining data points satisfy the mass balance. The value of $k_{optical}$ lay between 9.5 and 30; whereas the suspension densities in zone two were between 10 and 30 kg/m^3_{Susp}. Figure 10-9 shows the result for the nucleation rate.

$$B_{PSD} = \frac{\Delta m_{v,PSD,0}}{\Delta t} + \frac{1}{2} \cdot \beta_0 \cdot \left(\overline{m}_{v,PSD,0}\right)^2$$

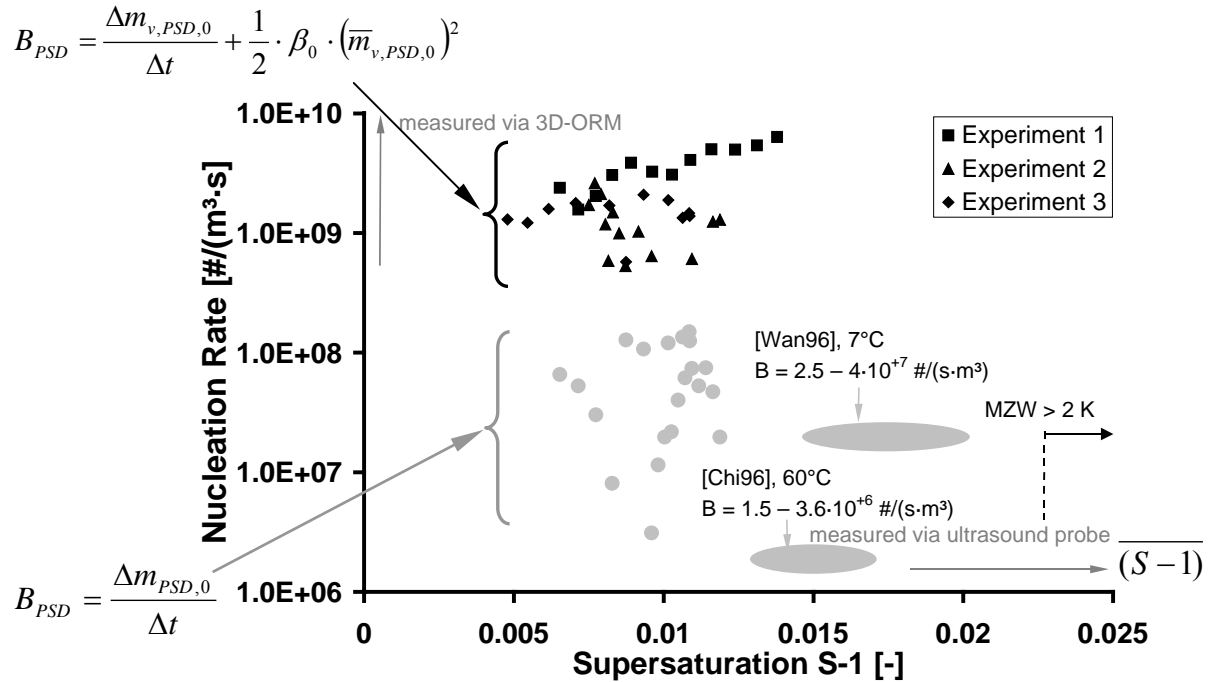$$B_{PSD} = \frac{\Delta m_{PSD,0}}{\Delta t}$$

Figure 10-9: Comparison between nucleation rates of ammonium chloride determined from experimental data using a "differential approach" and literature data

Assuming no agglomeration for the NH_4Cl-$MnCl_2$-water system comparable results to Chianese et al. [Chi96] and Wang et al. [Wan96] are obtained. By considering agglomeration during the evaluation, the nucleation rate increased by 1 to 2 orders of magnitude. The "true" nucleation rate is even higher, since particles were only recorded from a size of 1.56 μm onwards. Chianese et al. [Chi96] mentioned difficulties in measuring the small supersaturation value. Therefore, an estimation being half of the metastable zone width (S-1) = 0.018 was used, instead. Metastable zone widths are reported in the range of 2-4 K depending on the additive concentration [Chi96], similar to the values found within this work (1-3 K, 2 K = (S-1) = 0.022).

Figure 10-10 shows the determined growth rates. Depending on the method of evaluation, the growth rate is characterised as a change in length or as a change in volume. The evaluation using the equation $dL/dt = G_{PSD,1}$ neglects any agglomeration. In other words, the agglomeration of two particles is treated as a growth process. By doing so, the determined growth rate is higher than "reality".

$$\frac{dL}{dt} = G_{PSD,1} = \frac{\Delta m_{PSD,1}}{\overline{m}_{PSD,0} \cdot \Delta t}$$

$$\frac{dV}{dt} = G_{v,PSD} = \frac{\Delta m_{v,PSD,1}}{\overline{m}_{v,PSD,0} \cdot \Delta t}$$
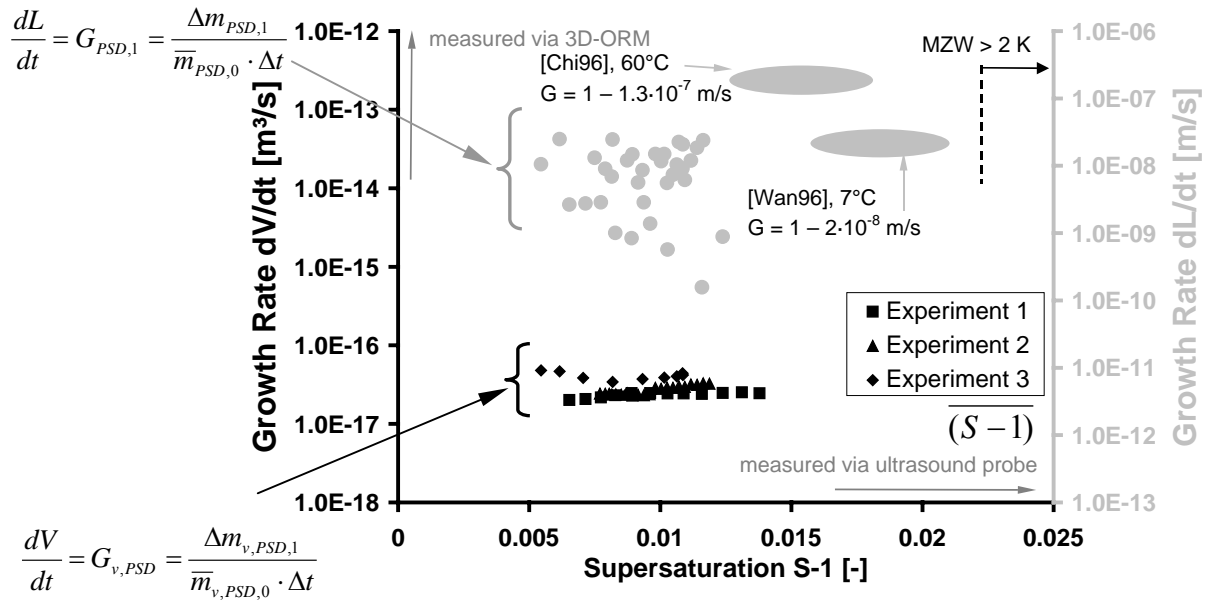
Figure 10-10: Comparison between crystal growth rates of ammonium chloride determined from experimental data using a "differential approach" and literature data

The results obtained by neglecting agglomeration compare well to data from the literature. Only the determined supersaturation value is, again, slightly shifted to the left. The low volume based growth rate confirms that the steep increase in size, observed during the experiment, can only be caused by agglomeration. The extent of agglomeration is quantified via the size-independent agglomeration kernel that is plotted versus the supersaturation in figure 10-11.
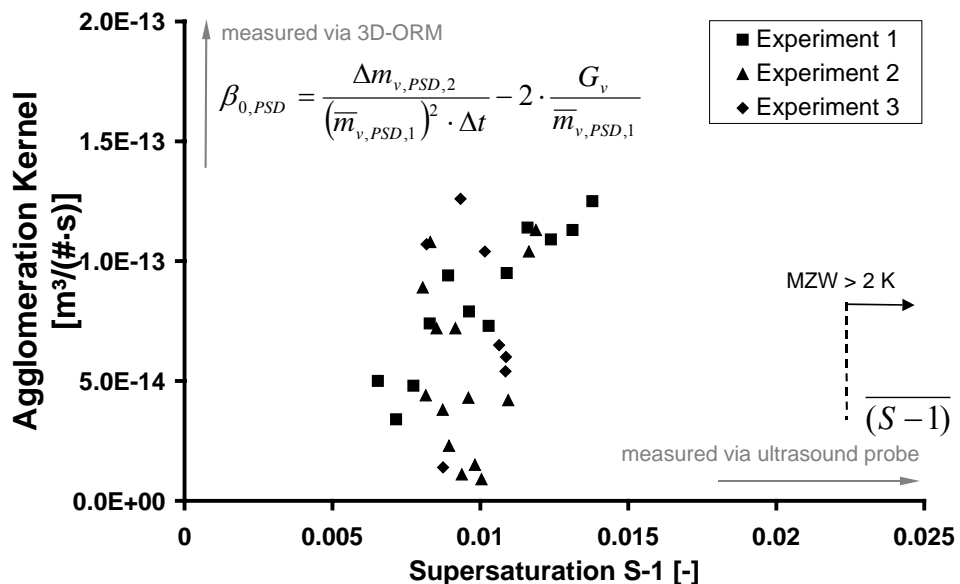

Figure 10-11: Size-independent agglomeration kernel of ammonium chloride determined from experimental data using a "differential approach"

The values of the agglomeration kernel are similar to $CaSO_4$ hemihydrate [Mou96] and $BaCO_3$ [Che03].

In total, nine kinetic experiments using the model-based experimental design strategy were designed and performed. However, only three of them could actually be used for the determination of the kinetics. On the one hand, the supersaturation was very small (referring to a temperature difference of 1 K) making it prone to experimental errors. On the other hand, encrustation formed fast on the ultrasound probe (most sincere of all case studies). Because of fast crystallization and the small dynamic measurement window, only a small "time interval" (zone two) remained for kinetic analysis (see chapter 8). As a consequence of the large scattering, a correlation of the determined kinetic data was not made. However, the results provide a reasonable order of magnitude of the underlying rate coefficients.

In the literature it is not unusual to intentionally model the crystallization process with nucleation and growth kinetics, only, even agglomeration plays a role (see for example Togkalidou et al. [Tog04]). This assumption leads generally to large confidence intervals since the model does not capture all important kinetic effects. A parameter estimation of nucleation and growth rate constants, neglecting agglomeration, using the data described above, was made by Elter [Elt07]. This allowed calculating the next experiment using model-based experimental design, although not strictly valid. A typical confidence interval of the nucleation order "b" was 1.29 ± 1.59 whereas for the growth rate order "g" values in the range of 1.27 ± 0.71 were obtained [Elt07].

Although the suspension density has a strong influence on the chord length distribution and although the determination of the crystallization kinetics remained difficult within this work, NH_4Cl seem to be an ideal model system. NH_4Cl shows good back scattering properties and different kinetic phenomena can be studied by employing an additive. The measurements can be improved by employing a laser scanner with a lower detection size limit and a faster laser speed. Due to the fast crystallization process, the actual measurement interval becomes important.

10.2 Ascorbic Acid

10.2.1 Experimental Data and Model Predictions

Ascorbic acid is also known under the name vitamin C. It is an optically active (chiral) substance. It oxidises within aqueous solution, turning the colourless solution into yellow after 1 to 2 days (see also Halász et al. [Hal93]). The first set of experiments was made with a saturated solution at 20 °C that was cooled down to 5 °C. Due to a long induction time and the fact that the 3D-ORM stopped working by being exposed to 5 °C for a longer period, the initial temperature of all ascorbic acid experiments was increased to 40 or 50 °C. Figure 10-12 shows the temperature profiles as well as seed size and mass for five experiments that were used to estimate the kinetic constants of ascorbic acid. During the first experiments using model-based experimental design, it was noticed that within the time frame of the experiment, the crystallization mainly took place after the final temperature was reached. Therefore, it was decided to perform three additional experiments by cooling down the solution starting from 40 or 50 °C as fast as possible (dashed line). The experiment three, four and five can therefore be characterised as "between" a classical desupersaturation experiment for the growth rate measurement and a classical experiment for measuring induction times [Gar02]. To ease the illustration of the different profiles, the abscissa is scaled to 150 minutes.
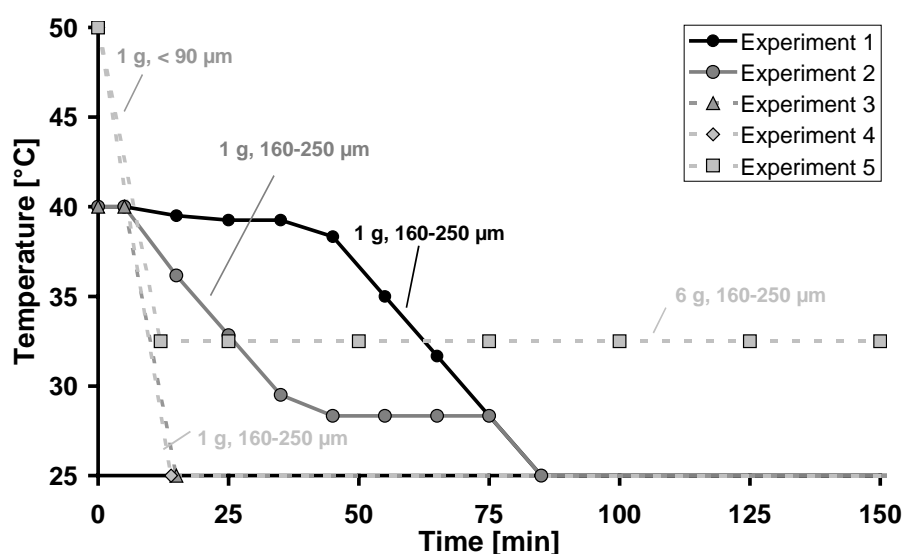

Figure 10-12: Temperature profiles of the thermostat as well as seed size and mass used for the kinetic experiments (solid line: conditions are calculated using model-based experimental design, dashed line: conditions are based on engineering judgment, experiment 3 starts at 40 °C, experiment 4 at 50 °C)

The experimental data and model predictions are exemplary discussed for experiment two (figures 10-13 and 10-14). For additional data it is referred to the appendix (chapter A.8). From figure 10-13 it can be seen, as intended, the seed crystal surface is not enough to prevent nucleation. The overall particle size remained nearly constant throughout the experimental run since nucleation dominated the process. Considering all experiments, it can

be observed that the maximum of the nucleation rate versus time appears always later than the maximum of the supersaturation versus time and growth rate versus time. This indicates that the nucleation rate is not only determined by the supersaturation. The entire experiment can be split in four characteristic zones as already described in chapter 8.3.1. Zone zero is characterised by the time interval between the start of the experiment up to the time point where seed crystals were added. Recorded measurements in zone one and three were disregarded since the experimental data were not in line with the mass balance. It becomes evident that only a small part (zone two) of the entire data is used for the estimation of the kinetic constants. During the subsequent modelling, the start of zone two was set equal to the initial time $(t = 0)$.

A comparison between experiment and simulation is given in figure 10-14. The values that are incorporated in the objective function (moments and concentration) are described very well. Nevertheless, also the mean particle size $L_{PSD,[1,0]}$, $L_{PSD,[3,2]}$ and the CV-value can be regarded as a good fit by looking at the scale of the ordinate. By evaluating all data sets (see also appendix (chapter A.8)) it can be seen that the CV ($Q_{PSD,0}$) value predicted by the model is always larger than the experimental measured one. One possible, out of multiple reasons, might be that larger crystals at the upper end of the distribution are not well detected.
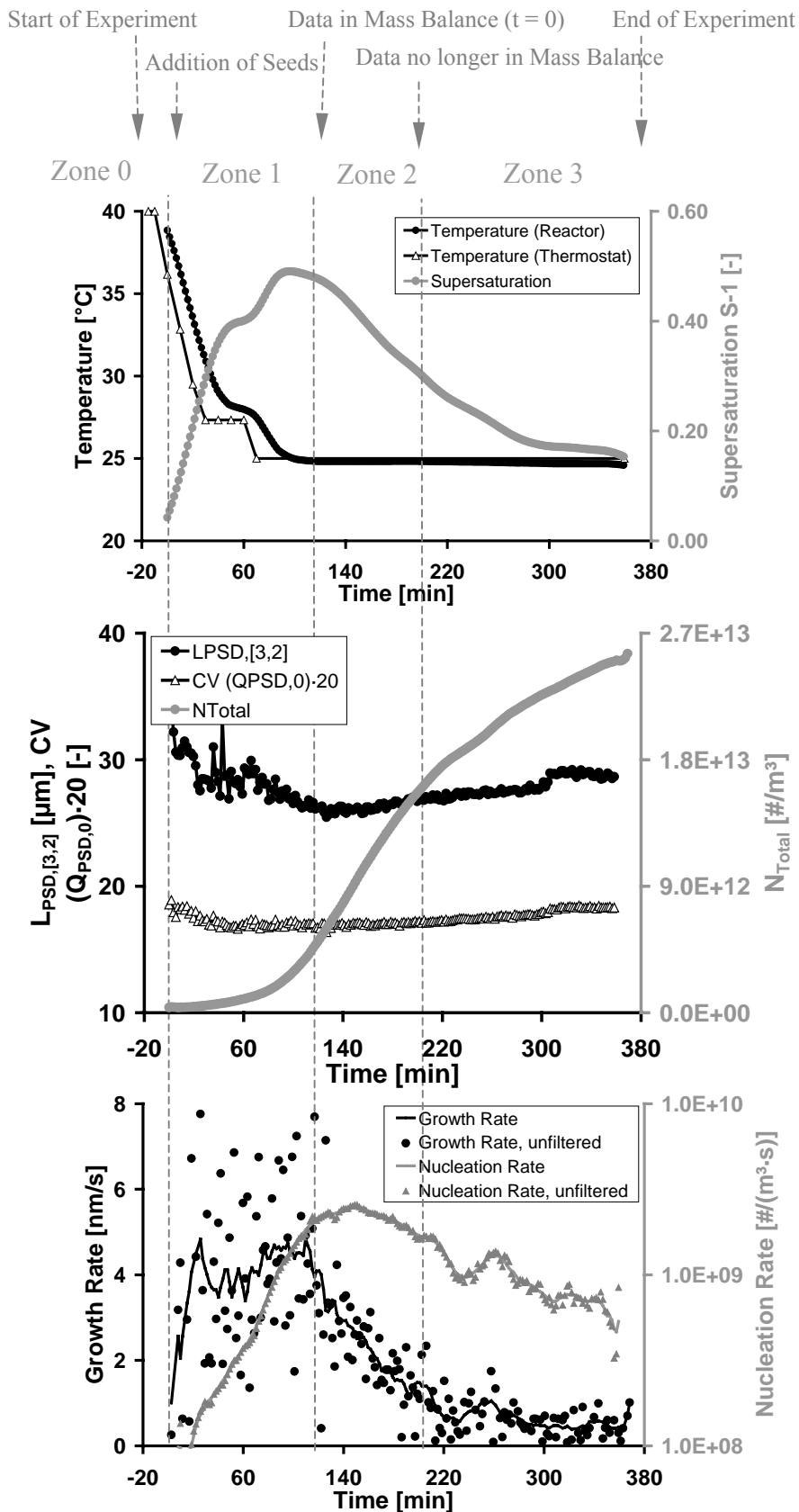
Figure 10-13: Experimental data and calculated parameters for the crystallization of ascorbic acid (experiment 2, zone 2: from 120 to 200 min)
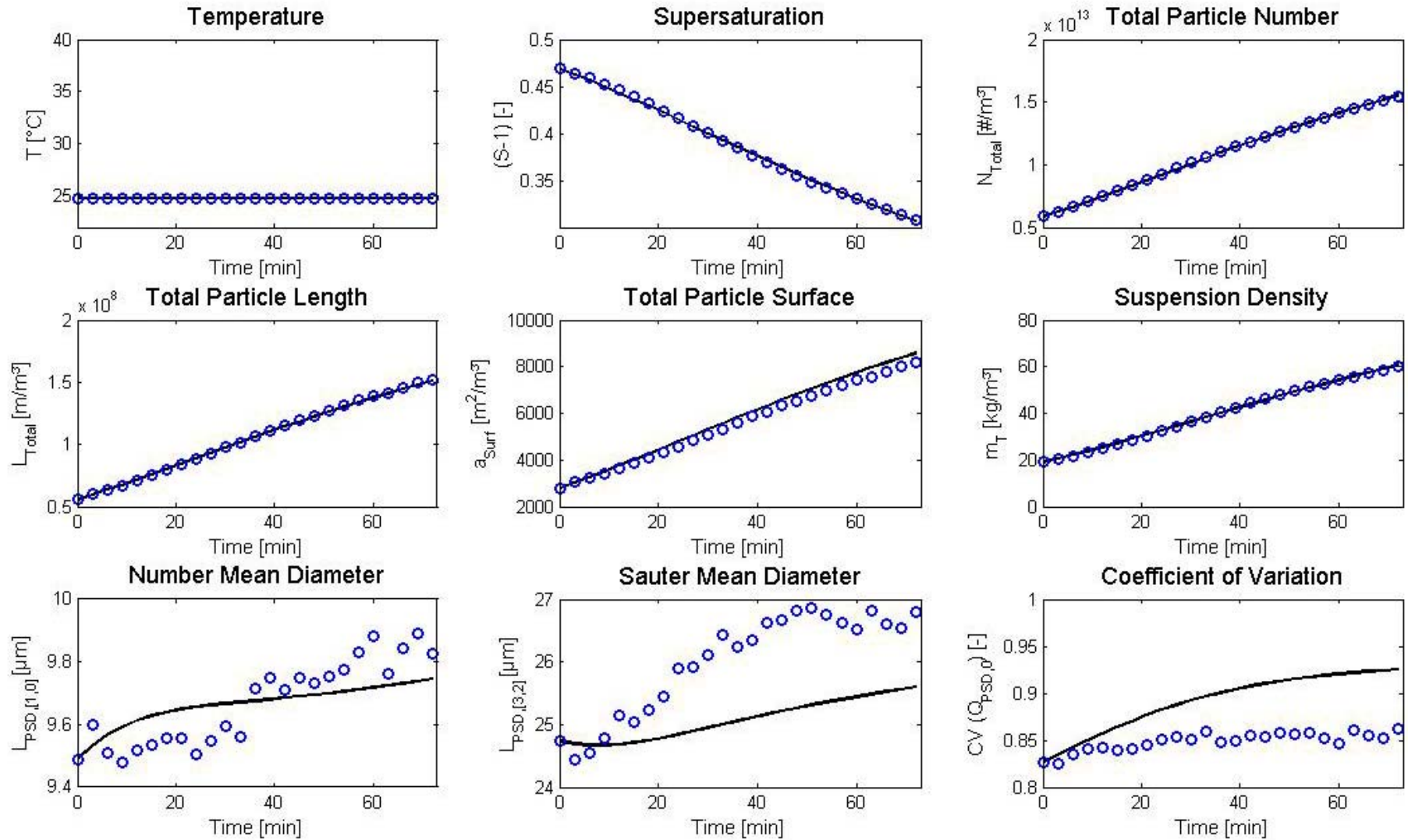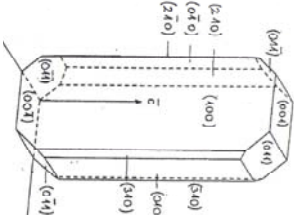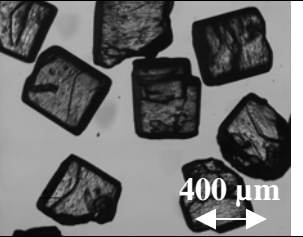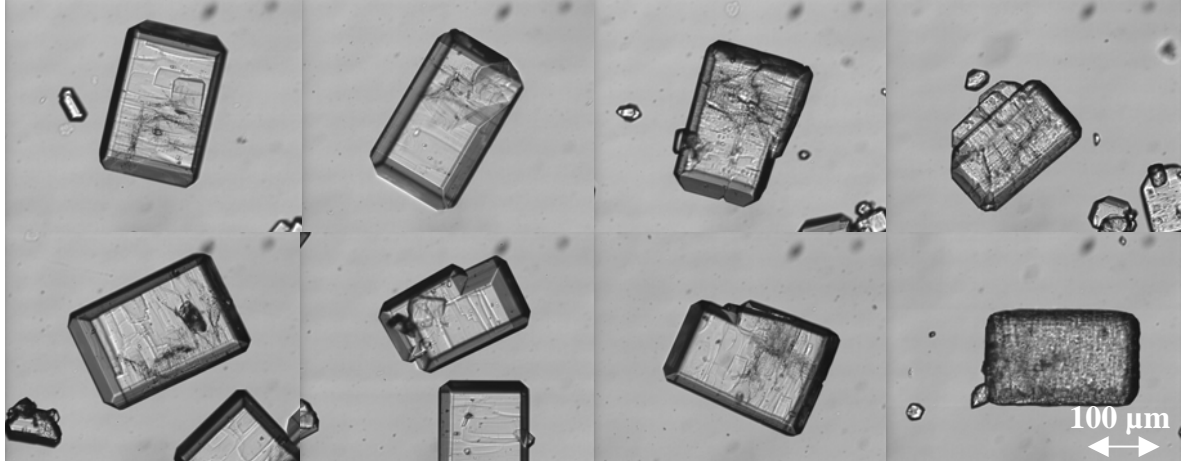
Figure 10-14: Comparison between experimental data (circles) and simulation (line) (experiment 2, zone 2: 80 min, every third measurement point)

Table 10-1: Morphologies of ascorbic acid

Literature (Crystal Faces)[Bod95]	Modelled Shape	Crystals used for Calibration/ Seed Crystals
Experimental Observed Morphologies		

10.2.2   Results and Discussion

In the literature mainly nucleation and growth kinetics of ascorbic acid are discussed. Only Schirg et al. [Sch01] and Wierzbowska et al. [Wie08] observed agglomeration of small ascorbic acid crystals (< 5 μm). The crystallization of ascorbic acid was investigated by Halász et al. [Hal93] and Bodor et al. [Bod93] using ultrasound irradiation. The nucleation order b was determined and an order of magnitude of the respective growth rate was estimated. Later, Bodor et al. [Bod99] extracted the kinetics from batch experiments using a population balance model. Unfortunately, not all values of the determined parameters are provided. Matynia et al. [Mat99] studied the nucleation of ascorbic acid using metastable zone width measurements. Whereas, Omar [Oma06b] investigated the growth rate, using desupersaturation experiments. Recently, Wierzbowska et al. [Wie08] studied the crystallization of ascorbic acid using a draft tube MSMPR crystallizer. Equation 10.3, valid for 20 °C (B [#/(m³·s)] = 0.2-2.4·10^{+8}, G [m/s] = 1.8-7.1·10^{-8}, m$_T$ [kg/m³$_{Susp}$] = 31 - 418), was derived,

$$B = 2.64 \cdot 10^{14} \cdot G^{1.2} \cdot \left(m_T\right)^{0.99} \qquad\qquad\qquad \textbf{(10.3)}$$

however, no supersaturation data was provided. The actual number of publications providing rate constants (k$_b$, b, k$_g$, g) for the ascorbic acid – water system remains rather low. Figure 10-15 summarises data from literature compared to those obtained within this work:
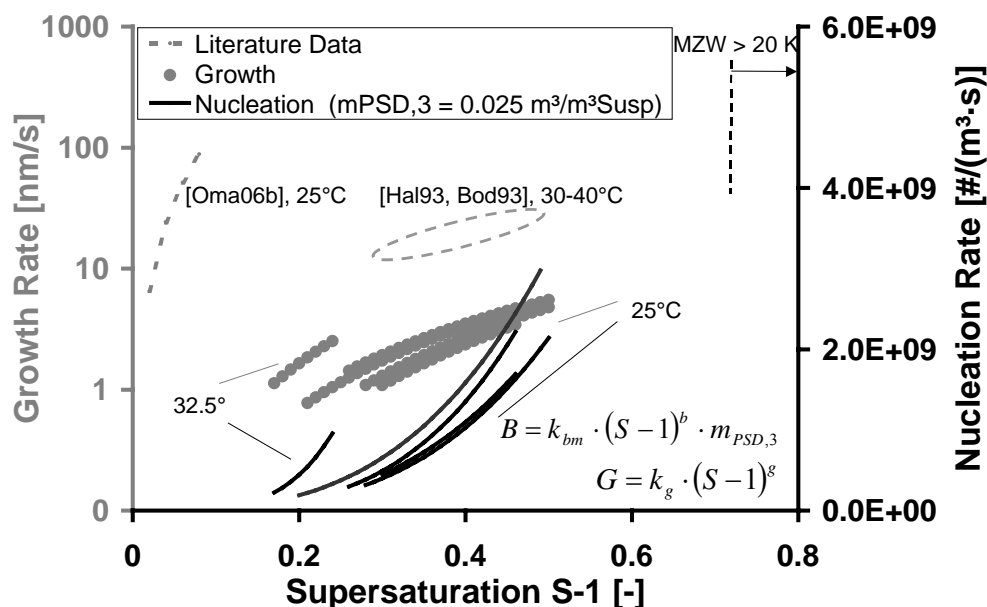

Figure 10-15: Comparison between nucleation and growth kinetics of ascorbic acid determined within this work (nucleation: black lines, growth: grey dots) and literature (grey dashed lines)

The metastable zone width for primary heterogeneous nucleation was determined to be 20 K ((S-1) = 0.75), in chapter 8.1. In the literature, the metastable zone width varies within a wide

range from 5 to 50 K depending on the specific process conditions [Hal93, Mat99, Oma06a, Wie07]. A review of literature revealed a large scattering in solubility data among different authors (see appendix, chapter A.1). A visible clear solution can conveniently be cooled down from 40 to 25 °C without nucleation taking place [Hal93]. Consequently, long induction times are generally observed within literature [Hal93] as within this work. The addition of seeds to a highly supersaturated solution did not lead to an immediate nucleation burst. During the actual experiment the nucleation rate was determined to be in the order of secondary nucleation. The crystal quality ranged from "unhurt" to "hurt" plate-like crystals (see table 10-1). Similar results are reported within literature. Bodor et al. [Bod99] and Wierzbowska et al. [Wie08] concluded that secondary nucleation was important, since often crystals of low morphological quality and multi-peak distributions were obtained. This is mirrored by the nucleation rate model. It was noticed that the model predictions were only satisfactory if the second moment $m_{PSD,2}$ (surface area) or the third moment $m_{PSD,3}$ (suspension density) was included into the rate equation. Schirg et al. [Sch01] concluded from their experiments that secondary nucleation of ascorbic acid is mainly driven by supersaturation and not by attrition or breakage of larger particles.

The growth rate was determined to be in the range of "integration controlled" that is also indicated by the high growth rate order (see table 10-2). It explains the low rate of desupersaturation after the addition of seeds, resulting in batch times between 150 and 550 minutes that have also been observed within literature [Bod93, Bod99, Sch01]. The lower growth rate, compared to Halász et al. [Hal93] and Bodor et al. [Bod93] can be partly attributed to the dependence of the 3D-ORM on the suspension density (see chapter 8.2.2). The results given by Omar [Oma06b] are not in agreement. Omar [Oma06b] measured growth kinetics using the method of desupersaturation curves. The time of desupersaturation was only in the order of 30 minutes at 25 °C. A fast growth rate was consequently calculated. The differences described between different authors and the data derived within this work must be discussed on the background of chapter 4.3.

All determined kinetic rate constants, valid for the supersaturation range given in figure 10-15, are summarised in table 10-2.

Table 10-2: Determined kinetic rate constants for ascorbic acid (95% confidence region, χ^2 - distribution), optical factor applied to close the mass balance, suspension density range of zone two

No. of Exp.	b [-]	$\ln(k_b\ [\#/(m^3{\cdot}s)])$	g [-]	$\ln(k_g\ [m/s])$	$k_{optical}$ [-]	$m_T\ [kg/m^3_{Susp}]$
1	3.29±0.037	27.45±0.031	2.55±0.038	-17.35±0.032	130	10-60
2	3.10±0.076	27.34±0.068	2.69±0.086	-17.39±0.078	125	15-60
3	3.17±0.061	27.70±0.054	2.26±0.022	-17.44±0.020	115	20-100
4	4.21±0.078	30.27±0.112	2.33±0.155	-16.46±0.227	105	10-45
5*	3.52±0.078	27.94±0.074	2.07±0.040	-17.57±0.339	72	20-80

*values valid for 32.5 °C, all other data is valid for 25°C

Although a calibration of the 3D-ORM data (see chapter 8) was only made up to 55 kg/m³$_{Susp}$, it was noticed during the experiment that the mass balance could be closed up to suspension

densities of 100 kg/m³_Susp. The "newly" introduced "optical factor", although theoretically constant, varies between the individual experiments. On the one hand, the scanning depth T, as shown by Ruf et al. [Ruf00], depends on the actual particle size distribution measured. On the other hand, errors within the supersaturation measurement or changes within particle shape can contribute to variations within the absolute value. Further research in understanding the measurement of laser scanners is necessary (see chapter 11).

Values for b have been determined to be 2.43 [Hal93] or 5.88 [Bod99] for primary and 1.93 [Hal93] or 7.1 [Bod99] for secondary nucleation. Values for g have been determined to be 0.72 [Bod99] or 1.88 [Oma06b]. Since the confidence intervals, determined within this work, are relatively small, it can be concluded that the model captures all predominant mechanisms. During the model-based evaluation isothermal conditions prevailed (data within zone 2, only), since the crystallization of ascorbic acid started to kick in when the final temperature was reached. Experiment 1 to 4 correspond to a temperature of 25 °C, whereas experiment 5 to 32.5 °C. The influence of the temperature on the kinetic can clearly be marked in figure 10-15. From the initial four experiments that were designed using model-based experimental design, only two could be evaluated (experiment one and two). For one experiment, the mass balance could not be closed for a certain minimum number of consecutive data points (time interval of zone two was smaller 20 minutes, see chapter 8). Whereas for the other experiment the estimation of parameters did not lead to an unique result, although the experimental data could be described with the kinetic constants given in table 10-2.

In order to improve the crystallization of ascorbic acid from water, alcohols (methanol, ethanol, iso-propanol) are often added to the solution. Data on metastable zone width are reported by various authors [Mat99, Oma06a, Wie07]. Wierzbowska et al. [Wie07] determined a nucleation order of 2. It is generally found that the growth rate increases with the addition of an alcohol up to values of $G = 10^{-7}$ m/s [Che00, Oma06b]. Equations 10.4 and 10.5 were derived by Chen et al. [Che00] for the crystallization from a water-ethanol mixture within the temperature range of 20 to 43 °C (B [#/(m³·s)], G [m/s], Δc [kg/m³] = 2-67 ((S-1) ≈ 0 – 0.2), $N_{Stirrer}$ [1/s] = 550 - 720, m_T [kg/m³] = 129 - 457, T [K], R_{uni} [J/(mol·K)])

$$B = 7.2 \cdot 10^7 \cdot e^{\left(-\frac{33000}{R_{uni} \cdot T}\right)} \cdot \left(N_{Stirrer}\right)^{1.5} \cdot \Delta c^{0.85} \cdot \left(m_T\right)^{1.85} \approx 2 - 4 \cdot 10^9 \ \#/(m^3 \cdot s) \qquad (\ 10.4\ )$$

$$G = 0.44 \cdot e^{\left(-\frac{52000}{R_{uni} \cdot T}\right)} \cdot \Delta c^{1.4} \approx 1 \cdot 10^{-8} - 4 \cdot 10^{-7} \ m/s \qquad (\ 10.5\ )$$

The determined activation energies are 33 kJ/mol and 52 kJ/mol for nucleation and growth, respectively.

10.2.3   Short-cut Method for Determining Kinetics

10.2.3.1   Nucleation

Within this work emphasis was placed on the pre-processing of laser scanner data. The objective was thereby to convert the instrument recordings characterised by the "counts" (counts [#/s]) and CLD (n_{CLD} [#/(s·m)]) to the respective format needed for population balance modelling (total number of particles (N_{Total} [#/m³]) and PSD (n_{PSD} [#/(m·m³)])). To circumvent the ill-posed problem of reconstructing the PSD from the CLD three alternative ways can be defined:

I.   Using only moments to model the crystallization behaviour (see chapter 5.3.2)

II.   Transforming the predicted PSD given by the population balance model into a CLD, instead of reconstructing the PSD from its measured CLD (so called forward calculation). Consequently, the objective function to determine the kinetics minimises the differences between the measured and predicted CLD instead of the respective PSD

III.   Treating the CLD as it would be a PSD. In other words, the CLD is used without any pre-treatment of the measured data or changes in the population balance model ("short-cut method").

Figure 10-16 illustrates the described relation between instrument recordings and the input format for population balance modelling.
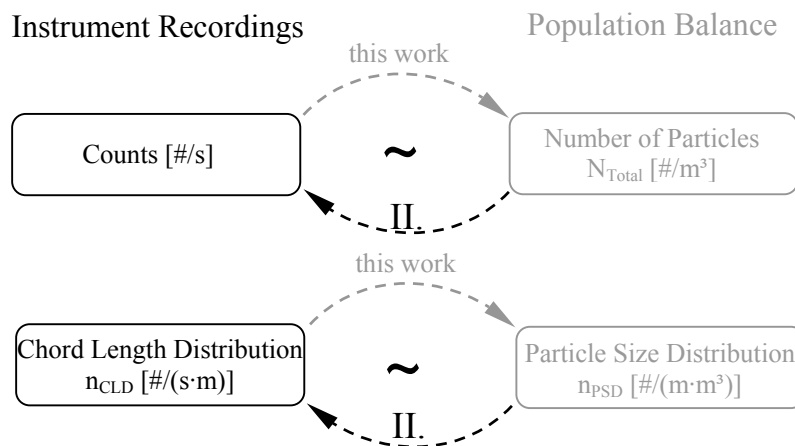

Figure 10-16: Illustration of the relation between instrument recordings and the input format for population balance modelling

The short-cut method, described by Roman numeral III has become popular [Tog04, Hea06, Mén06, Dan07, Tri08] since for the reconstruction of the PSD advanced mathematical methods are necessary. It allows a fast way of evaluating any recorded data. The chapter tries to elucidate how the direct use of the CLD influences the determined kinetics compared to the use of the respective PSD.

Using the experimental data from chapter 10.2.1 (experiment 2), figure 10-17 compares the raw measured and corrected "counts" with the total number of particles (N_{Total}). As described in detail in chapter 8.3.1, the total number of particles is related to the minus first moment of the CLD and is not the "counts" given by the instrument.
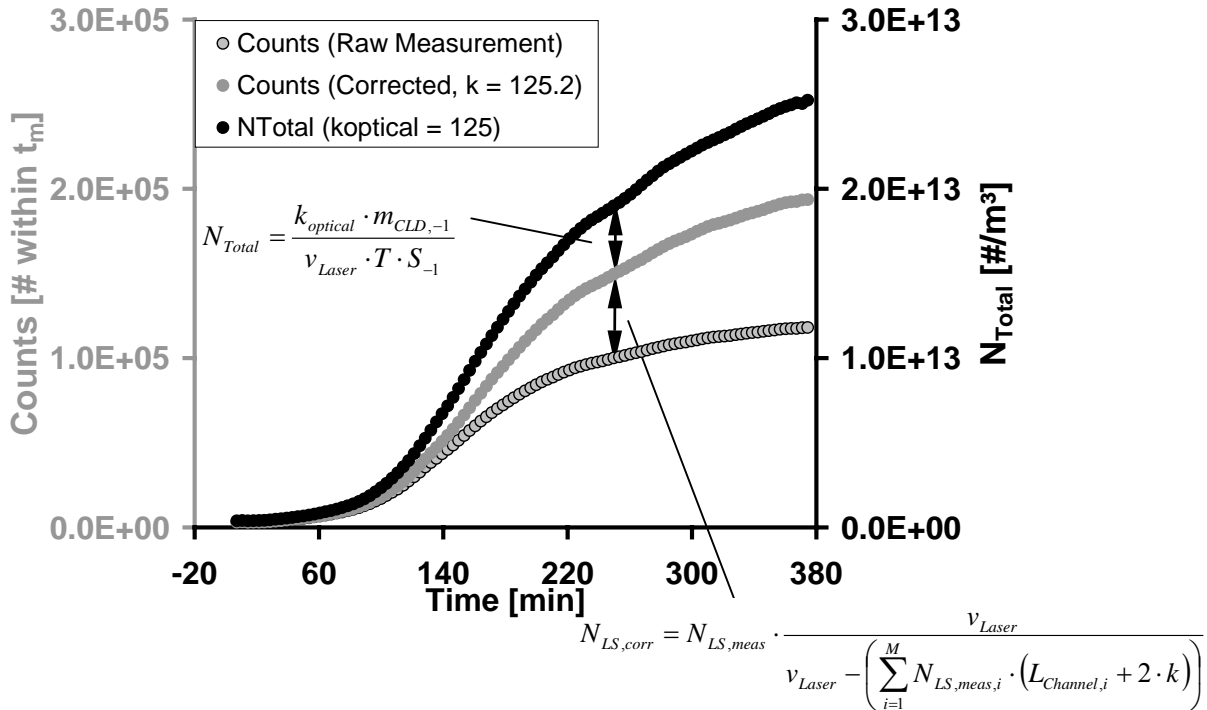

Figure 10-17: The effect of equation 8.4 and equation 8.11 (chapter 8) on the recorded "counts"

Figure 10-17 illustrates that the mathematical "treatments" via equation 8.4 (using a dead length k, chapter 8.2.1) and equation 8.11 (using $k_{optical}$, chapter 8.3.1) applied within this work, do not influence the overall qualitative profile. However, the absolute values of each curve are different.

From the data presented in figure 10-17, the "rate of counts" or nucleation rate can easily be calculated. The "rate of counts" is thereby based on "counts within the measurement interval t_m [#/s]" whereas the nucleation rate is based on a volume ([#/(m³·s)]). The results are shown in figure 10-18. Again, all three curves show a similar qualitative behaviour.
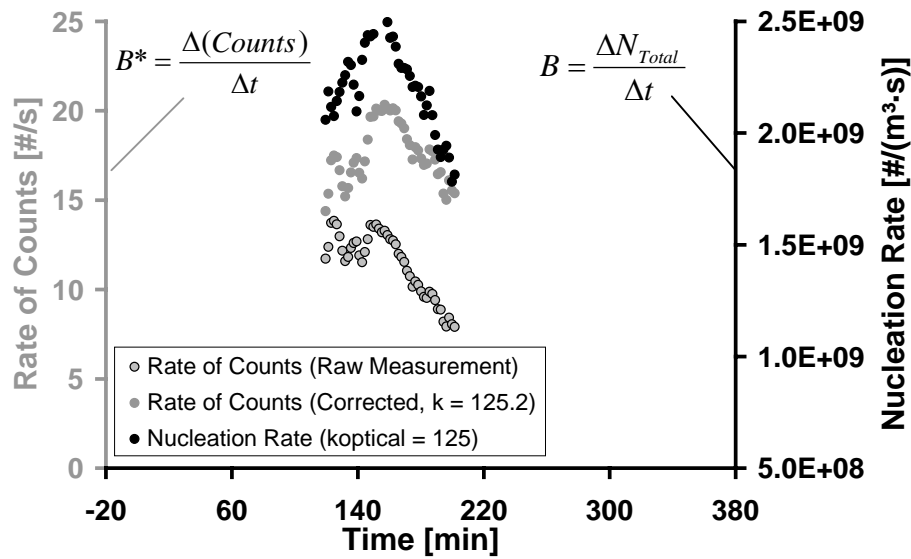
Figure 10-18: Comparison between the "rate of counts" (chord length distribution) and nucleation rate (particle size distribution), data from zone 2, only

If only qualitative information about the nucleation behaviour is important, the short-cut method delivers adequate results. However, if the actual nucleation rate must be determined, the direct use of the instrument recordings fails. The laser scanner instrument only provides information about counts per second, whereas the nucleation rate is based on a volume. According to chapter 8.3.1, the order of magnitude of the scanned volume lies in the range of $5 \cdot 10^{-9} - 5 \cdot 10^{-7}$ m³ per second. A value of $1.6 \cdot 10^{-8}$ m³ was determined by Méndez del Rio et al. [Mén06]. As a first approach, these values can be used to convert the "rate of counts" to a more meaningful value. Other authors simply use the mass of solvent of the entire crystallizer as a base [Tog04, Tri08].

10.2.3.2   Growth

The growth rate of a crystal collective can be characterised by the change of the number mean size $L_{PSD[1,0]}$ versus time (total length of crystals/total number of crystals) [Ran88, Sha05, Dan07, Al08, Tri08]. The relation between the CLD and PSD was described in detail in chapter 5.3.2.2. Equation 10.6 relates the number mean size of the CLD ($L_{CLD[1,0]}$) to the mean particle size $L_{PSD[2,1]}$ of the PSD.

$$L_{CLD,[1,0]} = \frac{m_{CLD,1}}{m_{CLD,0}} = \frac{v_{Laser} \cdot T \cdot S_1 \cdot m_{PSD,2}}{v_{Laser} \cdot T \cdot S_0 \cdot m_{PSD,1}} = \underbrace{\frac{\pi}{4}}_{Sphere} \cdot L_{PSD,[2,1]} \qquad (10.6)$$

Figure 10-19 shows the respective mean sizes versus time. Similar to the previous chapter, no matter what mean size is plotted, the qualitative information remains essentially the same.
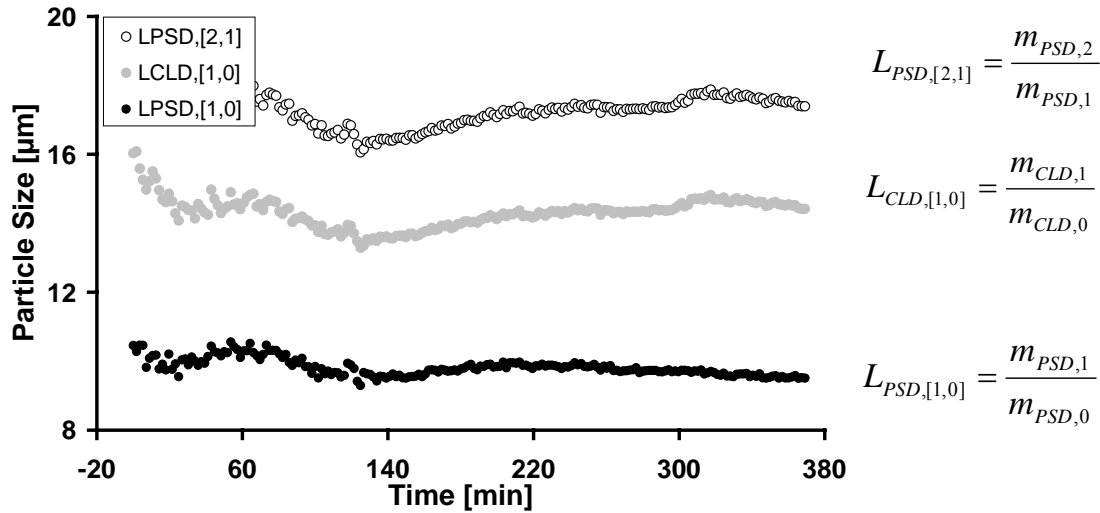
Figure 10-19: Mean particle sizes based on the chord length or particle size distribution

Using equation 3.31 (chapter 3) and equation 5.3 (chapter 5), equation 10.7 relates the growth rate calculated from the CLD to the growth rate calculated from the respective PSD.

$$\frac{dL}{dt} = G_{CLD,1} = \frac{\Delta m_{CLD,1}}{\overline{m}_{CLD,0} \cdot \Delta t} = \frac{v_{Laser} \cdot T \cdot S_1 \cdot \left(m_{PSD,2,t2} - m_{PSD,2,t1}\right)}{v_{Laser} \cdot T \cdot S_0 \cdot \left(\dfrac{m_{PSD,1,t1} + m_{PSD,1,t2}}{2}\right) \cdot \Delta t} = \frac{\pi}{4} \cdot \frac{\Delta m_{PSD,2}}{\overline{m}_{PSD,1} \cdot \Delta t} \qquad (10.7)$$

The calculated growth rates are shown in figure 10-20. Since the individual mean size data in figure 10-19 scatters, all negative size differences were neglected during the evaluation.
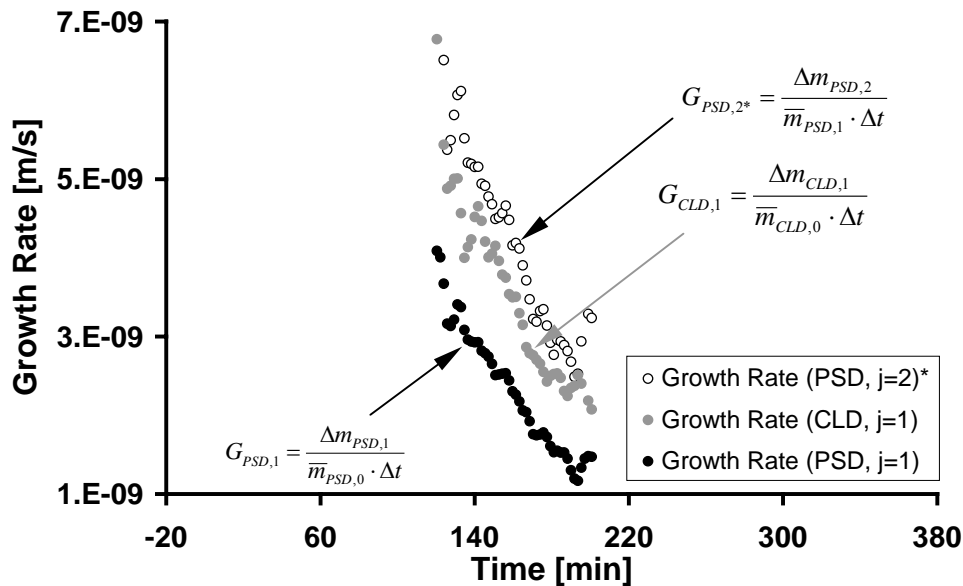

Figure 10-20: Growth rates based on the chord length or particle size distribution (data from zone 2, only)

In accordance to equation 10.7 the growth rate calculated using the CLD (grey points), is smaller than the growth rate calculated by using the first and second moment of the PSD (white points). The result validates the CLD-PSD transformation used within this work.

However, since $L_{PSD[1,0]}$ relates to $L_{CLD[0,-1]}$, the actual growth rate characterised by total length of all crystals divided by the total number of all crystals is the smallest. The difference between the growth rates calculated from the CLD and its respective PSD depends on the assumed crystal shape, the characteristic size that is defined during the deconvolution and the actual mathematical method to solve the ill-posed problem.

Overall it can be concluded that the use of the raw measured CLD leads to different rate constants (k_b, b, k_g, g) as would be obtained by using a PSD. The short-cut method remains especially suited for early stage development activities, if only optimisations or controlling of process parameters and product qualities are of interest. Conversely, if the objective is to obtain rate constants comparable to other literature data or for use within a population balance model, a deconvolution of the CLD or its moments or a translation of the predicted PSD to a CLD is necessary. The direct use of the instrument recordings, as made by several authors [Sha05, Dan07, Al08, Tri08], can be regarded as a grey-box model that "lies" in between a first-principle and black-box model. Since the deconvolution of the CLD using the current models described in chapter 5.3.2 is static, the CLD shows a similar dynamic behaviour as the reconstructed PSD [Tog04]. However, with improving first principle models for the deconvolution of the CLD (see for example Kail et al. [Kai07, Kai08]) the conclusion might have to be revisited.

10.3   α-Glycine

10.3.1   Polymorphic Transformation

At ambient temperature and pressure different polymorphs can be crystallized being α-, β- or γ-glycine. The β-form is the least stable form. It can be obtained by using water/methanol or water/ethanol solvent mixtures [Tor05]. The crystallization of glycine from an aqueous solution follows the Ostwald's "Rule of Stages". In other words, the metastable α-form crystallizes first and transforms subsequently into the stable γ-form [Par03, Dok04a, Che07b, Pro07, Yan08]. The crystallization is thereby controlled by the kinetics rather than by thermodynamics [Par03, Tor05]. The transition point is between 165 and 201 °C [Par03] (melting temperature T_m = 262 °C, $T_{Decomposition}$ = 292 °C [Ull07]). According to Chew et al. [Che07b], the growth rate of γ-glycine is 500 times slower than the respective rate of α-glycine. Therefore, it seems to be not surprising that α-glycine was discovered in 1910, whereas γ-glycine not before 1954 [Tow04, Che07b].

The solution-mediated transformation of α- to the γ-form is influenced by various factors: Sakai et al. [Sak92] found that the transformation of a wet powder of α-glycine can be accelerated at higher temperature, higher initial γ-glycine content and higher humidity. Approximately 5% of dry α-glycine crystals transformed to the γ-form within 30 days. Igarashi et al. [Iga03] studied the transformation in a batch and WWDJ (*W*all-*W*etter, *D*ouble-deck *J*acket) crystallizer. The time for the solution-mediated transformation at 30 to 40 °C was in the range of 2 to 3 days. At least 7 days were needed in a batch reactor. Doki et al. [Dok04a] investigated the effect of seed loading and supersaturation on the transformation in a batch crystallizer, operated at 40-50 °C. At a high seed loading of α-glycine (mass$_{Seed}$/mass$_{theoretical\ yield}$ = 0.33) only α-glycine crystallized within the first hour. At lower seed loadings γ-glycine crystals occurred within the course of the experiment, being 3 hours. However, no quantitative information on the actual amount of γ-glycine was reported. Louhi-Kultanen et al. [Lou06] used high intensity sonocrystallization to study the crystallization behaviour of glycine. The γ-form was always obtained as the minor form. The concentration ranged from approximately 20% at 40-50 °C down to approximately 10% at 20-30 °C. Chew et al. [Che07b] estimated the solution-mediated phase transformation to be weeks, whereas Yang et al. [Yan08] reported a time frame of 34 h at 25 °C.

Within the course of this work, the temperature range was set between 5 to 20 °C, being lower than the temperature levels of the references discussed above. Furthermore, the time frame, in particular the time where "zone two" ends (chapter 8.3.1), was for three experiments smaller 55 minutes and for one experiment smaller 150 minutes. It is therefore assumed that no significant precipitation of γ-glycine takes place. This is confirmed by using optical microscopy (see table 10-3). According to various references, α-glycine crystals are elongated and characterised by a prismatic shape [Dok04a, Tow04, Ito05, Tor05, Pro07, Yan08]. In comparison, γ-glycine crystals are often of a rounded-up to bi-pyramidal shape [Dok04a, Ito05, Che07b, Pro07, Yan08].

10.3.2   Experimental Data and Model Predictions

To narrow down the batch time, four initial experiments were made prior to the actual kinetic experiments. Figure 10-21 shows the temperature profiles as well as seed size and mass for the experiments that were used to estimate the kinetic parameters. The temperature profiles calculated via model-based experimental design (solid lines) are a balance of the maximum and minimum cooling rate set within the software. The experiments based on engineering judgment (dashed lines) are especially suited for determining the nucleation (fast initial cooling, experiment 2) and the growth rate constants (controlled cooling, experiment 1).
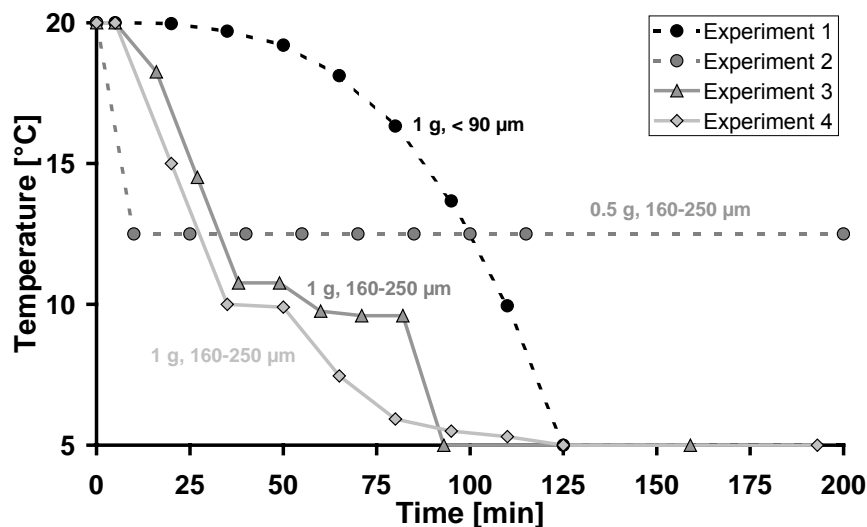

Figure 10-21: Temperature profiles of the thermostat as well as seed size and mass used for the kinetic experiments (solid line: conditions are calculated using model-based experimental design, dashed line: conditions are based on engineering judgment)

The experimental data and model predictions are exemplary discussed for experiment 4 (figures 10-22 and 10-23). For additional data it is referred to the appendix (chapter A.9).

Similar to ascorbic acid, as intended, the seed crystal surface is not enough to prevent nucleation during the experiment. The overall particle size did not change significantly throughout the experiments since nucleation dominated the process. However, in contrast to ascorbic acid, the maximum of the nucleation rate versus time "appeared" at the same time point as the maximum of the supersaturation and growth rate versus time. The entire experiment can be split in four distinct zones as already described in chapters 8.31 and 10.2.1. Zone zero is characterised by the time interval between the start of the experiment up to the time point where seed crystals were added. Recorded measurements in zone one and three were disregarded since the experimental data were not in line with the mass balance. During the subsequent modelling, the start of zone two was set equal to the initial time (t = 0). It becomes evident that only a small part of the entire experimental data set is used for estimating the kinetic constants.

From figure 10-23, that compares the experimental data and model prediction it can be seen that the supersaturation and third moment (suspension density) are always in good agreement,

since the mass balance is closed. For the first and second moment (total length and surface area), the mean particle sizes $L_{PSD,[1,0]}$, $L_{PSD,[3,2]}$ and CV ($Q_{PSD,0}$) value a systematic deviation from the model prediction is observed. Apart from experiment 1, the model predictions of the total particle length, total particle surface and mean size $L_{PSD,[1,0]}$ are larger than the respective experimental data. In contrast, the model predictions for the CV-value and Sauter diameter $L_{PSD,[3,2]}$ are, apart from experiment 1, smaller than the respective experimental values.
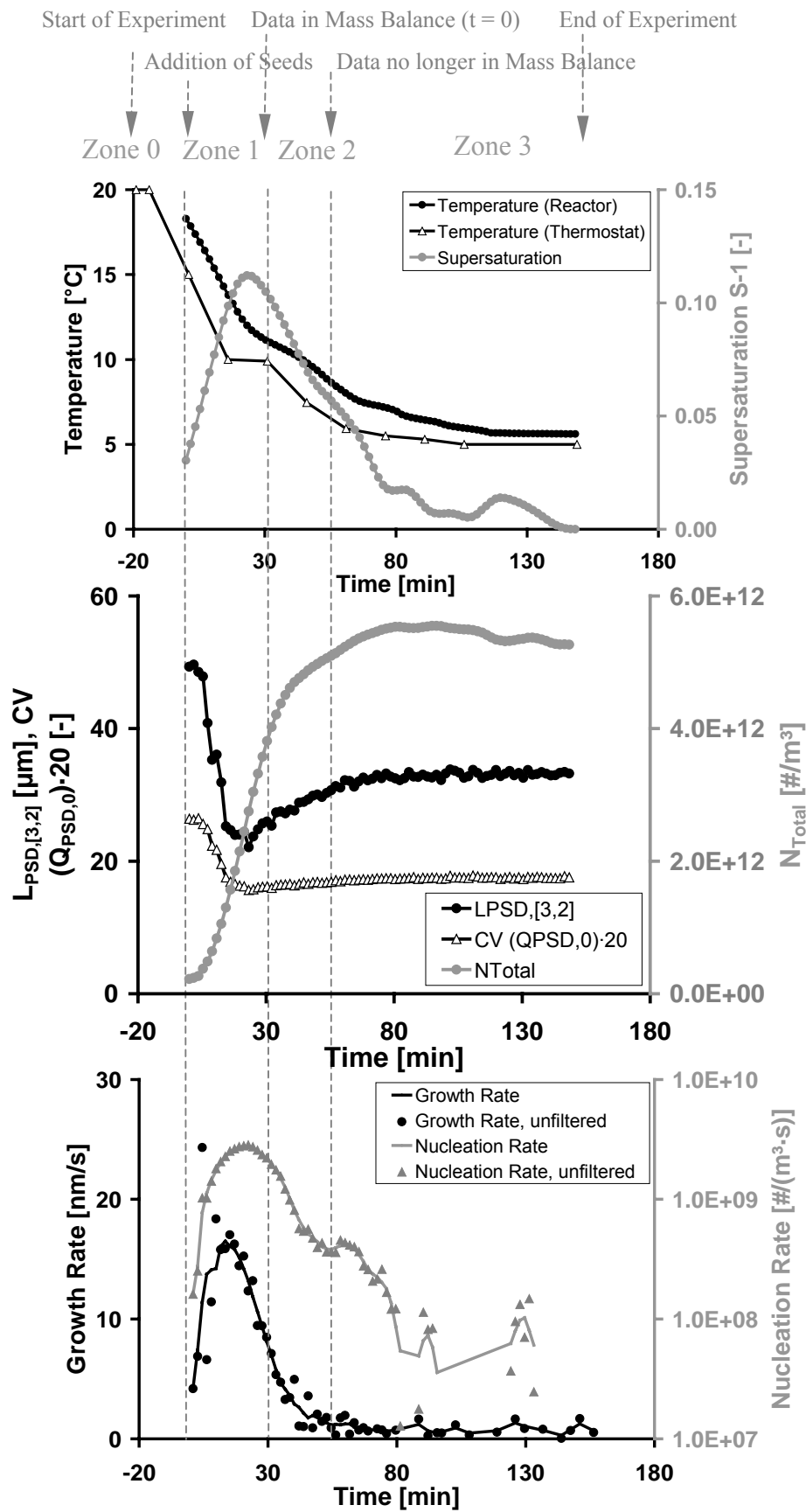
Figure 10-22: Experimental data and calculated parameters for the crystallization of α-glycine (experiment 4, zone 2: from 30 to 57 min)
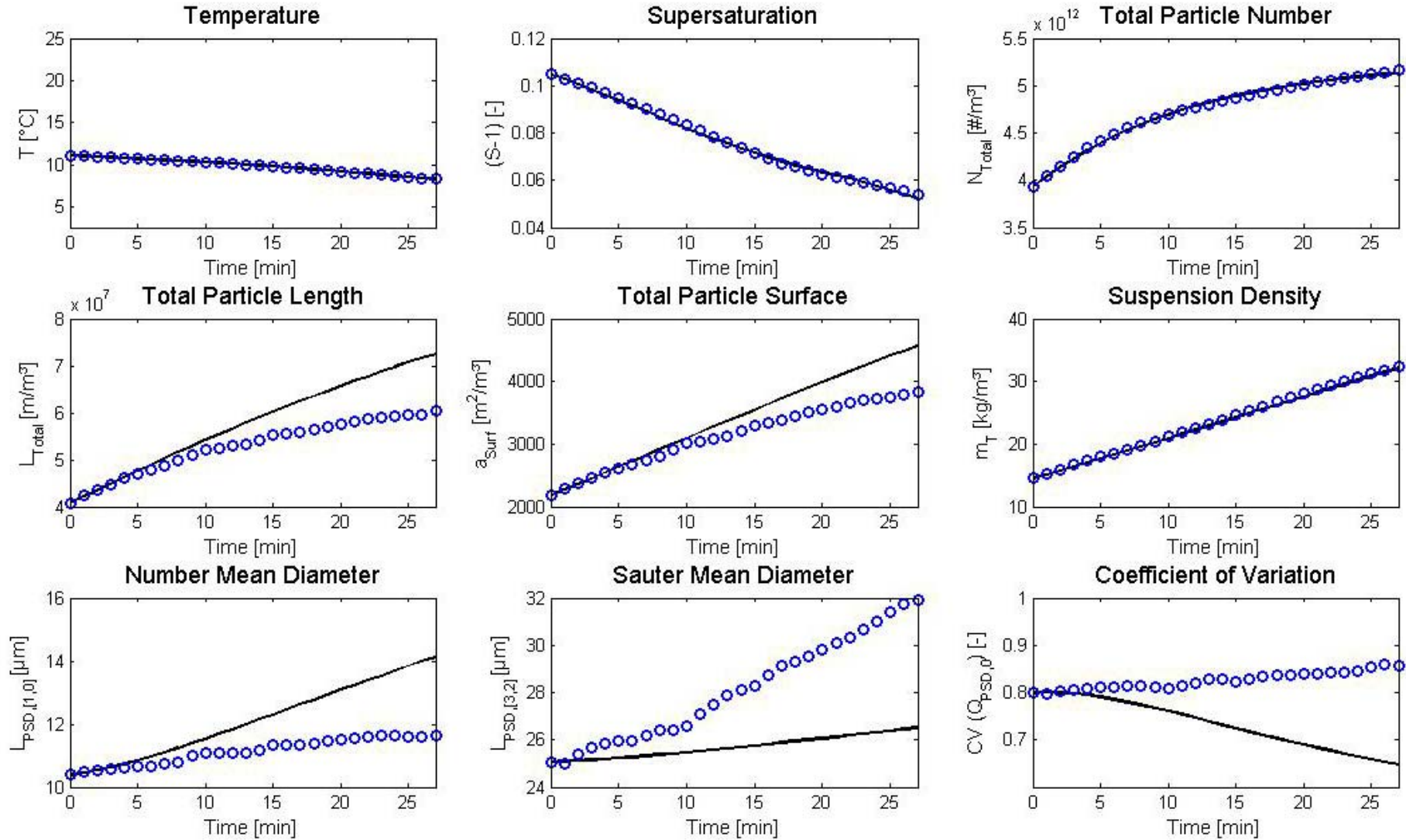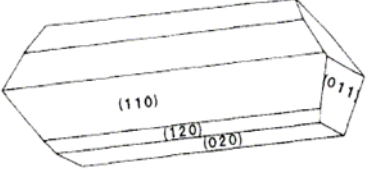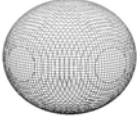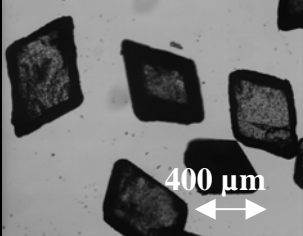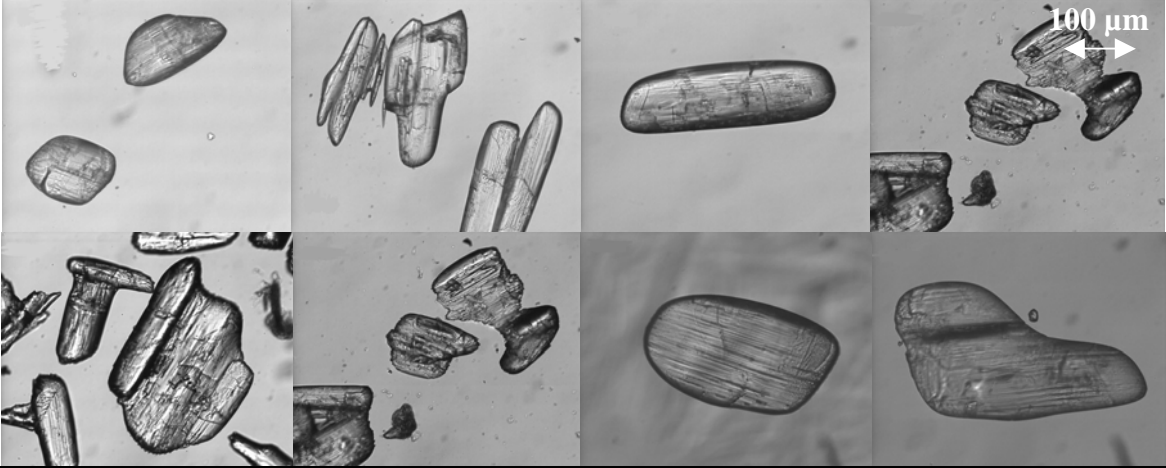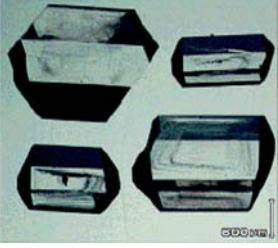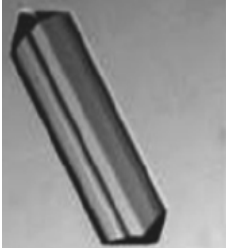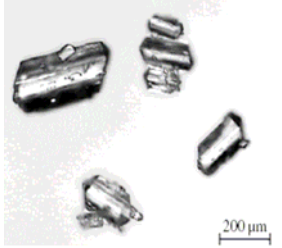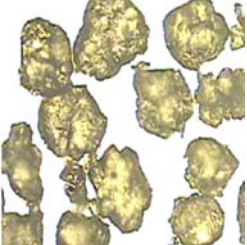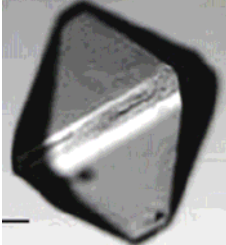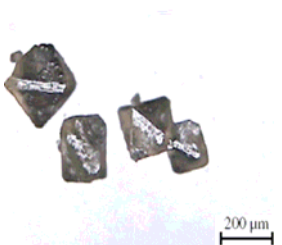
Figure 10-23: Comparison between experimental data (circles) and simulation (line) (experiment 4, zone 2: 27 min)

Table 10-3: Morphologies of α- and γ-glycine

Literature (Crystal Faces, α-Glycine) [Boe91]	Modelled Shape	Crystals used for Calibration/ Seed Crystals
		400 µm
Experimental Observed Morphologies		
		100 µm
Experimental Morphologies of α-Glycine		
[Tor05]	[Pro07]	[Yan08]	
		200 µm	
Experimental Morphologies of γ-Glycine		
[Che07b]	[Pro07]	[Yan08]	
		200 µm	

10.3.3   Results and Discussion

Although glycine is extensively studied in respect to polymorphism, surprisingly little kinetic data in form of rate constants is available. Li et al. [Li92] measured the growth rate for single crystals (20 °C, lnS: 0.015 – 0.08, G [μm/min]) deriving equations 10.8 and 10.9.

$$G_{\{011\}} = (84 \pm 8) \cdot (\ln S)^2 \cdot \tanh\left(\frac{0.08 \pm 0.02}{\ln S}\right)$$

(10.8)

$$G_{\{010\}} = (28 \pm 13) \cdot (\ln S)^2 \cdot \tanh\left(\frac{0.03 \pm 0.02}{\ln S}\right)$$

(10.9)

Li et al. [Li92] concluded that growth rate dispersion might play a role. Moscosa-Santillán et al. [Mos00] used the MSMPR crystallizer to study the kinetic behaviour, however, providing no rate coefficients. Using in-situ optical microscopy, agglomeration was found to be insignificant during batch crystallization [Che07a]. From the literature, no evidences about additional mechanisms for the crystallization of α-glycine, apart from nucleation and growth, were found. Figure 10-24 summarises data from the literature as well as those obtained within this work.
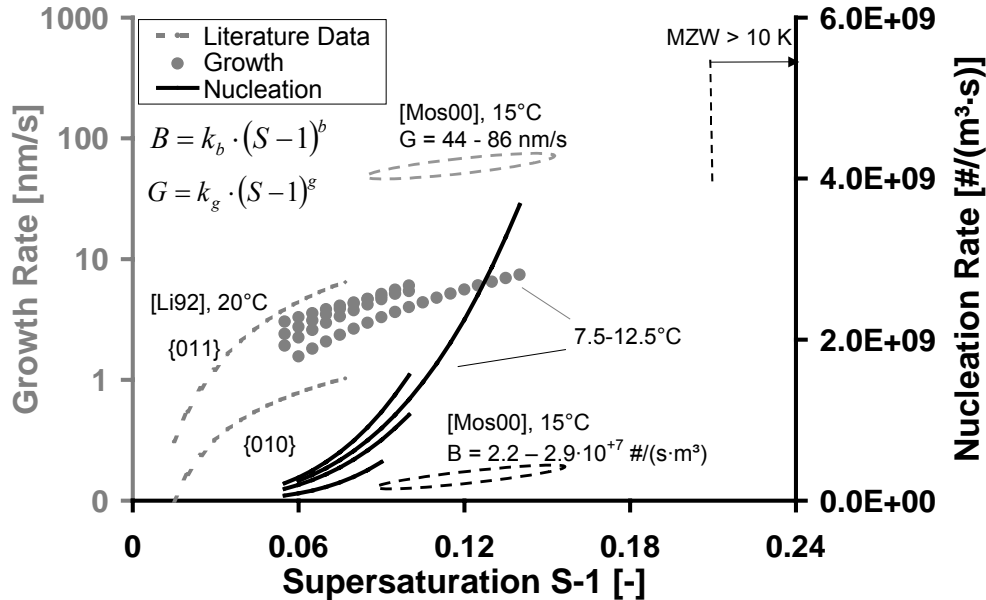
Figure 10-24: Comparison between nucleation and growth kinetics of α-glycine determined within this work (nucleation: black lines, growth: grey dots) and literature (black and grey dashed lines)

The metastable zone width for primary heterogeneous nucleation was determined to be 10 K ((S-1) = 0.214) as described in chapter 8.1. Literature data ranges between 12 and 15 K [Gin93, Na95, Yi06, Che07a]. The nucleation rate determined within this work and by Moscosa-Santillán et al. [Mos00] is in the order of secondary nucleation. An influence of the

second or third moment of the particle size distribution on the nucleation rate could not be verified (model discrimination).

As for ascorbic acid, the growth rate is in the order of "integration controlled". It compares well with the data reported by Li et al. [Li92] assuming the "Burton, Cabrera and Frank" growth law to be valid. The kinetics determined by Moscosa-Santillán et al. [Mos00] are slightly faster. For a detailed discussion on variations between kinetics determined by different authors, it is referred to chapter 4.3.

Table 10-4 summarises all determined kinetic rate constants, valid for the supersaturation range given in figure 10-24. The kinetic constants are valid for a narrow temperature range of 7.5 to 12.5 °C. The observed variation in $k_{optical}$ between individual experiments is discussed in chapter 10.2.2.

Table 10-4: Determined kinetic rate constants for α-glycine (95% confidence region, χ^2 - distribution), optical factor applied to close the mass balance, suspension density range of zone two

No. of Exp.	b [-]	$\ln(k_b\ [\#/(m^3 \cdot s)])$	g [-]	$\ln(k_g\ [m/s])$	$k_{optical}$ [-]	$m_T\ [kg/m^3_{Susp}]$
1	3.19±0.123	28.29±0.251	1.84±0.109	-15.09±0.236	130	10-40
2	4.15±1.708	29.98±4.286	1.80±0.591	-14.83±1.513	58	8-16
3	3.30±0.549	28.40±1.307	1.54±0.132	-15.37±0.325	68	10-28
4	3.30±0.293	28.77±0.707	0.98±0.116	-16.77±0.291	100	10-35

Moscosa-Santillán et al. [Mos00] determined a nucleation order b of 2.4. Values for g have been determined to be 1.2 [Mos00] or 1.3±0.2 and 1.5±0.2, for the set of {010} and {011} faces, respectively [Li92]. The confidence intervals are relatively small, but larger, compared to ascorbic acid. Although all parameters are in the expected order of magnitude, it seems that the model does not capture all active mechanisms and/or the experimental data is not as accurate. From initial seven experiments using the model-based experimental design only two were used for the determination of the kinetics. For two experiments, the parameter estimation did not lead to a unique result, although the experimental data could be described with the kinetic constants given in table 10-4. For three experiments it was not possible to close the mass balance for a certain minimum number of consecutive data points (time interval of zone two was smaller 20 minutes). Additional experimental data can be found by Pertig [Per08].

Table 10-3 shows a compilation of morphologies, compromising seed crystals (also used for calibration), crystals at the end of the batch experiments or from the literature. It allows gaining further insight into the respective crystallization phenomena. The experimentally obtained morphologies are ranging from intact to irregular shapes. However, it remains difficult to verify, if certain crystals are the result of agglomeration or breakage. The rounded corners can be the result of an already started dissolution of the metastable α-glycine. Further investigations are necessary that make use of X-ray powder diffraction to verify the assumption that no significant crystallization of γ-glycine took place during the relatively short time interval of the experiment.

10.4   Conclusion

A laboratory batch crystallizer equipped with an in-situ "3 Fold Dynamical Optical Reflectance Measurement" and an ultrasound velocity probe were used in combination with the developed 4 step procedure for data pre-processing, model-based experimental design and analysis to determine the crystallization kinetics of ammonium chloride, ascorbic acid and α-glycine.

Ammonium Chloride
Ammonium chloride forms dendrites when crystallized from water resulting in sincere breakage. Therefore, manganese chloride as an additive was used to tailor the morphology from a dendritic to a more compact shape. However, using the additive, in addition to nucleation and growth, a strong tendency towards agglomeration was observed that mainly took place at a length scale smaller than the detection limit of the "3 Fold Dynamical Optical Reflectance Measurement". Because of the small dynamic measurement window as well as difficulties to monitor the supersaturation, the experimental data was evaluated using a "differential approach", only. This allowed approximate nucleation, growth rates and the agglomeration kernel to be determined. The results are valid for a supersaturation of (S-1) = 0.005 - 0.015 (S in [kg/kg solvent]).

$$B \approx 0.5 - 6.3 \cdot 10^9 \ \#/(m^3{}_{Susp} \cdot s)$$

$$G_v \approx 2 - 4.8 \cdot 10^{-17} \ m^3/s$$

$$\beta \approx 1.0 \cdot 10^{-14} - 1.5 \cdot 10^{-13} \ m^3{}_{Susp}/(\#\cdot s)$$

Further studies should make use of a laser scanner with a lower detection limit, a faster laser speed as well as advanced population balance models.

Ascorbic Acid
Ascorbic acid forms plate-like crystals. The kinetics can be mainly described by nucleation and growth. Using a moment model a good description of the experimental data was obtained indicated by small confidence intervals of the estimated kinetic parameters. The model captures therefore all predominant mechanisms. The kinetics are valid for a temperature of 25 °C, a supersaturation range of (S-1) = 0.2 - 0.5 (S in [kg/kg solvent]) and a suspension density of $m_T = 10 - 100$ kg/m³$_{Susp}$ ($m_{PSD,3} = 0.011 - 0.115$ m³/m³$_{Susp}$). The constants are the average of 4 individual experiments.

$$B = 1.79 \cdot 10^{12} \cdot (S-1)^{3.44} \cdot m_{PSD,3} \approx 0.19 - 3 \cdot 10^9 \ \#/(m^3{}_{Susp} \cdot s) \tag{10.10}$$

$$G = 3.48 \cdot 10^{-8} \cdot (S-1)^{2.46} \approx 0.7 - 5.5 \cdot 10^{-9} \; m/s \qquad\qquad (\textbf{10.11})$$

α-Glycine

Glycine forms different polymorphs. From an aqueous solution the metastable α-form nucleates first. The kinetic data determined within this work agreed well with the very little information available from the literature. However, systematic deviations between the experimental data and the model predictions of the moment model were observed asking for a more detailed study. Following kinetic equations have been determined, being valid for a temperature range of 7.5 – 12.5 °C and a supersaturation range of (S-1) = 0.05 – 0.14 (S in [kg/kg solvent]). The constants are the average of 4 individual experiments.

$$B = 3.44 \cdot 10^{12} \cdot (S-1)^{3.49} \approx 0.1 - 3.7 \cdot 10^{9} \; \#/(m^3{}_{Susp} \cdot s) \qquad\qquad (\textbf{10.12})$$

$$G = 1.81 \cdot 10^{-7} \cdot (S-1)^{1.54} \approx 1.6 - 7.4 \cdot 10^{-9} \; m/s \qquad\qquad (\textbf{10.13})$$

The determined kinetics are describing the most predominant effects, are in the right order of magnitude and were discussed against the background of the rarely available kinetic data from literature. Confidence intervals were determined for the kinetics of ascorbic acid and α-glycine. To better quantify and pinpoint the deviation between the model prediction and the experimental data or to literature data, further research into the specific kinetic mechanisms that are active as well as into the interpretation of the laser scanner measurement is necessary (see chapter 11). Especially the influence of the suspension density on the chord length distribution and therefore on the growth rate needs further investigations and quantifications. The use of more advanced population balance or instrument models will help to elucidate the underlying effects.

The methodology described within this work has been successfully tested and is capable of determining kinetic constants in a few batch experiments, however, not necessarily consecutive ones. In an ideal case it minimises time and resource expenditure and the amount starting material. However, it should not be underestimated the time and material needed for the calibration of the measurement instruments as well as the rather high rate of not successful experiments. Experiments were disregarded because of encrustation forming on the probe, the fact that the measured particle size distributions did not satisfy the mass balance for a certain minimum time frame or the estimation of the kinetic parameters did not lead to an unique result.

The overall work process described within this work has the distinct advantage if kinetic constants have to be determined for population balance modelling on a more regular basis within a short time frame, with a clear objective on mean kinetics that are based on a crystal collective and a large amount of experimental data points. The use of in-situ measurement probes and a model-based approach allows a rapid determination but also exclusion of kinetic mechanisms, directing further research to improve the population balance model. The described methodology is an addition to the methods described in the book "Measurement of

Crystal Growth and Nucleation Rates" [Gar02]. The choice of an individual method must be carefully balanced with the objective and resource constraints of the individual project.

A short-cut method that circumvents the complex data pre-processing has been discussed. It is based on the fact that the chord length distribution shows the same dynamic behaviour as the reconstructed particle size distribution. It was shown that this "short-cut" is practicable if the optimisation or the controlling of process parameters or product qualities are of interest. However, if rate constants comparable to other literature data or for the use within a population balance model have to be determined, the short-cut method fails.

11 Outlook

Following three main directions can be identified to improve the determined kinetics of ammonium chloride, ascorbic acid and glycine, obtained within this work:

I.   identifying the actual physical-based kinetic mechanisms that are active
II.   using more advanced population balance models and model discrimination techniques to extract the kinetic rate constants
III.   interpreting of the raw measured data of laser scanner instruments

Emphasis will be placed on Roman numeral III, since for Roman numerals I and II experimental protocols and advanced population balance models are available within literature or on a commercial basis.

The first laser scanners date back to the mid eighties [All88]. The instrument has been widely compared to other sizing techniques, is widely used for monitoring crystallization processes and many advances have been made in translating the chord length into a particle size distribution. However, up to now there are surprisingly hardly any single crystal studies such as made by Ruf et al. [Ruf00] and Worlitschek et al. [Wor03b]. The interpretation of specific results within this work or literature data remained challenging, particularly due to the lack of knowledge on single crystal measurements. Are differences between experimental data and model prediction caused by a too simplified model or because of an incorrect measurement of the particle itself? Various model systems can be designed where the refractive index difference between fluid and a single crystal (or a collective) or any other property such as surface structure are varied in a systematic manner. How do different optical properties of individual polymorphs (refractive index, surface structure, colour) influence the results during the monitoring of a solution-mediated phase transformation? How does the dynamical focal point of the "3 Fold Dynamical Optical Reflectance Measurement" influences the result compared to the "Focused Beam Reflectance Measurement" that uses a static focal point?

During the calibration it was found that with the current experimental set-up the "3 Fold Dynamical Optical Reflectance Measurement" undersizes all investigated particle systems compared to optical microscopy, sieving and laser diffraction analysis. Similar results are reported in literature for ascorbic acid and glycine by the use of the "Focused Beam Reflectance Measurement" instrument [Sch01, Yu08b]. According to chapter 5.3.2 a smaller overall chord length can theoretically, for example, be caused by chord splitting, particle screening, crystals with a strong curvature, a too low laser speed or the widening of laser. Although qualitative the behaviour can be discussed, quantitative data is missing. How do these effects relate to the physical properties of the investigated system? Are all effects equally important? Does chord concatenation (primary coincidence) compensate for certain described effects? A single crystal study could assist, again, in elucidating individual mechanisms, gaining a more comprehensive understanding of the measurement itself, helping in building more advanced models for pre-processing of laser scanner data and hence improving kinetic data.

12   Summary

The design of crystallization processes depends on a sound knowledge of the underlying kinetics of nucleation, growth, agglomeration, breakage, attrition and where applicable polymorphic transformation. Without that knowledge, any crystallizer design becomes speculative and the tailoring of crystal properties subjected to trial and error. A multiscale map was developed that illustrates all involved length and time scales (see chapter 2). The experimental determination of kinetics, therefore, still requires considerable time and resource expenditure.

The objective of this work is to improve the determination of crystallization kinetics by taking advantage of recent developments within in-situ measurement techniques as well as of recent developments on a methodology side given by the systematic work process called model-based experimental design and analysis. Both developments have been proven beneficial, the combination, however, is seldom employed. The background of the described developments and methods are outlined within chapters 3 to 5. A detailed literature review was made that allows classifying the methods applied and the results obtained.

A laboratory batch crystallizer equipped with an in-situ "3 Fold Dynamical Optical Reflectance Measurement" and an in-situ ultrasound probe measuring chord length distribution and supersaturation, respectively, were used to record experimental data (chapter 7). For performing model-based experimental design and analysis the software package described in detail by Chung et al. [Chu00] and Togkalidou et al. [Tog04] was selected. The experiments were designed using the criterion of D-optimality following a sequential experimental design strategy. The analysis was made by applying parameter estimation techniques along with the population balance approximated by a moment model.

Within this work, special emphasis was placed on the pre-processing of laser scanner instrument data that is critical for the current application. In a first step, the instrument performance towards handling different suspension densities was studied (see chapter 8). For all model systems, it was observed that the actual measurement depends on the respective suspension density. A suitability of the instrument for higher suspension densities than 3 to 6 vol% could not be verified for the model systems studied within this work. The observed shifts of the measured distribution as a function of the suspension density are particular important for the interpretation of raw in-situ measured data.

In a second step, based on a detailed literature review of laser scanner instruments (chapter 5.3), a new 4 step procedure for pre-processing of "Focused Beam Reflectance or 3 Fold Dynamical Optical Reflectance Measurement" data was developed (see figure 9-2, chapter 9). It consists of various independent developed mathematical tools from the literature as well as newly developed ones.

    I.   Extending the measurement range by introducing a "dead length", resulting in a linearisation of the measured "counts" versus suspension density (according to Heath et al. [Hea02])

II.   Converting the chord length to a normalized particle size distribution using the method of "Projection onto Convex Sets" (according to Worlitschek et al. [Wor03a])

III. Calculating the total number of particles per volume by assuming that the zero moment of the particle size distribution relates to the minus first moment of the respective chord length distribution (according to Wynn [Wyn03] and Vaccaro et al. [Vac06a]). To compensate for model assumptions, an "optical factor" is introduced.

IV.   Improving the particle size distribution by exploiting their statistical properties along with the corresponding balance equations (data reconciliation using Lagrange Multipliers)

It was shown that the laser scanner measurement data can be transformed into a format suitable for population balance modelling and that the particle size distribution satisfies the mass balance within a specific "time window" of the experiment. The procedure is associated with two constants that affect the measured "counts" (~ nucleation rate) but do not influence the normalised distribution (~ growth rate) (see chapter 8).

In a third step, the procedure for data pre-processing was integrated into an overall work process for model-based experimental design and analysis (see figure 9-2). Interface software was written that allows exchanging of experimental data between the individual software programs that have developed independently from each other within different programming languages using different data formats (see chapter 9).

Within a final step, it was demonstrated how the combination of in-situ measurement techniques with the developed procedure for data pre-processing as well as model-based experimental design and analysis allows determining crystallization kinetics of ammonium chloride (electrolyte), ascorbic acid (vitamin) and α-glycine (amino acid) (see chapter 10). A short-cut method that circumvents the complex pre-processing of the raw measured data from laser scanner instruments was evaluated.

Nomenclature

Roman symbols

A	[m²]	area
$A_{hom,het}$	[#/(m³·s)]	constants for homogenous or heterogeneous nucleation (based on m³ suspension)
a	[-]	shape factor of the gamma distribution ($a > 0$)
a	[various]	activity (depending on unit of concentration)
a_{Surf}	[m²/m³]	specific surface
$a_{1,2,3,4,5...}$	[various]	coefficients/empirical constants
B_{att}	[#/(m³·s)]	nucleation due to attrition (based on m³ suspension)
B_{het}	[#/(m³·s)]	heterogeneous nucleation rate (based on m³ suspension)
B_{hom}	[#/(m³·s)]	homogenous nucleation rate (based on m³ suspension)
B_{surf}	[#/(m³·s)]	surface nucleation rate (based on m³ suspension)
B_0	[#/(m³·s)]	overall nucleation rate (based on m³ suspension)
B^*	[#/s]	rate of counts
b	[-]	scale factor of the gamma distribution ($b > 0$)
b	[-]	nucleation rate order
C	[-]	corridor width
CV	[-]	coefficient of variation
c	[-]	concentration (based on [kg/kg solvent])
c_{mol}	[mol/m³]	concentration
c_{mass}	[kg/m³]	concentration
D_{AB}	[m²/s]	binary volumetric diffusion coefficient
$D_{Surface}$	[m²/s]	crystal surface diffusion coefficient
d_m	[m]	ion/molecular diameter
E	[-]	efficiency factor ($0 < E < 1$)
E_G	[J/mol]	activation energy of crystal growth
F	[various]	objective function
f	[-]	geometric correction factor or error
G	[m/s]	growth rate
G_j	[m/s]	growth rates based on different moments (j=1, 2, 3)
G_v	[m³/s]	growth rate based on crystal volume
g	[-]	growth rate order
H_V	[J/m³]	hardness of crystal
ΔH_m	[J/mol]	enthalpy of melting
i	[-]	index
j	[-]	index or exponent
K	[-]	constant (0.414, interfacial tension)
K_{eff}	[-]	efficiency constant
K	[m]	dead length before (and after) particle
k	[-]	kernel
k_A	[-]	area shape factor (spheres: 3.142)
k_{att}	[-]	constant
k_{BCF1}	[m/s]	constants within BCF law
k_{BCF2}	[-]	constants within BCF law
k_{B+S1}	[m/s]	constants within B+S law
k_{B+S2}	[-]	constants within B+S law
k_b or k_{bm}	[#/(m³·s)]	nucleation rate coefficient (based on m³ suspension)

k_{bSusp}	$[\#/(m^3 \cdot s)/(kg/m^3)^j]$	nucleation rate coefficient (based on m³ suspension)
k_{Boltz}	$[J/K]$	Boltzmann constant ($1.38 \cdot 10^{-23}$)
k_D	$[m/s]$	overall mass transfer coefficient
k_g	$[m/s]$	growth rate coefficient
$k_{optical}$	$[-]$	constant
k_V	$[-]$	volume shape factor (spheres: 0.524)
$k_{1,2,3..}$	$[various]$	constants
k_∞	$[m/s]$	frequency factor
L	$[various]$	Lagrangian
L	$[m]$	characteristic length, size of crystal
$L_{Channel,i}$	$[m]$	arithmetic average length of the ith channel
L_i	$[m]$	channel boundary (upper and lower)
L_{char}	$[-]$	characteristic length
L_{Det}	$[m]$	detection limit/size of instrument
L_N	$[m]$	size of a nuclei ($L_N = 0$)
L_{Total}	$[m]$	total particle length
$L_{50,i}$	$[m]$	median size (cumulative distribution $Q_i(5O)$)
$L_{[i,j]}$	$[m]$	mean size based on the ith and jth moment
l_{Cell}	$[m]$	cell length
M	$[-]$	number of channels of the chord length distribution
M_{mol}	$[kg/mol]$	molecular weight
$m_{CLD,j}$	$[\# \cdot m^j/s]$	jth moment of chord length distribution
$m_{Crystal}$	$[kg]$	mass of crystals
$m_{PSD,j}$	$[\# \cdot m^j/m^3]$	jth moment of PSD (based on m³ suspension)
$m_{Seed,j}$	$[\# \cdot m^j/m^3]$	jth moment of seed crystals (based on m³ suspension)
m_{Seed}	$[kg]$	mass of seeds
$m_{Solvent}$	$[kg]$	mass of solvent
m_T	$[kg/m^3]$	suspension density (based on m³ suspension)
$m_{v,j}$	$[\# \cdot m^{3j}/m^3]$	jth moment of PSD (based on volume coordinates and m³ suspension)
N	$[\#]$	number of particles
N_d	$[-]$	number of measurement points
$N_{LS,corr}$	$[\#/s]$	corrected total chord counts using a laser scanner
$N_{LS,meas}$	$[\#/s]$	total observed chord counts using a laser scanner
$N_{LS,meas,i}$	$[\#/s]$	number of i sized chord counts observed
N_m	$[-]$	number of measured variables
$N_{Stirrer}$	$[\#/s]$	stirrer speed
N_{Total}	$[\#/m^3]$	total number of particles (based on m³ suspension)
n	$[\#/(m \cdot m^3)]$	number density distribution (based on m³ suspension)
$n_{CLD,meas}$	$[\#/(s \cdot m)]$	measured chord length distribution
n_R	$[-]$	refractive index
n_v	$[\#/(m^3 \cdot m^3)]$	volume density distribution (based on m³ suspension)
n^*	$[\#]$	number of ions/molecules forming a critical nuclei
O	$[\#]$	number of suspension densities measurements
p	$[-]$	scaled size (chord length/characteristic particle size)
P	$[various]$	diagonal matrix (M+1 x M+1)
P	$[\#]$	number of sieve cuts
Q	$[-]$	extinction efficiency factor
Q	$[-]$	cumulative distribution
Q	$[various]$	vector (1 x M+1)
q	$[1/m]$	density distribution, linear spacing

q_{ln}	[-]	density distribution, logarithmic spacing ($1/\ln(L_i/L_{i+1})$)
R_{uni}	[J/(mol·K)]	universal gas constant (8.314)
r	[various]	scalar product ($Q \cdot x_{meas}$)
S	[-]	supersaturation (c/c_{eq}), here [kg solute/kg solvent]
Sc	[-]	Schmidt number (υ_F/D_{AB})
S_j	[-]	shape factor (chord length distribution of single particle)
T	[K]	temperature
T	[m]	scanning depth
$\dot{T}$	[K/s]	cooling rate
T_m	[K]	melting temperature
T_{Vessel}	[m]	vessel diameter
t	[s]	time
t_m	[s]	measuring time
U	[m/s]	ultrasound
V_m	[m³]	molecular volume
V_{molar}	[m³/mol]	molar volume
V_{Sample}	[m³]	sample volume
$V_{Suspension}$	[m³]	volume of suspensions
$v_{Diffusion}$	[m/s]	face growth rate limited by diffusion
v_{BCF}	[m/s]	face growth rate controlled by the BCF law
v_{B+S}	[m/s]	face growth rate controlled by the B+S law
v_{Heat}	[m/s]	face growth rate limited by heat transfer
v_{Laser}	[m/s]	laser speed
v_{PN}	[m/s]	face growth rate controlled by the PN law
v_0	[m/s]	overall rate
w	[-]	weight fraction
w_{ij}	[various]	weighting factor (inverse of measurement error variance)
x	[-]	mol fraction
x	[various]	vector (M+1 x 1)
y	[various]	vector (M+1 x 1)
$y_{i,j}$	[various]	matrix (measurements or model predictions)

Greek symbols

β_{ad}	[m²/N]	adiabatic compressibility
β_0	[m³/(#·s)]	size-independent agglomeration kernel (based on m³ suspension)
Γ	[J/m²]	surface energy/fracture resistance
γ	[-]	activity coefficient
γ_{CL}	[J/m²]	interfacial tension (crystal-liquid)
Δ	[-]	difference
ε	[various]	measurement error
$\varepsilon_{mean/local}$	[W/kg]	specific power input (m²/s³)
Θ	[-]	parameter vector (kinetic constants)
κ	[-]	condition number
λ	??	Lagrange multiplier
μ	[J/m³]	shear module
$\Delta\mu$	[J/mol]	change in chemical potential
ν	[-]	number of ions/molecules formed by dissociation
ν_{dh}	[1/s]	dehydration frequency of the cation
$\rho_{Crystal}$	[kg/m³]	crystal density

$\rho_{Crystal,mol}$	[mol/m³]	molar crystal density ($\rho_{Crystal}/M_{mol}$)
$\rho_{Solution}$	[kg/m³]	density of a solution
σ	[-]	relative supersaturation ($c-c_{eq}/c_{eq}$) = S-1
σ_{Ultra}	[m/s]	accuracy of ultrasound probe
τ_{Agg}	[s]	characteristic time of agglomeration
τ_{Diss}	[s]	characteristic time of dissolution
τ_{Growth}	[s]	characteristic time of crystal growth
$\tau_{Induction}$	[s]	characteristic time of induction
τ_{macro}	[s]	characteristic time of macro mixing
τ_{micro}	[s]	characteristic time of micro mixing
τ_{Res}	[s]	residence time
τ_{Rip}	[s]	characteristic time of ripening
υ_F	[m²/s]	kinematic viscosity
φ_V	[m³/m³]	volumetric hold up (based on m³ suspension)

Subscripts

CLD	chord length distribution
eq	equilibrium, saturated conditions
final	end or final value
max	maximum
meas	measurement
min	minimum
model	model prediction
PSD	particle size distribution
Seed	seeds
start	start or initial value
t1,2	time point 1 or 2
v	based on volume

Superscripts

Export	export
T	transposed matrix
*	intermediate
–	arithmetic average between two successive time points

Abbreviations

CV	coefficient of variation
CLD	chord length distribution
FBRM	focused beam reflectance measurement
MBED	model-based experimental design
$MnCl_2$	manganese chloride
MSMPR	mixed suspension mixed product removal
MZW	metastable zone width
NH_4Cl	ammonium chloride
PSD	particle size distribution
PVC	poly(vinyl chloride)
sat. S.	saturated solution
3D-ORM	3 fold dynamical optical reflectance measurement

References

[Aal03]   Aaltonen, J, Rantanen, J., Siiriä, S., Karjalainen, M., Jorgensen, A., Laitinen, N., Savolainen, M., Seitavuopio, P., Louhi-Kultanen, M., Yliruusi, J.: Polymorph Screening Using Near-Infrared Spectroscopy, Analytical Chemistry 75 (2003) 19, 5267-5273

[Abb07]   Abbas, A., Romagnoli, J. A.: Multiscale modelling, simulation and validation of batch cooling crystallization, Separation and Purification Technology 53 (2007) 153-163

[Abb02]   Abbas, A., Nobbs, D., Romagnoli, J. A.: Investigation of on-line optical particle characterization in reaction and cooling crystallization systems. Current state of the art, Measurement Science and Technology 13 (2002) 349-356

[Abe08]   Abebe, S. B., Wang, X. Z., Li, R., Roberts, K. J., Lai, X.: The information content in NIR spectral data for slurries of organic crystals, Powder Technology 179 (2008) 3, 176-183

[Aki05]   Akiti, O., Yeboah, A., Bai, G., Armenante, P. M.: Hydrodynamic effects on mixing and competitive reactions in laboratory reactors, Chemical Engineering Science 60 (2005) 2341-2354

[Al08]   Al Nasser, W. N., Shaikh, A., Morriss, C., Hounslow, M. J., Salman, A. D.: Determining kinetics of calcium carbonate precipitation by inline technique, Chemical Engineering Science 63 (2008) 1381-1389

[Al06]   Al-Kandary, J. A., Al-Jimaz, A. S., Abdul-Latif, A.-H. M.: Viscosities, Densities, and Speeds of Sound of Binary Mixtures of Benzene, Toluene, o-Xylene, m-Xylene, p-Xylene, and Mesitylene with Anisole at (288.15, 293.15, 298.15, and 303.15) K, Journal of Chemical and Engineering Data 51 (2006) 2074-2082

[Ala04]   Alamdari, A., Tabkhi, F.: Kinetics of hexamine crystallization in industrial scale, Chemical Engineering and Processing 43 (2004) 803-810

[All03]   Allen, T.: Powder sampling and particle size determination, Elsevier Amsterdam, 2003

[All88]   Allen, T., Davies, R.: An Evaluation of the Lab-Tec 100 Particle Size Analyzer, Particle Size Analysis, Proceedings, 6th Particle Size Analysis Conference 19.-20.04 1988, Guildford/UK, ed. by Lloyd, P.J., Wiley Chichester, 1988, 33-44

[Alo02]   Alopaeus, A., Koskinen, J., Keskinen, K. I., Majander, J.: Simulation of the population balances for liquid-liquid systems in a non-ideal stirred tank. Part 2-parameter fitting and the use of the multiblock model for dense dispersions, Chemical Engineering Science 57 (2002) 1815-1825

[Aou99]   Aoun, M., Plasari, E., David, R., Villermaux, J.: A simultaneous determination of nucleation and growth rates from batch spontaneous precipitation, Chemical Engineering Science 54 (1999) 1161-1180

[Ape07]   Apelblat, A., Manzurola, E.: Vapour pressure and volumetric studies in aqueous solution with ascorbate ions, Journal of Molecular Liquids 131-132 (2007) 7-16

[Ape89]   Apelblat, A., Manzurola, E.: Solubility of ascorbic, 2furancarboxylic, glutaric, pimelic, salicyclic, and o-phthalic acids in water from 279.15 to 342.15 K, and apparent molar volumes of ascorbic, glutaric, and pimelic acids in water at 298.15 K, Journal of Chemical Thermodynamics 21 (1989) 1005-1008

[Are07]   Arellano-Garcia, H., Schöneberger, J., Körkel, S.: Optimale Versuchsplanung in der chemischen Verfahrenstechnik, Chemie Ingenieur Technik 79 (2007) 10, 1625-1638

[Asp02]   Asprey, S.P., Macchietto, S.: Designing robust optimal dynamic experiments, Journal of Process Control 12 (2002) 545-556

[Ath99]   Atherton, J. H.: Process Development: Physicochemical Concepts, Oxford Chemistry Primers 79, Oxford University Press Oxford, 1999

[Aue05]   Auer, G.: White Pigments, in: Industrial Inorganic Pigments, 3rd Edition (eds.: Buxbaum, G., Pfaff, G.), Wiley-VCH Weinheim, 2005, 51-97

[Bal05]   Baldyga, J., Krasinski, A.: Precipitation of Benzoic Acid in Continous stirred tank - Effects of Agglomeration, Proceedings, 16th International Symposium on Industrial Crystallization 11.-14.09 2005, Dresden/Germany, ed. by Ulrich, J., VDI-Berichte 1901, VDI-Verlag Düsseldorf, 2005, 411-416

[Bal99]   Bałdyga, J., Bourne, J. R.: Turbulent Mixing and Chemical Reactions, Wiley Chichester, 1999

[Ban02]   Banga, J. R., Versyck, K. J., Van Impe, J. F.: Computation of Optimal Identification Experiments for Nonlinear Dynamic Process Models: a Stochastic Global Optimization Approach, Industrial and Engineering Chemistry Research 41 (2002) 2425-2430

[Bar08]   Bardow, A.: Optimal Experimental Design of ill-posed problems: The METER Approach, Computers and Chemical Engineering 32 (2008) 115-124

[Bar06]   Barthe, S., Rousseau, R.W.: Utilization of Focused Beam Reflectance Measurement in the Control of Crystal Size Distribution in a Batch Cooled Crystallizer, Chemical Engineering and Technology 29 (2006) 2, 206-211

[Bar05]   Barrett, P., Smith, B., Worlitschek, J., Bracken, V., O'Sullivan, B., O'Grady, D.: A Review of the Use of Process Analytical Technology for the Understanding and Optimization of Production Batch Crystallization Processes, Organic Process Research and Development 9 (2005) 348-355

[Bar04]   Bardow, A.: Model-based Experimental Analysis of Multicomponent Diffusion in Liquids, Dissertation: RWTH Aachen, Fortschritt-Berichte VDI 3(821), VDI-Verlag Düsseldorf, 2004

[Bar99]   Barrett, P., Glennon, B.: In-line FBRM Monitoring of Particle Size in Dilute Agitated Suspension, Particle and Particle Systems Characterization 16 (1999) 207-211

[Bar96]   Barreiros, F. M., Ferreira, P. J., Figueiredo, M.: Calculating Shape Factors from Particle Sizing Data, Particle and Particle Systems Characterization 13 (1996) 368-373

[Bau99]   Baumann, K.-H., Schmerwitz, F.: Growth Rate Dispersion in Batch Crystallization, Proceedings, 14th International Symposium on Industrial Crystallization 12.-16.09 1999, Cambridge/UK, ed. by Garside, J., Proceedings CD, IChemE Rugby, 1999

[Bau93]   Baumann, K.-H.: Kinetic Coefficient from Batch Crystallization Experiments, Proceedings, 12th Symposium on Industrial Crystallization 21.-23.09 1993, Warsaw/Poland, ed. by Rojkowski, Z. H., Zaklad Poligraficzny "Wlodarski" Warsaw, 1993, 4-107-4-112

[Bau84]   Baumann, K.-H., Voigt, H.: Technische Massenkristallisation, Akademie-Verlag Berlin, 1984

[Bec04]   Beckmann, W.: Grundlagen der Kristallisation, Agglomeration bei der Kristallisation, in: Kristallisation in der Industrie, (ed. Hofmann, G.), Wiley-VCH Weinheim, 2004, 63-129

[Ber04]   Bernardo, A., Calmanovici, C. E., Miranda, E. A.: Induction Time as an Instrument to Enhance Comprehension of Protein Crystallization, Crystal Growth & Design 4 (2004) 4, 799-805

[Ber03]   Bermingham, S. K.: A Design Procedure and Predictive Models for Solution Crystallisation Processes - Development and Application, Dissertation: Technical University Delft, Delft University Press Delft, 2003

[Ber97]   Berry, D. A., Ng, K. M.: Synthesis of Crystallization-Distillation Hybrid Separation Processes, AIChE Journal 43 (1997) 7, 1751-1762

[Ber86]   Berglund, K. A.: Summary of Recent Research on Growth Rate Dispersion of Contact Nuclei, Chemical Engineering Communications 41 (1986) 357-360

[Bla01]   Blandin, A. F., Mangin, D., Nallet, V., Klein, J. P., Bossoutrot, J. M.: Kinetics identification of salicylic acid precipitation through experiments in a batch stirred vessel and a T-mixer, Chemical Engineering Journal 81 (2001) 91-100

[Bla88]   Black, S. N., Davey, R. J.: Crystallization of amino acids, Journal of Crystal Growth 90 (1988) 136-144

[Blo05]   Bloemen, H. H. J., De Kroon, M. G. M.: Transforming of Chord Length Distributions into Particle Size Distributions Using Least Square Techniques, Particulate Science and Technology 23 (2005) 377-386

[Bod99]   Bodor, B., Lakatos, B. G.: Crystal Growth of L-Ascorbic Acid in Programmed Batch Cooling Crystallization, Hungarian Journal of Industrial Chemistry Veszprém 27 (1999) 297-230

[Bod95]   Bodor, B., Dódony, I.: Crystallization of Vitamin C under different experimental conditions, Hungarian Journal of Industrial Chemistry Veszprém 23 (1995) 289-291

[Bod93]   Bodor, B., Halasz, S., Vassanyi, I.: Crystallization Parameters Influencing Size, Habit and Purity of Vitamin C, Proceedings, 12th Symposium on Industrial Crystallization 21.-23.09 1993, Warsaw/Poland, ed. by Rojkowski, Z. H., Zaklad Poligraficzny "Wlodarski" Warsaw, 1993, 4-065-4-070

[Boh07]   Bohnet, M. (ed.): Mechanische Verfahrenstechnik, Wiley-VCH Weinheim, 2007

[Boh92]   Bohlin, M., Rasmuson, A. C.: Modeling of Growth Rate Dispersion in Batch Cooling Crystallization, AIChE Journal 38 (1992) 12, 1853-1863

[Boi91]   Boistelle, R.: Aspects of Protein Crystallization: Techniques and Kinetics, in: Advances in Industrial Crystallization (eds.: Garside, J., Davey, R., Jones, A.G.), Butterworth Heinemann Oxford, 1991, 131-147

[Bou03]   Bourne, J. R.: Mixing and the Selectivity of Chemical Reactions, Organic Process Research and Development 7 (2003) 471-508

[Bou80]   Bourne, J. R.: The influence of solvent on crystal growth kinetics, AIChE Symposium Series 193 (1980) 76, 59-64

[Bou78]   Bourne, J. R., Davey, R. J., McCulloch, J.: The growth kinetics of hexamethylene tetramine crystals from a water/acetone solution, Chemical Engineering Science 33 (1978) 199-204

[Bou76a]   Bourne, J. R., Davey, R. J.: The role of solvent-solute interactions in determining crystal growth mechanism from solution, Part II. The growth kinetics of hexamethylene tetramine, Journal of Crystal Growth 36 (1976) 287-296

[Bou76b]   Bourne, J. R., Davey, R. J.: The role of solvent-solute interactions in determining crystal growth mechanism from solution, Part I. The surface entropy factor, Journal of Crystal Growth 36 (1976) 278-286

[Bou76c]   Bourne, J. R., Davey, R. J.: The Growth of Hexamethylene Tetramine Crystals from Ethanolic Solutions, Journal of Crystal Growth 34 (1976) 230-238

[Box92]   Boxmann, A.: Particle Size Measurement for the control of industrial crystallizer, Dissertation: Technical University Delft, Delft University Press Delft, 1992

[Bra04]   Braun, B., Groen, H., Tschernjaew, J.: Production-Scale Particle Design of a Pharmaceutical Intermediate, Crystal Growth & Design 4 (2004) 5, 915-920

[Bra02]   Braatz, R. D., Hasebe, S.: Particle Size and Shape Control in Crystallization Processes, AIChE Symposium Series 326 (2002) 307-327

[Bra96]   Bramley, A. S., Hounslow, M. J., Ryall, R. L.: Aggregation during Precipitation from Solution: A Method for Extracting Rates from Experimental Data, Journal of Colloid and Interface Science 183 (1996) 155-165

[Bri06]   Briesen, H.: Simulation of crystal size and shape by means of a reduced two-dimensional population balance model, Chemical Engineering Science 61 (2006) 104-112

[Brö07]   Bröckel, U., Meier, W., Wagner, G. (eds.): Product Design and Engineering: Volume 1 Basics and Technologies, Wiley-VCH Weinheim, 2007

[Bud87]   Budz, J., Jones, A. G., Mullin, J. W.: Agglomeration of Potassium Sulphate Crystals in MSMPR Crystallizer, AIChE Symposium Series 253 (1987) 83, 78-84

[Bun49]   Bunn, C. W.: Crystal growth from solution. II. Concentration gradients and the rates of growth of crystals, Discussions of the Faraday Society 5 (1949) 132-144

[Bur08]   Burton, R. C., Ferrari, E. S., Davey, R. J., Hopwood, J., Quayle, M. J., Finney, J. L., Bowron, D. T.: The Structure of a Supersaturated Solution: A Neutron Scattering Study of Aqueous Urea, Crystal Growth & Design 8 (2008) 5, 1559-1565

[Bur01]   Burke, M. W., Leardi, R., Judge, R. A., Pusey, M. L.: Quantifying Main Trends in Lysozyme Nucleation: The effect of Precipitant concentration, supersaturation and impurities, Crystal Growth & Design 1 (2001) 4, 333-337

[Cai06]   Caillet, A., Puel, F., Fevotte, G.: In-line monitoring of partial and overall solid concentration during solvent-mediated phase transition using Raman spectroscopy, International Journal of Pharmaceutics 307 (2006) 201-208

[Cal05]   Calderon De Anda, J., Wang, X. Z., Roberts, K. J.: Multi-scale segmentation image analysis for the in-process monitoring of particle shape with batch crystallizers, Chemical Engineering Science 60 (2005) 1053-1065

[Cam05a]   Cameretti, L. F., Sadowski, G.: Modeling of Aqueous Electrolyte Solutions with Perturbed-Chain Statistical Associated Fluid Theory, Industrial and Engineering Chemistry Research 44 (2005) 3355-3362

[Cam05b]   Cameron, I. T., Wang, F. Y., Immanuel, C. D., Stepanek, F.: Process systems modelling and applications in granulation: A review, Chemical Engineering Science 60 (2005) 3723-3750

[Cao99]   Cao, Z., Groen, H., Hammond, R. B., Lai, X., Liang, K., Mougin, P., Roberts, K. J., Savelli, N., Thomas, A. F., White, G., Wilkinson, D., Baker, M., Dale, D., Erk, P., Latham, D., Merrifield, D., Oliver, R., Roberts, D., Wood, W., Ford, L.: Monitoring the crystallization of organic speciality chemical products via on-line analytical techniques, Proceedings, 14th International Symposium on Industrial Crystallization 12.-16.09 1999, Cambridge/UK, ed. by Garside, J., Proceedings CD, IChemE Rugby, 1999

[Car85]   Cardew, P. T., Davey, R. J.: The kinetics of solvent-mediated phase transformation, Proceedings of the Royal Society of London, Series A: Mathematical, Physical and Engineering Sciences, 398 (1985) 1815, 415-428

[Cha07]   Charpentier, J.-C.: Modern Chemical Engineering in the Framework of Globalization, Sustainability and Technical Innovation, Industrial and Engineering Chemistry Research 46 (2007) 3465-3485

[Cha04]   Charpentier, J.-C., McKenna, T. F.: Managing complex systems: some trends for the future of chemical and process engineering, Chemical Engineering Science 59 (2004) 1617-1640

[Cha02]   Charpentier, J.-C.: The triplet "molecular processes-product-process" engineering: the future of chemical engineering?, Chemical Engineering Science 57 (2002) 4667-4690

[Cha91]   Charmolue, H., Rousseau, R. W.: L-Serine Obtained by Methanol Addition in Batch Crystallization, AIChE Journal 37 (1991) 8, 1121-1128

[Cha82]   Chang, C.-T., Epstein, M. A. F.: Identification of Batch Crystallization Control Strategies using Characteristic Curves, AIChE Symposium Series 215 (1982) 78, 68-75

[Che07a]   Chew, J. W., Black, S. N., Chow, P. S., Tan, R. B. H.: Comparison between Open-Loop Temperature Control and Closed Loop Supersaturation Control for Cooling Crystallization of Glycine, Industrial and Engineering Chemistry Research 46 (2007) 830-838

[Che07b]   Chew, J. W., Black, S. N., Chow, P. S., Tan, R. B. H., Carpenter, K.J.: Stable polymorphs: difficult to make and difficult to predict, CrystEngComm 9 (2007) 2, 128-130

[Che07c]   Chew, J. W., Chow, P. S., Tan, R. B. H.: Automated In-line Technique Using FBRM to Achieve Consistent Product Quality in Cooling Crystallization, Crystal Growth & Design 7 (2007) 8, 1416-1422

[Che04]   Chen, B. H., Bermingham, S., Neumann, A. H., Kramer, H. J. M., Asprey, S. P.: On the Design of Optimally Informative Experiments for Dynamic Crystallization Process Modeling, Industrial and Engineering Chemistry Research 43 (2004) 4889-4902

[Che03]   Chen, P.-C., Liu, S. M., Jang, C. J., Hwang, R. C., Yang, J. S., Jang, J. S.: Interpretation of gas-liquid reactive crystallization data using a size-independent agglomeration kernel, Journal of Crystal Growth 257 (2003) 333-343

[Che00]   Chen, H., Wang, J.: Crystallization Thermodynamic and Kinetic Behaviours of Vitamine C in Batch Crystallizer, Chinese Journal of Chemical Engineering 8 (2000) 2, 95-99

[Che97]   Chernov, A. A.: Protein versus conventional crystals: creation of defects, Journal of Crystal Growth 174 (1997) 354-361

[Chi96]   Chianese, A., Santilli, N., Söhnel, O.: Influence of admixtures and operating conditions on the crystallization of ammonium chloride, Journal of Crystal Growth 166 (1996) 1099-1104

[Cho04]   Choong, K. L., Smith, R.: Optimization of semi-batch reactive crystallization processes, Chemical Engineering Science 59 (2004) 1529-1540

[Chu04]   Chung, S. H., Ma, D. L., Fujiwara, M., Gunawan, R.Togkalidou, T., Braatz, R. D. Simulation, Parameter Estimation, Experimental Design, and Optimal Control of Batch Crystallization; University of Illinois: Urbana, IL, (downloaded 2004 at http://brahms.scs.uiuc.edu/lssrl/software)

[Chu00]   Chung, S. H., Ma, D. L., Braatz, R. D.: Optimal model-based experimental design in batch crystallization, Chemometrics and Intelligent Laboratory Systems 50 (2000) 83-90

[Chu99]   Chung, S. H., Ma, D. L., Braatz, R. D.: Optimal Seeding in Batch Crystallization, The Canadian Journal of Chemical Engineering 77 (1999) 590-596

[Cla88]   Clark, N. N., Turton, R.: Chord Length Distributions Related to Bubble Size Distributions in Multiphase Flow, International Journal of Multiphase Flow 14 (1988) 4, 413-424

[Cos07]   Costa, C. B. B., Maciel, M .R. W., Filho, R. M.: Considerations on the crystallization modelling: Population balance solution, Computers and Chemical Engineering 31 (2007) 206-218

[Cos06]   Costa, R., Moggridge, G. D., Saraiva, P. M.: Chemical Product Engineering: An Emerging Paradigm Within Chemical Engineering, AIChE Journal 52, (2006) 6, 1976-1986

[Cul02]   Cull, S.G., Lovick, J.W., Lye, G.J., Angeli, P.: Scale-down studies on the hydrodynamics of two-liquid phase biocatalytic reactors, Bioprocess and Biosystems Engineering 25 (2002) 143-153

[Dal98]   Dallos, A., Hajós-Szikszay, É., Liszi, J.: Enthalpies of solution and crystallization of L-ascorbic acid in aqueous solution, Journal of Chemical Thermodynamics 30 (1998) 263-270

[Dal33]   Dalton, J. B.; Schmidt, C. L. A.: The solubilities of certain amino acids in water, the densities of their solutions at twenty-five degrees and the calculated heats of solution and partial molal volumes, Journal of Biological Chemistry 103 (1933) 549-578

[Dan07]   Dang, L., Wei, H., Zhu, Z., Wang, J.: The influence of impurities on phosphoric acid hemihydrate crystallization, Journal of Crystal Growth 307 (2007) 104-111

[Dan04]   Daniels, R.: In situ Particle Sizing in Concentrated Dispersions, Skin Care Forum, 36, 2004 (http://www.scf-online.com/english/36_e/contents36_e.htm)

[Dat04]   Datta, S., Grant, D. J. W.: Crystal Structures of drugs: advances in determination, prediction and engineering, Nature Reviews (Drug Discovery) 3 (2004) 42-57

[Dav06]   Davies, R.: Particle Characterization - A Journey, 5th World Congress on Particle Technology 23.-27.04. 2006 Orlando/USA, 2006 (presentation, www.erc.ufl.edu/publications/)

[Dav02]   Davey, R. J., Allen, K., Blagden, N., Cross, W. I., Lieberman, H. F., Quayle, M. J., Righini, S., Seton, L., Tiddy, G. J. T.: Crystal engineering - nucleation, the key step, CrystEngComm 4 (2002) 47, 257-264

[Dav01]   Davey, R. J., Blagden, N., Righini, S., Alison, H., Quayle, M. J., Fuller, S.: Crystal Polymorphism as a Probe for Molecular Self-Assembly during Nucleation from Solutions: The Case of 2,6-Dihydroxybenzoic Acid, Crystal Growth & Design 1 (2001) 1, 59-65

[Dav00]   Davey, R., Garside, J.: From Molecules to Crystallizers - An Introduction to Crystallization, Oxford Chemistry Primers 86, Oxford University Press Oxford, 2000

[Dav95]   David, R., Marchal, P., Marcant, B.: Modelling of Agglomeration in Industrial Crystallization from Solution, Chemical Engineering and Technology 18 (1995) 302-309

[Dav86]   Davey, R., Fila, W., Garside, J.: The influence of biruet on the growth kinetics of urea crystals from aqueous solutions, Journal of Crystal Growth 79 (1986) 607-613

[Dav82]   Davey, R. J.: Solvent Effects in crystallization processes, Current Topics in Material Science 8 (1982) 429-479

[Day99]   Daymo, E. A., Hylton, T.D., May, T.H.: Acceptance testing of the Lasentec Focused Beam Reflectance Measurement (FBRM) monitor for slurry transfer applications at Hanford and Oak Ridge, Proceedings (Volume 3539), The International Society for Optical Engineering - Nuclear Waste Instrumentation Engineering 04.-05.09 1998 Boston/USA, ed. by Robertson, D. E., The International Society for Optical Engineering Bellingham, 1998, 82-92

[Den03]   Dennehy, R. D.: Particle Engineering Using Power Ultrasound, Organic Process Research and Development 7 (2003) 1002-1006

[Des03]   Desiraju, G. R. (ed.): Crystal Design: Structure and Function, Wiley Chichester, 2003

[Det07]   Dette, S. S., Stelzer, T., Römbach, E., Jones, M. J., Ulrich, J.: Controlling the Internal Diameter of Nanotubes by Changing the Concentration of the Antisolvent, Crystal Growth & Design 7 (2007) 9, 1615-1617

[Dir91]   Dirksen, J. A., Ring, T. A.: Fundamentals of Crystallization: Kinetic Effects on Particle Size Distributions and Morphology, Chemical Engineering Science 46 (1991) 10, 2389-2427

[Dok04a]   Doki, N., Yokota, M., Kido, K., Sasaki, S., Kubota, N.: Reliable and Selective Crystallization of the Metastable α-Form Glycine by Seeding, Crystal Growth & Design 4 (2004) 1, 103-107

[Dok04b]   Doki, N., Seki, H., Takano, K., Asatani, H. Yokota, M., Kubota, N.: Process Control of Seeded Batch Cooling Crystallization of the Metastable α-Form Glycine Using an In-Situ ATR-FTIR Spectrometer and an In-Situ FBRM Particle Counter, Crystal Growth & Design 4 (2004) 5, 949-953

[Dor06]   Dorao, C.A., Jakobsen, H. A.: The quadrature method of moments and its relationship with the method of weighted residuals, Chemical Engineering Science 61 (2006) 7795-7804

[Dou07]   Doughery, A., Nunnally, T.: The transient growth of ammonium chloride dendrites, Journal of Crystal Growth 300 (2007) 467-472

[Dow01]   Dowding, P. J., Goodwin, J. W., Vincent, B.: Factors governing emulsion droplet and solid particle size measurement performed using focused beam reflectance technique, Colloids and Surfaces A: Physicochemical and Engineering Aspects 192 (2001) 5-13

[Dun97]   Dunuwila, D. D., Berglund, K. A.: ATR FTIR spectroscopy for in situ measurement of supersaturation, Journal of Crystal Growth 179 (1997) 185-193

[Dun95]   Dunitz, J. D., Bernstein, J.: Disappearing Polymorphs, Accounts of Chemical Research 28 (1995) 193-200

[Dün07]   Dünnebier, G., Tups, H.: FDA PAT Initiative - Eine Anwendersicht zu technischen Möglichkeiten und aktueller industrieller Umsetzung, Chemie Ingenieur Technik 79 (2007) 12, 2019-2028

[Eft02]   Eftaxias, A., Font, J., Fortuny, A., Fabregat, A., Stüber, F.: Nonlinear kinetic parameter estimation using simulated annealing, Computers and Chemical Engineering 26 (2002) 1725-1733

[Ehr06]   Ehrl, L., Soos, M., Morbidelli, M.: Sizing Polydisperse Dispersion by Focused Beam Reflectance and Small Angle Static Light Scattering, Particle and Particle Systems Characterization 23 (2006) 438-447

[Elt07]   Elter, T.: Verwendung der modellbasierten Versuchsplanung zur Bestimmung kinetischer Konstanten bei der Kristallisation, Projekarbeit: Martin-Luther-Universität Halle-Wittenberg (Zentrum für Ingenieurwissenschaften Verfahrenstechnik/TVT), 2007

[Elw75]   Elwell, D., Scheel, H. J.: Crystal Growth from High-Temperature Solutions, Academic Press London, 1975

[Euh03]   Euhus, D. D.: Nucleation in Bulk Solutions and Crystal Growth on Heat-Transfer Surfaces During Evaporative Crystallization of Salts composed of Na_2CO_3 and Na_2SO_4, Dissertation: Georgia Institute of Technology, 2003 (http://smartech.gatech.edu/handle/1853/5401)

[Eur07]   European Pharmacopoeia 5.6 (Online Version, http://online.edqm.eu/entry.htm)

[Far94]   Farell, R. J., Tsai, Y.-C.: Modeling, Simulation and Kinetic Parameter Estimation in Batch Crystallization Processes, AIChE Journal 40 (1994) 4, 586-593

[Fév07]   Févotte, G.: In-situ Raman Spectroscopy for in-line control of pharmaceutical crystallization and solids elaboration processes: a review, Chemical Engineering Research and Design 85 (2007) A7, 906-920

[Fév04]   Févotte, G., Calas, J., Puel, F., Hoff, C.: Applications of NIR spectroscopy to monitoring and analysing the solid state during industrial crystallization processes, International Journal of Pharmaceutics 273 (2004) 159-169

[Fév02]   Févotte, G.: New perspectives for the on-line monitoring of pharmaceutical crystallization processes using in situ infrared spectroscopy, International Journal of Pharmaceutics 241 (2002) 263-278

[Fév96]   Févotte, G., Klein, J. P.: A new policy for the estimation of the course of supersaturation in batch crystallization, The Canadian Journal of Chemical Engineering 74 (1996) 372-384

[Fie07]   Fiebig, A., Jones, M. J., Ulrich, J.: Predicting the Effect of Impurity Adsorption on Crystal Morphology, Crystal Growth & Design 7 (2007) 9, 1623-1627

[Fin99]   Finnie, S. D., Ristic, R. I., Sherwood, J. N., Zikic, A. M.: Morphological and growth rate distributions of small self-nucleated paracetamol crystals grown from pure aqueous solutions, Journal of Crystal Growth 207 (1999) 308-318

[For06]   Forsberg, K. M., Rasmuson, A. C.: Crystal growth kinetics of iron fluoride trihydrate, Journal of Crystal Growth 296 (2006) 213-220

[Fra07]   Franceschini, G., Macchietto, S.: Validation of a Model for Biodiesel Production through Model-Based Experiment Design, Industrial and Engineering Chemistry Research 46 (2007) 1, 220-232

[Fuj05]   Fujiwara, M., Nagy, Z. K., Chew, J. W., Braatz, R. D.: First-principles and direct design approaches for the control of pharmaceutical crystallization, Journal of Process Control 15 (2005) 493-504

[Fuj02]   Fujiwara, M., Chow, P. S., Ma, D. L., Braatz, R. D.: Paracetamol Crystallization Using Laser Backscattering and ATR-FTIR Spectroscopy: Metastability, Agglomeration and Control, Crystal Growth & Design 2 (2002) 5, 363-370

[Gah99a]   Gahn, C., Mermann, A.: Brittle fracture in crystallization processes. Part A. Attrition and abrasion of brittle solids, Chemical Engineering Science 54 (1999) 1273-1282

[Gah99b]   Gahn, C., Mermann, A.: Brittle fracture in crystallization processes. Part B. Growth of fragments and scale-up of suspension crystallizers, Chemical Engineering Science 54 (1999) 1283-1292

[Gal07]   Galvanin, F., Macchietto, S., Bezzo, F.: Model-Based Design of Parallel Experiments, Industrial and Engineering Chemistry Research 46 (2007) 3, 871-882

[Gar04]   Gardner, C. R., Almarsson, O., Chen, H., Morissette, S., Peterson, M., Zhang, Z. et al.: Application of high throughput technologies to drug substance and drug product development, Computers and Chemical Engineering 28 (2004) 943-953

[Gar02]   Garside, J., Mersmann, A., Nyvlt, J.: Measurement of Crystal growth and nucleation rates, 2nd Edition, IChemE Rugby, 2002

[Gar85]   Garside, J.: Industrial Crystallization from Solution, Chemical Engineering Science 40 (1985) 1, 3-26

[Gar84]   Garside, J., Tavare, N. .S.: Crystallization as Chemical Reaction Engineering, IChemE Symposium Series 87 (1984) 767-782

[Gar80]   Garside, J., Shah, M. B.: Crystallization Kinetics from MSMPR Crystallizer, Industrial and Engineering Chemistry Process Design and Development 19 (1980) 509-514

[Gar75]   Garside, J., Janssen-van Rosmalen, R., Bennema, P.: Verification of Crystal Growth Rate Equations, Journal of Crystal Growth 29 (1975) 353-366

[Gas03]   Gasteiger, J., Engel, T. (eds.): Chemoinformatics - A Textbook, Wiley-VCH Weinheim, 2003

[Gav97]   Gavezotti, A., Filippini, G., Kroon, J., van Eijck, B. P., Klewinghaus, P.: The Crystal Polymorphism of Tetrolic Acid (CH$_3$C $\equiv$ CCOOH): A Molecular Dynamics Study of Precursors in Solution, and a Crystal Structure Generation, Chemistry A European Journal 3 (1997) 6, 893-899

[Gel69]   Gellert, W., Küstner, H., Hellwich, M., Kästner, H. (eds.): Kleine Enzyklopädie - Mathematik, 4th Edition, VEB Bibliographisches Institut Leipzig, 1969

[Gen05]   Genceli, F. E., Himawan, C., Witkamp, G. J.: Inline determination of supersaturation and metastable zone width of MgSO$_4$·12H$_2$O with conductivity and refractive index measurement techniques, Journal of Crystal Growth 275 (2005) e1757-e1762

[Geo07]   Georgia State University, Department of Chemistry, http://chemistry.gsu.edu/glactone/PDB/Proteins/Classic/132l.html, 2007

[Ger01]   Gerstlauer, A. A.: Population Model for Crystallization Processes using Two Independent Particle Properties, Chemical Engineering Science 56 (2001) 2553-2565

[Gin93]   Ginde, R. M., Myerson, A. S.: Effect of impurities on cluster growth and nucleation, Journal of Crystal Growth 126 (1993) 216-222

[Gin92]   Ginde, R. M., Myerson, A. S.: Cluster Size estimation in binary supersaturated solutions, Journal of Crystal Growth 116 (1992) 41-47

[Giu03]   Giulietti, M., Guardani, R., Nascimento, A. O., Arntz, B.: In-Line Monitoring of Crystallization Processes using Laser Reflection Sensor and a Neural Network Model, Chemical Engineering and Technology 26 (2003) 3, 267-272

[Gla04]   Glade, H., Ilyaskarov, A. M., Ulrich, J.: Determination of Crystal Growth Kinetics Using Ultrasonic Technique, Chemical Engineering and Technology 27 (2004) 4, 736-740

[Gór05]   Górak, A., Schoenmakers, H.: Positionspapier des VDI·GVC-Fachausschusses "Fluidverfahrenstechnik", Chemie Ingenieur Technik, 77 (2005) 9, 1443-1449

[Gra05]   Granberg, R. A., Rasmuson, Å. C.: Crystal Growth Rates of Paracetamol in Mixtures of Water + Acetone + Toluene, AIChE Journal 51 (2005) 9, 2441-2456

[Gra01]   Granberg, R. A., Ducreux, C., Gracin, S., Rasmuson, Å. C.: Primary Nucleation of paracetamol in acetone-water mixtures, Chemical Engineering Science 56 (2001) 2305-2313

[Gro07]   Grosch, R., Briesen, H., Marquardt, W.: Generalization and Numerical Investigation of QMOM, AIChE Journal 53 (2007) 1, 207-227

[Gro06]   Grohe, B., Rogers, K. A., Goldberg, H. A., Hunter, G. K.: Crystallization kinetics of calcium oxalate hydrates studied by scanning confocal interference microscopy, Journal of Crystal Growth 295 (2006) 148-157

[Gro00]   Grossmann, I. E., Westerberg, A. W.: Research Challenges in Process Systems Engineering, AIChE Journal 46 (2000) 9, 1700-1703

[Grö03]   Grön, H., Borissova, A., Roberts, K. J.: In-Process ATR-FTIR Spectroscopy for Closed-Loop Supersaturation Control of a Batch Crystallizer Producing Monosodium Glutamate Crystals of Defined Size, Industrial and Engineering Chemistry Research 42 (2003) 198-206

[Hal93]   Halász, S., Bodor, B.: On the morphological and chemical stability of vitamin C crystals, Journal of Crystal Growth 128 (1993) 1212-1217

[Hal53]   Hall, J. R., Wishaw, B. F., Stokes, R. H.: The Diffusion Coefficients of Calcium Chloride and Ammonium Chloride in Concentrated Aqueous Solutions at 25°C, Journal of the American Chemical Society 75 (1953) 1556-1560

[Han02]   Hansen, G., Liu, S., Lu, S.-Z., Hellawell, A.: Dendritic array growth in the systems NH_4Cl-H_2O and $[CH_2CN]_2$-H_2O: steady state measurements and analysis, Journal of Crystal Growth 234 (2002) 731-739

[Har01]   Hartel, R. W.: Crystallization in foods, Aspen food engineering series, Aspen Publication Gaithersburg, 2001

[Hay95a]   Hayakawa, O., Nakahira, K., Tsubaki, J.-I.: Comparison of Particle Size Analysers and Evaluation of its Measuring Technique with Fine Ceramic Powders (Part 1) - Oxide Powders, JFCC Review 7 (1995) 136-142

[Hay95b]   Hayakawa, O., Nakahira, K., Tsubaki, J.-I.: Evaluation of Fine Ceramics Raw Powders with Particle Size Analyzers having Different Measuring Principle and Its Problem, JFCC Review 7 (1995) 150-157

[Hea06]   Heath, A. R., Bahri, P. A., Fawell, P. D., Farrow, J. B.: Polymer Flocculation of Calcite: Population Balance Model, AIChE Journal 52 (2006) 5, 1641-1653

[Hea02]   Heath, A. R., Fawell, P. D., Bahri, P. A., Swift, J. D.: Estimating Average Particle Size by Focused Beam Reflectance Measurement (FBRM), Particle and Particle Systems Characterization 19 (2002) 84-95

[Hef03]   Hefter, G. T., Tomkins, R. P. T. (eds.): The Experimental Determination of Solubilities, Wiley Series in Solution Chemistry, Wiley Chichester, 2003

[Hei08a]   Heijna, M. C. R., van Enckevort, W. J. P., Vlieg, E.: Growth Inhibition of Protein Crystals: A Study of Lysozyme Polymorphs, Crystal Growth & Design 8 (2008) 1, 270-274

[Hei08b]   Heinrich, J., Elter, T., Ulrich, J.: Determination of crystallization kinetics using laser reflectance measurements and model-based experimental design and analysis, Proceedings, 17th International Symposium on Industrial Crystallization 14.-17.09 2008, Maastricht/Netherlands, ed. by Jansens, P., Ulrich, J., EFCE Event Number 665, 2008, 675-682

[Hei08c]   Heinrich, J., Ulrich, J.: Im Online-Einsatz – Bestimmung des Gehaltes and Saccharose und invertiertem Zucker, Lebensmitteltechnik 7/8 (2008), 48-49

[Hei07]   Heinrich, J., Ulrich, J.: Determination of Crystallization Kinetics using Novel Technologies, Proceedings, International Congress on Particle Technology (PARTEC 2007) 27.-29.03. 2007 Nürnberg/Germany, ed. by Peukert, W., Schreglmann, C., Proceedings CD, Nürnberg Messe GmbH Nürnberg, 2007

[Hei06]   Heinrich, J.: Neuheiten im Bereich der Kristallisation und Kristallisatoren (ACHEMA Berichte), Chemie Ingenieur Technik 78 (2006) 10, 1466-1471

[Hei05]   Heinrich, J., Ulrich, J.: General considerations on predicting the influence of solubility on the maximum achievable particle size - A case study on pseudo-polymorphs, Proceedings, 16th International Symposium on Industrial Crystallization 11.-14.09 2005, Dresden/Germany, ed. by Ulrich, J., VDI-Berichte 1901, VDI-Verlag Düsseldorf, 2005, 85-90

[Hei94]   van der Heijden, A. E. D. M., van Rosmalen, G. M.: Industrial Mass Crystallization, in: Handbook of Crystal Growth 2 (Bulk Crystal Growth), Part A: Basic Techniques (ed.: D. T. J. Hurle), Elsevier Science Publishers Amsterdam, 1994, 315-415

[Hil06]   Hilfiker, R. (ed.): Polymorphism in the pharmaceutical industry, Wiley-VCH Weinheim, 2006

[Hin83]   Hindmarsh, A. C.: "ODEPACK, A Systematized Collection of ODE Solvers, in Scientific Computing, Volume 1 (IMACS Transactions on Scientific Computation) (eds.: Stepleman, R. S., Carver, M.), North-Holland Publ. Co. Amsterdam, 1983, 55-64

[Hip00]   Hipp, A. K., Walker, B., Mazzotti, M., Morbidelli, M.: In-Situ Monitoring of Batch Crystallization by Ultrasound Spectroscopy, Industrial and Engineering Chemistry Research 39 (2000) 783-789

[Hob91]   Hobbel, E. F., Davies, R., Rennie, F. W., Allen, T., Butler, L.E.: Modern Methods of On-Line Size Analysis for Particulate Process Streams, Particle and Particle Systems Characterization 8 (1991) 29-34

[Hof05]   Hofmann, G., Situation of Plant Construction in Industrial Crystallization - A process Intensification, Proceedings, 16th International Symposium on Industrial Crystallization 11.-14.09 2005, Dresden/Germany, ed. by Ulrich, J., VDI-Berichte 1901, VDI-Verlag Düsseldorf, 2005, 759-772

[Hof04]   Hofmann, G. (ed.): Kristallisation in der Industrie, Wiley-VCH Weinheim, 2004

[Hoj07]   Hojjati, H., Sheikhzadeh, M., Rohani, S.: Control of Supersaturation in a Semibatch Antisolvent Crystallization Process Using a Fuzzy Logic Controller, Industrial and Engineering Chemistry Research 46 (2007) 4, 1232-1240

[Hor06]   ter Horst, J. H., Kramer, H. J. M., Jansens, P. J.: Towards a Crystalline Product Quality Prediction Method by Combining Process Modeling and Molecular Simulations, Chemical Engineering and Technology 29 (2006) 2, 175-181

[Hou06]   Hounslow, M. J., Reynolds, G. K.: Product Engineering for Crystal Size Distribution, AIChE Journal 52 (2006) 7, 2507-2517

[Hou81]   House, W. A.: Kinetics of Crystallization of Calcite from Calcium Bicarbonate Solutions, Journal of the Chemical Society, Faraday Transactions 1: Physical Chemistry in Condensed Phases 77 (1981) 341-359

[Hu08]   Hu, X., Cunningham, J. C., Winstead, D.: Study growth kinetics in fluidized bed granulation with at-line FBRM, International Journal of Pharmaceutics 347 (2008) 54-61

[Hu06]   Hu, B., Angeli, P., Matar, O. K., Lawrence, J., Hewitt, G. F.: Evaluation of Drop Size Distribution from Chord Length Measurements, AIChE Journal 52 (2006) 3, 931-939

[Hu05]   Hu, Y, Liang, J. K., Myerson, A. S., Taylor, L. S.: Crystallization Monitoring by Raman Spectroscopy: Simultaneous Measurement of Desupersaturation Profile and Polymorphic Form in Flufenamic Acid Systems, Industrial and Engineering Chemistry Research 44 (2005) 1233-1240

[Hu04]   Hu, Q., Rohani, S., Wang, D. X., Jutan, A.: Nonlinear Kinetic Parameter Estimation for Batch Cooling Seeded Crystallization, AIChE Journal 50 (2004) 8, 1786-1794

[Huk03]   Hukkanen, E. J., Braatz, R. D.: Measurement of Particle Size Distribution in Suspension Polymerzation using in situ laser backscattering, Sensors and Actuators B96 (2003) 451-459

[Hul64]   Hulburt, H. M., Katz, S.: Some problems in particle technology - A statistical mechanical formulation, Chemical Engineering Science 19 (1964) 555-574

[Hur93]   Hurle, D. T. J. (ed.): Handbook of Crystal Growth, Fundamentals, Part A: Thermodynamics and Kinetics, Elsevier Science Publishers Amsterdam, 1993

[Iga03]   Igarashi, K., Sasaki, Y., Azuma, M., Noda, H., Ooshima, H.: Control of Polymorphs on the Crystallization of Glycine Using a WWDJ Batch Crystallizer, Engineering in Life Sciences 3 (2003) 3, 159-163

[Iss05]   Issanchou, S., Cognet, P., Cabassud, M.: Sequential Experimental Design Strategy for Rapid Kinetic Modeling of Chemical Synthesis, AIChE Journal 51 (2005) 1773-1781

[Ito05]   Itoa, A., Yamanobe-Hadab, M., Shindo, H.: In situ AFM observation of polymorphic transformation at crystal surface of glycine, Journal of Crystal Growth 275 (2005) 1691-1695

[Jag96]   Jagadesh, D., Kubota, N., Yokota, M., Sato, A., Tavare, N. S.: Large and mono-sized product crystals from natural cooling mode batch crystallizer, Journal of Chemical Engineering of Japan 29 (1996) 5, 865-873

[Jäg06]   Jäger, K., Ulrich, J.: Influence of Additives on the Growth Behaviour of Sodium Chloride Crystals, Proceedings, 13th International Workshop on Industrial Crystallization 13.-15.09 2006, Delft/Netherlands, ed. by Jansens, P. J., ter Horst, J. H., Jiang, S., IOS Press Amsterdam, 2006, 217-222

[Jan06]   Jansens, P. J.: Industrial Crystallization - from molecular mechanics to mechanical design, DECHMA Tätigkeitsbericht 2005 (Blick in die Forschung), Himmer AG Augsburg, 2006

[Jef03]   Jeffers, P., Raposo, S., Lima-Costa, M.-E., Connolly, P., Glennon, B., Kieran, P.M.: Focussed beam reflectance measurement (FBRM) monitoring of particle size and morphology in suspension cultures of Morinda citrifolia and Centaurea calcitrapa, Biotechnology Letters 25 (2003) 2023-2028

[Jim92]   Jimbo, G., Tsubaki, J., Yamamoto, H.: Comparison of the measured results of particle size by several kinds of measuring instruments (Report of Japanese Working Parties), Proceedings, Particle Size Analysis 17.-19.09 1991, Loughborough/UK, ed. by Stanley-Wood, N. G., Lines, R. W., The Royal Society of Chemistry Cambridge, 1992, 67-80

[Joh07]   John, V., Angelov, I., Öncül, A.A., Thévenin, D.: Techniques for the reconstruction of a distribution from a finite number of its moments, Chemical Engineering Science 62 (2007) 2890-2904

[Joh99]   John, M. R.: Crystallization, Proteins, Kinetics, in: Encyclopedia of Bioprocess Technology: Fermentation, Biocatalysis and Bioseparation (eds.: Flickinger, M. C., Drew, S. W.), Volume 2, Wiley New York, 1999, 755-765

[Jon02]   Jones, A. G.: Crystallization Process Systems, Butterworth-Heinemann Oxford, 2002

[Jon86]   Jones, A. G., Budz, J., Mullin, J. W.: Crystallization Kinetics of Potassium Sulfate in an MSMPR Agitated Vessel, AIChE Journal 32 (1986) 12, 2002-2006

[Jud04]   Judat, B., Kind, M.: Morphology and Internal Structure of Barium Sulfate - Derivation of a new Growth Mechanism, Journal of Colloid and Interface Science 269 (2004) 341-353

[Jud03]   Judat, B.: Über die Fällung von Bariumsulfat - Vermischungseinfluß und Partikelbildung, Dissertation: TH-Karlsruhe, Shaker Aachen, 2003

[Jud95]   Judge, R. A., Johns, M. R., White, E. T.: Protein Purification by Bulk Crystallization: The Recovery of Ovalbumin, Biotechnology and Bioengineering 48 (1995) 316-323

[Kag05]   Kagoshima, M., Mann, R.: Interactions of Precipitation and Fluid Mixing with Model Validation by Electrical Tomography, Chemical Engineering Research and Design 83 (2005) A7, 806-810

[Kah70]   Kahlweit, M.: On the dendritic growth of NH_4Cl crystals from aqueous solutions, Journal of Crystal Growth 6 (1970) 125-129

[Kai08]   Kail, N., Briesen, H., Marquardt, W.: Analysis of FBRM Measurements by means of a 3D Optical Model, Powder Technology 185 (2008) 3, 211-222

[Kai07]   Kail, N., Briesen, H., Marquardt, W.: Advanced Geometrical Modeling of Focused Beam Reflectance Measurement (FBRM), Particle and Particle Systems Characterization 24 (2007) 184-192

[Kal07]   Kalbasenka, A. N., Spierings, L. C. P., Huesman, A. E. M., Kramer, H. J. M.: Application of Seeding as a Process Actuator in a Model Predictive Control Framework for Fed-Batch Crystallization of Ammonium Sulphate, Particle and Particle Systems Characterization 24 (2007) 40-48

[Kal05]   Kalbasenka, A. N., Virone, C., Huesman, A. E. M., Kramer, H. J. M.: Application of an ultrasonic analyser for supersaturation measurement in an 1100-L DTB Crystallizer, Proceedings, 16th International Symposium on Industrial Crystallization 11.-14.09 2005, Dresden/Germany, ed. by Ulrich, J., VDI-Berichte 1901, VDI-Verlag Düsseldorf, 2005, 1105-1110

[Kas00]   Kashchiev, D. Nucleation: Basic Theory with Applications, Butterworth-Heinemann Oxford, 2000

[Kel99]   Kelkar, V. V., Ng, K. N.: Design of Reactive Crystallization Systems Incorporating Kinetics and Mass-Transfer Effects, AIChE Journal 45 (1999) 1, 69-81

[Kel87]   Keller II, G. E.: Separations: new directions for an old field, AIChE Monography Series 83 (1987) 17, 54

[Kem08]   Kempkes, M., Eggers, J., Mazzotti, M.: Measurement of particle size and shape by FBRM and in situ microscopy, Chemical Engineering Science 63 (2008) 19, 4656-4675

[Kes06]   Kessler, R. W. (ed.): Prozessanalytik: Strategien und Fallbeispiele aus der industriellen Praxis, Wiley-VCH Weinheim, 2006

[Kim01]   Kim, K.-J., Mersmann, A.: Estimation of metastable zone width in different nucleation processes, Chemical Engineering Science 56 (2001) 2315-2324

[Kim96]   Kim, S., Myerson, A. S.: Metastable Solution Thermodynamic Properties and Crystal Growth Kinetic, Industrial and Engineering Chemistry Research 35 (1996) 1078-1084

[Kin02]   Kind, M.: Colloidal Aspects of Precipitation Processes, Chemical Engineering Science 57 (2002) 4287-4293

[Kin94]   Kind, M., Wellinghoff, G.: Vergleich der Lösungskristallisation organischer und anorganischer Stoffsysteme, Chemie Ingenieur Technik 66 (1994) 8, 1064-1068

[Kin89]   Kind, M.: Über die Übersättigung während der Kornkristallisation aus Lösungen, Dissertation: Technical University of München, München, 1989

[Kle91]   Klein, J. P.: Chemical Reaction Engineering Models and their Application to Crystallization Processes, in: Advance in Industrial Crystallisation (eds.: J. Garside, R. J. Davey, A. G. Jones), Butterworth-Heinemann Oxford, 1991, 182-196

[Kna86]   Knapp, H.: Physical Properties in Process Design - Past, Present and Future, Fluid Phase Equilibrium 29 (1986) 1-21

[Kni91]   Knight, C. A., Cheng, C. C., Devries, A. L.: Adsorption of a helical antifreeze peptides on specific ice crystal surface planes, Biophysical Journal 59 (1991) 2, 409-418

[Koc06]   Kockmann, N.: Micro Process Engineering - Fundamentals, Devices, Fabrication and Applications, Wiley Series in Advanced Micro and Nanosystems, Volume 5, Wiley-VCH Weinheim, 2006

[Kou05]   Kougoulos, E., Jones, A. G., Wood-Kaczmar, M. W.: Modelling Particle disruption of an organic fine chemical compound using Lasentec focused beam reflectance monitoring (FBRM) in agitated suspension, Powder Technology 155 (2005) 153-158

[Kör02]   Körkel, S.: Numerische Methoden für Optimale Versuchsplanungsprobleme bei nichtlinearen DAE-Modellen, Dissertation: University of Heidelberg, IWR Heidelberg, 2002

[Kra03a]   Kramer, H. J. M., Jansens, P. J.: Tools for design and control of industrial crystallizers - state of the art and future needs, Chemical Engineering and Technology 26 (2003) 3, 247-255

[Kra03b]   Kraume, M. (ed.): Mischen und Rühren - Grundlagen und moderne Verfahren, Wiley-VCH Weinheim, 2003

[Kra88]   Kraume, M., Zehner, P.: Suspendieren im Rührbehälter - Vergleich unterschiedlicher Berechnungsgleichungen, Chemie Ingenieur Technik 60 (1988) 11, 822-829

[Kue97]   Kühberger, M., Mersmann, A.: Improved Product Quality at a cooling crystallization process by measurement and control of supersaturation, Chemical Engineering Research and Design 75 (1997) A2, 213-218

[Kwo06]   Kwok, K. S., Chan, H. C., Chan, C. K., Ng, K. M.: Experimental Determination of Solid-Liquid Equilibrium Phase Diagrams for Crystallization-Based Process Synthesis, Industrial and Engineering Chemistry Research 44 (2005) 3788-3798

[Lac99]   Lacmann, R., Herden, A., Mayer, C.: Kinetics of Nucleation and Crystal Growth - Review, Chemical Engineering and Technology 22 (1999) 4, 279-289

[Lan02]   Langston, P. A.: Comparison of least-squares method and Bayes' theorem for deconvolution of mixture composition, Chemical Engineering Science 57 (2002) 2371-2379

[Lan01]   Langston, P. A., Jones, T. F.: Non-Spherical 2-Dimensional Particle Size Analysis from Chord Measurements using Bayes' Theorem, Particle and Particle Systems Characterization 18 (2001) 12-21

[Lar07]   Larson, P. A., Rawlings, J. B., Ferrier, N. J.: Model-based object recognition to measure crystal size and shape distributions from in-situ video images, Chemical Engineering Science 62 (2007) 1430-1441

[Lar86]   Larson, M. A., Garside, J.: Solute Clustering and Interfacial Tension, Journal of Crystal Growth 76 (1986) 88-92

[Law04]   Lawrence, X. Y., Lionberger, R. A., Raw, A. S., D'Costa, R., Wo, H., Hussain, A. S.: Applications of process analytical technology to crystallization processes, Advanced Drug Delivery Reviews 56 (2004) 349-369

[Law97]   Law, D. J., Bale, A. J., Jones, S. E.: Adaptation of focused beam reflectance measurement to in-situ particle sizing in estuaries and coastal waters, Marine Geology 140 (1997) 47-59

[Lec95]   Lechuga-Ballesteros, D., Rodriguez-Hornedo, N.: The influence of additives on the growth kinetics and mechanism of L-aniline crystals, International Journal of Pharmaceutics 115 (1995) 139-149

[Lee02]   Lee, K., Lee, J. H., Yang, D. R., Mahoney, A. W.: Integrated run to-run and on-line model-based control of particle size distribution for a semi-batch precipitation reactor, Computers and Chemical Engineering 26 (2002) 1117-1131

[Lee79]   van Leeuwen, C., Blomen, L. J. M. J.: On the presentation of growth curves for growth from solution, Journal of Crystal Growth 46 (1979) 96-104

[Les02]   Leschonski, K.: Particle Size Analysis and Characterization of a Classification Process, in: Ullmann's Encyclopedia of Industrial Chemistry, 7th Edition, Wiley Weinheim, 2007 (Online Version)

[Les84]   Leschonski, K.: Representation and Evaluation of Particle Size Analysis Data, Particle Characterization 1 (1984) 89-95

[Lew01]   Lewiner, F., Klein, J. P., Puel, F., Févotte, G.: On-line ATR FTR measurement of supersaturation during solution crystallization processes. Calibration and applications on three solute/solvent systems, Chemical Engineering Science 56 (2001) 2069-2084

[Li07a]   Li, C., Kirkwood, K. L., Brayer, G. D.: The Biological Crystallization Resource: Facilitating Knowledge-Based Protein Crystallizations, Crystal Growth & Design 7 (2007) 11, 2147-2152

[Li07b]   Li, J., Xiao, J., Huang, Y., Lou, H. H.: Integrated Process and Product Analysis: A Multiscale Approach to Paint Spray, AIChE Journal 53 (2007) 11, 2841-2857

[Li06]   Li, M., Wilkinson, D., Patchigolla, K.: Obtaining Particle Size Distribution from Chord Length Measurements, Particle and Particle Systems Characterization 23 (2006) 170-174

[Li05a]   Li, M., Wilkinson, D., Patchigolla, K.: Comparison of Particle Size Distributions Measured Using Different Techniques, Particulate Science and Technology 23 (2005) 265-284

[Li05b]   Li, M., Wilkinson, D.: Determination of non-spherical particle size distribution from chord length measurements. Part 1: Theoretical Analysis, Chemical Engineering Science 60 (2005), 3251-3265

[Li05c]   Li, M., Wilkinson, D., Patchigolla, K.: Determination of non-spherical particle size distribution from chord length measurements. Part 2: Experimental validation, Chemical Engineering Science 60 (2005) 4992-5003

[Li92]   Li, L., Rodríguez-Hornedo, N.: Growth kinetics and mechanism of glycine crystals, Journal of Crystal Growth, 121 (1992) 33-38

[Lie99]   Lier, O.: Solvent Effects in Crystallization Processes, Proceedings, 14th International Symposium on Industrial Crystallization 12.-16.09 1999, Cambridge/UK, ed. by Garside, J., Proceedings CD, IChemE Rugby, 1999

[Lin08]   Lindenberg, C., Schöll, J., Vicum, L., Mazzotti, M., Brozio, J.: L-Glutamic Acid Precipitation: Agglomeration Effects, Crystal Growth & Design 8 (2008) 1, 224-237

[Lin07]   Lin, Y., Thomsen, K., de Hemptinne, J.-C.: Multicomponent Equations of State for Electrolytes, AIChE Journal 53 (2007) 4, 989-1005

[Lio04]   Liotta, V., Sabesan, V.: Monitoring and Feedback Control of Supersaturation Using ATR-FTIR to Produce an Active Pharmaceutical Ingredient of a Desired Crystal Size, Organic Process Research and Development 8 (2004) 488-494

[Liu07]   Liu, X., Hatziavramidis, D., Arastoopour, H., Myerson, A. S.: CFD Simulations for Analysis and Scale-up of Anti-Solvent Crystallization, AIChE Journal 52 (2007) 10, 3621-3625

[Löf02]   Löffelmann, M., Mersmann, A.: How to measure supersaturation?, Chemical Engineering Science 57 (2002) 4301-4310

[Lor04]   Lorenz, H.: Heterogene Prozesse am Beispiel der Verbrennung fester Stoffe und der Kristallisation aus Lösung, Habilitationsschrift: Otto-von-Guericke Universität Magdeburg, 2004 (http://diglib.uni-magdeburg.de/Dissertationen/2004/heilorenz.htm)

[Lou06]   Louhi-Kultanen, M., Karjalainen, M., Rantanen, J., Huhtanen, M., Kallas, J.: Crystallization of glycine with ultrasound, International Journal of Pharmaceutics 320 (2006) 23-29

[Lov05]   Lovick, J., Mouza, A. A., Paras, S. V., Lye, G. J., Angeli, P.: Drop size distribution in highly concentrated liquid-liquid dispersions using a light back scattering method, Journal of Chemical Technology and Biotechnology 80 (2005) 545-552

[Lu06]   Lu, J., Wang, J.-K.: Agglomeration, Breakage, Population Balance, and Crystallization Kinetics of Reactive Precipitation Process, Chemical Engineering Communications 193 (2006) 891-902

[Lüh96]   Lühmann, J.: Optische on-line Meßtechnik zur Bestimmung der Kristallwachstumsgeschwindigkeit, Dissertation: University of Bremen, Aachen - Mainz, 1996

[Ma08]   Ma, C. Y., Wang, X. Z., Roberts, K. J.: Morphological Population Balance for Modeling Crystal Growth in Face Directions, AIChE Journal 54 (2008) 1, 209-222

[Mac07]   Machefer, S., Schnitzlein, K.: Inline Concentration Monitoring of Binary Liquid Mixtures in the Presence of a Dispersed Gas Phase with a Modified Speed of Sound Immersion Probe, Chemical Engineering and Technology 30 (2007) 10, 1381-1390

[Mah02]   Mahoney, A. W., Lorenz, H., Perlberg, A., Seidel-Morgenstern, A.: Determination of Particle Size Distribution from inline Laser Backscattering Measurements, Proceedings, 15th International Symposium on Industrial Crystallization 15.-18.09 2002, Sorrento/Italy, ed. by Chianese, A., Proceedings CD, Associazione Italiana di Ingegneria Chimica Milano, 2002

[Mah00]   Mahnke, E. U., Büscher, K., Hempel, D. C.: A Novel Approach for the Determination of Mechanical Stresses in Gas-Liquid Reactors, Chemical Engineering and Technology 23 (2000) 6, 509-513

[Mah94]   Mahajan, A. I., Kirwan, D. J.: Nucleation and growth kinetics of biochemicals measured at high supersaturations, Journal of Crystal Growth 144 (1994) 281-290

[Mah93]   Mahajan, A. I., Kirwan, D. J.: Rapid precipitation of biochemicals, Journal of Physics D: Applied Physics 26 (1993) B176-B180

[Mal97]   Malvern Instruments Ltd., Sample Dispersion & Refractive Index Guide, Worcestershire, UK, 1997

[Mar06]   Marchisio, D. L., Soos, M., Sefcik, J., Morbidelli, M.: Role of Turbulent Shear Rate Distribution in Aggregation and Breakage Processes, AIChE Journal 52 (2006) 1, 158-173

[Mar05]   Marquardt, W.: Model-based experimental analysis of kinetic phenomena in multi-phase reactive systems, Chemical Engineering Research and Design 83 (2005) A6, 561-573

[Mar04]   Marquardt, W.: Model-Based Experimental Analysis: a Systems Approach to Mechanistic Modeling of Kinetic Phenomena, Proceedings, 6th International Conference on Foundations of Computer-Aided Process Design 11.-12.07 2004, Princeton/USA, ed. by Floudas, C. A., Agrawal, R., 2004, 165-183

[Mar88]   Marchal, P., David, R., Klein, J. P., Villermaux, J.: Crystallization and Precipitation Engineering - I. An Efficient Method for Solving Population Balance in Crystallization with Agglomeration, Chemical Engineering Science 43 (1988) 1, 59-67

[Mat07]   Mathys, A., Heinz, V., Schwartz, F. H., Knorr, D.: Impact of agglomeration on the quantitative assessment of Bacillus stearothermophilus heat inactivation, Journal of Food Engineering 81 (2007) 380-387

[Mat02]   Matsuoka, M.: Secondary Growth Phenomena in Industrial Crystallization and Their Effects on Crystal Quality, Journal of Chemical Engineering of Japan 35 (2002) 11, 1025-1037

[Mat99]   Matynia, A., Wierzbowska, B.: Nucleation of Vitamin C, 14th International Symposium on Industrial Crystallization 12.-16.09 1999, Cambridge/UK, ed. by Garside, J., Proceedings CD, IChemE Rugby, 1999

[Mat98]   Matthews, H. B., Rawlings, J. B.: Batch Crystallization of a Photochemical: Modeling, Control, and Filtration, AIChE Journal 44 (1998) 5, 1119-1127

[Mat93]   Matsuoka, M., Garside, J.: The significance of mass and heat transfer during crystal growth from solution and melts, Journal of Crystal Growth 129 (1993) 385-393

[Mat91]   Matsuoka, M., Garside, J.: Non-Isothermal effectiveness factors and the role of heat transfer in crystal growth from solutions and melts, Chemical Engineering Science 46 (1991) 1, 183-192

[McD01]   McDonald, K. A., Jackman, A. P., Hurst, S.: Characterization of plant suspension cultures using the focused beam reflectance technique, Biotechnology Letters 23 (2001) 317-324

[McP99]   McPherson, A.: Crystallization of biological macromolecules, Cold Spring Harbor Laboratory Press Cold Spring Harbor, 1999

[Mén06]   Méndez del Rio, J. R., Rousseau, R.W.: Batch and Tubular-Batch Crystallization of Paracetamol: Crystal Size Distribution and Polymorph Formation, Crystal Growth & Design 6 (2006) 6, 1407-1414

[Mer05]   Mersmann, A., Kind, M., Stichlmair, J.: Thermische Verfahrenstechnik: Grundlagen und Methoden, 2nd Edition, Springer Berlin, 2005

[Mer02]   Mersmann, A., Braun, B., Löffelmann, M.: Prediction of crystallization coefficients of the population balance, Chemical Engineering Science 57 (2002) 4267-4275

[Mer01]   Mersmann, A.: Crystallization Technology Handbook, 2nd Edition, Marcel Dekker New York, 2001

[Mer00a]   Merrow, E. W.: Problems and progress in particle processing, Chemical Innovation 30 (2000) 1, 43-41

[Mer00b]   Mersmann, A., Bartosch, K., Braun, B., Eble, A., Heyer, C.: Möglichkeiten einer vorhersagenden Abschätzung der Kristallisationskinetik, Chemie Ingenieur Technik 72 (2000) 1-2, 17-30

[Mer98]   Mersmann, A., Bartosch, K.: How to predict the metastable zone width, Journal of Crystal Growth 183 (1998) 240-250

[Mer95a]   Mersmann, A.: General prediction of statistically mean growth rates of a crystal collective, Journal of Crystal Growth 147 (1995) 181-193

[Mer95b]   Merkus, H. G., Bischof, O., Drescher, S., Scarlett, B.: Precision and Accuracy in Particle Sizing. Round-robin Results from Sedimentation, Laser Diffraction and Electrical Sensing Zone Using BCR 67, Preprints/Abstracts, 6th European Symposium Particle Characterization (PARTEC 1995) 21.-23.03 1995, Nürnberg/Germany, ed. by Leschonski, K., Nürnberg Messe GmbH Nürnberg, 1995, 427-436

[Mer91]   Mersmann, A., Angerhöfer, M., Gutwald, T., Sangl, R., Wang, S.: General prediction of crystal growth rates, Crystal Properties and Preparation 36-38 (1991) 657-665

[Mer90]   Mersmann, A.: Calculation of Interfacial Tensions, Journal of Crystal Growth 102 (1990) 841-847

[Mer89]   Mersmann, A., Kind. M.: Parameters Influencing the Mean Particle Size of a Crystalline Product, Chemical Engineering and Technology 12 (1989) 414-419

[Mer88]   Mersmann, A., Kind. M.: Chemical Engineering Aspects of Precipitation from Solution, Chemical Engineering and Technology 11 (1988) 264-276

[Met06]   Mettler Toledo, Lasentec® D600 - with FBRM® Technology, Hardware Manual, 2006

[Mil94]   Miller, S. M., Rawlings, J. B.: Model Identification and Control Strategies for Batch Cooling Crystallizers, AIChE Journal 40 (1994) 8, 1312-1327

[Mit02]   Mitrovic, A. Population balance based modeling, simulation, analysis and control of crystallization processes, Dissertation: University of Stuttgart, Fortschritt-Berichte VDI 3(749), VDI-Verlag Düsseldorf, 2002

[Moh02]   Mohan, R., Myerson, A. S.: Growth kinetics: a thermodynamic approach, Chemical Engineering Science 57 (2002) 4277-4285

[Mon97]   Monnier, O., Fevotte, G., Hoff, C., Klein, J. P.: Model identification of batch cooling crystallizations through calorimetry and image analysis, Chemical Engineering Science 52 (1997) 7, 1125-1139

[Mon96]   Monnier, O., Klein, J.-P., Hoff, C., Ratsimba, B.: Particle Size Determination by Laser Reflection: Methodology and Problems, Particle and Particle Systems Characterization 13 (1996) 10-17

[Mos00]   Moscosa-Santillán, M., Bals, O., Faudeut, H., Porte, C., Delacroix, A.: Study of batch crystallization and determination of an alternative temperature-time profile by on-line turbidity analysis - application to glycine crystallization, Chemical Engineering Science 55 (2000) 3759-3770

[Mou96]   Moussaouiti, M. El., Boistell, R., Bouhaouss, A., Klein, J. P.: Agglomeration Kinetics of calcium sulphate hemihydrate crystals in sulpho-phosporic solutions, Journal of Crystal Growth 169 (1996) 118-123

[MTS07]   Meßtechnik Schwartz GmbH, WinORM 4.8 Reference Manual, Revision 42, LT-Research GmbH, 2007

[MTS06]   Meßtechnik Schwartz GmbH, Particle Size Sensor Technology, MTS Fingerprint Sensor Technology - vom Labor bis zum Prozess, 2006

[MTS04]   Meßtechnik Schwartz GmbH, WinORM 3.4 Manual, 2004

[Mul05]   Mullin, J. W.: Crystallization and Precipitation, in: Ullmann's Encyclopedia of Industrial Chemistry, 7th Edition, Wiley Weinheim, 2007 (Online Version)

[Mul01]   Mullin, J. W.: Crystallization, 4th Edition, Butterworth-Heinemann Oxford, 2001

[Mül01]   Müller, F., Polke, R., Schäfer, M., Scholz, N.: Particle System Characterization and Modelling, Particle and Particle Systems Characterization 18 (2001) 248-253

[Mye02]   Myerson, A. S. (ed.): Handbook of Industrial Crystallization, 2nd Edition, Butterworth-Heinemann Boston, 2002

[Mye99]   Myerson, A. S. (ed.): Molecular Modelling Applications in Crystallization, Cambridge University Press New York, 1999

[Mye86]   Myerson, A. S., Decker, S. E., Welping, F.: Solvent Selection and Batch Crystallization, Industrial and Engineering Chemistry Process Design and Development 25 (1986) 4, 925-929

[Na95]   Na, H.-S., Arnold, S., Myerson, A. S.: Water activity in supersaturated aqueous solutions of organic solutes, Journal of Crystal Growth 149 (1995) 229-235

[Nag07]   Nagy, Z. K.: Editorial, Special Issue Pharmaceutical Engineering, Chemical Engineering Research and Design 85 (2007) A7, 891

[Nai98]   Naito, M., Hayakawa, O., Nakahira, K., Mori, H., Tsubaki, J.: Effect of particle shape on the particle size distribution measured with commercial equipment, Powder Technology 100 (1998) 52-60

[Nan07]   Nanev, C. N.: On the Slow Kinetics of Protein Crystallization, Crystal Growth & Design 7 (2007) 8, 1533-1540

[Nar00]   Narasimhan, S., Jordache, C.: Data Reconciliation & Cross Error Detection, Gulf Publishing Company Houston, 2000

[Ner07]   Nere, N. K., Ramkrishna, D., Parker, B. E., Bell III, W. V., Mohan, P.: Transformation of the Chord-Length Distributions to Size Distributions for Non-spherical Particles with Orientation Bias, Industrial and Engineering Chemistry Research 46 (2007) 3041-3047

[Neu02]   Neumann, A. M., Kramer, H. J. M.: A Comparative Study of Various Size Distribution Measurement Systems, Particle and Particle Systems Characterization 19 (2002) 17-27

[Nic98]   Nichols, G., Frampton, C. S.: Physicochemical Characterization of the Orthorhombic Polymorph of Paracetamol Crystallized from Solution, Journal of Pharmaceutical Sciences 87 (1998) 6, 684-693

[Nie87]   Nielsen, A. E.: Rate Laws and Rate Constants in Crystal Growth, Croatica Chemica Acta 60 (1987) 3, 531-539

[Nie84a] Nielsen, A. E.: Electrolyte Crystal Growth Mechanism, Journal of Crystal Growth 67 (1984) 289-310

[Nie84b] Nielsen, A. E, Altintas, N. D.: Growth and Dissolution Kinetics of Aluminium Fluoride Trihydrate Crystals, Journal of Crystal Growth 69 (1984) 213-230

[Nie71]   Nielsen, A. E., Söhnel, O.: Interfacial tensions electrolyte crystal-aqueous solution from nucleation data, Journal of Crystal Growth 11 (1971) 3, 233-242

[Ntu07]   Ntuli, F., Lewis, A. E.: The influence of iron on the precipitation behaviour of nickel powder, Chemical Engineering Science 62 (2007) 14, 3756-3766

[Nýv95]   Nývlt, J., Ulrich, J.: Admixtures in Crystallization. VCH Weinheim, 1995

[Nýv94]   Nývlt, J., Karel, M., Pisarik, S.: Measurement of Supersaturation, Crystal Research and Technology 29 (1994) 3, 409-415

[Nýv70]   Nývlt, J., Rychly, R., Gottfried, J., Wurzelova, J.: Metastable Zone-Width of some aqueous solutions, Journal of Crystal Growth 6 (1970) 151-162

[Oha73]   Ohara, M., Reid, R. C.: Modeling Crystal Growth Rates from Solution, Prentice-Hall Englewood Cliffs, 1973

[Oht98]   Ohtaki, H. (ed.): Crystallization Processes, Wiley Series in Solution Chemistry, Wiley Chichester, 1998

[Ola07]   Olaya, M. M., Marcilla, A., Serrano, M. D., Botella, A., Reyes-Labarta, J. A.: Simultaneous Correlation of Liquid-Liquid, Liquid-Solid, and Liquid-Liquid-Solid Equilibrium Data for Water + Organic Solvent + Salt Ternary Systems. Anhydrous Solid Phase, Industrial and Engineering Chemistry Research 46 (2007) 7030-7037

[Oma06a]   Omar, W., Ulrich, J.: Effect of the addition of alcoholic miscible co-solvents on the properties of ascorbic acid in its supersaturated aqueous solution, Crystal Research and Technology 41 (2006) 5, 431-436

[Oma06b]   Omar, W.: Effect of Solvent Composition on Crystallization Process of Ascorbic Acid, Chemical Engineering and Technology 29 (2006) 1, 119-123

[Oma99]   Omar, W., Ulrich, J.: Application of Ultrasonics in the On-line Determination of Supersaturation, Crystal Research and Technology 34 (1999) 3, 379-389

[Ono04]   Ono, T., Kramer, H. J. M., ter Horst, J. H., Jansens, P. J.: Process Modeling of the Polymorphic Transformation of L-Glutamic Acid, Crystal Growth & Design 4 (2004) 6, 1161-1167

[Ort67]   Orttung, W. H., Armour, R. W.: Polarizability Anisotropy from Crystal Refractive Indices. I. Lorentz Internal Field Approximation with Application to Amino Acid Data, The Journal of Physical Chemistry 71 (1967) 9, 2846-2853

[Oul07]   Oullion, M., Puel, F., Fevotte, G., Righini, S., Carvin, P.: Industrial batch crystallization of a plate-like organic product. In situ monitoring and 2D-CSD modelling. Part 2: Kinetic modelling and identification, Chemical Engineering Science 62 (2007) 833-845

[Par03]   Park, K., Evans, J. M. B., Myerson, A. S.: Determination of Solubility of Polymorphs Using Differential Scanning Calorimetry, Crystal Growth & Design 3 (2003) 6, 991-995

[Pat08]   Patchigolla, K., Wilkinson, D.: Characterization of Organic and Inorganic Chemicals Formed by Batch-Cooling Crystallization: Shape and Size, Industrial and Engineering Chemistry Research 47 (2008) 3, 804-812

[Pat06]   Patchigolla, K., Wilkinson, D., Li, M.: Measuring Size Distribution of Organic Crystals of Different Shapes Using Different Technologies, Particle and Particle Systems Characterization 23 (2006) 138-144

[Pat97]   Pattnaik, P., Batish, V. K., Grover, S., Ahmed, N.: Bacterial ice nucleation: Prospects and perspectives, Current Science 72 (1997) 5, 316-320

[Pea04]   Pearson, A. P., Glennon, B., Kieran, P. M.: Monitoring of cell growth using the focused beam reflectance method, Journal of Chemical Technology and Biotechnology 79 (2004) 1142-1147

[Pea03]   Pearson, A. P., Glennon, B., Kieran, P. M.: Comparison of Morphological Characteristics of Streptomyces natalensis by Image Analysis and Focused Beam Reflectance Measurement, Biotechnology Progress 19 (2003) 1342-1347

[Peb96a]   van Peborgh Gooch, J. R., Hounslow, M. J.: Monte Carlo Simulation of Size-Enlargement Mechanisms in Crystallization, AIChE Journal 42 (1996) 7, 1864-1874

[Peb96b]   van Peborgh Gooch, J. R., Hounslow, M. J.: Discriminating between size-enlargement mechanisms, Chemical Engineering Research and Design 74 (1996) A7, 803-811

[Per08]   Pertig, D.: Experimentelle Untersuchungen zur Kinetik von Glycin, Projektarbeit: Martin-Luther-Universität Halle-Wittenberg (Zentrum für Ingenieurwissenschaften Verfahrenstechnik/TVT), 2008

[Per05a]   Perlberg, A., Lorenz, H., Seidel-Morgenstern, A.: Crystal Growth Kinetics via Isothermal Seeded Batch Crystallization: Evaluation of Measurement Techniques and Application to Mandelic Acid in Water, Industrial and Engineering Chemistry Research 44 (2005) 1012-1020

[Per05b]   Perlberg, A., Lorenz, H., Seidel-Morgenstern, A.: Aspects of crystal growth in chiral systems on the example of mandelic acid in water, Proceedings, 16th International Symposium on Industrial Crystallization 11.-14.09 2005, Dresden/Germany, ed. by Ulrich, J., VDI-Berichte 1901, VDI-Verlag Düsseldorf, 2005, 689-694

[Per97]   Perry, R. H., Green, D. W. (eds.): Perry's Chemical Engineers' Handbook, 7th Edition, McGraw-Hill New York, 1997

[Peu05]   Peukert, W.: General Concepts in Nanoparticle Technology and their possible Implication on Culture Science and Philosophy, Powder Technology 158 (2005) 133-140

[Pöl05]   Pöllänen, K., Häkkinen, Antti, Reinikainen, S.-P., Louhi-Kultanen, M., Nyström, L.: ATR-FTIR in monitoring of crystallization processes: comparison of indirect and direct OSC methods, Chemometrics and Intelligent Laboratory Systems, 76 (2005) 25-35

[Pon06]   Pons, M.-N., Milferstedt, K., Morgenroth, E.: Modeling of chord length distributions, Chemical Engineering Science 61 (2006) 3962-3973

[Pos05]   Postigo, M. A., Kind, M.: On the development of an in-line sensor for measuring supersaturation in crystallization processes - feasibility study on a total reflection polarimeter, Proceedings, 16th International Symposium on Industrial Crystallization 11.-14.09 2005, Dresden/Germany, ed. by Ulrich, J., VDI-Berichte 1901, VDI-Verlag Düsseldorf, 2005, 1147-1152

[Pro07]   Profio, G. D., Tucci, S., Curcio, E., Drioli, E.: Selective Glycine Polymorph Crystallization by Using Microporous Membranes, Crystal Growth & Design 7 (2007) 3, 526-530

[Pue03]   Puel, F., Fevotte, G, Klein, J. P.: Simulation and analysis of industrial crystallization processes through multidimensional population balance equations. Part 2: a study of semi-batch crystallization, Chemical Engineering Science 58 (2003) 3729-3740

[Qam08a]   Qamar, S., Ashfaq, A., Angelov, I., Elsner, M. P., Warnecke, G., Seidel-Morgenstern, A.: Numerical solutions of population balance models in preferential crystallization, Chemical Engineering Science 63 (2008) 1342-1352

[Qam08b]   Qamar, S., Warnecke, G., Elsner, M. P., Seidel-Morgenstern, A.: A Laplace transformation based technique for reconstructing crystal size distributions regarding size independent growth, Chemical Engineering Science 63 (2008) 2233-2240

[Qiu91]   Qiu, Y., Rasmuson, A. C.: Crystal growth rate parameters from isothermal desupersaturation experiments, Chemical Engineering Science 46 (1991) 7, 1659-1667

[Qu05]   Qu, H., Pöllänen, K., Louhi-Kultanen, M., Kilpiö, T., Oinas, P., Kallas, J.: Batch cooling crystallization study based on in-line measurement of supersaturation and crystal size distribution, Journal of Crystal Growth 275 (2005) el857-el862

[Qui04]   Quintana-Hernández, P., Bolanos-Reynoso, E., Miranda-Castro, B., Salcedo-Estrada, L.: Mathematical Modeling and Kinetic Parameter Estimation in Batch Crystallization, AIChE Journal 50 (2004) 7, 1407-1417

[Rag05]   Ragot, J., Chadli, M., Maquin, D.: Mass Balance Equilibration: A Robust Approach Using Contaminated Distribution, AIChE Journal 51 (2005) 5, 1569-1575

[Ram02]   Ramkrishna, D, Mahoney, A. W.: Population balance modelling - Promise for the future, Chemical Engineering Science 57 (2002) 595-606

[Ram00]   Ramkrishna, D.: Population balances. Theory and applications to particulate systems in engineering, Academic Press New York, 2000

[Ram85]   Ramkrishna, D.: The status of population balances, Reviews in Chemical Engineering, 3 (1985) 49-95

[Ran88]   Randolph, A. D., Larson, M. A.: Theory of Particulate Processes, 2nd Edition, Academic Press London, 1988

[Rap96]   Raphael, M., Rohani, S.: On-line estimation of solids concentrations and mean particle size using a turbidimetry method, Powder Technology 89 (1996) 157-163

[Raw93]   Rawlings, J. B., Miller, S. M., Witkowski, W. R.: Model Identification and Control of Solution Crystallization Processes: A Review, Industrial and Engineering Chemistry Research 32 (1993) 1275-1296

[Ret92]   Retgers, J. W.: Beiträge zur Kenntnis des Isomorphismus V, Zeitschrift für Physikalische Chemie, Stöchiometrie und Verwandtschaftslehre, 9 (1892) 267-322

[Rev03]   Reviakine, I., Georgiou, D. K., Vekilov, P. G.: Capillarity effects on crystallization kinetics: insulin, Journal of the American Chemical Society 125 (2003) 38, 11684-11693.

[Ric05]   Ricard, F., Brechtelsbauer, C., Xu, X. Y., Lawrence, C. J.: Monitoring of Multiphase Pharmaceutical Processes using Electrical Resistance Tomography, Chemical Engineering Research and Design 83 (2005) A7, 796-805

[Rit85]   Rittner, S., Steiner, R.: Die Schmelzkristallisation von organischen Stoffen und ihre großtechnische Anwendung, Chemie Ingenieur Technik 57 (1985) 2, 91-102

[Rob90]   Robinson, D., Anderson, J. E., Lin, J.-L.: Measurement of Diffusion Coefficients of Some Indoles and Ascorbic Acid by Flow Injection Analysis, Journal of Physical Chemistry 94 (1990) 1003-1005

[Rod89]   Rodriguez-Clemente, R.: Complexing and Growth Units in Crystal Growth From Solutions of Electrolytes, Journal of Crystal Growth 98 (1989) 671-629

[Roe06]   Roelands, C. P. M., ter Horst, J. H., Kramer, H. J. M., Jansens, P. J.: Analysis of Nucleation Rate Measurements in Precipitation Processes, Crystal Growth & Design 6 (2006) 6, 1380-1392.

[Roh90]   Rohani, S., Bourne, J. R.: A simplified Approach to the Operation of a Batch Crystallizer, The Canadian Journal of Chemical Engineering 68 (1990) 799-807

[Rom00]   Romagnoli, J., Sanchez, Z.: Data Processing and Reconciliation for Chemical Process Operations (Process Systems Engineering), Volume 2, Academic Press London, 2000

[Ros86]   Rosenberger, F.: Inorganic and Protein Crystal Growth - Similarities and Differences, Journal of Crystal Growth 76 (1986) 618-636

[Rou05]   O´Rourke, A. M., MacLoughlin, P. F.: A comparison of measurement techniques used in the analysis of evolving liquid-liquid dispersions, Chemical Engineering and Processing 44 (2005) 885-894

[Roz06]   Rozsa, L.: Seed Master 2: A universal crystallization transmitter and automatic seeding device, International Sugar Journal 108 (2006) 1296, 683-695

[Ruf00]   Ruf, A., Worlitschek, J., Mazzotti, M.: Modeling and Experimental Analysis of PSD Measurements through FBRM, Particle and Particle Systems Characterization 17 (2000) 167-179

[Sai98]   Saikumar, M. V., Glatz, C. E., Larson, M. A.: Lysozyme crystal growth and nucleation kinetics, Journal of Crystal Growth 187 (1998) 277-288

[Sak92]   Sakai, H., Hosogai, H., Kawakita, T., Onuma, K., Tsukamoto, K.: Transformation of α-glycine to γ-glycine, Journal of Crystal Growth 116 (1992) 421-426

[Sam00]   Samant, K. D., Berry, D. A., Ng, K. M.: Representation of High Dimensional, Molecular Solid-Liquid Phase Diagrams, AIChE Journal 46 (2000) 12, 2435-2455

[Sam01]   Samant, K. D., Ng, K. M.: Representation of High-Dimensional Solid-Liquid Phase Diagrams of Ionic Systems, AIChE Journal 47 (2001) 4, 861-879

[San07]   Sangwal, K.: Additives and Crystallization Processes: From Fundamentals to Applications, Wiley Chichester, 2007

[San02]   Sangwal, K.: On the nature of supersaturation barriers observed during the growth of crystals from aqueous solutions containing impurities, Journal of Crystal Growth 242 (2002) 215-228

[Sar07]   Sarkar, D., Rohani, S., Jutan, A.: Multiobjective Optimization of Semibatch Reactive Crystallization Processes, AIChE Journal 53 (2007) 5, 1164-1177

[Say02]   Sayan, P., Ulrich, J.: The effect of particle size and suspension density on the measurement of ultrasonic velocity in aqueous solutions, Chemical Engineering and Processing 41 (2002) 281-287

[Sca03]   Scarlett, B.: Measuring and Interpreting Particle Size Distribution, American Pharmaceutical Review 6 (2003) 4, 93-101

[Sca02]   B. Scarlett: Perspective - Particle Populations - to balance or not to balance, that is the question!, Powder Technology 125 (2002) 1-4

[Sca96]   Scarlett, B.: Characterization of Particles and Powders, Materials Science and Technology 7A(Processing of Ceramics, Part 1) (1996) 99-125

[Sca85]   Scarlett, B.: Measurement of Particle Size and Shape, some Reflections on the BCR Reference Material Programme, Particle Characterization. 2 (1985) 1-6

[Sch07]   Schwaab, M., Pinto, J. C.: Optimum reference temperature for reparameterization of the Arrhenius equation. Part 1: Problems involving one kinetic constant, Chemical Engineering Science 62 (2007) 2750-2764

[Sch06a]   Schlomach, J. Feststoffbildung bei technischen Fällprozessen - Untersuchung zur industriellen Fällung von Siliziumdioxid und Calciumcarbonat, Dissertation: University of Karlsruhe, Universitätsverlag Karlsruhe, 2006

[Sch06b]   Schwarzer, H.-C., Schwertfirm, F., Manhart, M., Schmid, H.-J., Peukert, W.: Predictive simulation of nanoparticle precipitation based on the population balance equation, Chemical Engineering Science 61 (2006) 167-181

[Sch06c]   Schöll, J., Bonalumi, D., Vicum, L., Mazzotti, M., Müller, M.: In Situ Monitoring and Modeling of the Solvent-Mediated Polymorphic Transformation of L-Glutamic Acid, Crystal Growth & Design 6 (2006) 4, 881-891

[Sch05]   Schmidt, L. D.: The Engineering of Chemical Reactions, 2nd Edition, Oxford University Press Oxford, 2005

[Sch02]   Schreiner, A., König, A.: Influence of Impurities on Nucleation and Growth rates of Organic melts, Chemical Engineering and Technology 25 (2002) 2, 181-187

[Sch01]   Schirg, P., Wissler, P.: Verfolgung und Optimierung der Kühlungskristallisation von Vitamin C mit einer Lasentec FBRM In-Line Partikelmesssonde, Chemie Ingenieur Technik 73 (2001) 4, 377-381

[Sch00]   Scheel, H. J.: Historical aspects of crystal growth technology, Journal of Crystal Growth 211 (2000) 1-12

[Sch99]   Schmerwitz, F.: Chargenkristallisation und Wachstumsdispersion - Experimentelle und theoretische Untersuchungen, Dissertation: Martin-Luther-University Halle-Wittenberg, 1999 (http://sundoc.bibliothek.uni-halle.de/diss-online/99/99H339/index.htm)

[Sea06]   Seader, J. D., Henley, E. J.: Separation process principles, 2nd Edition, Wiley Hoboken, 2006

[Sed99]   Seddon, K. R., Zaworotko, M. (eds.): Crystal Engineering, Kluwer Academic Publishers Dordrecht, 1999

[Sen06]   SenoTech GmbH, LiquiSonic - Ultraschall-Analysegerät für Flüssigkeiten, Produktbeschreibung, 2006

[Ses00]   Sessiecq, P., Gruy, P., Cournil, M.: Study of ammonium chloride crystallization in a mixed vessel, Journal of Crystal Growth 208 (2000) 555-568

[Sev97]   Seville, J. P. K., Tüzün, U., Clift, R.: Processing of Particulate Solids, Blackie Academic & Professional London, 1997

[Sha05]   Shaikh, A. A., Salman, A.D., Mcnamara, S., Littlewood, G., Ramsay, F., Hounslow, M. J.: In Situ Observation of the Conversion of Sodium Carbonate to Sodium Carbonate Monohydrate in Aqueous Suspension, Industrial and Engineering Chemistry Research 44 (2005) 9921-9930

[Sha96]   Sha, Z. L., Hatakka, H., Louhi-Kultanen, M., Palosaari, S.: Crystallization Kinetics of potassium sulphate in an MSMPR stirred crystallizer, Journal of Crystal Growth 166 (1996) 1105-1110

[Sha79]   Shamim, M., Khoo, S. B.: Some physical properties of aqueous L-Ascorbic Acid solutions, Australian Journal of Chemistry 32 (1979) 2293-2295

[She08]   Sheikhzadeh, M., Trifkovic, M., Rohani, S.: Real-time optimal control of an anti-solvent isothermal semi-batch crystallization process, Chemical Engineering Science 63 (2008) 829-839

[She01]   Sherwood, J. N., Ristic, R. I.: The influence of mechanical stress on the growth and dissolution of crystals, Chemical Engineering Science 56 (2001) 2267-2280

[Shi05]   Shi, D., Mhaskar, P., El-Farra, N. H., Christofides, P. D.: Predictive control of crystal size distribution in protein crystallization, Nanotechnology 16 (2005) 5562-5574

[Sla95]   Slaughter, D. W., Doherty, M. F.: Calculation of solid-liquid equilibrium and crystallization paths for melt crystallization processes, Chemical Engineering Science 50 (1995) 1679-1694

[Söh92]   Söhnel, O., Garside, J.: Precipitation - Basic Principles and Industrial Application, Butterworth Heinemann Oxford, 1992

[Söh78]   Söhnel, O., Mullin, J. W.: Expressions of supersaturation for systems containing hydrates, partially dissociated electrolytes and mixture of electrolytes, Chemical Engineering Science 33 (1978) 1535-1538

[Som01]   Sommer, K.: 40 Years of Presentation Particle Size Distributions - Yet Still Incorrect?, Particle and Particle Systems Characterization 18 (2001) 22-25

[Sot00]   Sotowa, K.-I., Naito, K., Kano, M., Hasebe, S., Hashimoto, I.: Application of the method of characteristics to crystallizer simulation and comparison with finite difference for controller performance evaluation, Journal of Process Control 10 (2000) 203-208

[Spa94]   Sparks, R. G., Dobbs, C. L. (Errata): The use of laser backscattering instrumentation for the on-line measurement of the particle size distribution of emulsion, Particle and Particle Systems Characterization 11 (1994) 404

[Spa93]   Sparks, R. G., Dobbs, C. L.: The use of laser backscattering instrumentation for the on-line measurement of the particle size distribution of emulsion, Particle and Particle Systems Characterization 10 (1993) 279-289

[Sta01]   Stahl, M., Aslund, B. L., Rasmuson, A. C.: Reaction Crystallization Kinetics of Benzoic Acid, AIChE Journal 47 (2001) 7, 1544-1560

[Sti95]   Stieß, M.: Mechanische Verfahrenstechnik 1, 2nd Edition, Springer-Verlag Berlin, 1995

[Str04]   Strege, C.: On (pseudo-) polymorphic phase transformations, Dissertation: Martin-Luther-University Halle-Wittenberg, 2004 (http://sundoc.bibliothek.uni-halle.de/diss-online/04/04H318/index.htm)

[Tad02]   Tadayyon, A., Rohani, S., Bennett, M. K.: Estimation of Nucleation and Growth Kinetics of Ammonium Sulfate from Transients of a Cooling Batch Seeded Crystallizer, Industrial and Engineering Chemistry Research 41 (2002) 6181-6193

[Tad98]   Tadayyon, A., Rohani, S.: Determination of Particle Size Distribution by Par-Tec® 100: Modeling and Experimental Results, Particle and Particle Systems Characterization 15 (1998) 127-135

[Tad97]   Tadayyon, A., Rohani, S., Pons, M.-N. On-line Measurement of Solids Concentration or the Mean Particle Size in a Saturated Slurry Containing Background Particles Using a Turbidity Method, Particle and Particle Systems Characterization 14 (1997) 138-141

[Tai07]   Tait, S., White, E. T., Litster, J. D., Liu, L. X.: Attrition and Secondary Nucleation for Protein Crystallization, Proceedings, International Congress on Particle Technology (PARTEC 2007) 27.-29.03. 2007 Nürnberg/Germany, ed. by Peukert, W., Schreglmann, C., Proceedings CD, Nürnberg Messe GmbH Nürnberg, 2007

[Tan96]   Tanneberger, U., Lacmann, R., Herden, A., Klapper, H., Schmiemann, D., Becker, R. A., Mersmann, A., Zacher, U.: The Dispersion of Growth Rate as a Result of Different Crystal Perfection, Journal Crystal Growth 166 (1996) 1074-1077

[Tav95]   Tavare, N. S.: Industrial Crystallization - Process Simulation Analysis and Design, Plenum Press London, 1995

[Tav87]   Tavare, N. S.: Batch crystallizers: A review, Chemical Engineering Communications 61 (1987) 1-6, 259-318

[Tav86]   Tavare, N. S., Garside, J.: Simultaneous Estimation of Crystal Nucleation and Growth Kinetics from Batch Experiments, Chemical Engineering Research and Design 64 (1986) 109-118

[Tav79]   Tavare, N. S., Chivate, M. R.: Growth and Dissolution Kinetics of Potassium Sulphate crystals in a fluidised bed crystallizer, Transactions of the Institution of Chemical Engineers 57 (1979) 35-42

[Tei05]   Teipel, U., Sisler, M.: Crystal Size Analysis - Comparison of Different Methods, Proceedings, 16th International Symposium on Industrial Crystallization 11.-14.09 2005, Dresden/Germany, ed. by Ulrich, J., VDI-Berichte 1901, VDI-Verlag Düsseldorf, 2005, 529-543

[Tei02]   Teipel, U.: Problems in Characterizing Transparent Particles by Laser Light Diffraction Spectrometry, Chemical Engineering and Technology 25 (2002) 1, 13-21

[Tho05]   Thomsen, K.: Modeling electrolyte solutions with the extended universal quasichemical (UNIQUAC) model, Pure and Applied Chemistry 77 (2005) 3, 531-542

[Tit02]   Titiz-Sargut, S, Ulrich, J.: Influence of Additives on the Width of the Metastable Zone, Crystal Growth & Design 2 (2002) 5, 371-374

[Tit03]   Titiz-Sargut, S, Ulrich, J.: Application of a protected ultrasound sensor for the determination of the width of the metastable zone, Chemical Engineering and Processing 42 (2003) 841-846

[Tog04]   Togkalidou, T., Tung, H.-H., Sun, Y., Andrews, A. T., Braatz, R. D.: Parameter Estimation and Optimization of a Loosely Bound Aggregating Pharmaceutical Crystallization Using in Situ Infrared and Laser Backscattering Measurements, Industrial and Engineering Chemistry Research 43 (2004) 6168-6181

[Tog01a]   Togkalidou, T., Fujiwara, M., Patel, S., Braatz, R. D.: Solute concentration prediction using chemometrics and ATR-FTIR spectroscopy, Journal of Crystal Growth 231 (2001) 534-543

[Tog01b]   Togkalidou, T., Braatz, R.D., Johnson, B.K., Davidson, O., Andrews, A.: Experimental Design and Inferential Modeling in Pharmaceutical Crystallization, AIChE Journal 47 (2001) 1, 160-168

[Tor05]   Torbeev, V. Y., Shavit, E., Weissbuch, I., Leiserowitz, L., Lahav, M.: Control of Crystal Polymorphism by Tuning the Structure of Auxiliary Molecules as Nucleation Inhibitors. The β-Polymorph of Glycine Grown in Aqueous Solutions, Crystal Growth & Design 5 (2005) 6, 2190-2196

[Tow04]   Towler, C. S., Davey, R. J., Lancaster, R. W., Price, C. J.: Impact of Molecular Speciation on Crystal Nucleation in Polymorphic Systems: The Condrum of γ-Glycine and Molecular 'Self Poisoning', Journal of the American Chemical Society 126 (2004) 13347-13353

[Tre96]   Treivus, E. B.: The relation between the Rate of Crystal Growth and Substance Solubility, Crystallography Reports 41 (1996) 5, 896-902

[Tri08]   Trifkovic, M., Sheikhzadeh, M., Rohani, S.: Kinetics Estimation and Single and Multi-Objective Optimization of a Seeded, Anti-Solvent, Isothermal Batch Crystallizer, Industrial and Engineering Chemistry Research 47 (2008) 1586-1595

[Ukr07]   Ukrainczyk, M., Kontrec, J., Babic-Ivancic, V., Brecevic, L., Kralj, D.: Experimental design approach to calcium carbonate precipitation in a semicontinous process, Powder Technology 171 (2007) 192-199

[Ull07]   Ullmann's Encyclopedia of Industrial Chemistry, 7th Edition, Wiley Weinheim, 2007 (Online Version)

[Ulr07]   Ulrich, J., Jones, M.: Fundamentals of Crystallization, in: Product Design and Engineering: Volume 1 Basics and Technologies (eds.: Bröckel, U., Meier, W., Wagner, G.), Wiley-VCH Weinheim, 2007, 33-58

[Ulr05]   Ulrich, J., Heinrich, J.: Reaktivkristallisation, Chemie Ingenieur Technik 77 (2005) 11, 1759-1772

[Ulr04]   Ulrich, J., Jones, M. J.: Industrial Crystallization - Developments in Research and Technology, Chemical Engineering Research and Design 82 (2004) 1567-1570

[Ulr03a]   Ulrich, J.: Solution Crystallization - Developments and New Trends, Chemical Engineering and Technology 26 (2003) 8, 832-835

[Ulr03b]   Ulrich, J., Glade, J. (eds.): Melt Crystallization, Shaker Verlag Aachen, 2003

[Ulr02a]   Ulrich, J., Strege, C.: Some aspects of the importance of metastable zone width and nucleation in industrial crystallizers, Journal of Crystal Growth 237-239 (2002) 2130-2135

[Ulr02b]   Ulrich, J.: Crystallization, in: Kirk-Othmer Encyclopedia of Chemical Technology, Volume 8, Wiley Weinheim, 2006 (Online Version)

[Ulr94]   Ulrich, J.: Entwicklungen bei der Lösungskristallisation in den letzten Jahren, Chemie Ingenieur Technik 66 (1994) 10, 1341-1345

[Ulr90]   Ulrich, J., Stepanski, M.: Use of the Laser Diffraction Technique for Particle Size Measurement at High Suspension Densities, Particle and Particle Systems Characterization 7 (1990) 25-29

[Ulr89]   Ulrich, J.: Growth Rate Dispersion - a Review, Crystal Research and Technology 24 (1989) 3, 249-257

[Ulr88]   Ulrich, J., Özoguz, Y., Stepanski, M.: Zur Begriffsklarung in der technischen Kristallisation, Chemie Ingenieur Technik 60 (1988) 6, 481-483

[Ulr85]   Ulrich, J., Ueno, t., Toyokura, K.: On the problem of the "effective" secondary nuclei, Chemical Engineering Science 40 (1985) 7, 1245-1250

[Vac06a]   Vaccaro, A., Sefcik, J., Morbidelli, M.: Modeling Focused Beam Reflectance Measurement and its Application to Sizing of Particles of Variable Shape, Particle and Particle Systems Characterization 23 (2006) 360-373

[Vac06b]   Vaccaro, A., Sefcik, J., Wu, H., Morbidelli, M., Bobet, J., Fringant, C.: Aggregation of Concentrated Polymer Latex in Stirred Vessels, AIChE Journal 52 (2006) 8, 2742-2759

[Vac03]   Vaccari, G., Tamburini, E., Tosi, S., Sgualdino, G., Bernardi, T.: In-line Control and Automatic Management of Industrial Crystallizations using NIR Technique, Chemical Engineering and Technology 26 (2003) 3, 273-276

[Ver02]   Verkoeijen, D., Pouw, G. A., Meesters, G. M. H., Scarlett, B.: Population balances for particulate processes—a volume approach, Chemical Engineering Science 57 (2002) 2287-2303

[Vic07]   Vicum, L., Mazzotti, M.: Multi-scale modeling of a mixing-precipitation process in a semibatch stirred tank, Chemical Engineering Science 62 (2007) 3513-3527

[Vog59]   Vogel, R.: Die heterogenen Gleichgewichte, 2nd Edition, Akademische Verlagsgesellschaft Geest & Portig K.-G. Leipzig, 1959

[Vol06]   Vollmer, U., Raisch, J.: Control of batch crystallization - A system inversion approach, Chemical Engineering and Processing 45 (2006) 874-885

[Vol03]   Vollmer, U., Raisch, J.: Control of batch cooling crystallization processes based on orbital flatness, International Journal of Control 76 (2003) 16, 1635-1643

[Wan08]   Wang, X. Z., Roberts, K. J., Ma, C.: Crystal growth measurement using 2D and 3D imaging and the perspectives for shape control, Chemical Engineering Science 63 (2008) 1173-1184

[Wan07]   Wang, X. Z., Calderon De Anda, J., Roberts, K. J.: Real-Time Measurement of the Growth Rates of Individual Crystal Facets Using Imaging and Image Analysis A Feasibility Study on Needle-shaped Crystals of L-Glutamic Acid, Chemical Engineering Research and Design 85 (2007) 7, 921-927

[Wan06]   Wang Z., Wang, J., Dang, L.: Nucleation, Growth, and Solvated Behavior of Erythromycin as Monitored in Situ by Using FBRM and PVM, Organic Process Research and Development 10 (2006) 450-456

[Wan96]   Wang, J. K., Ouyang, S. L., Zhang, Y.M.: Research on assessment of addition agent of crystallization with dynamic method, Tianjin University, 1996

[War06]   Ward, J. D., Mellichamp, D. A., Doherty, M. F.: Choosing an Operating Policy for Seeded Batch Crystallization, AIChE Journal 52 (2006) 6, 2046-2054

[Wei03]   Weissbuch, I., Lahav, M., Leiserowitz, L.: Toward Stereochemical Control, Monitoring, and Understanding of Crystal Nucleation, Crystal Growth & Design 3 (2003) 2, 125-150

[Wes03]   Westhoff, G. M., van de Rijt, J., Kramer, H. J. M., Jansens, P. J.: Modeling Growth Rate Dispersion in Industrial Crystallizers, Chemical Engineering and Technology 26 (2003) 3, 286-291

[Wes99]   Westad, F., Martens, H.: Shift and intensity modelling in spectroscopy - general concept and applications, Chemometrics and Intelligent Laboratory Systems 45 (1999) 361-370

[Whi07]   White, E. T., Tan, W. H., Ang, J. M., Tait, S., Litster, J. D.: The density of a protein crystal, Powder Technology 179 (2007) 55-58

[Wib05]   Wibowo, C., Kelkar, V. V., Samant, K. D., Schroer, J. W., Ng, K. M.: Development of reactive crystallization processes, in: Integrated Chemical Processes (eds.: Sundmacher, K., Kienle, A., Seidel-Morgenstern, A), Wiley-VCH Weinheim, 2005, 339-358

[Wib02a]   Wibowo, C., Ng, K. M.: Visualization of High-Dimensional Phase Diagrams of Molecular and Ionic Mixtures, AIChE Journal 48 (2002) 5, 991-1000

[Wib02b]   Wibowo, C., Samant, K. D., Ng, K. M.: High-Dimensional Solid-Liquid Phase Diagrams Involving Compounds and Polymorphs, AIChE Journal 48 (2002) 10, 2179-2192

[Wie08]   Wierzbowska, B., Piotrowski, K., Koralewska, J., Matynia, A., Hutnik, N., Wawrzyniecki, K.: Crystallization of vitamin C in a continuous DT MSMPR crystallizer - Size independent growth kinetic model approach, Crystal Research and Technology 43 (2008) 4, 381-389

[Wie07]   Wierzbowska, B., Matynia, A., Piotrowski, K., Koralewska, J.: Solubility and nucleation in L(+)-ascorbic acid-methanol-ethanol-water system, Chemical Engineering and Processing 46 (2007) 351-359

[Wil99]   Williams-Seton, L., Davey R. J., Lieberman, H. F.: Solution Chemistry and Twinning in Saccharin Crystals: A Combined Probe for the Structure and Functionality of the Crystal-Fluid Interface, Journal of the American Chemical Society 121 (1999) 4563-4567

[Wil92]   Williams, R. A., Peng, S. J., Naylor, A.: In situ measurement of particle aggregation and breakage kinetics in a concentrated suspension, Powder Technology 73 (1992) 75-83

[Wil55]   Wilke, C. R., Chang, P. C.: Correlation of diffusion coefficient in dilute solutions, AIChE Journal 1 (1955) 264-270

[Win99]   Wintermantel, K.: Process and Product Engineering - Achievements, Present and future Challenges, Chemical Engineering Science 54 (1999) 1601-1620

[Wit00]   Witjes, H., Melssen, W. J., Zandt, H. J. A., van der Graaf, M., Heerschap, A., Buydens, L. M. C.: Automatic Correction for Phase Shifts, Frequency Shifts, and Lineshape Distortions across a series of single resonance lines in large spectral data sets, Journal of Magnetic Resonance 144 (2000) 35-44

[Wit95]   Witt, W., Röthele, S.: Laser Diffraction - unlimited?, Preprints/Abstracts, 6th European Symposium Particle Characterization (PARTEC 1995) 21.-23.03 1995, Nürnberg/Germany, ed. by Leschonski, K., Nürnberg Messe GmbH Nürnberg, 1995, 277-290

[Wit90]   Witkowski, W. R., Miller, S. M., Rawlings, J. B.: Light-Scattering Measurements to Estimated Kinetic Parameters of Crystallization, ACS Symposium Series 438(Crystallization as a Separations Process) (1990) 102-114

[Wor05]   Worlitschek, J., Hocker, T., Mazzotti, M.: Restoration of PSD from Chord Length Distribution Data using the Method of Projections onto Convex Sets, Particle and Particle Systems Characterization 22 (2005) 81-98

[Wor04]   Worlitschek, J., Mazzotti, M.: Model-Based Optimization of Particle Size Distribution in Batch-Cooling Crystallization of Paracetamol, Crystal Growth & Design 4 (2004) 5, 891-903

[Wor03a]   Worlitschek, J.: Monitoring, Modelling and Optimization of Batch Cooling Crystallization, Dissertation: Swiss Federal Institute of Technology (ETH Diss Nr. 15189), 2003 (http://e-collection.ethbib.ethz.ch/view/eth:27189)

[Wor03b]   Worlitschek, J., Mazzotti, M.: Choice of the Focal Point Position Using Lasentec FBRM, Particle and Particle Systems Characterization 20 (2003) 12-17

[Wyn03]   Wynn, E. J. W.: Relationship between particle-size and chord-length distributions in focused beam reflectance measurement: stability of direct inversion and weighting, Powder Technology 133 (2003) 125-133

[Wyn97]   Wynn, E. J. W., Hounslow, M. J.: Coincidence correction for electrical-zone (Coulter-Counter) particle size analysers, Powder Technology 93 (1997) 163-175

[Wyp00]   Wypych, G.: Knovel Solvents - A Properties Database, ChemTec Publishing, (2000), Online version available at: http://www.knovel.com/knovel2/

[Xu03]   Xu, R., Guida, O. A. D.: Comparison of sizing small particles using different technologies, Powder Technology 132 (2003) 145-153

[Yaw03]   Yaws, C. L.: Yaws' Handbook of Thermodynamic and Physical Properties of Chemical Compounds, Knovel, 2003, Online version available at: http://www.knovel.com/knovel2/

[Yan08]   Yang, X., Lu, J., Wang, X.-J., Ching, C.-B.: Effect of sodium chloride on the nucleation and polymorphic transformation of glycine, Journal of Crystal Growth 310 (2008) 604-611

[Yi06]   Yi, Y. J., Myerson, A. S.: Laboratory Scale Batch Crystallization and the Role of Vessel Size, Chemical Engineering Research and Design 84 (2006) A8, 721-728

[Yu08a]   Yu, W., Erickson, K.: Chord Length Characterization Using Focused Beam Reflectance Measurement Probe - Methodologies and Pitfalls, Powder Technology 185 (2008) 24-30

[Yu08b]   Yu, Z. Q., Chow, P. S. Tan, R. B. H.,: Interpretation of Focused Beam Reflectance Measurement (FBRM) Data via Simulated Crystallization, Organic Process Research and Development 12 (2008) 4, 646-654

[Yu05]   Yu, Z. Q., Tan, R. B. H., Chow, P. S.: Effects of operating conditions on agglomeration and habit of paracetamol crystals in anti-solvent crystallization, Journal of Crystal Growth 279 (2005) 477-488

[Zha04]   Zhang, G. P., Rohani, S.: Dynamic Optimal Control of Batch Crystallization Processes, Chemical Engineering Communications 191 (2004) 356-372

Appendix

A.1   Physical and Chemical Properties of Model Systems

Within this work the following substances were used:

- Ammonium chloride (Carl Roth GmbH + Co. KG, > 99.5% Ph. Eur., USP, BP)
- Ascorbic acid (KMF-optiChem, L(±)-Ascorbic Acid, crystalline, pure)
- Glycine (Carl Roth GmbH + Co. KG, > 99%, for synthesis, α-aminoacetic acid)
- Manganese chloride, tetrahydrate (Merck KGaA, p.a.)
- Distilled water

Figure A-1 shows the respective solubility of the investigated model systems.
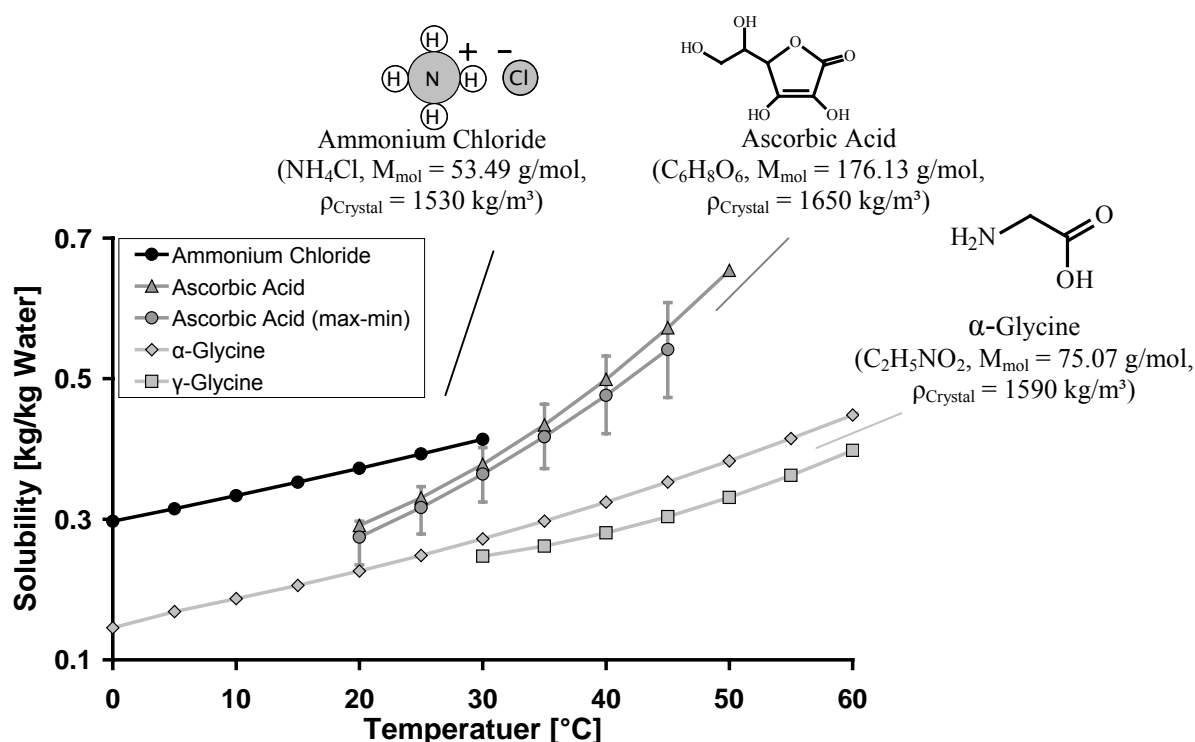
Figure A-1: Solubility data for the investigated model systems [Mul01, Par03, Oma06b]

By comparing literature references (see table A-1), a significant scattering of the solubility values for ascorbic acid was found. The bars are indicating the respective maximum and minimum values. Within this work, the data from Apelblat et al. [Ape89] and Omar et al. [Oma06a] were found to be applicable. Although the solubility for glycine is often reported in literature, it is sometimes not mentioned to which polymorph the solubility data belongs. However, only a minor scattering of the α-glycine solubility data from different authors was found. Within this work the solubility data by Park et al. [Par03] was used. Table A-1 summarises the empirical constants that were derived to predict the solubility using equation A.1 (c_{eq} [kg solute/kg water], T [°C]).

$$c_{eq} = a_1 \cdot T^2 + a_2 \cdot T + a_3 \qquad\qquad\qquad\text{(A.1)}$$

Table A-1: Empirical constants for equation A.1 (solubility)

Substance	a_1	a_2	a_3	Valid Range	References for Solubility Data
Ammonium Chloride	1.25000E-05	3.51500E-03	2.97150E-01	0 – 30 °C	[Mul01]
Ascorbic Acid	1.53732E-04	1.85994E-03	1.95591E-01	20 – 50 °C	[Ape89, Hal93, Mat99, Bod99, Oma06a]
α-Glycine	2.67480E-05	3.19730E-03	1.52109E-01	0 – 30 °C	[Dal33, Sak92, Par03, Iga03, Yi06, Che07]

The liquid density of the saturated solution was calculated using equation A.2 (ρ_{eq} [kg/m³], T [°C]) with empirical constants given in table A-2

$$\rho_{eq} = a_1 \cdot T^2 + a_2 \cdot T + a_3 \qquad\qquad\qquad\text{(A.2)}$$

Table A-2: Empirical constants for equation A.2 (liquid density of a saturated solution)

Substance	a_1	a_2	a_3	Valid Range	References for Liquid Density Data
Ammonium Chloride	-5.00000E-03	6.10000E-01	1.06610E+03	0 – 30 °C	[Mul01]
Ascorbic Acid	8.19936E-03	1.90699E+00	1.05735E+03	15 – 45 °C	[Ape07]
α-Glycine (ideal solution)	-3.90280E-03	1.61076E+00	1.04432E+03	5 – 40 °C	[Dal33], T=25 °C, ρ_{eq} = 1084.5 [Gin92], T=25 °C, ρ_{eq} = 1071.0

Experimental data for the heat of crystallization or solution and the interfacial tension are given in table A-3.

Table A-3: Heat of crystallization or solution and interfacial tension for model systems

Substance	Data	Reference
Heat of Crystallization/Solution [kJ/mol]		
Ammonium Chloride	15.9 (heat of solution, dilute solution, 25 °C)	[Mul01]
Ascorbic Acid	23.0 (heat of solution, dilute solution, 25 °C) 20.8-21.8 (heat of solution, saturated solution, 25 °C) (-)19.7 - (-)31.0 (heat of crystallization, 25 °C)	[Ape89] [Dal98, Oma06a] [Dal98, Che00]
Interfacial Tension (γ_{CL} [J/m²]), Solvent: Water		
Ammonium Chloride	0.027	[Mer90]
Glycine	0.04	[Bla88]

Figure A-2 shows the ratio of the activity coefficients (γ/γ_{eq}) as a function of the supersaturation for all investigated substances. The arrows highlighting the individual supersaturation range studied (zone two).
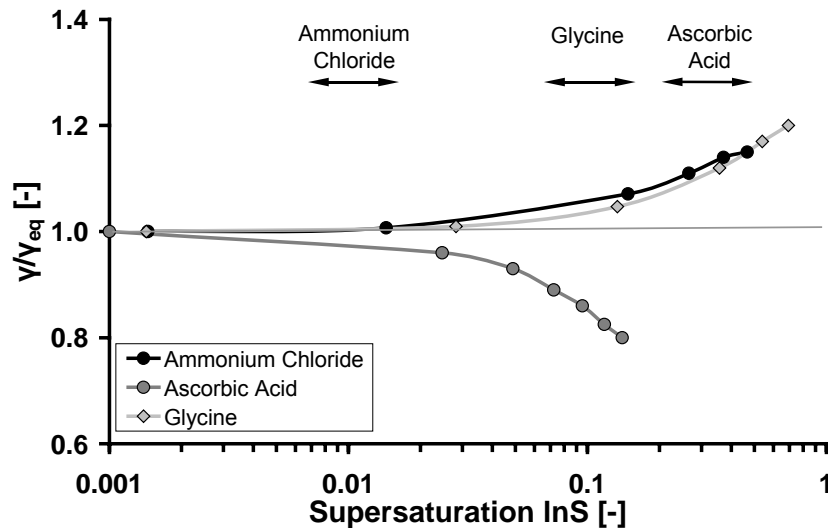
Figure A-2: Ratio of activity coefficients as a function of supersaturation at 25 °C [Moh02, Oma06b], arrows are indicating the experimental range (see chapter 10)

The use of activity coefficients was neglected for ammonium chloride and glycine. The extrapolation of the activity coefficient for ascorbic acid derived by Omar [Oma06b] seemed to be too uncertain.

Figure A-3 shows the binary diffusion coefficient for ammonium chloride [Hal53, Oht98] and glycine [Gin92] versus the concentration. For ascorbic acid, a diffusion coefficient of $5.8 \cdot 10^{-10}$ m²/s was determined by Robinson et al. [Rob90] at a concentration of 0.009 kg/kg water.
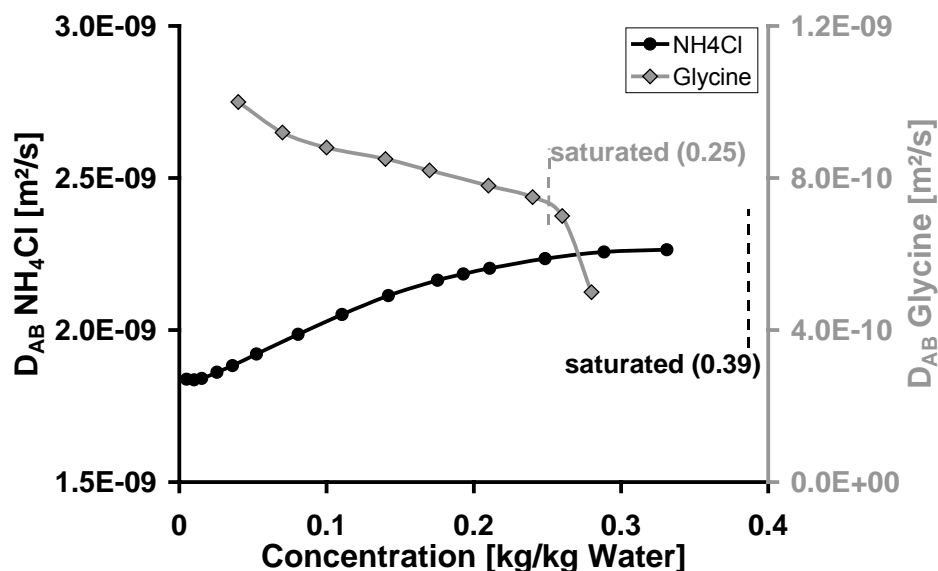
Figure A-3: Diffusion coefficient as a function of concentration at 25 °C [Hal53, Gin92]

The diffusion coefficient tends to decrease rapidly within the supersaturated regime [Gin92, Mye02].

A.2   Comparison between Laser Scanner and Laser Diffraction Instruments

From round robin studies it is known that a "single" particle analyser is generally capable of measuring the size distribution with a high precision [Jim92, Hay95a, Hay95b, Mer95b, Hay98]. Often the median particle size between duplicates or replicates differ only in the range of $L_{50} = \pm 2$ to 3% [Mer95b]. However, by comparing the same instrument class from different vendors (for example all laser diffraction and scattering instruments) a variation within the median particle size in the range of $L_{50} = \pm 25\%$ to 50% is observed [Mer95b, Hay98, Hay95a]. The variation can mainly be attributed to different instrument designs, if applicable, different deconvolution algorithms and individual operators using different instrument settings and sample preparation procedures. The results are dependent on the particle shape and if a narrow or wide particle size distribution is investigated. The variations of the respective measurements tend to be larger at the upper and lower end of the particle size distribution [Jim92, Hay95b].

By comparing different instrument classes of particle analysers, it must be distinguished if spherical or non-spherical particles are investigated. For spherical particles, the result does not depend on the orientation of the particle. Additionally, only one "characteristic length", the diameter, can be defined. Hayakawa et al. [Hay95a] investigated various distributions of spherical particles using different instrument principles. It was found out that the median particle size, between different instrument classes, differs in the range of $\pm 50\%$ to 100%, depending if a narrow or wide particle size distribution was studied.

Within crystallization processes, generally, non-spherical (irregular) particles are observed. Thereby, each instrument class responses different to particles that deviate from sphere and/or show non-ideal optical conditions [Nai98, Pat06]. Additionally, if a deconvolution of the raw measured data is applicable, spherical particle are generally assumed regardless the actual morphology [Neu02]. By comparing instruments based on different physical principles, the variation within the median particle sizes for non-spherical particles can become intolerable high ($L_{50} > \pm 100\%$) [Jim92, Hay95a, Hay95b, Mer95b, Bar96, Hay98, Nai98, Pat06].

Besides various distributions (for example: Q_0, Q_1, Q_2, Q_3) and mean sizes (for example: L_{median}, L_{mode}, L_{mean}) different characteristic sizes that describe a non-spherical particle can be defined. It can be distinguished between geometrical lengths (for example: L_{length}, L_{width}, $L_{diagonal}$), geometrical equivalent diameters (for example: L_{volume}, $L_{surface}$, $L_{projected\ area}$) and physical equivalent diameters corresponding to an individual equipment class (for example: L_{sieve}, $L_{settling}$, L_{stokes}, $L_{scattering}$). A relation between these characteristic sizes is necessary to complement any comparison among instruments. In general, the interrelation is given by the relation $L_{char-1} \approx f(shape)\ L_{char-2}$ [Les84, Les02, Gar02, Li05a, Pat06]. For further details it is referred to the following references [Sca85, Sca96, Les02, Sca03] and figure A-4(b). Randolph and Larson [Ran88] proposed to choose the characteristic length for any crystal shape in such a way that the relation between the surface (k_A) and volume shape factor (k_V) is

equal to 6. For a detailed discussion on the characteristic length measured by the laser scanner instrument it is referred to Vaccaro et al. [Vac06a].

Various studies have been made that compare the FBRM with other sizing techniques [Dow01, Hea02, Abb02, Tei05, Li05a, Pat08]. Thereby, often glass, ceramic beads, Duke standards, BCR quartz powders, PVC, silica and emulsion drops are taken as particulate systems. For the comparison, however, only the chord length distribution (or some weighted form) without any deconvolution, is used. The results are ranging from oversizing, undersizing, poor performance in differentiating median sizes up to a good agreement. A good agreement of the deconvoluted FBRM signal to other sizing techniques was found by Worlitschek et al. [Wor05] and Li et al. [Li05c].

Figure A-4(a) compares the 3D-ORM measurement with laser diffraction. The result shown in figure A-4(a) is typical for all substances and individual sieve cuts studied within this work. For a thorough comparison it is referred to figure A-5. The chord length distribution was converted to a particle size distribution using the method described in chapter 9.2.1. The volume distribution was subsequently obtained by weighting. The distribution refers to a suspension density of 11 kg/m^3_{Susp} and a measuring time of 12 minutes. To ease the comparison, the number of channels of the distribution measured by the 3D-ORM was changed to number of the laser diffraction device.
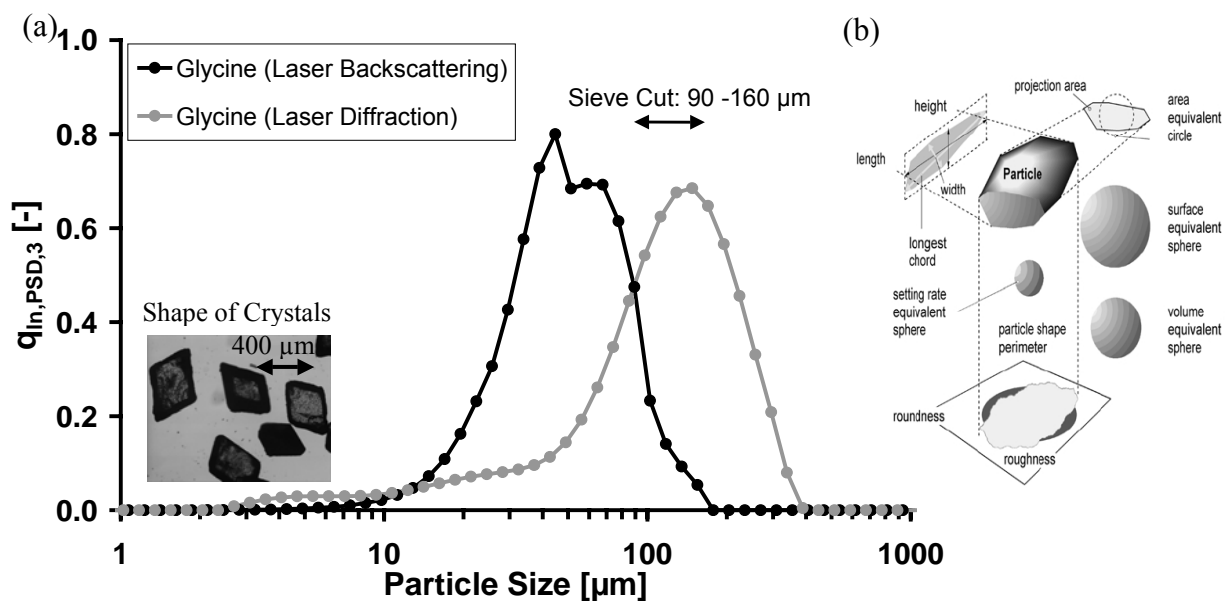
Figure A-4: (a) Comparison between a laser scanner and a laser diffraction device (sieve cut: 90-160 μm), (b) illustration of various characteristic lengths [Mül01]

Both measurement principles are not in good agreement with the respective sieve cut of 90 – 160 μm. The laser diffraction device measured particles up to 400 μm. Additionally, tails towards smaller sizes were observed for α-glycine and ascorbic acid (see figure A-5). According to Neumann et al. [Neu02] these tails are typical for flakes and tablet like particles. Teipel [Tei02] showed that those tails could also be caused by transparent crystals. An evaluation using the Mie-theory instead, as suggested by Teipel [Tei02], led to no significant changes.

In comparison, the laser scanner showed a clear undersizing of the respective sieve cut, as also observed by various other authors [Hea02, Li05a, Pat08, Hu08]. Patchigolla et al. [Pat08] reported differences within the median size of up to 200 µm. The systematic undersizing can be cause by several non-ideal conditions that are described in detail in chapter 5.3.2. Contrary, Chew et al. [Che07a] found the square weighted chord length distribution of α-glycine crystals to be in close agreement with image analysis.

Figure A-5 shows the particle size measurement using the laser scanner and laser diffraction device for different sieve cuts. The capability to distinguish between different particle sizes depends on the substance and instrument (see chapter 8.2.2). Both instrument therefore record different particle size distributions that would lead to different crystal growth kinetics.

Ammonium Chloride
Laser Scanner (at 10 kg/m³$_{Susp}$)   Laser Diffraction
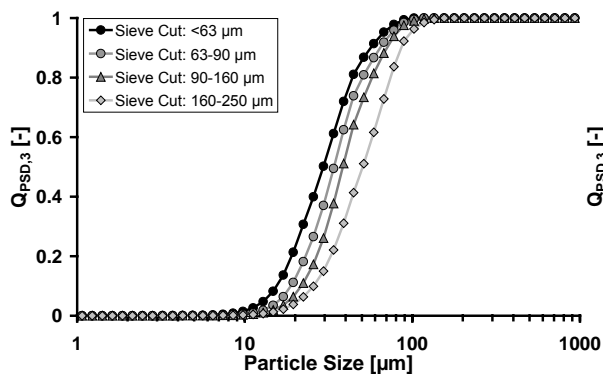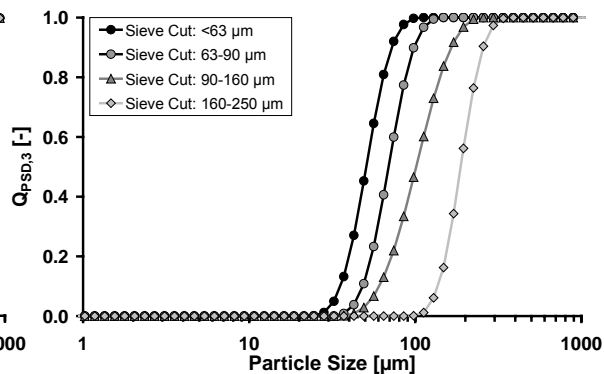
Ascorbic Acid
Laser Scanner (at 11 kg/m³$_{Susp}$)   Laser Diffraction
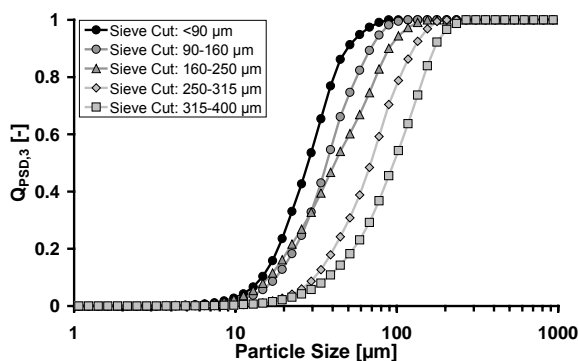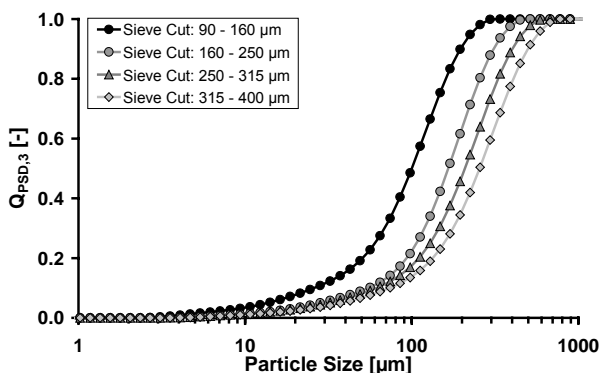
α-Glycine
Laser Scanner (at 11 kg/m³$_{Susp}$)   Laser Diffraction
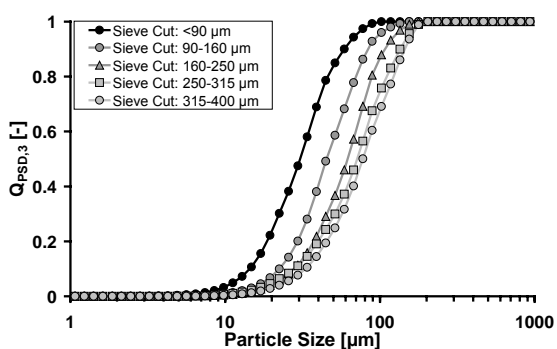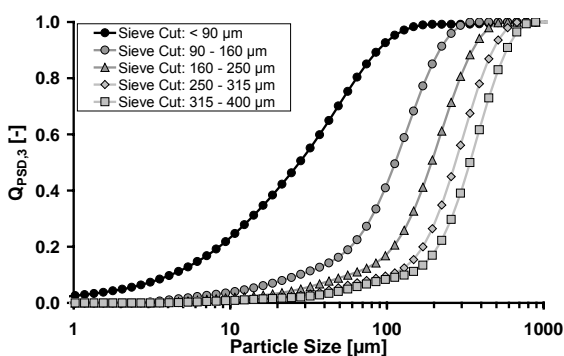
Figure A-5: Comparison between laser scanner and laser diffraction instruments; the chord length distribution of the laser scanner was converted using the method described in chapter 9.2.1 and subsequently weighted to a Q$_{PSD,3}$ distribution, the laser diffraction data was evaluated using the Fraunhofer diffraction theory*

*sieve cuts vary between the individual model substances

A.3   Additional Data for Chapter 8.1

Ammonium Chloride

(a)

(b)

Ascorbic Acid

(a)

(b)

Glycine

(a)

(b)
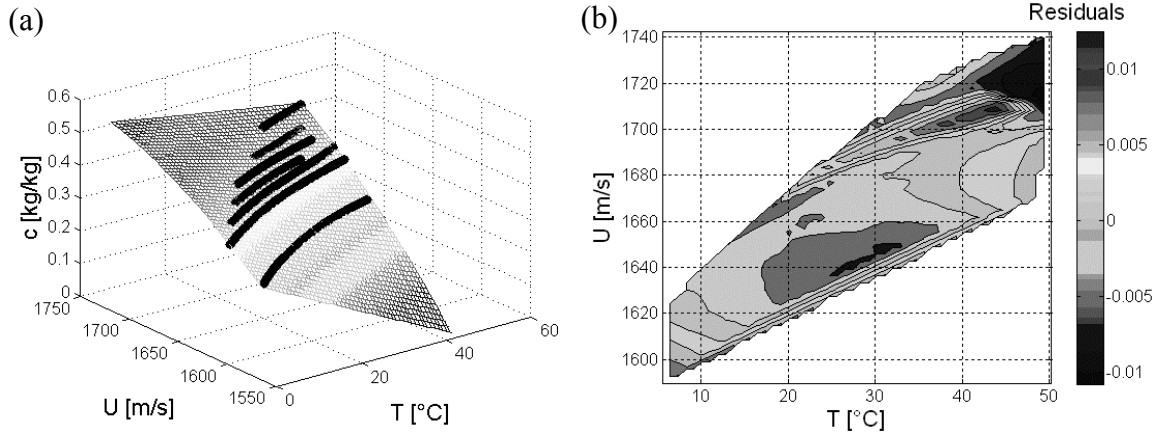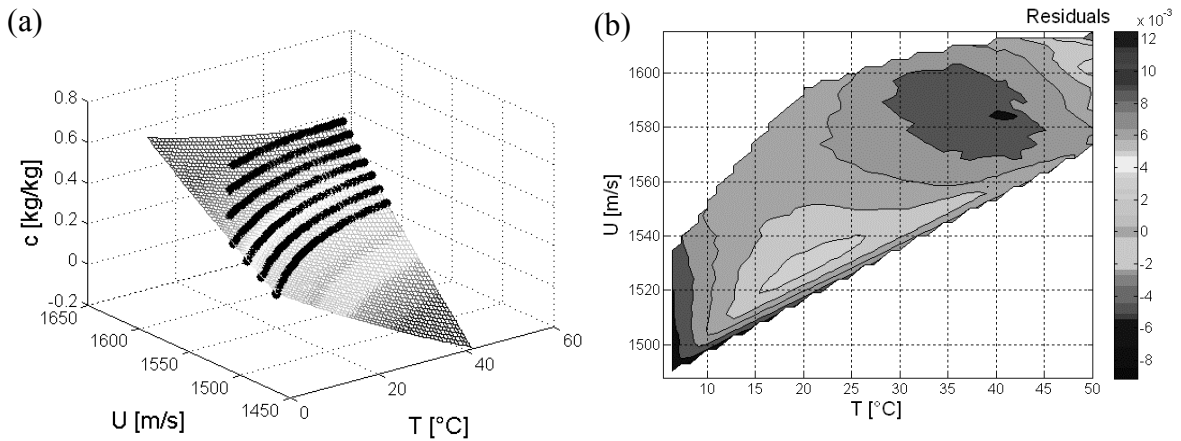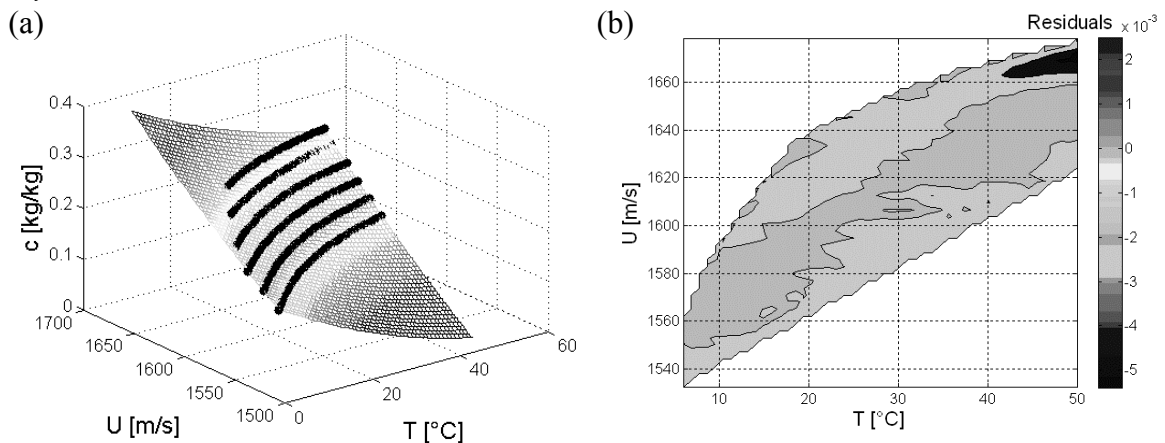
Figure A-6: Calibration of the ultrasound probe (a) Comparision between experimental data (black dots) and model prediction (shaded surface) using equation 8.3, (b) residuals between experimental data and prediction

A.4   Additional Data for Chapter 8.2.1

Ammonium Chloride (Experimental Range: 10-30 kg/m³$_{Susp}$)
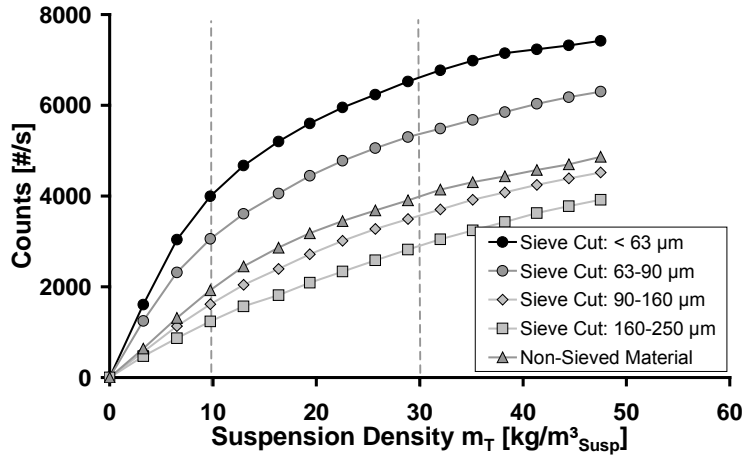
Ascorbic Acid (Experimental Range: 10-100 kg/m³$_{Susp}$)
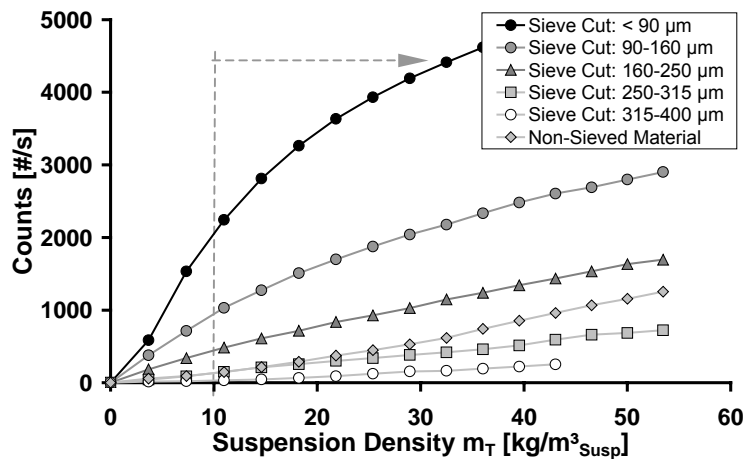
α-Glycine (Experimental Range: 8-40 kg/m³$_{Susp}$)
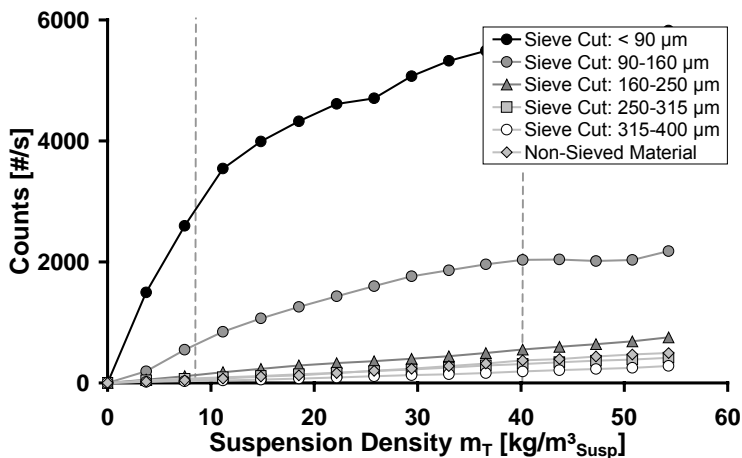
Figure A-7: The effect of the suspension density on the measured "counts"*

*sieve cuts vary between the individual model substances

A.5   Additional Data for Chapter 8.2.2

Ammonium Chloride

Sieve Cut: 63-90 μm
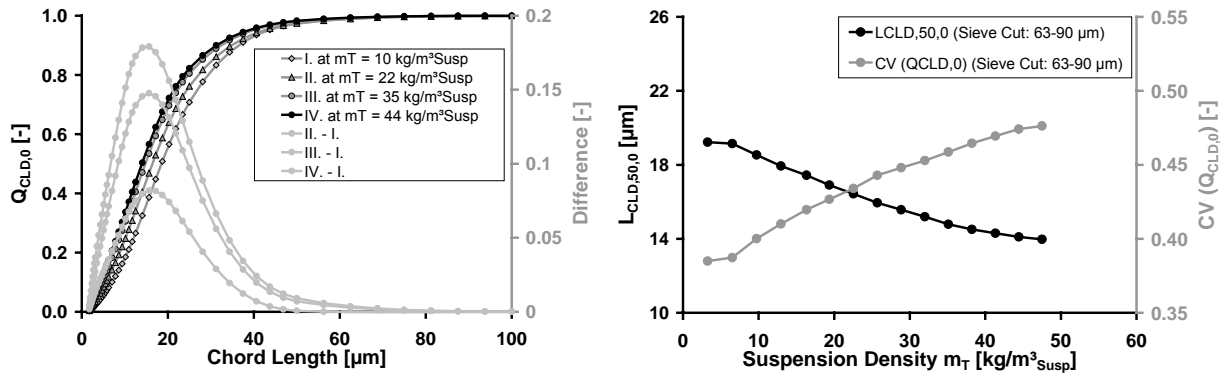
Sieve Cut: 90-160 μm
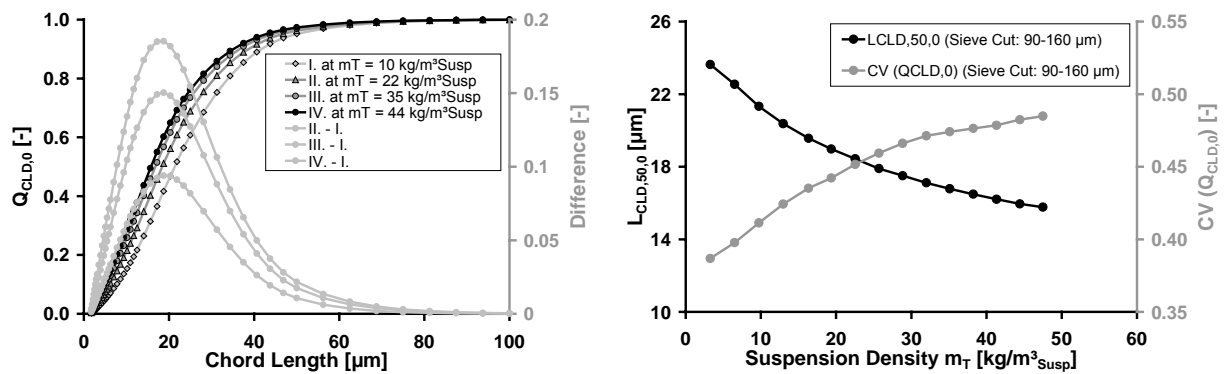
Non-Sieved Material
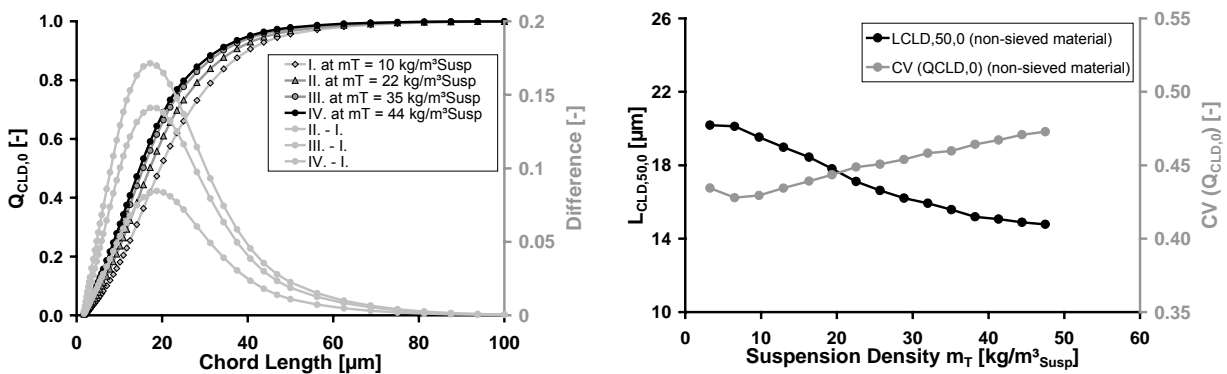
Figure A-8: The effect of the suspension density on the cumulative distribution ($Q_{CLD,0}$), the median chord length and on the CV-value of the $Q_{CLD,0}$ distribution*

*all other sieve cuts (< 63 μm, 160-250 μm) showed similar results

Ascorbic Acid

Sieve Cut: < 90 μm
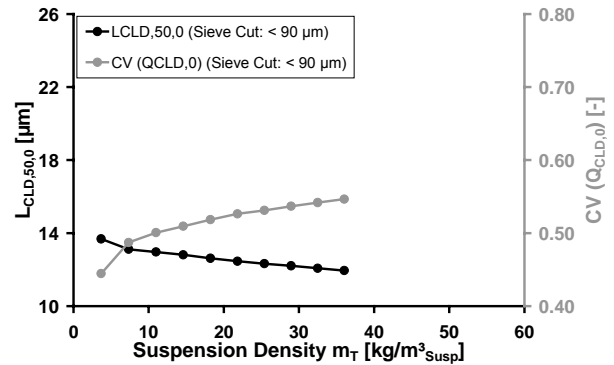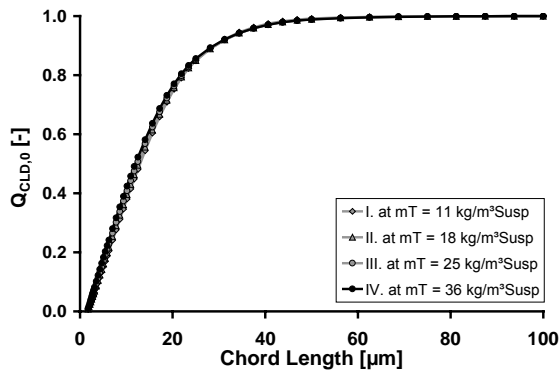
Sieve Cut: 90-160 μm
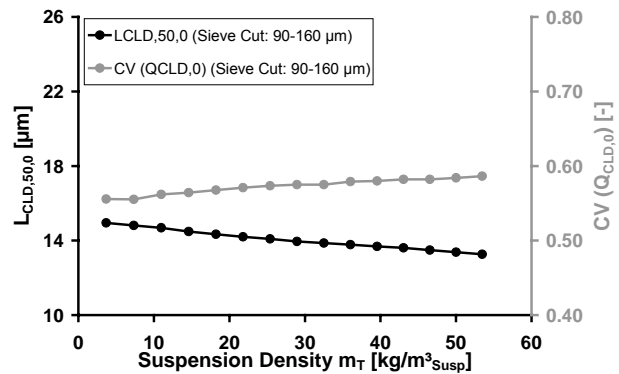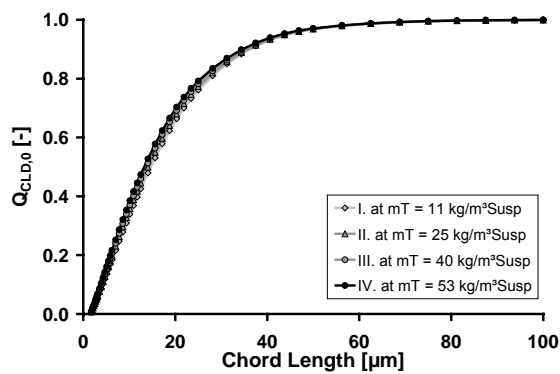
Non-Sieved Material
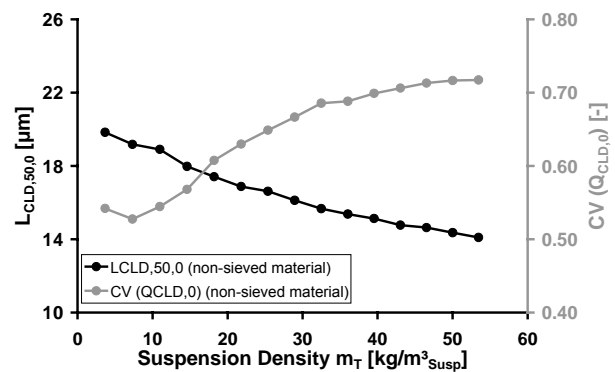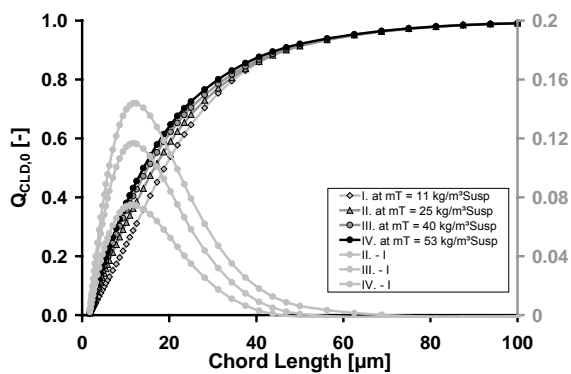
Figure A-9: The effect of the suspension density on the cumulative distribution ($Q_{CLD,0}$), the median chord length and on the CV-value of the $Q_{CLD,0}$ distribution*

*all other sieve cuts (160-250 μm, 250-315 μm, 315-400 μm) showed similar results

α-Glycine

Sieve Cut: < 90 µm
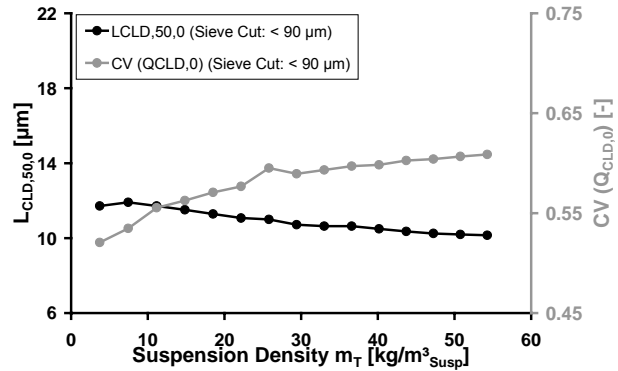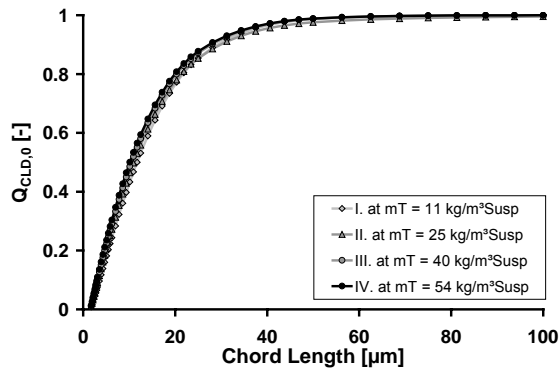
Sieve Cut: 90-160 µm
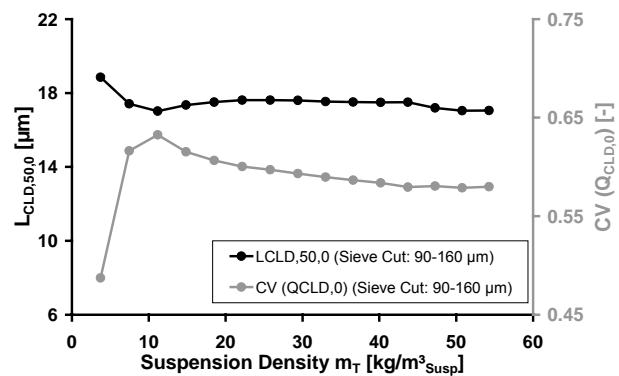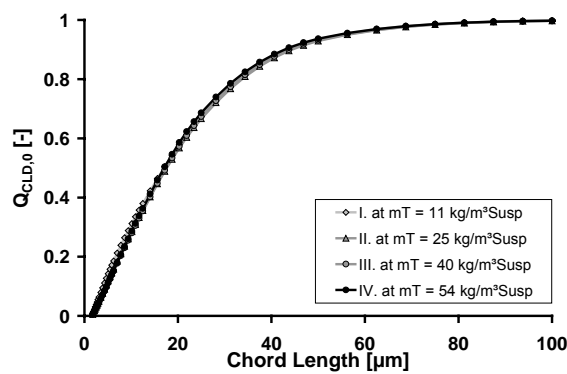
Non-Sieved Material
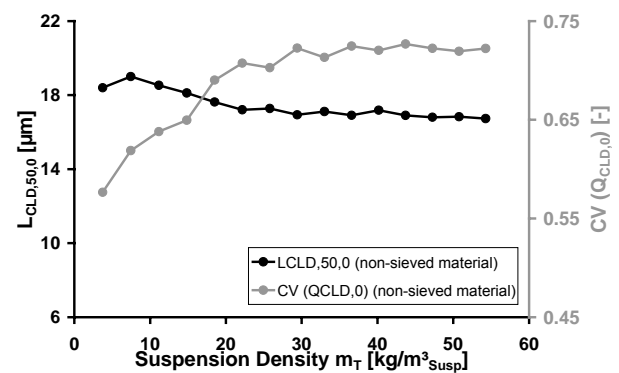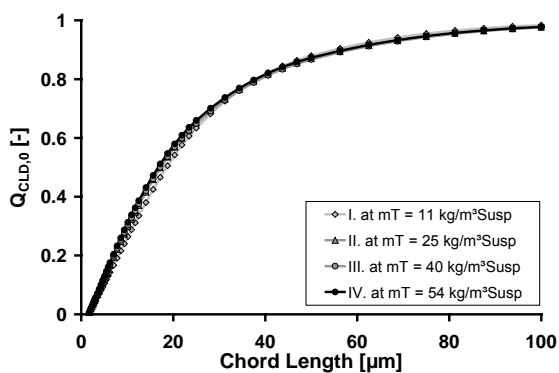
Figure A-10: The effect of the suspension density on the cumulative distribution ($Q_{CLD,0}$), the median chord length and on the CV-value of the $Q_{CLD,0}$ distribution*

*all other sieve cuts (160-250 µm, 250-315 µm, 315-400 µm) showed similar results

A.6   Additional Data for Chapter 8.3.1

Ammonium Chloride (Experiment 1)
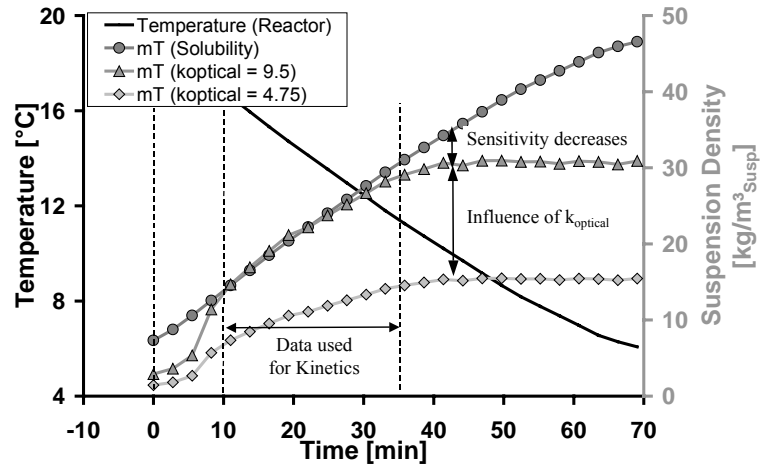
Ascorbic Acid (Experiment 1)
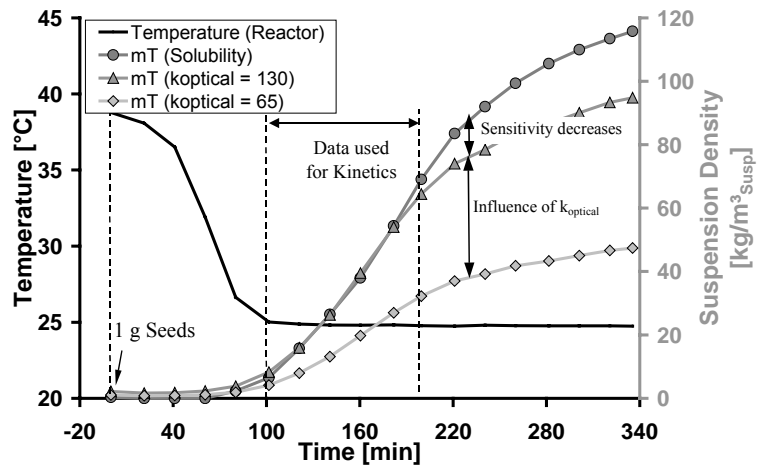
α-Glycine (Experiment 4)
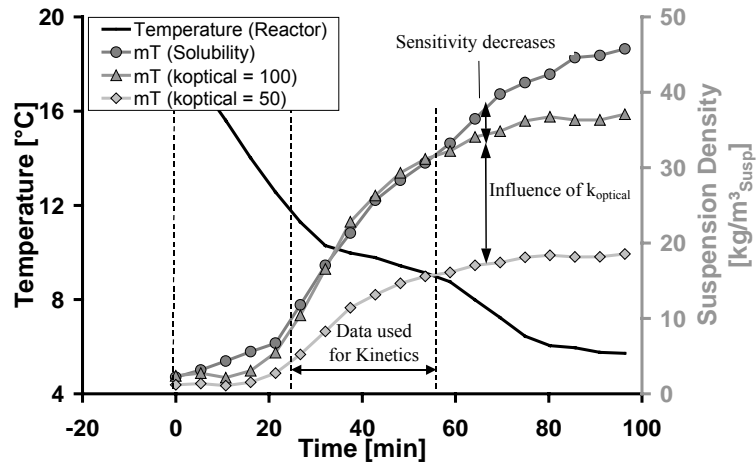
Figure A-11: Influence of the optical factor on the calculated suspension density (m_T) in comparison to the suspension density calculated via the solubility and supersaturation measurement ($m_{T(Solubility)}$) (not every measurement point is shown)

A.7   Additional Data for Chapter 8.3.2

Ammonium Chloride (Experiment 1)
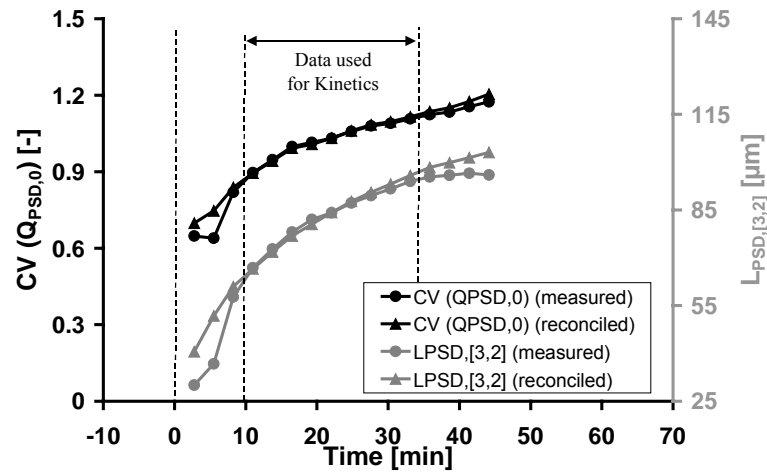
Ascorbic Acid (Experiment 1)
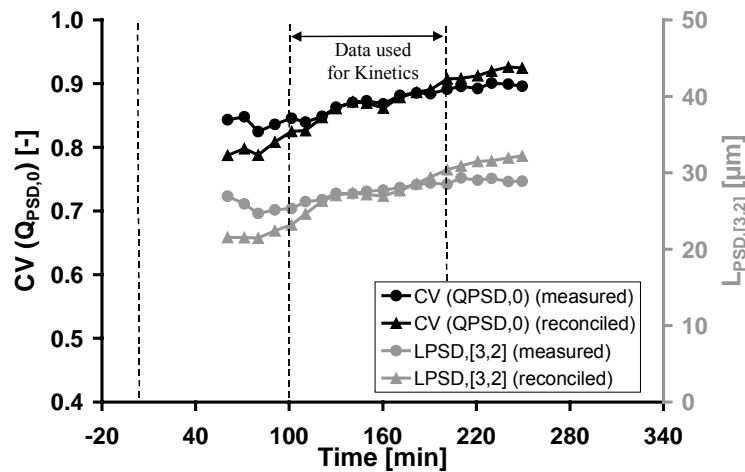
α-Glycine (Experiment 4)
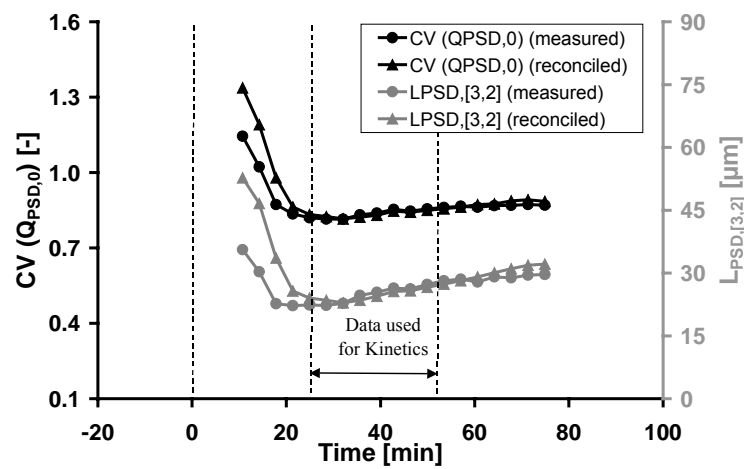
Figure A-12: Effect of data reconciliation on the Sauter diameter and CV-value (not every measurement point is shown)
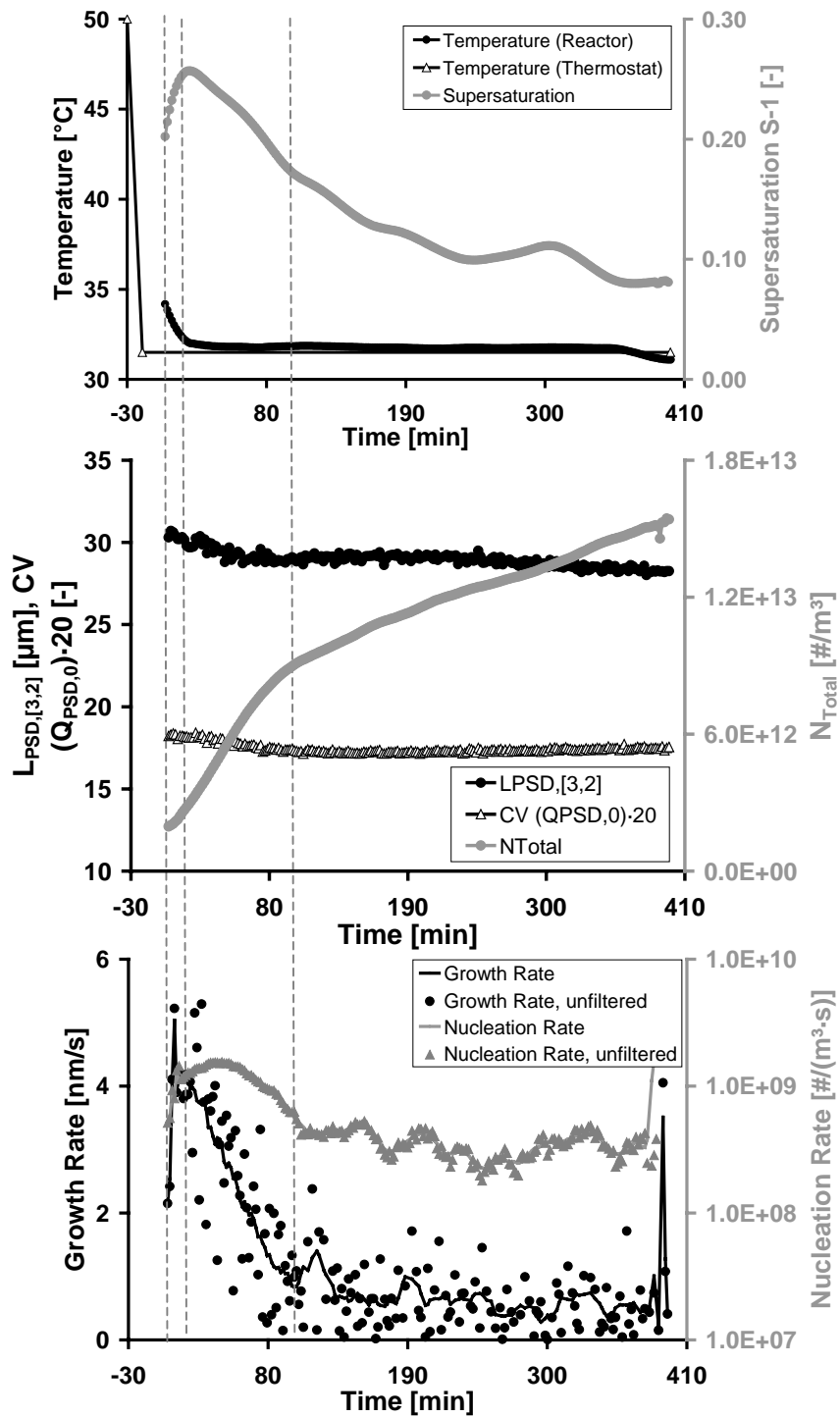
A.8 **Additional Data for Chapter 10.2 (Ascorbic Acid)**
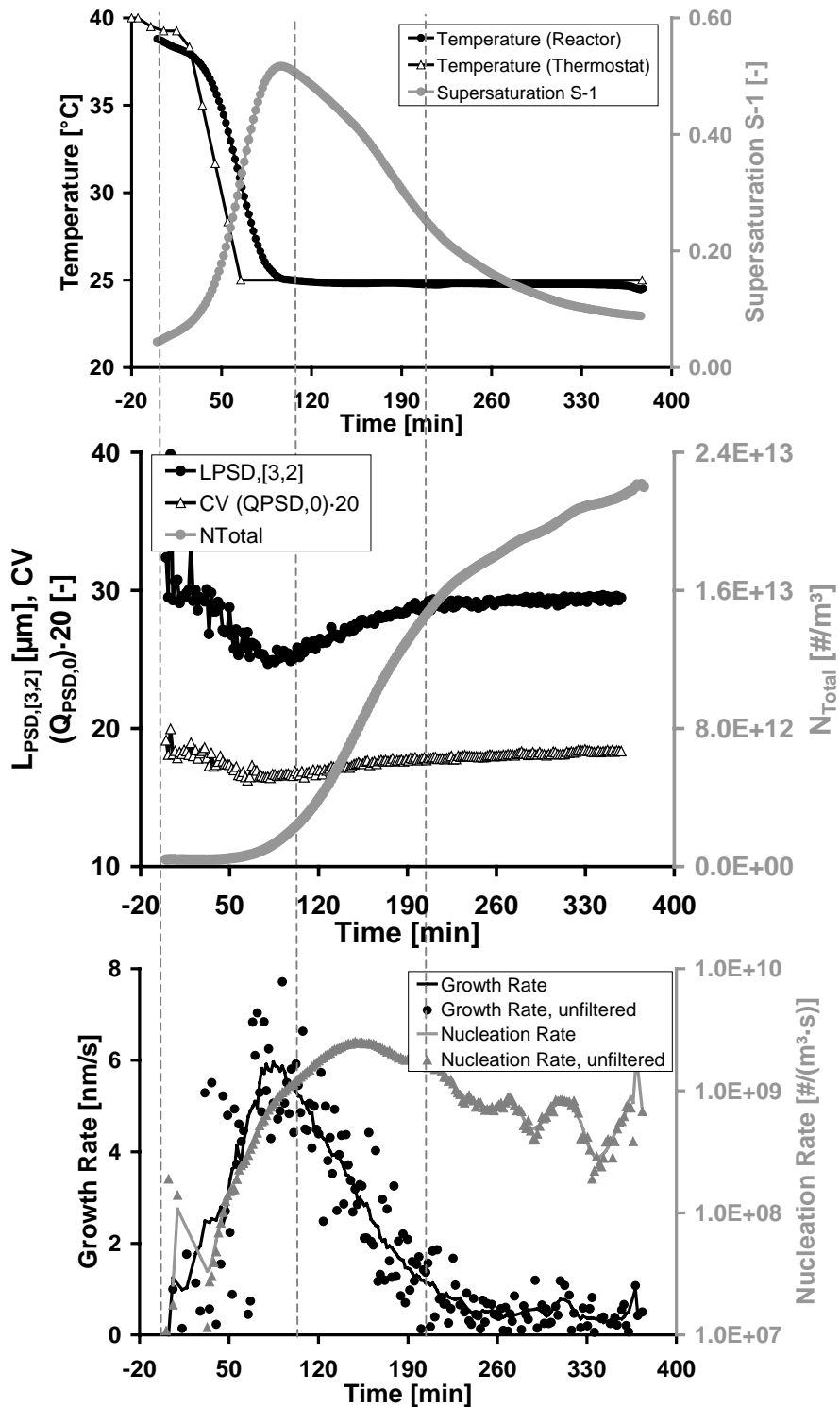
Figure A-13: Experimental data and calculated parameters for the crystallization of ascorbic acid (experiment 1, zone 2: from 100 to 200 min)
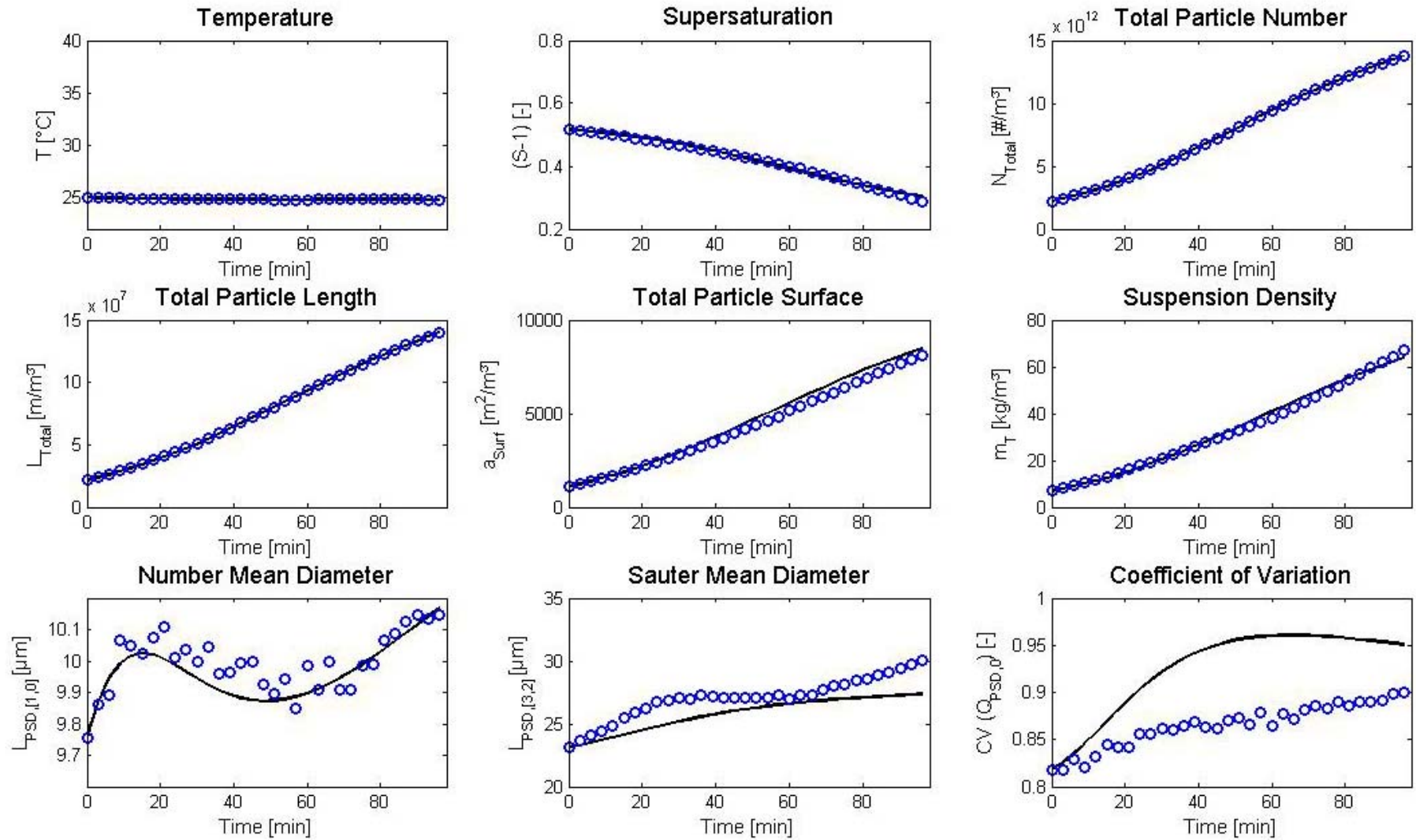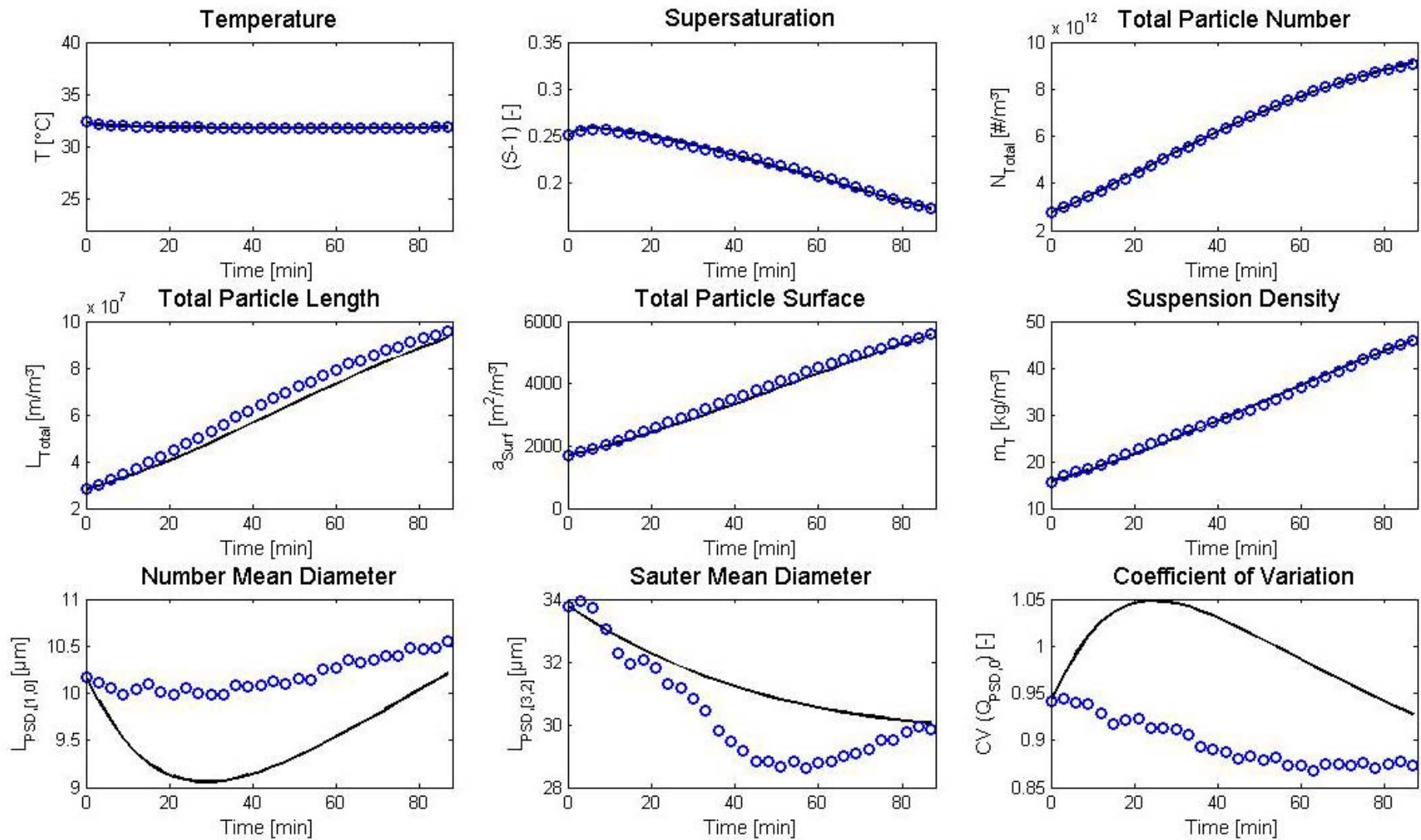
Figure A-14: Comparison between experimental data (circles) and simulation (line) (experiment 1, zone 2: 100 min, every third measurement point)
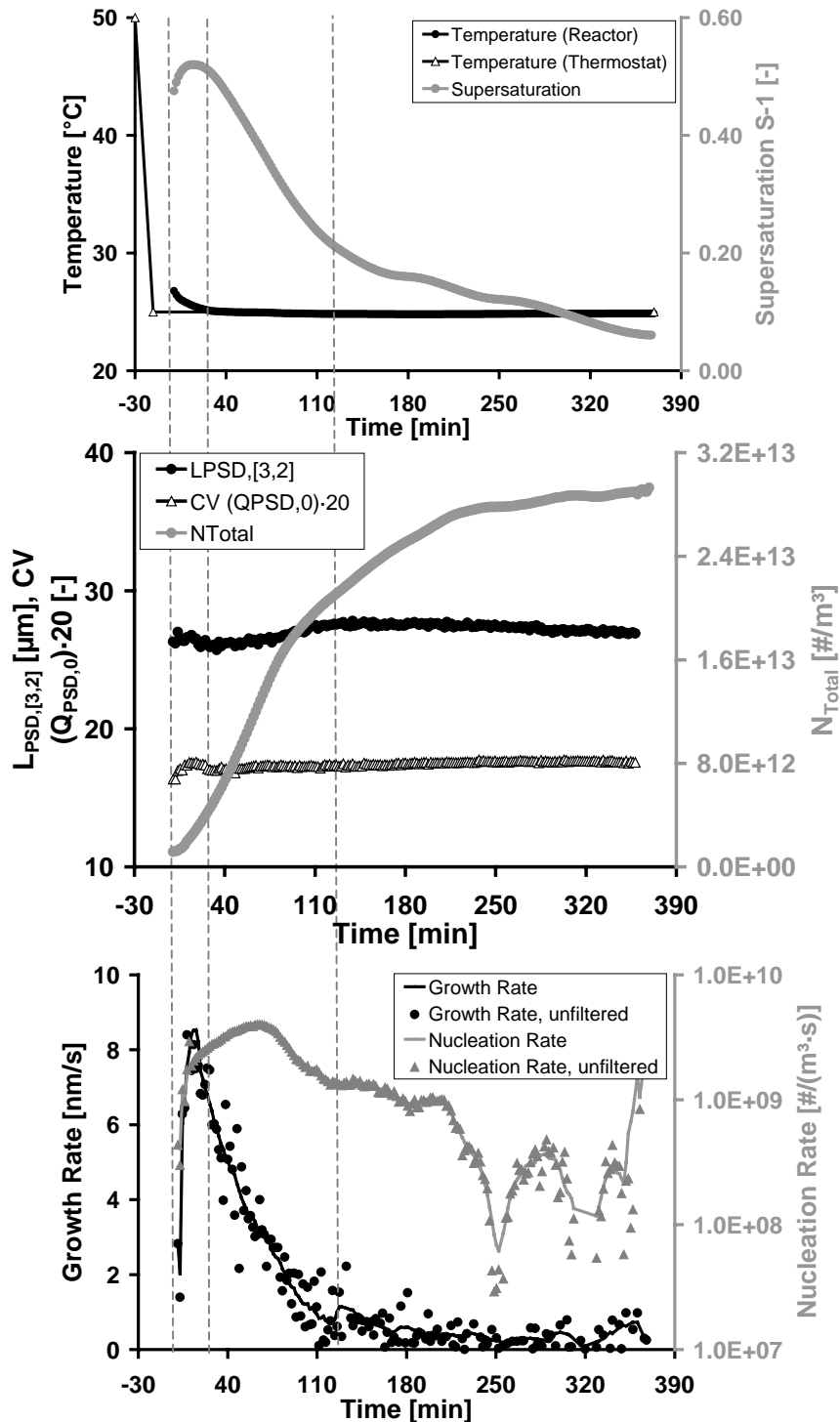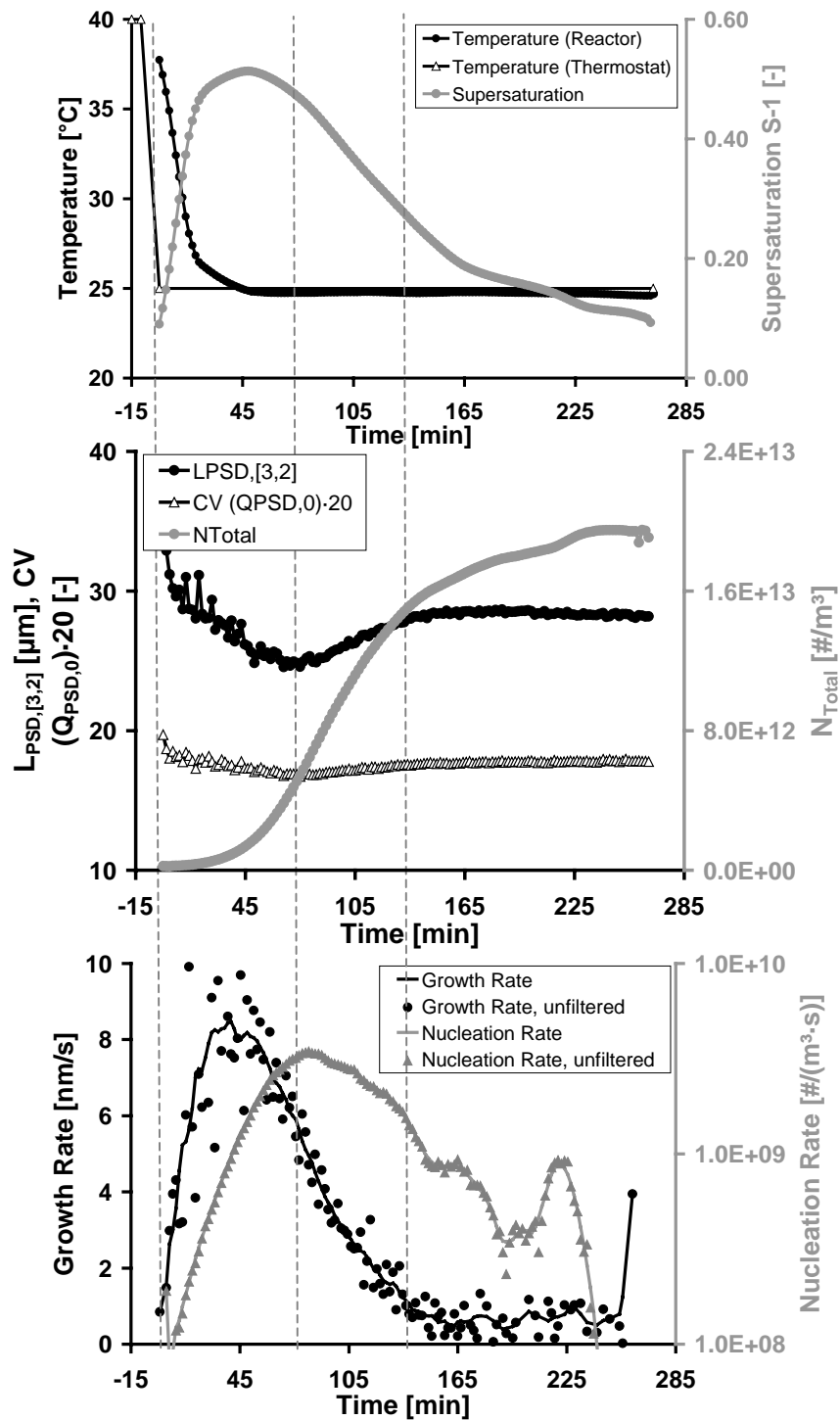
Figure A-15: Experimental data and calculated parameters for the crystallization of ascorbic acid (experiment 3, zone 2: from 25 to 125 min)
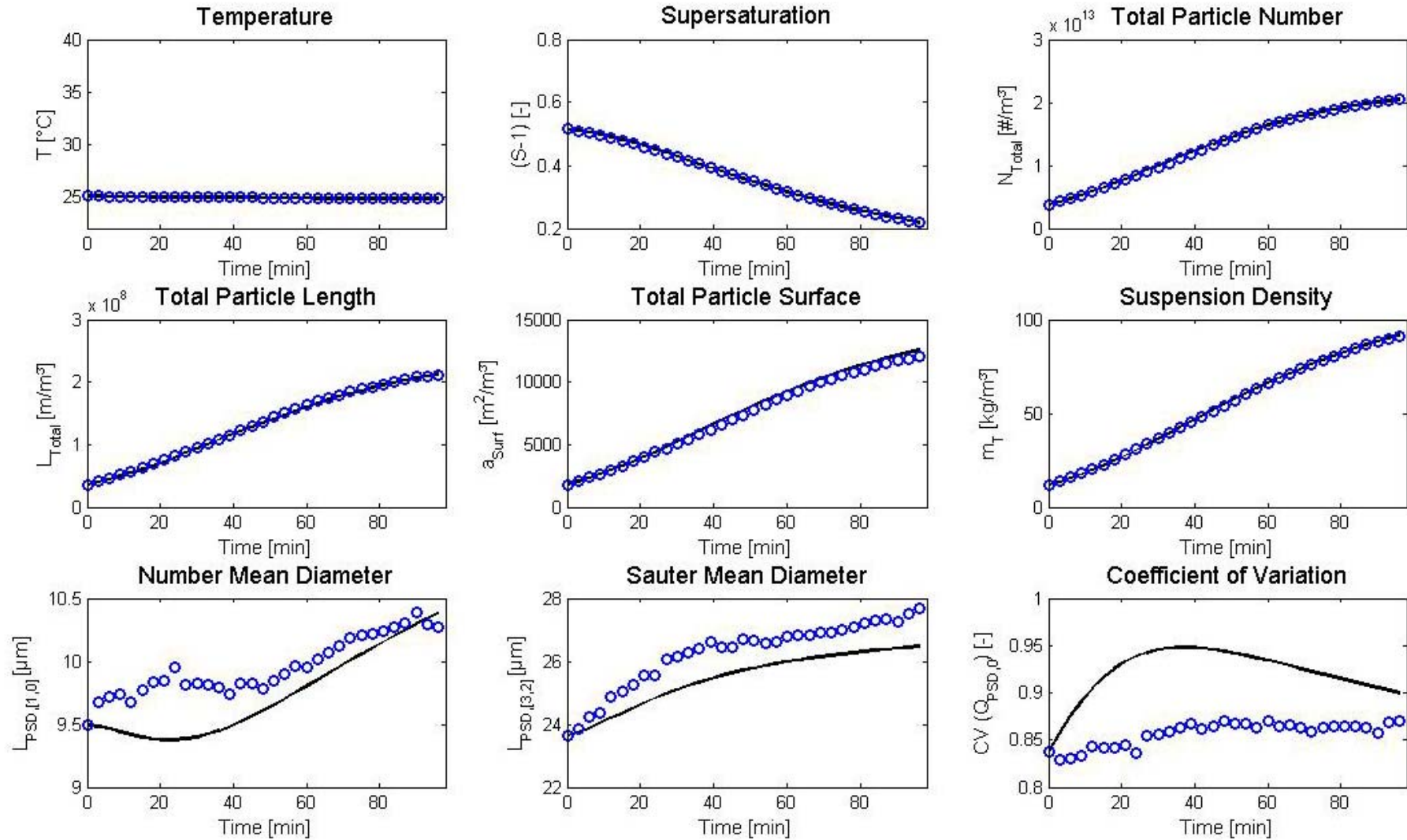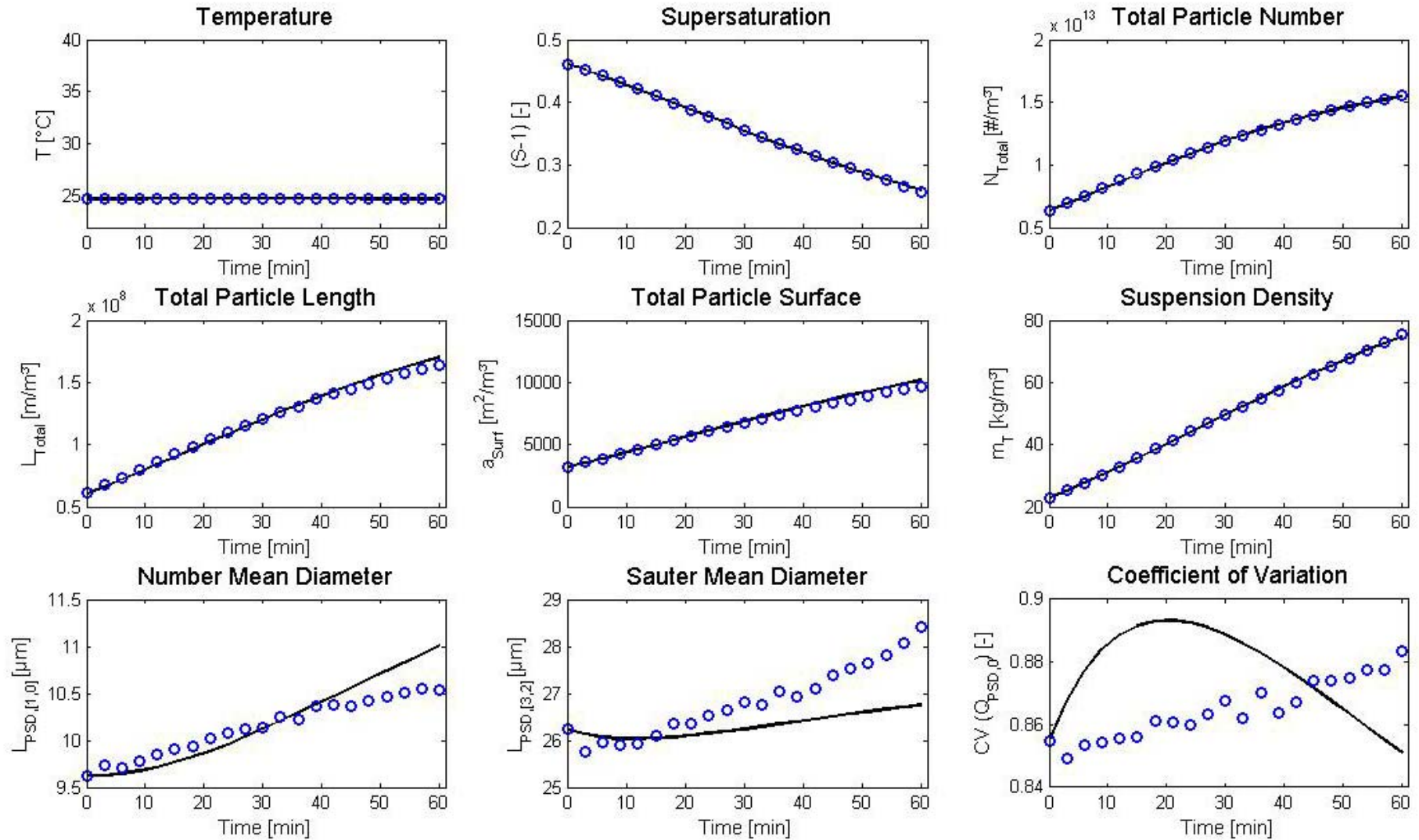
Figure A-16: Comparison between experimental data (circles) and simulation (line) (experiment 3, zone 2: 100 min, every third measurement point)
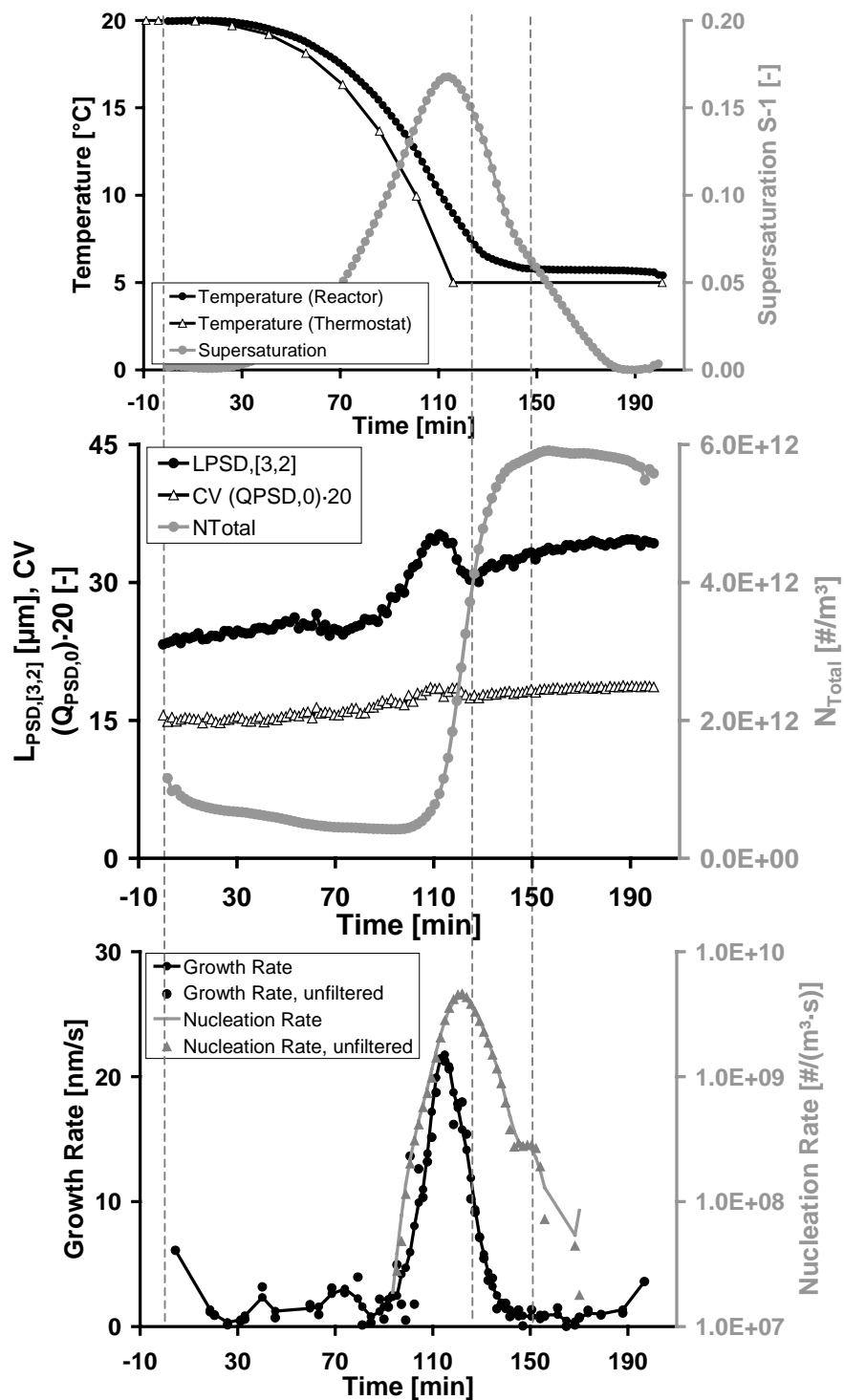
Figure A-17: Experimental data and calculated parameters for the crystallization of ascorbic acid (experiment 4, zone 2: from 10 to 100 min)

Figure A-18: Comparison between experimental data (circles) and simulation (line) (experiment 4, zone 2: 90 min, every third measurement point)

Figure A-19: Experimental data and calculated parameters for the crystallization of ascorbic acid (experiment 5, zone 2: from 80 to 140 min)

Figure A-20: Comparison between experimental data (circles) and simulation (line) (experiment 5, zone 2: 60 min, every third measurement point)

A.9 **Additional Data for Chapter 10.3 (α-Glycine)**

Figure A-21: Experimental data and calculated parameters for the crystallization of α-glycine (experiment 1, zone 2: from 125 to 150 min)
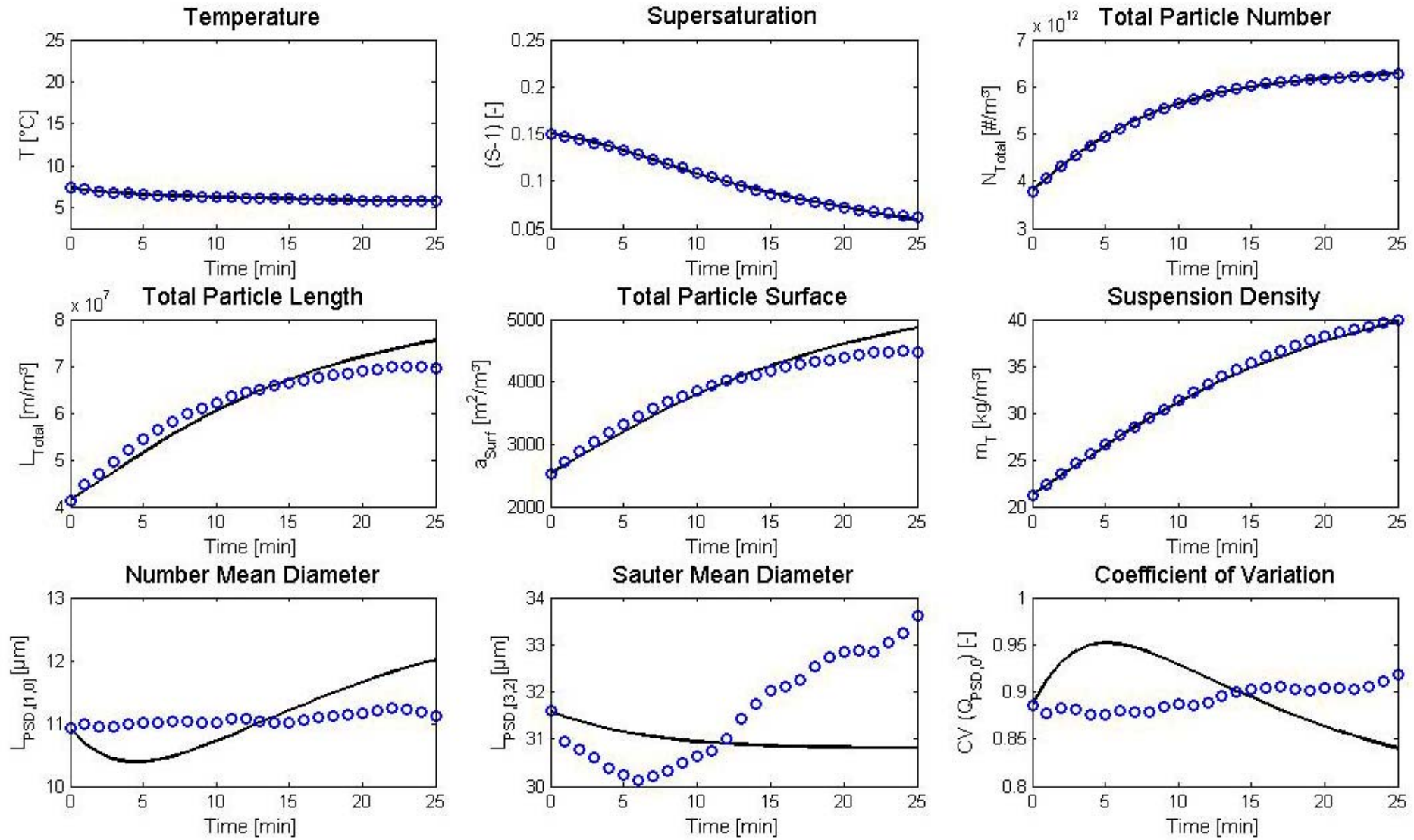
Figure A-22: Comparison between experimental data (circles) and simulation (line) (experiment 1, zone 2: 25 min)
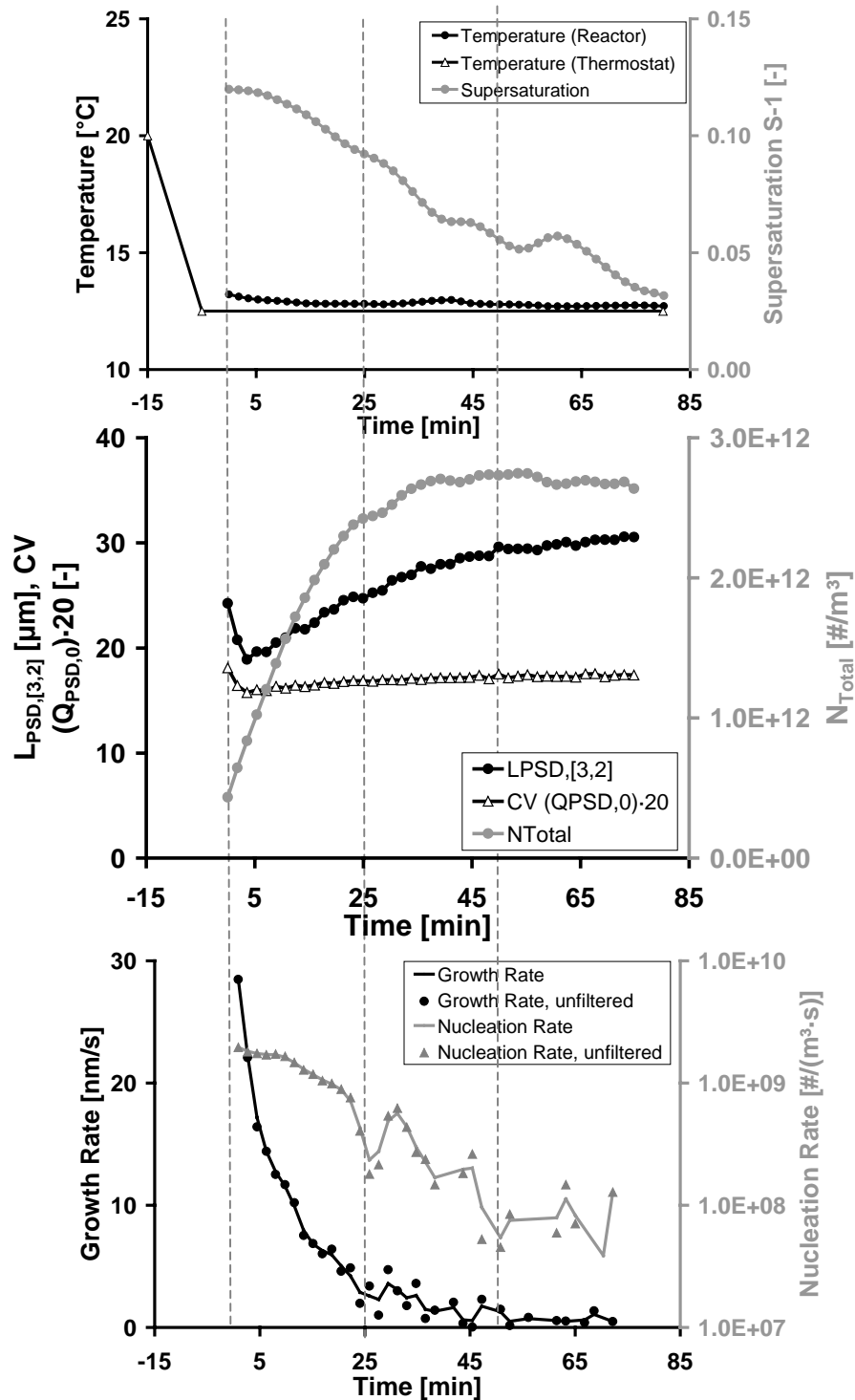
Figure A-23: Experimental data and calculated parameters for the crystallization of α-glycine (experiment 2, zone 2: from 25 to 50 min)
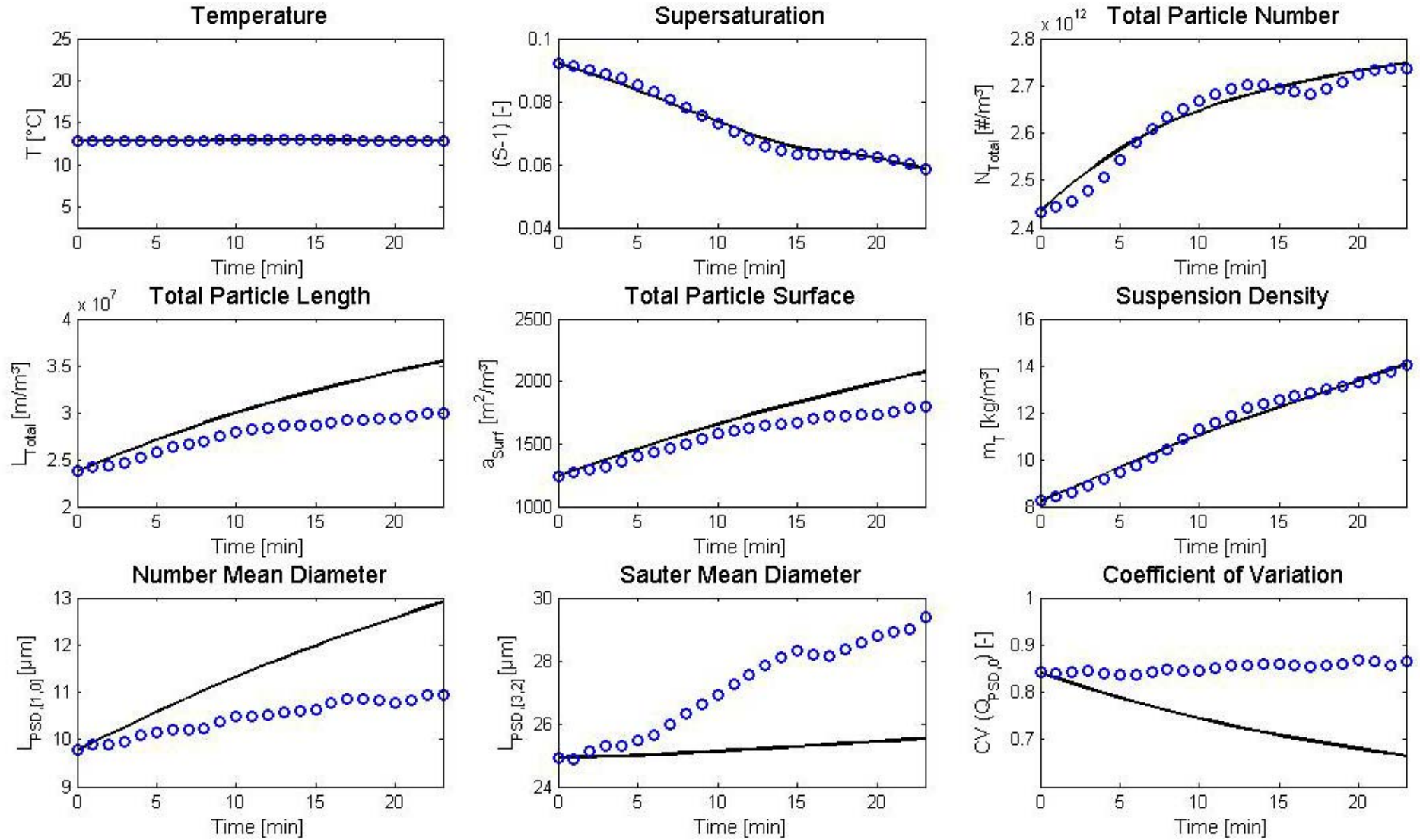
Figure A-24: Comparison between experimental data (circles) and simulation (line) (experiment 2, zone 2: 25 min)
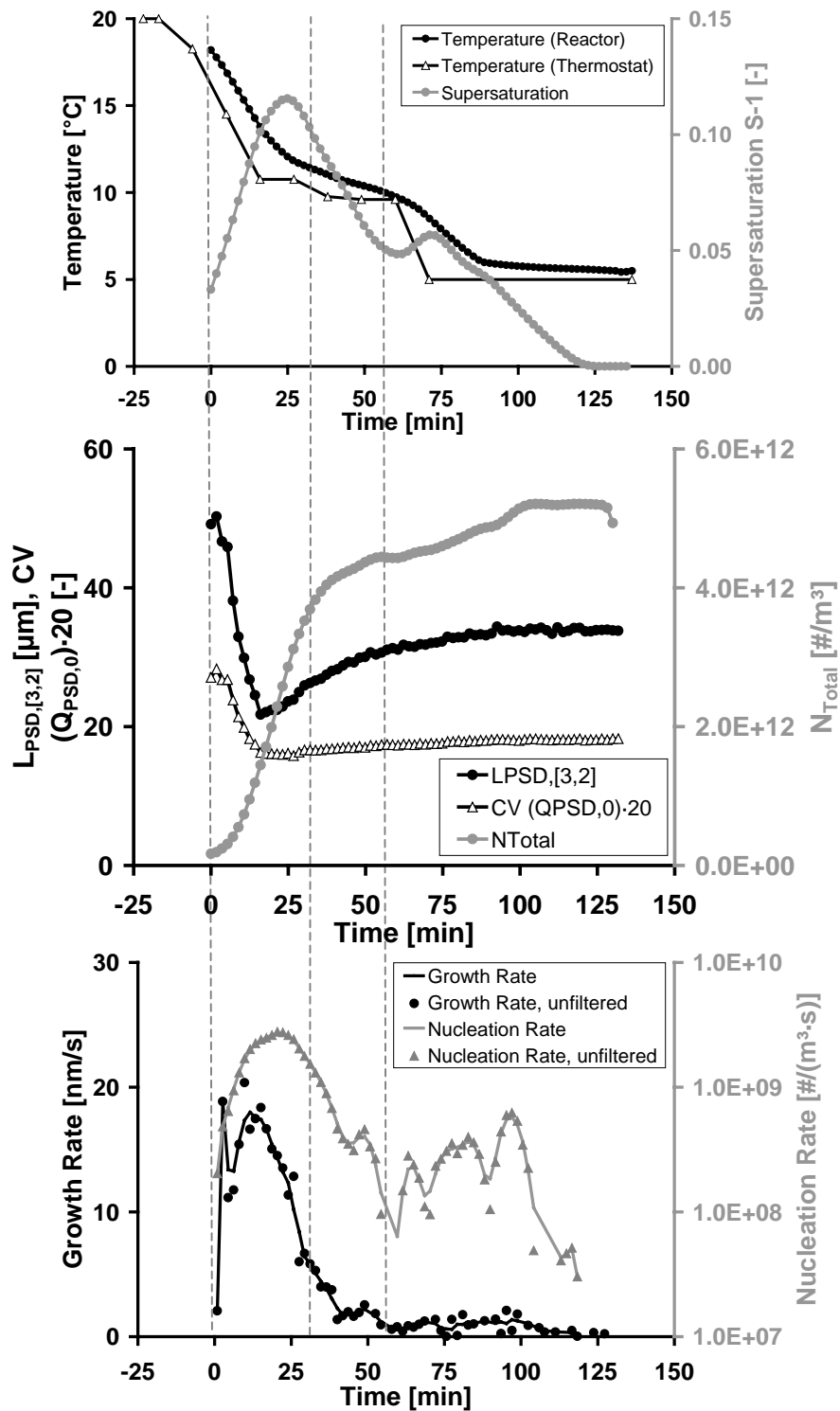
Figure A-25: Experimental data and calculated parameters for the crystallization of α-glycine (experiment 3, zone 2: from 30 to 55 min)
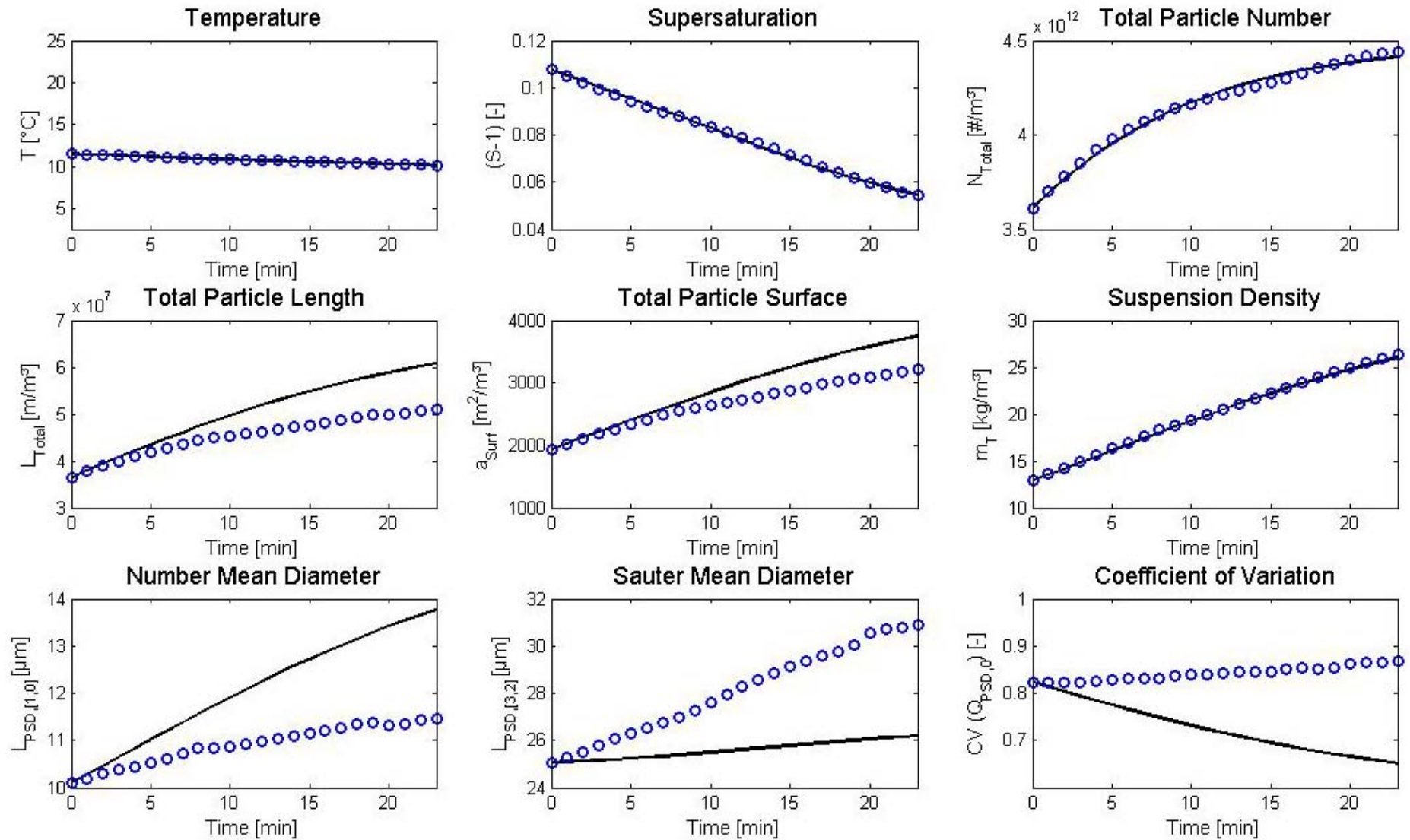
Figure A-26: Comparison between experimental data (circles) and simulation (line) (experiment 3, zone 2: 25 min)

Curriculum Vitae

Jörg Heinrich

11th of May, 1978	born in Wolfen (Sachsen-Anhalt), Germany
1984 - 1991	'Polytechnische Oberschule' (German type of elementary school), Sandersdorf, Germany
1991 - 1996	'Anne - Frank Gymnasium' (German type of grammar school), Sandersdorf, Germany, 'Abitur'
1996 - 1997	Civil Service as an Alternative to Military Service
1997 - 2003	Environmental Engineering, Martin-Luther-University Halle-Wittenberg, Halle, Germany, 'Diplom-Ingenieur'
2001 - 2002	Junior Chemical Engineer, GlaxoSmithKline plc, Department of Strategic Technologies, Tonbridge, United Kingdom
2003 - 2007	Research Assistant (PhD-Student), Martin-Luther-University Halle-Wittenberg, 'Zentrum für Ingenieurwissenschaften, Verfahrenstechnik/TVT', Halle, Germany
2007 - present	Process Engineer, DOW Olefinverbund GmbH, Department of Engineering Solutions, Schkopau, Germany

Halle (Saale), 19.09.2008   Jörg Heinrich

List of Publications

Heinrich, J., Elter, T., Ulrich, J.: Determination of crystallization kinetics using laser reflectance measurements and model-based experimental design and analysis, Proceedings, 17th International Symposium on Industrial Crystallization 14.-17.09 2008, Maastricht/Netherlands, ed. by Jansens, P., Ulrich, J., EFCE Event Number 665, 2008, 675-682

Heinrich, J., Ulrich, J.: Im Online-Einsatz – Bestimmung des Gehaltes and Saccharose und invertiertem Zucker, Lebensmitteltechnik 7/8 (2008), 48-49

Heinrich, J., Ulrich, J.: Tailoring Morphology and Particle Size Distributions via Crystallization, Book of Abstracts Volume 2, European Congress of Chemical Engineering (ECCE-6) 16.-20.09 2007 Copenhagen/Denmark, ed. by Gani, R., Dam-Johansen, K., EFCE Event Number 669, Nørhaven Book Denmark, 2007, 497-498

Heinrich, J., Ulrich, J.: Determination of Crystallization Kinetics using Novel Technologies, Proceedings, International Congress on Particle Technology (PARTEC 2007) 27.-29.03. 2007 Nürnberg/Germany, ed. by Peukert, W., Schreglmann, C., Proceedings CD, Nürnberg Messe GmbH Nürnberg, 2007

Heinrich, J., Ulrich, J.: Influence of Growth Regimes on Growth Rate Dispersion, Proceedings, 13th International Workshop on Industrial Crystallization 13.-15.09 2006, Delft/Netherlands, ed. by Jansens, P. J., ter Horst, J. H., Jiang, S., IOS Press Amsterdam, 2006, 177-184

Heinrich, J.: Neuheiten im Bereich der Kristallisation und Kristallisatoren (ACHEMA Berichte), Chemie Ingenieur Technik 78 (2006) 10, 1466-1471

Ulrich, J., Heinrich, J.: Reaktivkristallisation, Chemie Ingenieur Technik 77 (2005) 11, 1759-1772

Heinrich, J., Ulrich, J.: General considerations on predicting the influence of solubility on the maximum achievable particle size - A case study on pseudo-polymorphs, Proceedings, 16th International Symposium on Industrial Crystallization 11.-14.09 2005, Dresden/Germany, ed. by Ulrich, J., VDI-Berichte 1901, VDI-Verlag Düsseldorf, 2005, 85-90

Heinrich, J., Ulrich, J.: Modelling and Controlling of Multivariate Processes – A Case Study on Reactive Crystallization, Proceedings, 12th International Workshop on Industrial Crystallization 7.-9.09 2006, Halle/Germany, ed. by Jones, M. J., Ulrich, J., Universitätsdruckerei Martin-Luther-Universität Halle-Wittenberg, Halle, 2005, 133-140